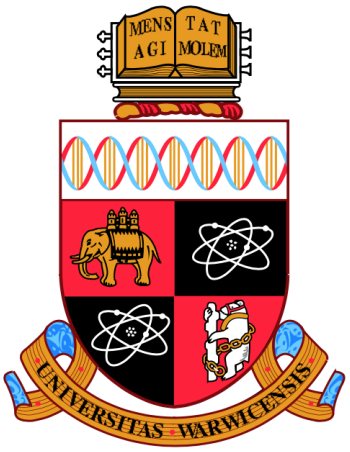

Simulation of Nonadiabatic Charge Transfer During Molecular Scattering at Metal Surfaces

by

Daniel Corken

Thesis

Submitted to the University of Warwick

in partial fulfilment of the requirements

for admission to the degree of

Doctor of Philosophy in Chemistry

Department of Chemistry

June 2023

Contents

List of Tables

List of Figures

Acknowledgments

I would first like to thank my supervisors Prof. Reinhard Maurer and Prof. Nicholas Hine for there guidance, support and patience throughout my PhD. I would also like to thank all the members of the Maurer group for their support, friendship and creating the best working environment I have ever experienced.

A special thank you goes to the mental health and well-being team at Warwick who have provided me with help and support throughout my time at the university. In particular to Sarah Meharg and Emma Foottit who helped me in my darkest hour and without whom I would not be here today.

Finally I would like to thank my family who have always supported me.

Declarations

This thesis is submitted to the University of Warwick in support of my application for the degree of Doctor of Philosophy. It has been composed by myself and has not been submitted in any previous application for any degree.

The work presented (including data generated and data analysis) was carried out by the author except in the cases outlined below:

Collaborators Gang Meng and Bin Jiang from the University of Science and Technology of China provided a machine learned model that outputs energies and diabatic coupling. The model was used to generate 2D potential energy surfaces in Section 5.3.1. I also used those potential energy surfaces to perform dynamics simulations that are described in Chapter 6. Use of data generated using the machine learned model is clearly indicated in the main text.

Abstract

The development of the next generation of heterogeneous catalysts requires a deep understanding of the fundamental processes that occur when molecules interact with metal surfaces. A key challenge to this goal is that nonadiabatic processes represent a key energy dissipation pathway when molecules interact with metal surfaces. Such processes lay outside the Born-Oppenheimer potential energy surface (PES) picture that is ubiquitous throughout chemistry and upon which electronic structure methods in computational chemistry rely. Modeling such systems is challenging because they combine large inhomogeneous models, in-plane periodicity with a need to combine electronic excitations with vibrational effects.

The dynamics algorithm independent electron surface hopping (IESH), which attempts to account for nonadiabatic effects when molecules interact with metal surfaces, has shown promise in reproducing experimental observations. IESH simulations require two diabatic PESs, of neutral and anionic charge transfer states. This thesis aims to create accurate diabatic PESs using the linear expansion delta self-consistent field (le-ΔSCF) excited state method. The two forms of le-ΔSCF, density based (ρle-ΔSCF) and wavefunction based (Ψle-ΔSCF) are assessed for the systems of NO-Au(111) and CO-Au(111). Only ρle-ΔSCF is shown to be a viable methodology for constructing charge constrained diabatic PESs due to SCF convergence issues. A new methodology for defining charge constraints in ρle-ΔSCF, which accounts for charge transfer between molecule and metal in the ground state, is developed and used to construct 2D diabatic PESs as a function of molecule-surface separation and molecule bond length, for CO interacting with Au(111) and Ag(111). IESH dynamics simulations of CO scattering from Au(111) and Ag(111) across a range of initial vibrational states and translational kinetic energies are performed and the results are compared to other methods and to experiment.

Abbreviations

- 2D - Two-dimensional
- 3D - Three-dimensional
- AIMD - *Ab initio* molecular dynamics
- BOA - Born-Oppenheimer approximation
- CDFT - Constrained density functional theory
- DFT - Density functional theory
- DOF - Degrees of freedom
- DOS - Density of states
- EHP - Electron hole pairs
- FSMO - Free standing molecular over-layer
- FSSH - Fewest switches surface hopping
- GAC - Generalised adiabatic connection
- GGA - Generalised gradient approximation
- HF - Hartree-Fock
- HOMO - Highest occupied molecular orbital
- HSOMO - Highest singly occupied molecular orbital

- ICS - Image charge stabilisation
- IESH - Independent electron surface hopping
- KS - Kohn-Sham
- le-ΔSCF - Linear expansion delta self consistent field
- LUMO - Lowest unoccupied molecular orbital
- MIM - Metal-insulator-metal devices
- ML-CDFT - Machine learned constrained density functional theory
- MODOS - Molecular orbital projected density of states
- MQCD - Mixed quantum-classical dynamics
- MDEF - Molecular dynamics with electronic friction
- NAMD - Nonadiabatic molecular dynamics
- PBC - Periodic boundary conditions
- PES - Potential energy surface
- PAW - Projector augmented wave
- REMPI - Resonance enhanced multi-photon ionisation
- SCF - Self-consistent field
- SEP - Stimulated emission pumping
- SOMO - Singly occupied molecular orbital
- TD-DFT - time dependent density functional theory
- UHV - Ultra-high vacuum

Chapter 1

Introduction

The chemistry of surfaces has been the recipient of a great deal of interest and effort, over the past century in particular, and rightly so. The modern world as we know it owes much to technologies that have been made possible by our increasingly detailed understanding of this unique realm of chemistry. A surface in the context of surface chemistry is the interface between two phases of matter, for example solid-gas, solid-liquid, liquid-gas *etc.* The work presented in this thesis deals exclusively with the solid-gas class of surfaces, specifically, the interface of a crystalline metal interacting with gas phase molecules and how to model their physics. Such surfaces represent an interesting challenge in chemistry because they are interfaces between two better known and usually more easily understood areas of chemistry: the solid phase and the gas phase. Crystals are highly ordered periodic structures that can be efficiently and accurately modelled by taking advantage of the 3D periodicity by introducing periodic boundary conditions (PBC) into models. Gas phase molecular chemistry is rich and complex, but the species involved are very often small enough that sophisticated high-level theories can be applied to model them. Surface chemistry offers the challenge of combining the two domains. Surface systems are periodic in only two dimensions, x and y. Surfaces also possess unique chemistry because when a bulk crystal is cleaved, the exposed surface has electronic and vibrational 'surface' states that are 2D localised to the top few layers of the exposed surface. In particular, metal surfaces provide access to potentiall new areas of chemistry because of these surface states that enable new chemistry when molecules interact with the surface, via the transfer for electrons from the to the molecules [1].

Two dominant areas of application that have played a big part (though certainly not the only part) in motivating the advancement of surface science are semiconductors and heterogeneous metal catalysts. It is difficult to overstate the impact

semiconductor technology has had on modern life. Almost all of us use devices every day, such as mobile phones, tablet computers, and PCs that contain semiconductor chips with billions of individual transistors on them. The rapid reduction in size of an individual transistor on a semiconducting surface, that makes powerful computation so fast and commonplace, has relied heavily on surface characterisation techniques of ever increasing sophistication and precision to better understand and design semiconductor chips [2].

Another major area of focus in surface science that has had an equally, if not more, important impact on the world today is heterogeneous catalysis. Society today is reliant on catalytic surfaces in ways that most people take for granted or are entirely unaware of, such as the generation of commercially important chemicals and fuels, or the reduction of pollutants expelled from automobile exhausts using catalytic converters. Perhaps the most striking and far reaching example of this impact is the Haber-Bosch process [3, 4].

At the turn of the 20^{th} century humanity was facing an existential crisis when intensive farming was depleting the nitrogen content of soils, which is essential for healthy crops and good yields [5]. The primary source of fixed nitrogen used at the time to replenish the soils was guano, the excrement of seabirds (or bats) that had built up into large deposits over many years. Unfortunately guano deposits build up far too slowly to keep up with the demand and were a quickly dwindling resource. An alternative method of reintroducing fixed nitrogen to soils was desperately required to avoid crop failure leading to mass starvation in the coming decades. One of the simplest nitrogen containing molecules that can be readily converted to more complex nitrogen containing molecules, which can then be used by plants, is ammonia (NH_3). The constituent elements are abundant all over the earth, and yet for centuries scientists failed to find an efficient way to convert N_2 and H_2 into NH_3. Many experiments that can essentially be boiled down to variations on the idea of putting the gasses into a container and exposing them to extreme temperatures and pressures where attempted, but alas, the yields of ammonia were pitiful. It was only in 1908 after Fritz Haber performed a similar experiment in the presence of an osmium catalyst that ammonia was produced in significant yields [3]. Just three years later Bosch had made the first mass production ammonia plant [4]. Both men subsequently received Nobel prizes for their respective work; they had solved the existential crisis that was facing humanity, as no longer would millions potentially starve when depleted soils could no longer produce high yields of crops. Now, replenishing the nitrogen content of soils was simple, using fertilizers derived from NH_3. It was the inclusion of the catalytic surface chemistry of Os that made the

process viable. Since the initial work of Haber and Bosch, the process has been further optimised and the osmium surface has been replaced, primarily with iron-based catalysts; however, work to find new and more efficient catalysts continues to this day [6].

A host of other industrially, commercially and environmentally significant chemical reactions are routinely carried out all over the world using heterogeneous catalysis. Another important example is the catalytic converters that are mandatory in all modern cars with internal combustion engines [7]. Pt, Pd and Rh based catalysts, along with cerium oxide as a promoting agents, are used to convert toxic and environmentally damaging NO_X molecules to benign N_2 and oxidise any residual hydrocarbons present in combustion engine exhausts, due to incomplete combustion of the fuel, to CO_2. Without the widespread use of catalytic converters, levels of air pollution, particularly in urban areas, would be much higher and have huge impacts on public health [7].

Clearly, having a deep and rigorous theoretical understanding of the processes that govern surface catalysis is incredibly important, not to mention extremely valuable. For the last 100 years the majority of catalyst development has been a costly process of trial and error in which potential catalytic materials and additives are screened empirically in different ratios and under different conditions until the most optimal combinations are found [2, 8]. Such is the value of new catalysts, however, that this cost has been endured and new catalysts have been developed. Since the 1950 and 60s there has been an explosion in the available techniques for analysing and characterising surfaces based on their composition, structure and morphology, electronic states and the nature of molecular adsorption and reaction [1]. More recently the development of those experimental techniques has worked in tandem with accurate atomic scale theories based on quantum mechanics to accurately model these systems [9, 10]. There is a sense in which experimental surface science and theoretical surface models have 'met in the middle'.

One of the strengths and/or weaknesses of theoretical surface models, depending on what one is interested in, is that, due to large computational costs, they must be simplified to exclude much of the complexity of real world surfaces. This means the 'messiness' of real world chemistry, such as surface defects, step edges, high temperatures, complex mixtures, or aggregates of reactants and solvent effects are excluded. The reduction on complexity allows a sharp focus on the remaining degrees of freedom at the expense of all others. Experimentalists often seek to work with simplified systems in order to rigorously control as many degrees of freedom as possible. They have managed, at great effort, to also exclude much of the complexity

of practical catalyst under reactive conditions and instead work with so-called model catalysts. For example, by performing studies under ultra high vacuum conditions and using single crystals with low miller index surfaces exposed [1, 2]. The use of model catalysts ultimately means that a typical model used in theoretical atomic scale simulations, a clean slab of metal atoms interacting with a single molecule and surrounded by empty vacuum is, not as far from the experiments as it would be compared to a practical catalyst environment.

It is known that ultimately the chemical possesses unfolding at surfaces, catalytic or not, are governed by quantum mechanics, the rules of which are well understood. However, even setting aside the complexity of the chemical system itself, the sheer complexity in finding solutions to the equations that describe quantum mechanics present a huge barrier to modelling chemical processes. This problem was described eloquently be Dirac in 1929: 'The underlying physical laws necessary for the mathematical theory of a large part of physics and the whole of chemistry are thus completely known, and the difficulty is only that the exact application of these laws leads to equations much too complicated to be soluble' [11]. Therefore, the computational chemist must find reasonable ways of reducing complexity and making sensible approximations to both the physical system being modelled and the theory, and hence the equations, that describe them, to have any hope of gaining insight. A simplified description of the path our theoretical understanding takes when attempting to create accurate models of chemistry at metal surfaces, and in particular catalytic surfaces, is to reduce the complexity of the problems while still managing to capture the essential physics. There are 3 main forms these simplifications take and together they form the so-called standard model of surface science [9, 10]. Firstly, the level of theory; almost all first principles atomistic models used to study surface reactions are based on density functional theory (DFT), rather than using high-level quantum chemistry methods, that are more accurate than DFT. The second approximation is reduced dimensionality, where non-essential degrrees of freedom (DOF) are excluded from models. For example restricting substrate motion or modeling core electrons using pseudopotentials. The final approximation is to use the Born-Oppenheimer approximation (BOA) or the electronic adiabaticity approximation (described in detail in Section 2.1.2) to dramatically reduce the complexity of the numerical problems to be solved [12]. A much more detailed discussion of these approximations is given in Section 3.2. The work in this thesis uses all three of the aforementioned approximations to construct accurate models of interactions of diatomic molecules interacting with metal surfaces. In particular, this work focuses on the third approximation (BOA), including its consequences and ways to

accurately describe the non-adiabatic behaviour. The vast majority of the results displayed herein are focused on CO or NO molecules interacting with Au(111) or Ag(111) surfaces because these are systems that have been experimentally observed to display nonadiabatic behaviour and there is a large amount of very high quality data to compare to [10, 13–15]. CO/NO molecules in a vibrationally excited state can engage in nonadiabatic energy transfer when scattered from the metal surfaces. A significant proportion of the vibrational energy (often several quanta) is transferred from molecule to surface when vibrational modes of the molecule couple with electronic states of the metal and trigger the excitation of electron-hole pairs, which is a clear violation of the BOA since one of the main consequences of the BOA is that nuclear and electronic motion are decoupled. These systems are investigated using the occupation-constrained DFT method linear expansion ΔSCF (le-ΔSCF) [16, 17] to construct adiabatic and diabatic potentials in order to model the interaction between molecule and metal. The effectiveness of le-ΔSCF and the potentials is assessed. Subsequently the models are used to perform nonadiabatic molecular dynamics (NAMD) simulations using the independent electron surface hopping (IESH) [18] algorithm and the results are compared to trends from experiment.

The primary reason for this, aside from a general aspiration to build accurate models that can reproduce experimentally observed behaviour, is that previously published works in which a neutral and an anionic diabatic potential energy surface (PES) was constructed and combined with the IESH method for the system of NO on Au(111) are flawed in the way it modelled diabatic charge states [18, 19]. The anionic and neutral charge states of the molecule as it interacts with the surface were modelled by applying a small electric field, in order to move charge either from metal to molecule or vice versa. The use of an explicit excited state method such as le-ΔSCF, which was developed with the aim of being able to model charge transfer states of molecules absorbed on metal surfaces, can facilitate the construction of more accurate diabatic PESs [16]. Creating high quality diabatic PESs is important because it helps make clearer how much any flaws (or success) of IESH simulations is due to the IESH method itself, rather than the underlying PES.

This concludes the introduction chapter, which has provided a broad overview of the background and motivations for the work presented in this thesis. The structure of the remainder of this thesis is as follows: Chapter 2 provides a rigorous explanation of the theories that are used throughout the work presented in this thesis. Chapter 3 will describe previous works in the literature relating to nonadiabatic effects at metal surfaces, starting with experimental findings (3.1), followed by com-

putational studies (3.2). Chapter 4 will assess the ability of the le-ΔSCF method to model charge transfer states of CO and NO at metal surfaces and determine a reliable methodology, using le-ΔSCF, to construct diabatic PES. Chapter 5 will use the methodology developed in Chapter 4 to construct 1D and 2D PES for CO interacting with Au(111) and Ag(111) surfaces. Chapter 6 will use the 2D PES presented in Chapter 5 to perform nonadiabatic dynamics simulations of CO scattering from Au(111) and Ag(111) surfaces and compare the results to experimental observations. Finally, Chapter 7 will summarise the work presented in previous chapters and describe how future works might build on the work presented here.

Chapter 2

Theoretical overview

2.1 Quantum mechanical models of chemical systems

This section will describe how chemical systems are described using quantum mechanics, starting from the full many-body Schrödinger equation and introducing several approximations that reduce the complexity to enable computational models to be implemented.

2.1.1 The many-body problem

All information about a system in a pure quantum state is contained in the wavefunction $\Psi(\boldsymbol{r})$. Information regarding how the particles of the system interact with each other and how the wavefunction evolves over time is captured by the Schrödinger equation [20]:

$$\mathrm{i}\frac{\mathrm{d}}{\mathrm{d}t}\Psi(\boldsymbol{r}_1, \boldsymbol{r}_2, \ldots, \boldsymbol{r}_N, t) = \hat{H}\Psi(\boldsymbol{r}_1, \boldsymbol{r}_2, ..., \boldsymbol{r}_N, t), \tag{2.1}$$

where Ψ is a function of the positions of each particle $\boldsymbol{r}$ and time t in an N particle system. The time evolution of the Schrödinger equation is discussed later in this section. This section will be limited to discussion of solutions to the time-independent Schrödinger equation, so called stationary states:

$$\hat{H}\Psi_i(\boldsymbol{r}_1, \boldsymbol{r}_2, ..., \boldsymbol{r}_N) = E_i\Psi_i(\boldsymbol{r}_1, \boldsymbol{r}_2, ..., \boldsymbol{r}_N). \tag{2.2}$$

By removing the time dependence, the problem has been simplified to an eigenvalue problem, where Ψ_i are the eigenfunctions and E_i are the eigenvalues. The index i denotes a different solution on the eigenvalue spectrum, where $i = 1$ is the ground-state solution and each subsequent i is the $i - 1$ excited state.

The derivations in this chapter will use atomic units to make the equations

clearer. As an example, the Schrödinger equation for a single hydrogen atom in full SI units it is written as:

$$\left[-\frac{\hbar^2}{2m_e}\nabla^2 - \frac{e^2}{4\pi\epsilon_0 \boldsymbol{r}}\right]\Psi = E\Psi, \tag{2.3}$$

where $\hbar$ is Plank's constant h divided by 2π, m_e is the mass of an electron, $-e$ is the charge of an electron and ϵ_0 is the dielectric permittivity in vacuum. Eqn (2.3) can be rewritten in a dimensionless form if we say that $x, y, z \to \lambda x', \lambda y', \lambda z'$ and define λ such that it satisfies:

$$\frac{\hbar^2}{2m_e\lambda^2} = \frac{e^2}{4\pi\epsilon_0\lambda} = E_H, \tag{2.4}$$

where E_H is the atomic unit of energy called a Hartree. Solving Eqn (2.4) for λ gives:

$$\lambda = \frac{4\pi\epsilon_0\hbar^2}{m_e e^2} = a_0. \tag{2.5}$$

a_0 is the atomic unit of length, known as the Bohr radius. We can use the identities in Eqns (2.4) and (2.5) to rewrite Eqn (2.3) as:

$$E_H\left[-\frac{1}{2}\nabla'^2 - \frac{1}{\boldsymbol{r}'}\right]\Psi' = E\Psi'. \tag{2.6}$$

If we then set:

$$E' = \frac{E}{E_H}, \tag{2.7}$$

we obtain the dimensionless equation:

$$\left[-\frac{1}{2}\nabla'^2 - \frac{1}{\boldsymbol{r}'}\right]\Psi' = E'\Psi'. \tag{2.8}$$

This is the Schrödinger equation for the hydrogen atom written in atomic units. Any derived quantity can easily be converted back to SI units by a simple multiplication with the appropriate conversion factor, tables of which are available in many textbooks and online [21]. From this point on the prime notation will be omitted, but all quantities should be assumed to be in atomic units.

Using atomic units, the Hamiltonian energy operator in Eqn (2.2) is written explicitly as:

$$\hat{H} = -\sum_{i=1}^{N}\frac{1}{2}\nabla_i^2 - \sum_{A=1}^{M}\frac{1}{2M_A}\nabla_A^2 - \sum_{i=1}^{N}\sum_{A=1}^{M}\frac{Z_A}{r_{iA}} + \sum_{i=1}^{N}\sum_{j>i}^{N}\frac{1}{r_{ij}} + \sum_{A=1}^{M}\sum_{B>A}^{M}\frac{Z_A Z_B}{R_{AB}}. \tag{2.9}$$

The 1st and 2nd terms on the left side of Eqn (2.9) are the kinetic energies of the electrons and nuclei, respectively, where M_A is the ratio of the mass of nucleus A to the mass of an electron. The remaining three terms are energy contributions due the Coulomb interactions between the particles. Left to right they are: the electron-nuclear attraction, the electron-election repulsion and nuclear-nuclear repulsion for a system of N electrons and M nuclei. Since the wavefunction contains all the information about a system and the equations to capture it are known, it may seem that any system could in principle be described precisely by solving these equations, which would mean most of chemistry could be 'solved'. Unfortunately, solving the Schrödinger equation is an exceedingly difficult problem for the vast majority of chemically relevant systems. It can only be solved analytically for at most 2 particles. In terms of chemistry, this limits us to a lone hydrogen atom. The difficulty stems from the high-dimensional nature of the wavefunction, which requires $3(N + M)$ spatial variables, since each particle can move independently in three dimensions. The impracticality of solving the full Schrödinger equation and the ensuing search for simplifications to solve it, while retaining as much of the correct physics as possible, is known as the quantum many-body problem. To use a quantum mechanical treatment for chemically interesting systems, some significant approximations are required. The first and most important one is the Born-Oppenheimer approximation (BOA).

2.1.2 The Born-Oppenheimer approximation

As described above, the crux of the many-body problem is that there are too many coupled degrees of freedom (DOF) to make solving the time-independent Schrödinger equation computationally tractable. Born and Oppenheimer [12] suggested the separation of DOF where the coupling is weak. The prime candidates are nuclear and electronic motion. The mass of the protons and neutrons that constitute nuclei are approximately 1800 times greater than the mass of the electron. This means that electrons can respond to any change in the environment much more rapidly than the nuclei and, to a reasonable approximation, the electrons respond instantaneously to any change in nuclear positions. Another way of phrasing this is to say that we can approximate the uncertainty in the nuclear position as zero. In practice this is done by setting the $\hbar^2$ in the nuclear kinetic energy part of the many-body Hamiltonian to zero, which renders the entire nuclear kinetic energy term equal to zero. This new simplified Hamiltonian ($\hat{H}_{\mathrm{el}}(\boldsymbol{r};\boldsymbol{R})$), referred to as the electronic Hamiltonian, only depends parametrically on the nuclear coordinates and the associated electronic wavefunction (Ψ_{el}) is solved for a given set of fixed nuclear

coordinates. This first step of the BOA is called the clamped nuclei approximation:

$$\hat{H}_{\mathrm{el}} = -\sum_{i=1}^{N} \frac{1}{2}\nabla_i^2 - \sum_{i=1}^{N}\sum_{A=1}^{M} \frac{Z_A}{r_{iA}} + \sum_{i=1}^{N}\sum_{j>i}^{N} \frac{1}{r_{ij}} + \sum_{A=1}^{M}\sum_{B>A}^{M} \frac{Z_A Z_B}{R_{AB}}. \tag{2.10}$$

The rightmost term in $\hat{H}_{\mathrm{el}}$ is the nuclear repulsion term, which is a constant. The electronic Schrödinger equation associated with $\hat{H}_{\mathrm{el}}$ is:

$$\hat{H}_{\mathrm{el}}(\boldsymbol{r};\boldsymbol{R})\Psi_{\mathrm{el}}(\boldsymbol{r};\boldsymbol{R}) = E\Psi_{\mathrm{el}}(\boldsymbol{r};\boldsymbol{R}). \tag{2.11}$$

Finding approximate solutions to the electronic Schrödinger equation is at the heart of *ab initio* quantum chemistry and is the central task around which electronic structure software is built.

Let us suppose that we have a set of k solutions to Eqn (2.11). We can now rewrite the many-body wavefunction as an expansion:

$$\Psi(\boldsymbol{r},\boldsymbol{R}) = \sum_{k} \Psi_{\mathrm{n}}^{k}(\boldsymbol{R})\Psi_{\mathrm{el}}^{k}(\boldsymbol{r};\boldsymbol{R}), \tag{2.12}$$

with

$$\left\langle \Psi_{\mathrm{el}}^{k'} \middle| \Psi_{\mathrm{el}}^{k} \right\rangle = \delta_{k'k}, \tag{2.13}$$

and $\hat{H}_{\mathrm{el}}$ is diagonal:

$$\left\langle \Psi_{\mathrm{el}}^{k'} \middle| H_{\mathrm{el}} \middle| \Psi_{\mathrm{el}}^{k} \right\rangle = \delta_{k'k} E_k(\boldsymbol{R}). \tag{2.14}$$

If the full time independent Schrödinger equation is multiplied by $\Psi_{\mathrm{el}}^{k}(\boldsymbol{r};\boldsymbol{R})$ and integrated with with respect to $\boldsymbol{r}$ it results in a set of k coupled eigenvalue equations that no longer depend on $\boldsymbol{r}$ and now only depends on $\boldsymbol{R}$:

$$[\hat{H}_{\mathrm{n}}(\boldsymbol{R}) + \hat{H}_{\mathrm{el}}(\boldsymbol{R})]\Psi(\boldsymbol{R}) = E\Psi(\boldsymbol{R}) \tag{2.15}$$

$\Psi(\boldsymbol{R})$ in Eqn (2.15) is a vector of length k, in which the k^{th} element is $\Psi_{\mathrm{n}}^{k}(\boldsymbol{R})$. The matrix $\hat{H}_{\mathrm{n}}(\boldsymbol{R})$ is non-diagonal, with off-diagonal elements ($C_{k'k}$) representing coupling, through T_{n}, between different states k and k'. When this coupling is ignored, the Born-Oppenheimer nuclear Schrödinger equation is obtained:

$$[T_{\mathrm{n}} + E_k(\boldsymbol{R})]\Psi_{\mathrm{n}}^{k}(\boldsymbol{R}) = E\Psi_{\mathrm{n}}^{k}(\boldsymbol{R}). \tag{2.16}$$

Now that we have derived nuclear and electronic Schrödinger equations, the BOA is complete. However, it is important to understand under what circumstances

the BOA is a good and valid approximation to make and where it is likely to break down. To do this, we begin with the definition of the nuclear kinetic energy operator:

$$T_{\mathrm{n}} = \sum_{A} \sum_{\alpha=x,y,z} \frac{P_{A\alpha} P_{A\alpha}}{2M_A}, \tag{2.17}$$

where

$$P_{A\alpha} = -i \frac{\partial}{\partial \boldsymbol{R}_{A\alpha}}. \tag{2.18}$$

Using the equations above and by applying the Leibniz rule for differentiation we can write the matrix elements of T_{n} as:

$$(T_{\mathrm{n}}(\boldsymbol{R}))_{k'k} \equiv C_{k'k} = \delta_{k'k} T_{\mathrm{n}} - \sum_{A,\alpha} \frac{1}{M_A} \left\langle \Psi_{\mathrm{el}}^{k'} \right| P_{A\alpha} \left| \Psi_{\mathrm{el}}^{k} \right\rangle P_{A\alpha} + \left\langle \Psi_{\mathrm{el}}^{k'} \right| T_{\mathrm{n}} \left| \Psi_{\mathrm{el}}^{k} \right\rangle, \tag{2.19}$$

where the condition

$$\left\langle \Psi_{\mathrm{el}}^{k'} \right| P_{A\alpha} \left| \Psi_{\mathrm{el}}^{k} \right\rangle = \frac{\left\langle \Psi_{\mathrm{el}}^{k'} \right| [P_{A\alpha}, H_{\mathrm{el}}] \left| \Psi_{\mathrm{el}}^{k} \right\rangle}{E_k(\boldsymbol{R}) - E_{k'}(\boldsymbol{R})} \tag{2.20}$$

must be satisfied. The difference in energy between state k and k' appear in the denominator of Eqn (2.20), meaning that $C_{kk'}(\boldsymbol{R})$ will be small when the two states are well separated in energy. Since in the BOA these couplings are ignored, the BOA is most valid when the states under consideration are well separated in energy and it becomes a less valid approximation where states are closer in energy. For example, excited states of a molecule far from a conical intersection (regions in which PESs intersect one another) may be well modelled in a BOA picture, but as the molecule approaches the intersection, a treatment beyond the BOA would be required to accurately describe the unfolding physics. The consideration of energy spacing also explains why dynamics at metal surfaces are prone to violations of the BOA, because metal states are not well separated in energy and are more analogous to a continuum of states, where the nonadiabatic coupling is more likely to be large.

$$H_{\mathrm{n}} = -\sum_{A=1}^{M} \frac{1}{2M_A} \nabla_A^2 + E_{\mathrm{tot}}. \tag{2.21}$$

The values of E_{tot} for a given set of nuclear coordinates $\{R_A\}$ form the potential energy surfaces (PES) on which nuclear motion evolves. PESs based on the BOA are ubiquitous throughout chemistry to describe reactions and kinetics.

To avoid confusion, it should be noted that the separation of fast and slow DOF is called an adiabatic approximation. The Born-Oppenheimer approxima-

tion is an example of an adiabatic approximation. However, in the literature the phrases Born-Oppenheimer approximation and adiabatic approximation are often used interchangeably. For the remainder of this thesis the subscripts el and n will be dropped and all references to Hamiltonians should be assumed to be the electronic Hamiltonian, unless stated otherwise.

2.1.3 Spin Polarisation

The description of QM wavefunctions provided thus far has not made any mention of spin. For some closed shell systems in the electronic ground-state, wavefunctions that exclude spin and depend only on spatial variables may be sufficient to describe the essential physics of the system. However for many systems, in particular open-shell systems (those with unpaired electrons), explicit inclusion of spin is essential to correctly capture behaviour and the underlying physics. Spin is an intrinsic property of quantum mechanical particles. Electrons, and all other fermions, have a spin of $\frac{1}{2}$. Spin is described using two functions, $\alpha(\sigma)$ and $\beta(\sigma)$ representing spin up and spin down where σ is a spin variable. α and β form a complete and orthonormal basis.

$$\langle\alpha|\alpha\rangle = \langle\beta|\beta\rangle = 1, \tag{2.22}$$

$$\langle\alpha|\beta\rangle = \langle\beta|\alpha\rangle = 0. \tag{2.23}$$

The notation for the electronic wavefunction coordinates is changed to reflect the inclusion of spin. Whereas spatial wavefunctions are dependent on 3 spatial variables per particle, spin polarised wavefunctions also depend on a spin-variable, *i.e.*, 4 variables per particle. Therefore $\boldsymbol{r}$ is replaced with $\boldsymbol{x}$ where:

$$\boldsymbol{x} = \{\boldsymbol{r}, \sigma\}, \tag{2.24}$$

so the spin-polarised wavefunction is written as:

$$\Psi(\boldsymbol{x}_1, \boldsymbol{x}_2 ... \boldsymbol{x}_N). \tag{2.25}$$

With spin now included in the variables, all quantum numbers defining an electron are accounted for.

2.1.4 Orbitals

A wavefunction of a single electron in a many body system shall be referred to as an orbital $\psi(\boldsymbol{x})$. Mathematically, orbitals are spatial distribution functions that return

the probability density of finding an electron in an infinitesimal volume element $\mathrm{d}\boldsymbol{r}$ when squared $|\psi_i(\boldsymbol{r})|^2\mathrm{d}\boldsymbol{r}$. These wavefunctions should be smooth, continuous, multiply differentiable and square integratable. If spin is not important to the system under study, spatial orbitals can be used to produce reliable results. However, for the many cases where explicitly accounting for spin is required, we must use spin orbitals. A spatial orbital can be transformed into a spin orbital by multiplying a spatial orbital by a spin function α or β (spin up and spin down). The set of spatial or spin orbitals must be an orthonormal set. If a set of spatial orbitals which is orthonormal are transformed into spin orbitals, the set of spin orbitals will also be orthonormal.

$$\chi_{i,\alpha}(\boldsymbol{x}) = \psi_i(\boldsymbol{r})\alpha(\sigma). \tag{2.26}$$

$$\chi_{i,\beta}(\boldsymbol{x}) = \psi_i(\boldsymbol{r})\beta(\sigma). \tag{2.27}$$

2.1.5 Hartree products and Slater determinants

At this stage a further approximation based on partitioning the problem into easier to solve sub-problems is required. The many body electronic Hamiltonian can be broken into two terms as shown in Eqn (2.28)

$$\hat{H}_{\mathrm{elec}} = \hat{H}_0 + V_{\mathrm{e-e}}, \tag{2.28}$$

$$\hat{H}_0 = \sum_{i=1}^{\mathrm{N}} \hat{h}_i, \tag{2.29}$$

where $\hat{H}_0$ is the Hamiltonian operator of a system of N non-interacting electrons and $V_{\mathrm{e-e}}$ is the a term accounting for electron-electron repulsion. $\hat{h}_i$ is the Hamiltonian for the i^{th} non-interacting electron. The most sensible choice of eigenfunctions are the set of spin orbitals $\{\chi_{j,\sigma}\}$. Each $\hat{h}_i$ has a corresponding Schrödinger equation:

$$\hat{h}_{i,\sigma}\chi_{j,\sigma}(\boldsymbol{x}_i) = \epsilon_{j,\sigma}\chi_{j,\sigma}(\boldsymbol{x}_i). \tag{2.30}$$

By using non-interacting electrons, the many body wavefunction becomes a product of the contributing orbitals:

$$\Psi^{\mathrm{HP}}(\boldsymbol{x}_1, \boldsymbol{x}_2 ... \boldsymbol{x}_N) = \chi_{i,\sigma}(\boldsymbol{x}_1)\chi_{j,\sigma}(\boldsymbol{x}_2)...\chi_{k,\sigma}(\boldsymbol{x}_N). \tag{2.31}$$

Ψ^{HP} is known as the Hartree product and is an eigenfunction of $\hat{H}_0$, meaning the energy E is the sum of single particle eigenvalues:

$$E_{\text{HP}} = \sum_{i=1} \epsilon_i. \tag{2.32}$$

Ψ^{HP} alone will still fail, as currently written, to fully describe a QM system because it does not account for some quantum effects. The anti-symmetry principle requires that all electrons must be indistinguishable and that the wavefunction should change sign upon particle exchange.

$$\Psi(\boldsymbol{x}_1, ..., \boldsymbol{x}_i, ..., \boldsymbol{x}_j, ..., \boldsymbol{x}_N) = -\Psi(\boldsymbol{x}_1, ..., \boldsymbol{x}_j, ..., \boldsymbol{x}_i, ..., \boldsymbol{x}_N) \tag{2.33}$$

However, a single Hartree product state does distinguish between electrons. In the case of 2 electrons $(\boldsymbol{x}_1, \boldsymbol{x}_2)$ iin 2 spin orbitals (χ_1, χ_2), there are 2 possible Hartree products:

$$\Psi_{12}^{HP}(\boldsymbol{x}_1, \boldsymbol{x}_2) = \chi_1(\boldsymbol{x}_1)\chi_2(\boldsymbol{x}_2) \tag{2.34}$$

$$\Psi_{21}^{HP}(\boldsymbol{x}_1, \boldsymbol{x}_2) = \chi_1(\boldsymbol{x}_2)\chi_2(\boldsymbol{x}_1) \tag{2.35}$$

Thus ψ^{HP} distinguishes electrons χ_1 and χ_2. However, it did not change sign upon particle exchange. In practice, both indistinguishability and Eqn (2.33) are enforced by careful choice of how the many-body wavefunction is expressed, namely as a Slater determinant [22]:

$$\Psi(\boldsymbol{x}_1, \boldsymbol{x}_2 ... \boldsymbol{x}_N) = (N!)^{-\frac{1}{2}} \begin{vmatrix} \chi_i(\boldsymbol{x_1}) & \chi_j(\boldsymbol{x_1}) & ... & \chi_k(\boldsymbol{x_1}) \\ \chi_i(\boldsymbol{x_2}) & \chi_j(\boldsymbol{x_2}) & ... & \chi_k(\boldsymbol{x_2}) \\ \vdots & \vdots & \vdots & \vdots \\ \chi_i(\boldsymbol{x_N}) & \chi_j(\boldsymbol{x_N}) & ... & \chi_k(\boldsymbol{x_N}) \end{vmatrix} \tag{2.36}$$

A Slater determinant represents a linear combination of Hartree products for each possible pairing of electron and orbital. Each column represents an orbital and each row an electron. The $(N!)^{-\frac{1}{2}}$ term is a normalisation coefficient. When any two rows are swapped, the sign of the determinant and hence the sign of the wavefunction also changes sign, thereby fulfilling the requirement of Eqn (2.33). By including terms for each combination of electron and orbital, the electrons are treated identically.

2.2 Ground-state methods

2.2.1 Hartree-Fock Theory

Hartree-Fock (HF) theory is a practical and computationally cheap method for finding approximate solutions to the many-body Schrödinger equation [22–24]. HF was once the work-horse of the computational chemistry community. In modern times it is very rare that HF calculations are used on their own in any real research environment; however, a set of more advanced quantum chemistry methods known as post-Hartree-Fock methods often perform a HF calculations as an initial step [25]. In terms of being the work-horse of computational chemistry, this title now belongs to DFT. Never the less, HF provides a solid basis upon which many more accurate theories are built and therefore it will be briefly described here, before moving on to more advanced theories.

If the wavefunction that describes a system is a single Slater determinant of Hartree products, $|\Psi_0\rangle$, then in order to obtain the ground-state energy (and any subsequently derived properties), the wavefunction should be varied such that it minimises the equation:

$$E_0 = \langle \Psi_0 | \, \hat{H} \, | \Psi_0 \rangle \, . \tag{2.37}$$

The orbitals constituting the wavefunction are optimised self-consistently via the Hartree-Fock equation:

$$\hat{f}_i \chi(x_i) = \epsilon \chi(x_i), \tag{2.38}$$

where $\hat{f}_i$ is the effective one electron operator acting on electron i and is called the Fock operator:

$$\hat{f}_i = -\frac{1}{2}\nabla_i^2 - \sum_{A=1}^{M} \frac{Z_A}{r_{iA}} + V_i^{\mathrm{HF}}. \tag{2.39}$$

Importantly the last term, called the Hartree-Fock potential, V_i^{HF} reintroduces the electron-electron repulsion that was removed during the introduction of Hartree products. This is not the same many-body potential $V_{\mathrm{e-e}}$ that was removed, but rather an averaged potential that electron i will feel due to the other N-1 electrons. The variational principle states that the true ground-state energy is always lower (or equal) to any trial wavefunction for a given Hamiltonian. This means the HF ground state energy is obtained by starting with some initial guess of the orbitals and improving them iteratively until self-consistency is reached, according to algorithm in figure 2.2.1.

In summary, HF theory makes several approximations to the many-body electronic wavefunction to allow computationally tractable calculations of quantum

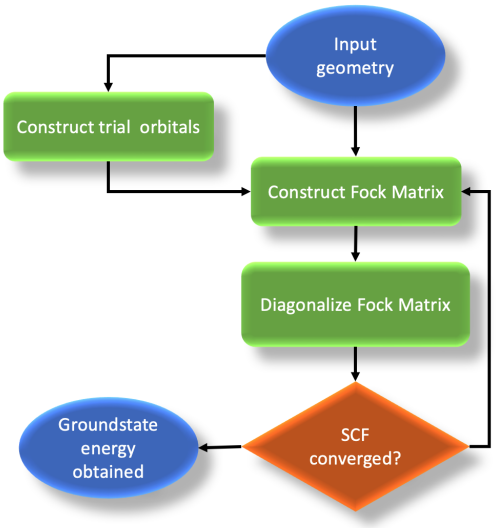

Figure 2.1: The SCF procedure for obtaining the HF ground-state energy.

mechanical systems. The key approximations are: first, separate the wavefunction in to the product of single particle orbitals and secondly, to account for the electron-electron repulsion using the mean-field approximation. Within the HF picture, there are two types of electron correlation: Fermi correlation and Coulomb correlation. Fermi correlation comes from exchange and is actually fully accounted for in HF theory; Coulomb correlation is what is missed by using the mean-field approximation for the electron-electron interaction.

2.2.2 Density functional theory

Density functional theory (DFT) is a formal quantum mechanical framework that uses the electron density $\rho(\boldsymbol{r})$ as the central quantity as opposed to the wavefunction. The motivation for using the electron density is that, no matter how many electrons a chemical system contains, the density is a function of only 3 spatial variables (x, y, z), while the wavefunction requires 3 additional variables for each electron in the system (4 if spin polarised). The computational cost of accurate wavefunction calculations scales poorly with system size and modelling any system of more than a few atoms becomes unfeasible without making significant approximations. Using the electron density as the central quantity in quantum mechanical calculations was considered as early as 1927 by Thomas and Fermi [26, 27], shortly after Schrödinger's introduction of the quantum mechanical wavefunction. However the Thomas-Fermi method could not produce reliable results, due to large errors arising primarily from the approximate treatment of kinetic energy and electron exchange, and a complete

neglect of correlation [28].

After the initial works of Thomas and Fermi, it took another 40 years until the seminal work of Hohenberg and Kohn [28] for the theoretical foundations of DFT to be formally established. Their primary contributions are two theorems that underpin all of modern DFT. The first establishes that the external potential V_{ext} is a unique functional of $\rho(\boldsymbol{r})$. The significance of this statement is that there exists an invertible 1-to-1 mapping of V_{ext} to $\rho(\boldsymbol{r})$. The proof of the 1st theorem is provided via a *reductio ad absurdum* approach as follows. Let us assume that there exist two external potentials, V_a and V_b that map to the same, non-degenerate, ground-state density $\rho_0(\boldsymbol{r})$. Since V_a and V_b are different, the Hamiltonians H_a and H_b must also have different ground-state wave functions ψ_a^0 and ψ_b^0. The ground-state energy of system a is shown in Eqn. (2.40) and Eqn. (2.41)

$$E_a^0 = \left\langle \Psi_a^0 \middle| \hat{H}_a \middle| \Psi_a^0 \right\rangle, \tag{2.40}$$

where

$$E_a^0 = \int \rho(\boldsymbol{r}) V_a(\boldsymbol{r}) d\boldsymbol{r} + F[\rho(\boldsymbol{r})]. \tag{2.41}$$

By replacing the ground-state wave function of a with that of b, we arrive at inequality (2.42):

$$E_a^0 < \left\langle \Psi_b^0 \middle| \hat{H}_a \middle| \Psi_b^0 \right\rangle. \tag{2.42}$$

We next add and subtract H_b:

$$E_a^0 < \left\langle \Psi_b^0 \middle| \hat{H}_a + \hat{H}_b - \hat{H}_b \middle| \Psi_b^0 \right\rangle. \tag{2.43}$$

$$E_a^0 < \left\langle \Psi_b^0 \middle| \hat{H}_a - \hat{H}_b \middle| \Psi_b^0 \right\rangle + E_b^0. \tag{2.44}$$

We now insert Eqn. (2.41) into Eqn. (2.44) and note that our assumption at the start of this proof states that the same $\rho_0(\boldsymbol{r})$ is returned by both V_a and V_b, so the terms that depend only on the density will cancel, giving Eqn. (2.45):

$$E_a^0 < \int \rho_0[V_a(\boldsymbol{r}) - V_b(\boldsymbol{r})] + E_b^0 \tag{2.45}$$

The systems a and b are as yet undefined, therefore the choice of a was arbitrary and it is equally valid to perform the same procedure, replacing a with b and visa versa.

$$E_b^0 < \int \rho_0[V_b(\boldsymbol{r}) - V_a(\boldsymbol{r})] + E_a^0 \tag{2.46}$$

By adding Eqns. (2.45) and (2.46), we arrive at Eqn. (2.47).

$$E_a^0 + E_b^0 > \int \rho_0[V_a(\boldsymbol{r}) - V_b(\boldsymbol{r})] + E_b^0 + \int \rho_0[V_b(\boldsymbol{r}) - V_a(\boldsymbol{r})] + E_a^0 \tag{2.47}$$

Clearly, the 2 integrals on the right hand side of Eqn. (2.47) will be of equal magnitude and opposite sign and therefore cancel out. This leads to the final inequality of this proof:

$$E_a^0 + E_b^0 > E_b^0 + E_a^0 \tag{2.48}$$

This is obviously nonsensical and implies that the initial assumption, that two different external potentials can return the same ground-state density, was incorrect; and there is a 1-to-1 mapping from the external potential to the ground-state density.

The second theorem of Hohenberg and Kohn states that $\rho(r)$ obeys a variational principle. Put another way, the density that minimises the total energy is the exact ground-state density. The second proof begins by observing from the first theorem that $\rho(\boldsymbol{r})$ uniquely determines V_{ext} and N. V_{ext} determines the Hamiltonian and therefore the exact ground-state wavefunction Ψ_0. This means that the wavefunction must be a unique functional of the density.

$$F[\rho(\boldsymbol{r})] = \langle \Psi | \hat{F} | \Psi \rangle \tag{2.49}$$

The work of Hohenberg and Kohn limits itself to V-representable densities, meaning densities, $\rho(\boldsymbol{r})$, that are ground-state densities of some external potential, V_{ext} [29]. The energies, $E_v[\rho(\boldsymbol{r})]$ associated with such densities may be expressed in terms of only the density and external potential, as in Eqn. (2.50), or in terms of the wavefunction and the external potential, as in Eqn. (2.51):

$$E_{\text{HK}}[\rho(\boldsymbol{r})] = \int \rho(\boldsymbol{r}) V_{\text{ext}}(\boldsymbol{r}) d\boldsymbol{r} + F[\rho(\boldsymbol{r})] \tag{2.50}$$

$$E_{\text{HK}}[\Psi] = \langle \Psi | \hat{F} | \Psi \rangle + \langle \Psi | \hat{V}_{\text{ext}} | \Psi \rangle \tag{2.51}$$

If we assume Ψ is the exact ground-state wavefunction associated with V_{ext}, then the variational principle states that replacing Ψ with any other wavefunction Ψ' will return a greater energy.

$$\langle \Psi | \hat{F} | \Psi \rangle + \langle \Psi | \hat{V}_{\text{ext}} | \Psi \rangle < \left\langle \Psi' \middle| \hat{F} \middle| \Psi' \right\rangle + \left\langle \Psi' \middle| \hat{V}_{\text{ext}} \middle| \Psi' \right\rangle \tag{2.52}$$

By referring to Eqn. (2.50) we see that

$$\int \rho(\boldsymbol{r}) V_{\text{ext}}(\boldsymbol{r}) d\boldsymbol{r} + F[\rho(\boldsymbol{r})] < \int \rho'(\boldsymbol{r}) V_{\text{ext}}(\boldsymbol{r}) d\boldsymbol{r} + F[\rho'(\boldsymbol{r})] \tag{2.53}$$

Expressed more succinctly, the final expression of Hohenberg-Kohn's 2$^{\text{nd}}$ theorem is:

$$E_{\text{HK}}[\rho] < E_{\text{HK}}[\rho'] \tag{2.54}$$

The work of Hohenberg and Kohn provided a formal basis for the use of the density as the central quantity in a quantum mechanical framework. However, they only proved the existence of a single (non-degenerate) ground-state density for a given external potential, but no insight on how to obtain that density practically. The following year, Kohn and Sham [30] described such a practical methodology. Now referred to as Kohn-Sham DFT (KS-DFT), virtually all modern implementations of DFT are based on KS-DFT. The conceptual leap of Kohn and Sham, which paved the way for DFT to become the workhorse of computational chemistry, was to introduce a fictitious density of non-interacting electrons, which experience a so-called Kohn-Sham effective potential V_{KS}. The reason this is so useful, is that the ground-state density of the non-interacting system is defined to be the same as that of the fully interacting system, while being computationally much easier to solve.

Kohn and Sham separated the universal energy functional of the non-interacting density ($E_{\text{KS}}[\rho]$) into 3 terms: the KS kinetic energy $\hat{T}_{\text{KS}}[\rho]$, the classical electrostatic energy also called the Hartree energy $E_{\text{H}}[\rho]$, and the so-called exchange correlation energy E_{XC}:

$$E_{\text{KS}}[\rho](\boldsymbol{r}) = \hat{T}_{\text{KS}}[\rho](\boldsymbol{r}) + E_{\text{H}}[\rho](\boldsymbol{r}) + E_{\text{xc}}[\rho](\boldsymbol{r}). \tag{2.55}$$

The kinetic energy of the non-interacting system is known exactly and is relatively simple to calculate as shown in Eqn (2.56). Inaccurate treatment of the kinetic energy had been a major source of error in the work of Thomas and Fermi that preceded KS-DFT.

$$\hat{T}_{\text{KS}}[\rho] = \sum_{i=1}^{N} \langle \psi_i | -\frac{1}{2}\nabla^2 | \psi_i \rangle \tag{2.56}$$

E_{xc} is a term that contains the corrections that are required to recover the exact energy from the non-interacting approximation made for the kinetic and Hartree energies. These corrections are all many-body effects. E_{xc} includes a correction for the self-interaction energy, which arises due to the fact that any electron interacting with the average potential of the total electron density will have itself contributed to the density. This leads to a spurious over-delocalisation of the density. E_{xc}

also corrects for any non-classical contributions to the electrostatic interaction including Pauli repulsion. Pauli repulsion is a quantum effect that stems from the anti-symmetrisation principle, and manifests as a repulsive force preventing electrons of the same spin from occupying the same state and space. E_{xc} also corrects for many-body correlations, which are forces which arise due to quantum fluctuation of electrons. An exact form of E_{xc} is unknown and all implementations of DFT require the use of an approximate XC functional. The non-interacting electrons are represented using KS-orbitals that each have an associated effective 1-particle equation:

$$[-\frac{1}{2}\nabla^2 + V_{\text{KS}}](\boldsymbol{r})]\psi_i(\boldsymbol{r}) = \epsilon_i\psi_i(\boldsymbol{r}), \tag{2.57}$$

where $V_{\text{KS}}[\rho](\boldsymbol{r})$ is the effective KS-potential,

$$V_{\text{KS}}[\rho](\boldsymbol{r}) = V_{\text{ext}}[\rho](\boldsymbol{r}) + V_{\text{H}}[\rho](\boldsymbol{r}) + V_{\text{xc}}[\rho](\boldsymbol{r}). \tag{2.58}$$

In order to impose the anti-symmetric exchange that all fermions are subject to, the KS wavefunction is expressed as a Slater determinant of the single particle wavefunctions, as described in the previous section. The use of single particle wavefunctions makes the scalability of DFT calculations much more favourable since, when N increases, the problem to be solved does not become more complex, *i.e.*, no additional degrees of freedom, but rather the list of single particle Schrödinger equations to be solved becomes longer. The density (interacting or not) can be recovered as the sum of the inner-products of the wavefunctions.

$$\rho(\boldsymbol{r}) = \sum_i^N |\langle r|\psi_i\rangle \langle\psi_i|r\rangle|^2 \tag{2.59}$$

The KS equations are then solved self-consistently to obtain the ground-state density and energy, as shown in Figure 2.2

2.3 Excited state methtods

2.3.1 TD-DFT

Ground state DFT is, as the name suggests, concerned with only ground state properties. In this regard it is an excellent method for investigating energies, forces, equilibrium geometries, density distributions and a host of other ground-state properties. There are methods that use ground-state DFT to approximate excited state properties, such as ΔSCF. However, such methods are often limited in the states

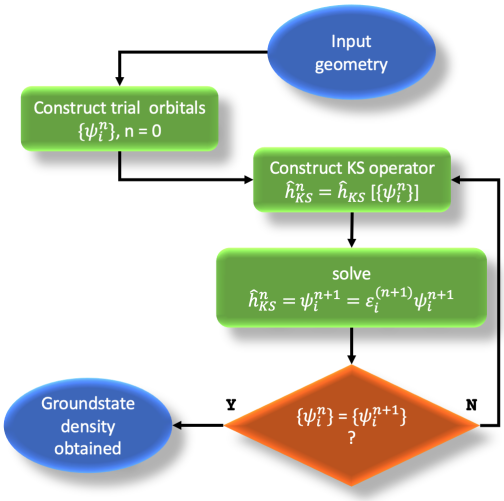

Figure 2.2: Flowchart for the SCF procedure to obtain the ground-state density in KS-DFT.

they can approximate, typically only higher lying stationary states. It does not allow one to describe the dynamical response of the system to some external perturbation. Time-dependent-DFT (TD-DFT) extends the static picture given by DFT to include time-dependent phenomena. For example, TD-DFT is well suited to describe the optical excitation of a molecule from its ground-state to an excited state. The formal justification of TD-DFT follows a similar structure to that used for ground-state DFT. First it will be shown that there is a one-to-one mapping of a time-dependent potential to time-dependent density. Secondly, the use of a KS formalism for TD-DFT will be described.

It is known from the time dependent Schrodinger equation that there is a 1-to-1 mapping of a time-dependent potential $V(\boldsymbol{r}, t)$ onto a time-dependent wave function $\Psi(t)$, and from $\Psi(t)$ one can recover a time dependent density $\rho(\boldsymbol{r}, t)$. What needs to be shown, and what the Runge Gross theorem proves is that this map can be made in reverse, *i.e.*, $\rho(\boldsymbol{r}, t) \rightarrow \Psi(\boldsymbol{r}, t) \rightarrow V(\boldsymbol{r}, t)$. The time-dependent density can completely describe the dynamics of the system. Runge and Gross proved that two different time dependent potentials $V(\boldsymbol{r}, t)$ and $V'(\boldsymbol{r}, t)$ will always produce two different time-dependent densities $\rho(\boldsymbol{r}, t)$ and $\rho'(\boldsymbol{r}, t)$ [31].

It is important to first make clear what it means for two densities to be different. In time dependent wavefunction theory, wave functions that differ by only a time dependent phase factor ($\alpha(t)$) are considered the same. The wavefunctions are complex valued functions and therefore will have a phase factor. The density, on the other hand, is a real valued function and therefore does not contain a phase

factor. If two time-dependent densities are constructed from two wave functions that differ only by an arbitrary phase factor, then the resulting densities will differ only by an additive time-dependent scalar function $c(t)$ and therefore under this definition the potentials in Eqn (2.60) would not be considered different.

$$V'(\boldsymbol{r},t) = V(\boldsymbol{r},t) + c(t) \rightarrow \Psi'(\boldsymbol{r},t) = e^{-i\alpha(t)}\Psi(t). \tag{2.60}$$

$$\frac{d\alpha}{dt} = c(t). \tag{2.61}$$

Eqns (2.60) and (2.61) show the relationship between the phase factors α(t) and scalar functions $c(t)$.

Runge and Gross first showed that the current density $j(\boldsymbol{r},t)$, the charge flux passing through the boundary enclosing the system, must diverge if the potentials are different. They then used this result to extend the proof using current density to the electron density:

$$V'(\boldsymbol{r},t) \neq V(\boldsymbol{r},t) + c(t) \rightarrow j'(\boldsymbol{r},t) \neq j(\boldsymbol{r},t). \tag{2.62}$$

TD-DFT is the workhorse of excited state calculations in computational chemistry. It offers a good balance between computational cost and accuracy. However, it retains the short-comings of static DFT, most notably the over-delocalisation of electron density due to the self interaction error. TD-DFT performs well when calculating optical excitation spectra, finding optimal geometries of excited states, and many other excited state properties [32, 33]. However, TD-DFT tends to perform poorly for high lying excited states and in instances of charge transfer [34–36].

2.3.2 ΔSCF

ΔSCF is a time-independent excited state DFT method that that prioritises computational efficiency, and is is similar to ground-state KS-DFT in terms of computational cost. In ΔSCF, one approximates the vertical excitation energy as the difference between two self-consistent solutions of the KS equations. The first is a normal KS-DFT ground-state solution. The second solution, the excited state energy, is the result of a SCF optimisation performed under the constraint of non-ground-state occupations of the KS states, such that the occupations mimic a single particle state to state transition relevant to the excited state of interest. For example, consider the simplest molecular system H_2. Self-consistently solving the KS-equations for the ground-state density will return a solution with both electrons in the σ bonding orbital. The lowest energy electronic excitation

is the $S_0 \rightarrow S_1$ transition; *i.e*; the promotion of a single electron to the σ^* orbital. The excited state energy can be approximated by running a second SCF optimisation, while constraining σ to be singly occupied. The vertical excitation energy is the difference between the energies of the two solutions, $E_{S_1} - E_{S_0}$. By applying this procedure while varying the system geometry, PESs are easily constructed. Despite its apparent simplicity, ΔSCF can, with appropriate choice of constraints and XC functional, produce energies of similar accuracy to TD-DFT in some molecular systems, as was shown for the case of organic dyes [37].

The earliest record of excited state calculations that can be considered ΔSCF were published in 1962 by Clementi [38] where two SCF solutions using analytical functions were employed. The method as it exists today is developed primarily by the works of Gunnarsson and Lundqvist [39], Zeigler [40] and von Barth [41]. ΔSCF was broadly considered an *ad-hoc* method for most of its history, up until 1999, ΔSCF was only proven to be formally justified for the lowest excitation of a given symmetry and was an otherwise unjustified method [42]. This would limit the method to a very small subset of all the excitations that are likely to be chemically relevant. For example, excitations in which a molecule with a singlet ground state is excited to a higher lying singlet, like the dihydrogen example, are important all across chemistry and physics; however, these excitations lay outside of the formally justified set. Ziegler proposed a solution to this problem by adding a simple empirical correction known as the Ziegler sum rule [40] for singlet to singlet transitions:

$$E_{\text{ex}} = 2E_{\text{singlet}} - E_{\text{triplet}}, \tag{2.63}$$

where E_{ex} is the corrected $S_0 \rightarrow S_1$ excitation energy, E_{singlet} and E_{triplet} are the ΔSCF excitation energies for $S_0 \rightarrow S_1$ and $S_0 \rightarrow T_1$ respectively. ΔSCF has been widely applied beyond this very limited sub-set of excitations and found to still perform well [37, 40]. The seemingly unwarranted accuracy of ΔSCF encouraged further work to find a formal justification. The Hohenberg and Kohn theorems only apply to V-representable densities, *i.e.*, densities that are ground states of some external potential. This is why all excited states, apart from the lowest energy state of a given symmetry, are outside the realm of KS-DFT. The work of Görling [42] provides an alternative and more general counterpart to the proofs of Hohenberg and Kohn for DFT. The key difference in Görling's work is that all electronic states are treated on an equal footing. The derivation invokes a so-called generalised adiabatic connection (GAC). Subsections of a Hilbert space, corresponding to N particles and antisymmetric wavefunctions, are extended by adding an additional

dimension representing the coupling (α) between electrons. $\alpha = 0$ corresponds to the non-interacting system and $\alpha = 1$ to the fully interacting system. While keeping the density and external potential fixed, moving from $\alpha = 0$ to $\alpha = 1$ creates a continuous path through the Hilbert space, and these paths are called GACs. As a consequence, each eigenstate of the $\alpha = 0$ system is adiabatically connected to an eigenstate of the $\alpha = 1$ system. Importantly, the energetic ordering of the eigenstates does not necessarily match; *i.e.*, a ground state of the a=0 system may be adiabatically connected to a higher-lying eigenstate of the a=1 system and vice versa.

GAC-DFT gives ΔSCF formal justification, with the caveat that an as yet unknown orbital-dependant functional, one that treats each electronic state differently, must be used. In practice ΔSCF calculations are carried out using XC functionals based on traditional ground state KS-DFT. Therefore, while in theory ΔSCF has a formal justification, as it is practiced it does not. However, even within KS-DFT all currently implemented functionals are themselves approximations of the true universal functional.

2.3.3 Linear expansion ΔSCF

Linear expansion ΔSCF (le-ΔSCF) is the excited state method used throughout the work in this thesis. It will be described briefly here, with a detailed discussion of the method and its intricacies in Chapter 4, as that chapter assesses the performance of the method applied across a range of systems and its limitations.

The majority of ΔSCF calculations in literature are performed on isolated molecular systems and these are the systems the method is best suited to, since the orbitals are typically well separated in both space and energy and so it is more likely that a single-particle state to state transition can be approximated by reordering the occupations of such orbitals. However, ΔSCF has been shown to perform similarly to TD-DFT at approximating band gaps when extended to crystalline solids, provided an appropriate functional is used [43]. The method is pushed beyond its limits at hybrid interfaces, for example molecules adsorbed at metal surfaces, especially in the case of charge transfer between metal and molecule. Consider an excitation of a metal electron to the LUMO of a molecule adsorbed at the metal surface. The ΔSCF procedure states that one should constrain the occupation of the LUMO to be 1.0. However, upon interaction with the surface the molecular LUMO is hybridised across a continuum of metal states, especially over the d-band in the case of transition metals. This means the choice of which orbital should be constrained to accept the

electron is not clear, since each state would only capture a small contribution on the transition. In fact, there is no way of approximating the transfer of an electron to a molecular resonance by changing the occupations of any subset of the full system KS states [16]. To be applicable to strongly hybridised systems, the method needed to be adapted. The shortcomings of ΔSCF motivated the development of le-ΔSCF [16].

Prior to the advent of le-ΔSCF, the best one could do to model charge transfer excitations of a molecule-metal system within the ΔSCF framework would be to select the orbital that has greatest overlap with the desired excitation state orbital. In some very simple cases, like H_2 on metals, this may be a reasonable approximation, since the S orbitals of hydrogen will likely have good overlap with S bands in the metal. However, even other simple diatomics (e.g. CO, NO, N_2) will hybridize strongly with the surface states, rendering ΔSCF unviable. The solution offered by Gavnholt *et al.* [16] is that, rather than only constraining occupations of KS orbitals, constraints are applied to new so-called resonance orbitals $|\Psi^c\rangle$ that are linear combinations of KS orbitals.

$$|\Psi^c\rangle = \sum_i C_i \left|\Psi^i\right\rangle, \tag{2.64}$$

where the superscript c represents the c^{th} resonance orbital/constrained state.

In principle, any arbitrary linear combination is possible, however the advantage of this adapted method is that it is possible to select a linear combination such that the resulting resonance orbital approximates a resonance on the molecule. In the example of charge transfer from metal to molecule, this would mean constructing the resonance orbital to approximate the unhybridised molecular LUMO, so that constraining its occupation would effectively constrain charge to the molecule and the constrained SCF solution would mimic the charge-transfer state. If multiple **k**-points are sampled, then the linear combination must be performed at each **k**-point separately. The question arises, of how to choose expansion coefficients, such that the linear combination best approximates a molecular resonance? The first step is to perform a single point calculation on a secondary system that represents the un-hybridised adsorbate, *i.e.* the molecule in gas phase. However, this 'gas phase' system must have the same unit-cell and **k**-point sampling as the full system, where typically one would use non-periodic boundary conditions or a much larger unit-cell and only sample a single **k**-point. Therefore, it is more accurate to call the 'gas phase' system a freestanding molecular over-layer (FSMO), since the system is a periodic array of freestanding molecules. Figure 2.3 shows a visualisation of how a

FSMO model compares to the full system and a true gas phase.

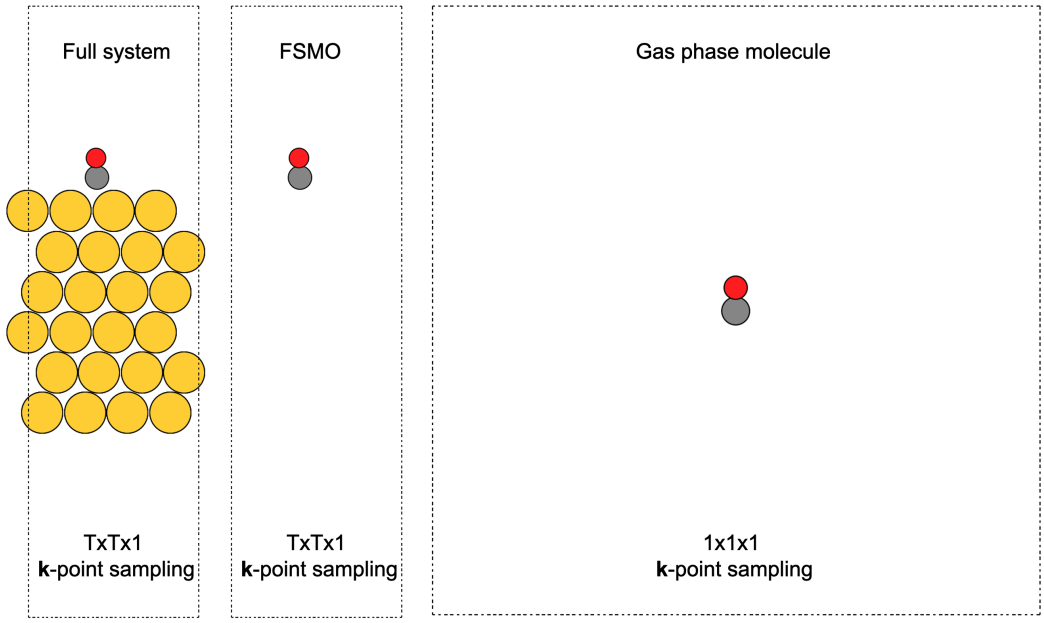

Figure 2.3: A full molecule-metal slab model (left) with several metal layers, in which the width of the unit cell (dashed lines) is defined by the dimensions of the metal slab. The **k**-point sampling of the full system uses a T × T × 1 grid, where T is an integer greater than 1. A FSMO model (middle) has identical unit cell and **k**-point sampling to the full system, but only contains the molecular atoms. A gas phase molecule model (right), where the molecule sits at the centre of a very large unit cell and only a single **k**-point is sampled.

The FSMO orbital most closely resembling the molecular resonance is then chosen as a target of the linear combination. Projector overlaps of the FSMO target orbital on to the full-system states are used to generate the expansion coefficients. Eqn (2.65) is the simplest form C_i takes and excludes any normalisation terms that are described in detail in chapter 4.

$$C_i = \langle \Psi_i | \phi_j \rangle \tag{2.65}$$

The FSMO target orbital should be based on the particular excitation of interest. In the case of charge transfer excitations between metal and molecule where there is no internal molecular excitation involved, the FSMO ground-state orbitals should be used. Upon transfer of a metal electron to the molecule, the orbitals of the molecule will respond and so will differ further from the ground-state FSMO orbitals. How-

ever, to more accurately model those orbitals would require a simulations of the molecular anion and so the FSMO calculation would have a negatively charged unit-cell. In practice the addition of a compensating background charge often renders the anionic FSMO target orbital a less suitable reference state and the FSMO groundstate orbitals are the better choice [17]. If the excited state of interest does involve internal rearrangement, for example a molecule in an S_1 state approaching a surface, it is beneficial to optimise the FSMO orbital to the S_1 solution. This can be easily achieved by using simple ΔSCF calculation to generate the FSMO orbitals. le-ΔSCF has been shown to perform well when modelling charge transfer at hybrid metal-organic interfaces, in the cases of small diatomics on Au(111) and azobenzene on Ag(111) [16, 17, 44, 45].

2.4 Dynamics

The theoretical considerations thus far have focused on how to calculate energies of a given quantum mechanical system in a specific geometry, *i.e.*, a static picture. Of course, nature is not static and it is often essential to be able to simulate dynamical processes to gain insight into chemical behaviour. This section will discuss how this is achieved. Firstly, Born-Oppenheimer *ab-initio* molecular dynamics (BO-AIMD) will be discussed before moving on to non-adiabatic molecular dynamics (NAMD), in particular surface hopping methods.

2.4.1 Adiabatic molecular dynamics

Although the word molecular appears in the phrase AIMD, it is not restricted to molecular systems and can, in principle, be applied to simulate the motion of any atomistic system. There are two essential ingredients required for AIMD. The first is the potential upon which the dynamics will unfold, which provides the energy and forces. The second is the algorithm for propagating the dynamics. The potential is calculated by solving the time-independent Schrödinger equation, as described in previous sections, for example using DFT. The potential may be precalculated by sampling relevant geometries and interpolating to construct a PES or calculated on-the-fly during each step of the simulation. The propagation algorithm most commonly uses Newton's second law, as shown in Eqn (2.66), and nuclei are treated as point like particles moving classically on the PES.

$$\boldsymbol{F}_A = M_A \boldsymbol{a}_A = M_A \frac{\mathrm{d}^2 \boldsymbol{R}_A}{\mathrm{d}t^2} = -\frac{\partial V(\boldsymbol{R})}{\partial \boldsymbol{R}_A}, \tag{2.66}$$

where the subscript A represents a given particle (nucleus) and $\boldsymbol{F}_A$, M_A, $\boldsymbol{a}_A$, and $\boldsymbol{R}_A$ are the force, mass, acceleration and position of that particle at time t. The rightmost term in Eqn (2.66) shows how the force can be calculated from the potential ($V(\boldsymbol{R})$). Since $\boldsymbol{a}_A$ is the second time derivative of position, integrating once with respect to time will give the velocity ($\boldsymbol{\nu}_A(t)$) and integrating twice would give the position as a function of time ($\boldsymbol{R}_A(t)$). If ($\boldsymbol{R}_A(t)$) is known then the dynamics of the system are known; however, for any system containing more than one nuclei it is not possible to obtain this function analytically. The most common way that positions of particles are propagated in time is via the velocity-Verlet algorithm [46], which updates the positions and velocities as follows:

$$\boldsymbol{R}_A(t+\Delta t) = \boldsymbol{R}_A(t) + \nu_A(t)\Delta t + \frac{F_A(t)}{2M_A}\Delta t^2 \tag{2.67}$$

$$\boldsymbol{\nu}_A(t+\Delta t) = \boldsymbol{\nu}_A(t) + \frac{F_A(t) + F_A(t+\Delta t)}{2M_A}\Delta t \tag{2.68}$$

where Δt is the time step and is the amount of time that will pass in between each snapshot that is explicitly calculated.

2.4.2 Nonadiabatic molecular dynamics

For many dynamical processes, it is sufficient to perform dynamics using the velocity-Verlet algorithm with a PES calculated using DFT. However, this is a strictly BOA picture and if a system displays nonadiabatic behaviour it will not be captured using this method. An alternative algorithm must then be used to propagate the dynamics, that may include multiple PESs as way for accounting for electronic transitions between different states (surfaces).

The essence of nonadiabatic dynamics of molecules interacting with metal surfaces is that the motion of nuclei couples to the electronic states of the metal, and energy is transferred, thereby altering the trajectories of the nuclei and the energy dissipation compared to a fully decoupled (BO) system. The Newns-Anderson Hamiltonian ($\hat{H}_{\mathrm{NA}}$) is a common way of coupling molecular states to so-called bath states, that represent a continuum of electronic states that mimic a metal [47–49].

$$\hat{H}_{\mathrm{NA}}(\boldsymbol{R}) = \hat{T}_{\mathrm{nuc}}(\boldsymbol{R}) + \hat{H}_{\mathrm{el}}^{\mathrm{NA}}(\boldsymbol{R}). \tag{2.69}$$

The first term on the right hand side of Eqn (2.69) is the familiar nuclear kinetic energy operator, but the other, $\hat{H}_{\mathrm{el}}^{\mathrm{NA}}$, is the Newns-Anderson electronic Hamiltonian, which contains all the information about the bath states and how they couple to

the molecular states:

$$\begin{aligned}\hat{H}_{\mathrm{el}}^{\mathrm{NA}}(\boldsymbol{R}) = U_0(\boldsymbol{R}) + (U_1(\boldsymbol{R}) - U_0(\boldsymbol{R}))\hat{c_a}^{\dagger}\hat{c_a} + \int_{E_{\min}}^{E_{\max}} \mathrm{d}\boldsymbol{\epsilon}\, \boldsymbol{\epsilon}\hat{c}_{\epsilon}^{\dagger}\hat{c}_{\epsilon} \\ + \int_{E_{\min}}^{E_{\max}} \mathrm{d}\boldsymbol{\epsilon}\, V(\boldsymbol{\epsilon};\boldsymbol{R})(\hat{c_a}^{\dagger}\hat{c}_{\epsilon} + \hat{c}_{\epsilon}^{\dagger}\hat{c_a}),\end{aligned} \tag{2.70}$$

$\hat{c}_a$, $\hat{c}_a^{\dagger}$,$\hat{c}_{\epsilon}$and $\hat{c}_{\epsilon}^{\dagger}$ are the creation and annihilation operators for an electron in the molecular adsorbate state (a), and metallic state ϵ. $E_{\min}$ and $E_{\max}$ are the lower and upper bounds of the metal band. U_0 and U_1 are the neutral and anionic diabatic PESs respectively. V describes the coupling of adsorbate orbital $|a\rangle$ to metal orbitals $\{|\epsilon\rangle\}$. One of the biggest strengths of the Newns-Anderson method is that it allows for a description of hybridisation between adsorbate and metal states as the molecule moves into areas of stronger coupling (close to the surface).

For any practical implementation, the continuum must be replaced by a discrete set of bath states. Therefore the integrals within Eqn (2.70) are transformed into summations, producing the discretized Newns-Anderson Hamiltonian:

$$\hat{H}_{\mathrm{el}}^{\mathrm{NA}}(\boldsymbol{R}) = U_0(\boldsymbol{R}) + (U_1(\boldsymbol{R}) - U_0(\boldsymbol{R}))\hat{c_a}^{\dagger}\hat{c_a} + \sum_{k=1}^{N_e} \epsilon_k \hat{c}_k^{\dagger}\hat{c}_k + \sum_{k=1}^{N_e} V_k(\boldsymbol{R})(\hat{c_a}^{\dagger}\hat{c}_k + \hat{c}_k^{\dagger}\hat{c_a}), \tag{2.71}$$

where k is the index of the k^{th} bath state.

In addition to the modified Hamiltonian, a new propagation algorithm is also required to perform MQCD. Where metal surfaces are involved, as is the case for the work in this thesis, a full quantum mechanical description of all degrees of freedom is not computationally tractable and a mixed quantum-classical dynamics (MQCD) approach is required. There are three stand out MQCD methods for molecule-metal interactions: Ehrenfest dynamics [50–52], molecular dynamics with electronic friction (MDEF) [53] and independent electron surface hopping (IESH) [54].

In Ehrenfest dynamics, the nuclei evolve on a mean-field PES that is averaged over all electronic states, which themselves are weighted according to their population. It is deterministic and so simulations are computationally efficient in comparison to MDEF and IESH, which are stochastic. However, the range of nonadiabatic systems it is able to describe well are limited to those where nonadiabatic coupling is weak. This makes it unsuitable for the type of systems investigated in the thesis, which involve explicit charge transfer between adsorbate and metal, and the nonadiabatic coupling is strong. In MDEF, the dynamics evolve on a single PES

where nonadiabatic excitation and energy transfer are accounted for via a frictional damping force. MDEF is also best suited to systems where nonadiabatic coupling is weak. This is exemplified by simulations of NO on an Au(111) surface where the single quanta vibrational (de)excitations are captured in the MDEF picture, but the experimentally observed multi-quanta (de)excitations are not [55].

IESH in contrast to Ehrenfest and MDEF methods is able to model adsorbate-metal systems that exhibit strong nonadiabatic coupling. The nuclei move on multiple PESs and can transition or 'hop' between the different surfaces and the probability of a hop occurring during any time step is governed by the nonadiabatic coupling. While Ehrenfest and MDEF both simulate dynamics on a single PES, albeit with modification to account for nonadiabatic energy transfer, the multiple PESs used in IESH make it well suited to describing dynamical processes that involve explicit charge transfer, such as in the cases if CO/NO scattering form Ag(111)/Au(111) studied in this thesis. For these reasons, the theory underlying the IESH method will be described in the following section.

IESH is a modification of the original trajectory surface hopping algorithm: fewest switches surface hopping (FSSH) [56]. The primary difference is that FSSH propagates a single many-electron wavefunction coherently during the dynamics. IESH instead treats each electron independently, and hence propagates N_e single electron wavefunctions, which collectively form a single Slater determinant. This adaptation makes running dynamics simulations for systems with many electrons (*i.e.* metals) much more efficient.

Eqn (2.72) shows how the dynamics will unfold in the IESH method. Nuclear motion will evolve according to the time-dependent classical Hamiltonian:

$$H_{\mathrm{IESH}}(\boldsymbol{R},t) = T_{\mathrm{nuc}}(\boldsymbol{R}) + U_0(\boldsymbol{R}) + \sum_{k\in\mathbf{s}(t)} \lambda_k(\boldsymbol{R}). \tag{2.72}$$

$U_0(\boldsymbol{R})$ is the state-independent term and represents the neutral diabatic surface. $\lambda_k(\boldsymbol{R})$ is the energy of the k^{th} single electron state. The sum over $\{\lambda_k(\boldsymbol{R})\}$ is restricted to occupied states. The time dependent occupations are captured by $\boldsymbol{s}(t)$. λ_k are eigenvalues of the electronic Hamiltonian shown in Eqn (2.73).

$$\begin{aligned}\hat{H}^1_{\mathrm{el}}(\boldsymbol{R}) = U_0(\boldsymbol{R}) + (U_1(\boldsymbol{R}) - U_0(\boldsymbol{R}))\,|a\rangle\langle a| + \sum_{k=1}^{N} \epsilon_k\,|k\rangle\langle k| \\ + \sum_{k=1}^{N} V_k(\boldsymbol{R})(|k\rangle\langle a| + |a\rangle\langle k|),\end{aligned} \tag{2.73}$$

The superscript 1 indicates a single electron operator. The states $|a\rangle$ and $|k\rangle$ are the adsorbate and metal states that correspond to the $\hat{c}_a$ and $\hat{c}_k$ operators, respectively. The nuclear and electronic dynamics are propagated separately via their respective Hamiltonians.

The many electron Hamiltonian ($\hat{H}_{\text{el}}$) can be diagonalised using the eigenvalues of $\hat{H}^1_{\text{el}}$:

$$\hat{H}_{\text{el}} = \sum_j \lambda_j(\boldsymbol{R}) b_j^\dagger b_j, \tag{2.74}$$

where $b_j^\dagger$ and b_j are the creation and annihilation operators for an electron in an adiabatic orbital $|\phi_j(\boldsymbol{R})\rangle$. An N_e electron eigenstate of $\hat{H}_{\text{el}}$ can then be constructed as a Slater determinant of one electron adiabatic orbitals:

$$|\boldsymbol{j}\rangle = |\phi_{j_1}, \phi_{j_1}, ...\phi_{j_{N_e}}|. \tag{2.75}$$

The nonadiabatic coupling between two adiabatic states j and k is:

$$d_{jk} = \frac{\left(U^\dagger(\boldsymbol{R}) \frac{\partial}{\partial \boldsymbol{R}} \hat{H}^1_{\text{el}}(\boldsymbol{R}) U(\boldsymbol{R})\right)_{jk}}{\lambda_j - \lambda_k}, \tag{2.76}$$

where $U(\boldsymbol{R})$ is the transformation operator that converts from the diabatic to adiabatic representation. At each step of a simulation, the coupling between the nuclear and electronic subsystems is captured by surface hops. This happens when the occupation function $s(t)$ changes, due to the evolution of the electronic subsystem. $s(t)$ is a vector containing the indices of all occupied states at each time step Δt. A maximum of one hop (a transition from an occupied state to an unoccupied state) is permitted per time step. The probability that a hop form state j to state k will occur is given by:

$$g_{k\to j} = \max\left(\frac{B_{jk}\Delta t}{A_{kk}}, 0\right), \tag{2.77}$$

with

$$B_{jk} = -2\text{Re}(A_{kj})\frac{p}{m} d_{jk}, \tag{2.78}$$

where p and m are the momentum and mass of the particle and A_{jk} is the element of the total density matrix A, corresponding to states j and k. The algorithm for running an IESH trajectory is as follows:

1. The initial nuclear coordinates ($\boldsymbol{R}$) and momenta are specified by the user. The electronic state is initialised as an eigenstate of the many electron Hamiltonian at $\boldsymbol{R}$. The adiabatic surface upon which the dynamics will initiate is

given by $\boldsymbol{k}$.

2. Nuclear propagation: the classical motion of the nuclei given by Eqn (2.72) is integrated over time step Δt.

3. Electronic propagation: the N_e electronic wavefunctions are integrated over Δt by solving the Schrödinger equation corresponding to $\hat{H}^1_{\text{el}}$.

4. Hopping probabilities $g_{k\to j}$ for switching from adiabatic surface $\boldsymbol{k}$ to all other surfaces $\boldsymbol{j}$ are calculated, provided $\boldsymbol{j}$ and $\boldsymbol{k}$ only differ by a single occupation. A random number (ζ) from a uniform distribution between 0 to 1 is generated. If $\zeta > g_{k\to j}$ no hop will occur at the current time step, return to step 2.

5. Perform hop: replace $\boldsymbol{k}$ with $\boldsymbol{j}$. Re-scale the velocities to maintain energy conservation. If there is insufficient energy to re-scale the velocity the hop (now referred to as a frustrated hop) is refused. Remain on surface $\boldsymbol{k}$ and return to step 2.

U_0 and U_1 can, in principle be any diabatic surfaces, but in the original implementation of IESH [54] and in this work they represent neutral and anionic diabats of a molecule interacting with a metal surface. In this work, U_0 always refers to the energy of a diabatic state modeled in a charge constrained form of DFT where the molecule (CO or NO) is forced to be neutral at all nuclear coordinates $\boldsymbol{R}$, and U_1 is where the molecule is forced instead to have an anionic charge state. This diabatic two state system can be represented as a 2×2 Hamiltonian, where diagonal elements are U_0 and U_1 and the off-diagonals are the effective coupling (V_c) as shown in Eqn (2.80). This can be transformed into an adiabatic representation via a diagonalisation process to give Eqn (2.81), where the diagonal elements are the adiabatic ground and excited state and off diagonals are 0.

$$H_{\text{a}} = \mathbf{P}^T \begin{pmatrix} U_0 & V_c \\ V_c & U_1 \end{pmatrix} \mathbf{P}. \tag{2.79}$$

$$V_c = \sqrt{(U_0 - E_0) + (U_1 - E_0)}. \tag{2.80}$$

$$H_{\text{a}} = \begin{pmatrix} E_0 & 0 \\ 0 & E_1 \end{pmatrix}. \tag{2.81}$$

The two state representation must be incorporated into a Newns-Anderson Hamil-

tonian in order to perform IESH dynamics simulations, which is expressed as:

$$H_{\mathrm{NA}} = \begin{pmatrix} U_1 - U_0 & c & \cdots & c \\ c & \epsilon_0 & & \\ \vdots & & \ddots & \\ c & & & \epsilon_M \end{pmatrix}, \tag{2.82}$$

where the first diagonal element is the difference between the two diabatic surfaces and the remaining diagonal elements are the energies of the bath states. The non-diagonal elements are f coupling elements c, which are fitted with the constraint that:

$$E_0 = U_0 + \sum_i f(\lambda_i)\lambda_i, \tag{2.83}$$

Eqn (2.83) represents the statement that the adiabatic ground state is equal to the sum of the energy of the lowest diabatic state and all occupied single electron states. The reason for this is that the same ground-state energy will be recovered from both the two state Hamiltonian and the Newns-Anderson Hamiltonian [57].

2.5 Conclusion

This chapter has described the theories that underpin the work presented in the remainder of this thesis; from pure theory in how quantum mechanics can be used do describe chemical systems to practical implementations of theories that can be used to run simulations and gain chemical insights. The results presented later in this work rely, in particular, upon applications of ground-state KS-DFT and excited state le-ΔSCF to construct PESs of molecule-metal systems and the nonadiabatics method IESH to run simulations of molecular scattering experiments.

Chapter 3

Nonadiabatic Molecule-Surface Interactions

3.1 Experimental Background

Processes that display physics that are in violation of the BOA are referred to as nonadiabatic processes. The essence of the BOA is that nuclear and electronic motion are decoupled. The physical consequence is that the full many-body wavefunction, which takes the position of each nucleus and each electron as a separate variable, is replaced by the product of a nuclear wavefunction and an electronic wavefunction. The nuclear wavefunction only depends on the nuclear positions. The electronic wavefunction, however, depends on the electron positions but only parametrically depends on the nuclear positions, as in Eqn (2.11). This product ansatz means that any nuclear dynamics, for example vibrational modes, are accounted for by the nuclear wavefunction and that electron dynamics, such as electronic transitions are accounted for by the electronic wavefunction. If, for example, energy were to flow between a vibrational mode and an electronic state, causing an electronic transition, this would be a violation of the BOA, and therefore nonadiabatic behaviour. For the vast majority of chemical systems, the BOA is a good approximation because it enables chemical dynamics to be described using adiabatic potential energy surfaces (PES) that are used throughout the study of chemistry; wherein each point on the surface represents a different nuclear configuration for which the electronic wavefunction is solved self-consistently to give the electronic energy. Stable structures are represented on a PES by local minima, transition states by saddle points, and reaction pathways are continuous paths from one minimum to another. Despite the prevalence and effectiveness of the BOA over a wide range of chemical

systems, there are some systems that require nonadiabatic effects to be accounted for in order to describe accurately, for example, photochemistry. It is now widely excepted that nonadiabatic effects can occur when molecules come into contact with metal surfaces because electronic excitation of metal electrons requires almost no energy and molecular motion is sufficient to cause the excitation of electron hole pairs [9, 10, 15]. The following sub-sections describe how our understanding of nonadiabatic effects, and which conditions enhance or suppress nonadiabatic processes, has been built up over time using increasingly sophisticated experimental techniques. In particular the focus is on two seminal experimental techniques: molecular beam scattering and chemicurrent experiments.

3.1.1 Atomic and Molecular Beam Scattering

In molecular (or atomic) beam scattering experiments, a beam of gas phase molecules (or atoms) is scattered from a surface under ultra-high vacuum (UHV) conditions [58]. Such experiments provide the most compelling and comprehensive evidence for nonadiabatic energy transfer between atoms/molecules and a metal surface. By carefully controlling the initial state (the translational kinetic energy in the case of atoms and additionally the rotational and vibrational states of molecules) and recording the final energies and states after scattering, details about the nonadiabatic energy transfer process can be revealed. There are several possible energy dissipation channels when molecules or atoms are scattered from surfaces. Both translational and vibrational energy can be transferred to the surface, via an adiabatic channel in which energy is transferred to/from surface phonon modes, or a nonadiabatic channel, where the excitation of electron hole pairs (EHP) in the metal states mediates the energy transfer. There is also reflective scattering where (almost) no energy is transferred, trapping where the molecule loses kinetic energy such that it cannot escape the surface, and finally, dissociation wherein molecular bonds are broken and new bonds to metal atoms are formed. A simple schematic of these processes is shown in Figure 3.1. Of all these processes, only those that are mediated by EHPs are nonadiabatic processes.

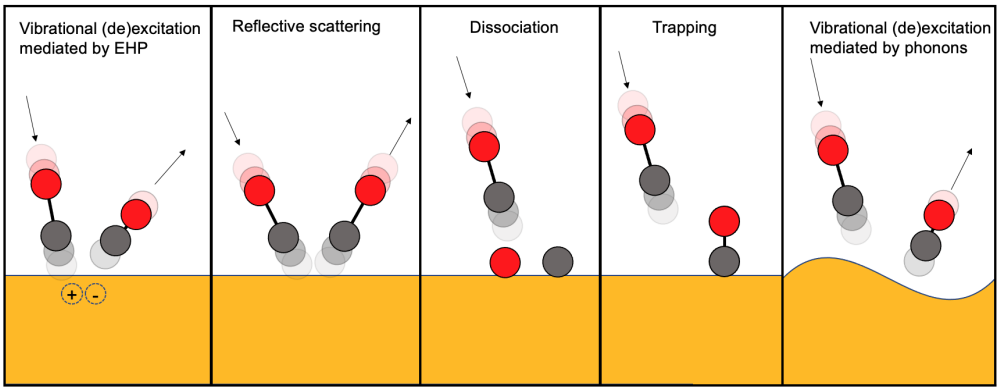

Figure 3.1: Schematic diagram of potential molecule-surface interactions and energy dissipation pathways during a beam scattering experiment.

An early example of nonadiabatic effects observed experimentally came from vibrational lifetimes of CO molecules on a Cu(100) surface, where infrared spectra indicated a vibrational life time in the picosecond range [59]. Later experiments using pump-probe spectroscopy improved this estimate to 2.0 ± 1.0 ps [60]. The observed lifetimes for the molecules adsorbed on the Cu(100) surface are extremely short when compared to the lifetimes on an insulating surface, such as NaCl, of approximately 4 ms [61]. Although the decreased vibrational lifetime of CO on metal surfaces was an indication that nonadiabatic effects may be at play, there were competing theoretical models that tried to replicate the experimental observations, some of which were adiabatic while others were nonadiabatic [62, 63]. No model was able to accurately reproduce all the experimental results, but by changing various input parameters both adiabatic and nonadiabatic models were able to reproduce some trends at the expense of others. By comparing different models and input parameters, Gross and Brenig observed that the nonadiabatic models predicted the NO survival probability (how likely NO is to remain in the initial vibrational state) is strongly dependent on the incidence translational energy (E_i), whereas this was not the case for the adiabatic models. The observation inspired Wodtke and coworkers to perform molecular beam scattering experiments using NO molecules in the $\nu = 2$ vibrational state, scattered from an Au(111) single crystal at different E_i ranging from 0.05–0.75 eV [64, 65]. They observed that increased E_i strongly promoted both excitation and deexcitation of the vibrational state, in line with the nonadiabatic models.

One question that immediately arises from Wodtke's results is, if molecules

in $\nu_i = 2$ can efficiently transfer energy nonadiabatically, what would be seen if the molecules had much more initial vibrational energy? Stimulated emission pumping (SEP) is an experimental technique for preparing molecules in a high-lying vibrational state of the electronic ground state [13]. It uses multiple laser pulses to achieve this: The first pulse (pump pulse) excites molecules to a non-ground electronic state (possibly but not necessarily also to a higher vibrational state). A second pulse (dump pulse) is then used to stimulate the deexcitation back to the ground electronic state, but a high lying vibrational state. Using SEP allows for a great deal of control over the initial vibrational states for any subsequent experiment. SEP is required because selection rules for purely vibrational excitations of molecules state $\Delta\nu = 1$. Sequential excitation of vibrational states is therefore highly impractical, if possible at all, and would lead to a distribution over many vibrational states for a collection of molecules.

Molecular beam scattering experiments, using SEP to prepare NO molecules in high lying vibrational states prior to scattering, revealed that the energy transfer process proceeds via multiquantum (de)excitation [66, 67]. A single crystal Au(111) surface was covered with an adlayer of Cs atoms, resulting in a metal surface with a low work function (1.3–1.6 eV). Importantly, the reduced work function is smaller than the vibrational energy of NO molecules excited to $\nu = 8$ or higher. This results in the emission of electrons from the surface when the highly excited NO molecules are scattered from it, transferring vibrational energy to EHPs in the metal. The kinetic energy of the exoelectrons was measured to ascertain the energy transferred. The energies correspond to several quanta of vibrational energy being transferred in a single step, as opposed to a stepwise process where only a single quanta is transferred at a time. Exoelectrons were only observed if the vibrational energy was greater than the work function and the limiting factor in the observed final kinetic energy distribution was the available vibrational energy. These experiments also showed that the energy transfer process is highly efficient. An unexpected finding from this experiment was that increasing incidence energy saw a small, but detectable, suppression of electron emission. This was initially incorrectly used to infer that increasing translational energy decreases vibrational (de)excitation probability. Later state-to-state experiments, in which both the initial and final (vibrational) states are directly observed, by the same group, showed this interpretation to be false. While it is true that electron emission is suppressed, this is due to a critical region 5–10 Å from the surface in which electron emission can occur. Increasing translational energy reduces the time a molecule spends in the critical region and therefore electron emission probability is reduced. The state-to-state experiments

were able to directly observe the final vibrational states of the scattered molecules, circumventing the need to add a Cs adlayer to the surface and rely on exoelectrons to infer the final vibrational state distributions. The state-to-state experiments showed that increasing incidence translational energy in fact promotes vibrational (de)excitation. The key points from this experiment are that the nonadiabatic energy transfer is incredibly efficient with large quantities of vibrational energy being transferred in a single scattering event and that higher vibrational states strongly promote nonadiabatic energy transfer into EHPs.

Having established that the dominant pathway for vibrational energy transfer processes is indeed nonadiabatic, studies were performed to elucidate the underlying mechanism. It is now widely accepted that the nonadiabatic vibrational energy transfer process proceeds via a so called vibrational auto-detachment mechanism [65, 67]. As the molecule approaches the surface, back-bonding via the LUMO (π^*) occurs and as the bond oscillates, the stability of the LUMO changes and charge from the surface oscillates into and out of the LUMO. Vibrational energy is transferred to the electronic states of the metal creating an electron hole pair. The excited electron hops from the surface to the molecule at or near the outer turning point of the vibration. As the bond compresses, the anionic molecule becomes less stable and a second transfer occurs from the molecule back to the metal. The neutral molecule leaves the surface in a lower vibrational state.

In the years following the experiments described above, there were several key advances in experimental techniques that enabled far greater control of the molecular degrees of freedom and additional information could be gleaned from the molecules after scattering from the surface:

- Extensions to the standard SEP scheme called pump-dump-sweep, allow for greater quantum state purity of the molecules by suppressing unwanted spontaneous emission from intermediate excited states that would otherwise pollute the sample with molecules in non-target vibrational states [68].

- Resonance enhanced multi-photon ionisation (REMPI) spectroscopy allows observation of the final vibrational state [69]. REMPI is a more direct way of gaining information on the state of the molecules and does not interfere with the scattering process itself, unlike earlier exoelectron experiments [69].

- In prior works, the orientation of the molecules could only be controlled using hexapole focusing, which could only be applied at low translational energies. A new technique called optical state selection with adiabatic orientation enables

selection of molecular orientation prior to the scattering event [70].

Using all of the aforementioned techniques in combination, Wodtke *et al* performed a comprehensive study of NO–Au(111) scattering to assess which degrees of freedom (DOF) are most important to promote or suppress nonadiabatic effects. The study used 5 different incidence translational energies (E_i) ranging from 0.05 to 0.97 eV, 3 different incidence vibrational states $\nu_i = 3, 11, 16$ and 2 molecular orientations, namley N towards the surface and O towards the surface [69, 71]. For all combinations of the molecular DOF explored, the dominating factor is the initial vibrational state (ν_i). There is a clear enhancement of vibrational energy transfer when molecules impact the surface with N facing the surface compared to O (see figure 3.2) that can be explained by noting that the auto-detachment mechanism involves the transfer of an electron from the metal into the LUMO of the molecule. The LUMO has more density at the N end and therefore if the molecule approaches the surface with N down there will be a greater overlap of the LUMO with the metal orbitals. Thus making the charge transfer more favourable than if the molecule approached with O facing the surface. However, when NO is in a sufficiently high vibrational state, the preference for the N down orientation makes very little difference as the probability of the transfer is already in excess of 0.95 as can be seen in figure 3.2. A similar trend is seen with respect to E_i. Larger E_i increases the probability of vibrational energy transfer. Again, if the molecules are in a high vibrational state, the vibrational energy transfer is so efficient that the effect of the translational energy diminishes and is not an important factor.

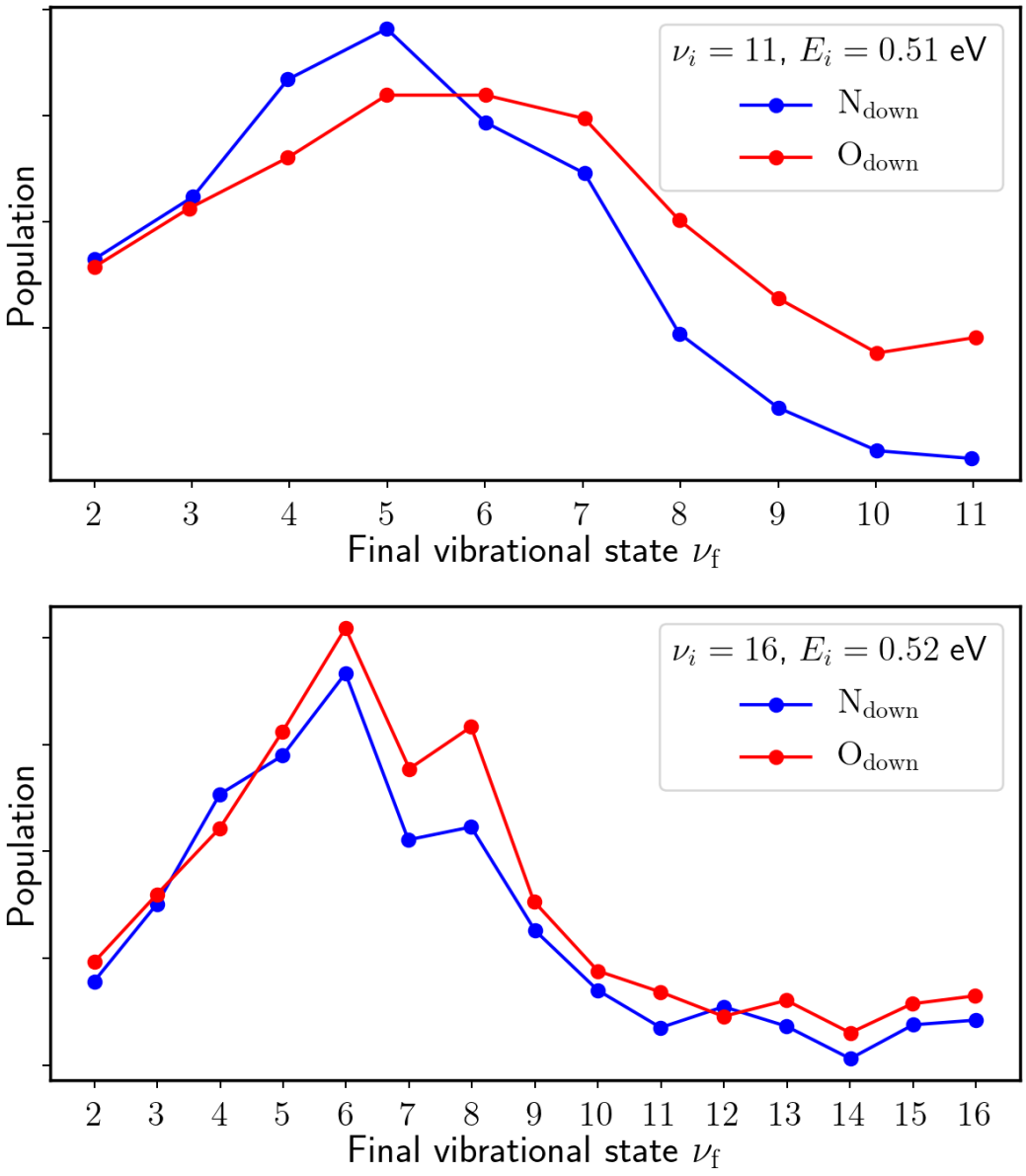

Figure 3.2: Experimental results of NO-Au(111) scattering experiments reproduced from [69] using WebPlotDigitizer. Final vibrational state populations are plotted for $\nu_i = 11$ (top) and $\nu_i = 16$ (bottom) with translational energies of 0.51 and 0.52 eV respectively. Note: the lack of numbers on the y axis mimics the way the data was presented in [69].

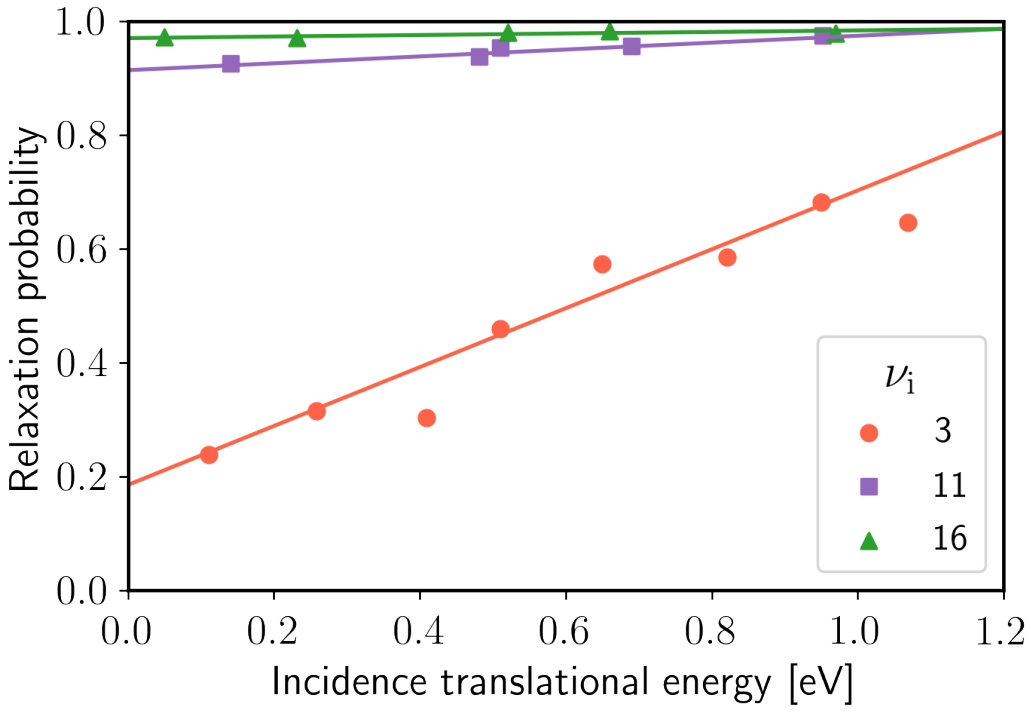

Figure 3.3: Results of NO-Au(111) scattering experiments reproduced from [69] using WebPlotDigitizer. Relaxation probability is plotted as a function of E_i for incident vibrational state $\nu_i = (3, 11, 16)$.

Having now covered the degrees of freedom of the molecule, let us turn our attention to the influence of the surface. When the Au(111) surface is replaced by an Ag(111) surface, the vibrational (de)excitation is enhanced [72]. Since the auto-detachment mechanism requires that a metal electron be transferred to the molecule, it should be obvious that the metal work function is an important parameter, with lower work functions promoting the transfer. The work function of Ag(111) is indeed lower, 4.7 eV compared to 5.3 eV [72]. However, there are other differences aside from the lower work function that may contribute to the increased efficiency of nonadiabatic energy transfer. The authors offer two additional considerations for explaining the mechanism for enhanced nonadiabatic energy transfer. Firstly, the adsorption energy of NO on Ag(111) is greater than for Au(111) indicating that the molecule is able to get closer to the surface before hitting a repulsive wall. The decreased molecule-metal distance may promote energy transfer. The second possible factor is that NO has been observed to dissociate on Ag(111) but not on Au(111). The auto-detachment mechanism relies upon the stretched bond to transfer the electron and form a transient ion. Therefore if the molecule is ap-

proaching the transition state to dissociation this may promote electron transfer. A similar effect has been observed for H_2 on Cu(111) where vibrational inelasticity is enhanced due to a dissociation transition state [73].

There are many examples of similar scattering experiments in the literature involving different small molecules and noble metals. In order to keep this section relevant to the work presented in this thesis, only two other systems will be discussed: CO/Au(111) and CO/Ag(111). CO is very similar to NO in many respects, and the CO anion is isoelectronic with neutral NO. However, CO has a significantly lower electron affinity, a parameter of central importance to the auto-detachment process. As a result, vibrationally excited CO has a much lower, but still observable probability and magnitude of nonadiabatic energy transfer. For example, for CO (ν=17) scattering from Au(111) with an incidence energy of 0.6 eV, the vibrational relaxation probability is around 35% while under the same conditions the vibrational relaxation probability for NO(ν=16) is greater than 98%. Apart from the decreased probabilities CO follows similar trends to NO. Increased translational energy enhances vibrational relaxation and relaxation with C facing the surface is more favourable than O facing the surface.

The explicit charge transfer steps in the auto-detachment process imply that the energy required to remove an electron from the surface, the work function (ϕ_{surf}), and the change in energy when an electron is added to the molecule, the electron affinity (E_{aff}) are properties of central importance in determining the extent of nonadiabatic energy transfer during scattering events. By reviewing all of their previous scattering results involving CO, NO, Au(111) and Ag(111), Wodtke and coworkers were able to construct a simple model for predicting the vibrational relaxation probability (P_{rlx}) [74]. They used the difference between two parameters as an estimate of P_{rlx}. The first is the energy difference between the neutral and anionic molecule at the classical outer turning point of a given vibrational state, denoted as $E_\nu(r_{\text{out}})$, which is E_{aff} at that bond length. The second is the ϕ_{surf}. The data from their model has been extracted and plotted in figure 3.4. The rationale is that $E_\nu(r_{\text{out}}) - \phi_{\text{surf}}$ is the energetic cost of transferring an electron from metal to molecule. The image charge stabilisation (ICS) must be of equal or greater magnitude in order to make the electron transfer step energetically feasible. ICS occurs when an anion approaches a metal and a partial positive compensating charge is induced in the metal, thereby stabilising the anion. Stabilisation increases with decreasing molecule-surface separation. However below a certain distance the molecule will hit a repulsive wall, which cannot be overcome by ICS. Wodtke and coworkers argue that when $E_\nu(r_{\text{out}}) - \phi_{\text{surf}} < 5.25$ eV the molecule cannot approach close

enough to the surface for ICS to make electron transfer feasible and so no relaxation is seen. Clearly there is strong correlation between P_{rlx} and $E_{\nu}(r_{\mathrm{out}}) - \phi_{\mathrm{surf}}$ and the model may allow for a reasonable estimation of relaxation probabilities for systems involving CO/NO and Ag/Au. However the model is quite limited because it is based on a minimal data-set from a small set of systems. It is not clear whether it can accurately describe vibrational relaxation in other systems. It also does not offer insight into the magnitude of the vibrational relaxation. It is important to seek out models that can accurately capture relaxation probabilities without relying on highly expensive computation and this model is an important step in the right direction. However, clearly this model needs to be compared to other systems including different metals and molecules before a rigorous assessment of the model efficacy can be made.

The high-quality data from state-to-state molecular beam scattering experiments, such as those described above, in which initial E_{i} and ν_{i} are systematically varied and compared to final distributions of ν_{f}, represent an ideal benchmark against which to measure the work that will be presented in this thesis. I will use the le-ΔSCF method to create diabatic PESs which will then be used to preform nonadiabatic dynamics simulations of molecular scattering events at metal surfaces. The success or failure of this methodology will be primarily determined by comparison to experimental results.

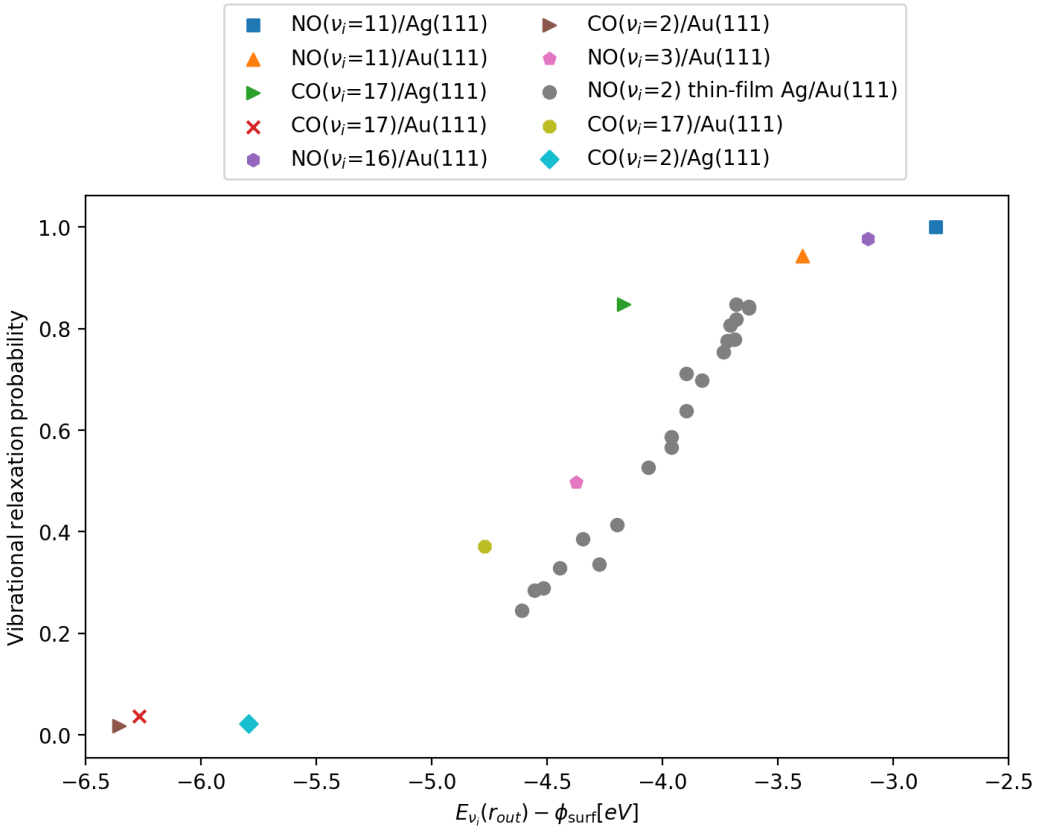

Figure 3.4: Vibrational relaxation probability of various combinations of CO, NO, Au and Ag as a function of $E_\nu(r_{\text{out}}) - \phi_{\text{surf}}$. Data has been reproduced from [74] using WebPlotDigitizer.

3.1.2 Chemicurrents

Chemicurrent experiments involve creating a device that will produce a measurable current when energy is transferred during the experiment which causes the excitation of EHPs [75]. Primarily there are two types of devices used, firstly metal-insulator-metal (MIM) devices and secondly Schottky diodes. MIMs have a top thin-film metal layer on which the chemistry of interest will take place, an insulating middle layer and a metal bottom layer. Electrodes are connected to the top and bottom layers. A Schottky diode is very similar; the top metal layer is a thin-film but the insulator is replaced with a semiconducting layer. The bottom layer is absent and the electrode connects directly to the semiconductor. In each case the second layer acts as a filter for electrons that may reach the bottom layer/contact. The basic principle is that energy from an interaction on the surface which leads to excitation of electron hole

pairs that, provided the electron (or hole) has sufficient kinetic energy, will travel through the conduction band of the insulator/semiconductor to the back contact and produce a current. This allows inference to be made regarding the rates and magnitude of energy being transferred to the electronic states of the metal. By making the Schottky diode using either n-doped or p-doped Si semiconductor layers, it is possible to observe negative and positive charge carriers, *i.e.*, electrons and holes [76].

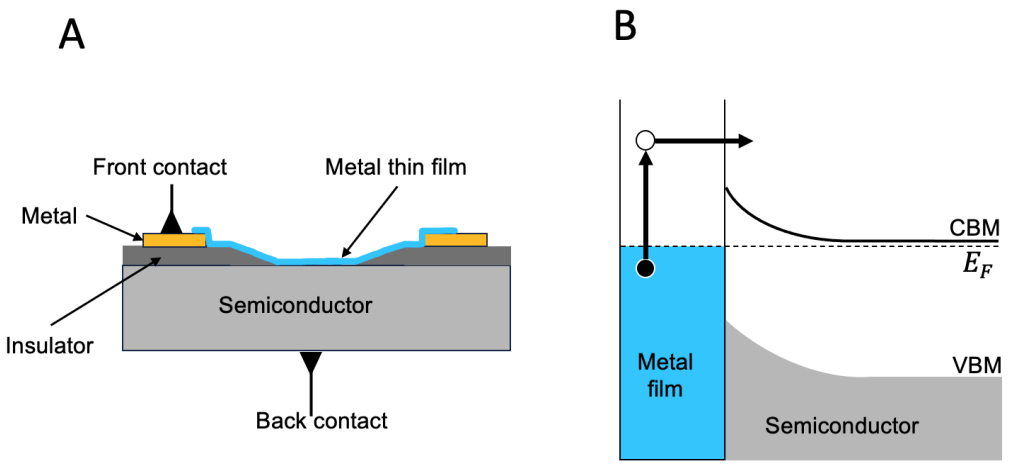

Figure 3.5: Panel A shows a diagram of a typical Schottky diode device used in chemicurrent experiments [76, 77]. Electrons (or holes) that are excited when atoms/molecules are scattered from the metal thin film surface can create a detectable current by travelling through the semiconductor layer, to the back contact, thereby completing the circuit. Panel B shows a band structure diagram representation of a Schottky diode producing a chemicurrent: An electron-hole pair is excited within the metal film. The electron (white circle) moves into the conduction band of the semiconductor, towards the back contact.

The majority of chemicurrent experiments in literature involve H_2 adsorption; however, experiments have also been performed for a variety of atomic and molecular species, such as NO, NO_2, O_2 and Xe, all of which produced measurable currents [76–79]. When NO was absorbed onto a Ag/n-Si Schottky diode, a strong current peak was observed for the initial NO adsorption [76]. This is further evidence that chemical interactions of NO with metal surfaces can directly excite electron-hole pairs through nonadiabatic energy transfer.

Evidence from chemicurrents is compelling but also suffers from some issues that should give pause when interpreting the data. While the scattering experiments

are performed using a single crystal and under UHV with very fine control of experimental degrees of freedom, chemicurrent experiments require fabrication of a device [75]. The device fabrication occurs under less rigorously controlled and non-UHV conditions, although the experiment in which the current is measured is performed under UHV conditions. For the initial chemicurrent experiments, adsorbing H on Ag films produced 30 times the current observed for a Cu film. The commonly accepted explanation for this is that the devices were prepared under different conditions, which indicates that precise control and characterisation of any devices used is essential in order to draw meaningful conclusions [10]. The extent to which device fabrication and experimental conditions may impact the observed chemicurrents in a given experiment is still an ongoing area of research [75], however the statement that the observation of chemicurrents is direct evidence of nonadiabatic energy transfer at metal surfaces is not in question.

The experimental evidence that nonadiabatic processes occur at the molecule-metal interface is vast and compelling. Teasing out the details of these processes has been and continues to be a long and complex process. There have been many advances in experimental techniques and understanding. However there is still much to be revealed. During the same time period there has been a huge effort to construct accurate computational models of these systems that has worked in tandem with experiment. The theoretical work will be described in the following section.

3.2 Computational Background

Surface chemistry is commonly modelled using first principles methods for a vast combination of molecules and surfaces. So much so, that that a so-called "standard model of surface reactivity" has been established [10]. Any realistic surface contains a vast number of atoms, and in a transition metal surface each atom contains many electrons. In order to make any simulation of such surfaces computationally tractable, approximations and simplifications must be made, while retaining as much of the correct physics as possible. For these reasons, the standard model of surface chemistry primarily consists of three approximations.

1. The level of theory. Almost all atomistic electronic structure models used to study surface reactions are based on DFT because of the balance it offers with respect to accuracy and cost [80]. Simple gas phase molecular reactivity is often modelled using high-level quantum chemistry methods, that are more accurate than DFT. However, the huge computational cost associated with applying these methods to surface chemistry makes them unfeasible to use and

DFT is the widely accepted method of choice. Additionally, the exchange-correlation functional used determines the level of theory within the DFT domain [81]. Simulations are typically performed at the generalised gradient approximation (GGA) level. While higher level functionals are available, such as meta-GGAs, the GGA level is seen as a reasonable compromise between accuracy and efficiency [80].

2. Reduced dimensionality. By their very nature metal surfaces contain many atoms and very many electrons. It would be impossible to treat realistically sized systems with any sort of rigor. The so-called slab model is used instead. A few layers of a metal substrate are placed in a unit-cell where the surface atoms span across the entire cell in x and y, but with a large vacuum gap above and below the substrate layers. PBC are enforced that repeat the unit cell in all three directions. The resulting model is then a stack, in the z direction, of infinitely wide slabs. The z distance between slabs in one unit cell and its neighbours must be large enough that there is no interaction between the slabs. To make the model more akin to a real surface, the bottom layers are fixed in their bulk positions while the top layers are allowed to relax. Finally, any atoms/molecules that will interact with the surface are added to the unit cell. The unit cell should have a sufficiently large vacuum gap that the adsorbate(s) only interact with the slab within the same unit cell and not the neighbour above. Once any adsorbates are added, it is also important to make sure that the unit cell is large enough in x and y that any lateral interactions between adsorbates in neighboring unit cells as close to zero as possible.

   The central task in any DFT calculation is obtaining the ground-state solution of the electron density ($\rho(\boldsymbol{R})$). This task is computationally intensive and formally scales on the order of N^3 with the number of electrons (N_e). Therefore for many systems, and particularly in the case of metal surfaces, it can greatly increase the efficiency of the calculation if N_e can be reduced. Chemistry is dominated by changes in the interactions of valence electrons while core electrons remain unaffected. This means that, whenever the electronic wavefunctions are being optimised, core electrons may be modelled by an effective potential rather than being explicitly included, without having an effect on the ground-state ρ that is obtained at the end of the calculation. The two most common schemes for replacing core electrons are the pseudopotential method and the projector augmented wave (PAW) method [82–84].

   Additionally, any nuclear DOF (*i.e.* atomic motion) that are deemed to be

non-essential to the chemistry in question may be restricted or excluded. For example, substrate motion may be excluded using a frozen surface approximation and reactant motion may be restricted to chemically relevant paths.

3. The Born-Oppenheimer approximation (BOA) or the electronic adiabaticity approximation is used in all DFT calculations to dramatically reduce the complexity of the numerical problems to be solved [12]. The resulting adiabatic PES, which are constructed by sampling different configurations of nuclear coordinates and solving the electronic problem with static nuclei at each configuration, are ubiquitous throughout the study of chemistry [21]. Common ideas in chemistry such as steric repulsion, transition states and activation energies are all references to the topology of the adiabatic PES.

For much of surface chemistry, the BOA is a valid approximation and the adiabatic PES works well in providing a description of the chemistry. However, as described in Section 3.1, molecules interacting with metal surfaces is a domain of chemistry where the BOA is less valid and can break down entirely. Experiments have shown that nonadiabatic channels can be a significant energy dissipation pathway in some molecule-metal systems, in particular via energy transfer between adsorbate motion and electronic states at metal surfaces. To account for such effects in models, the nonadiabaticity must be somehow 'added back in' after constructing potentials that rely on the BOA. Mixed quantum-classical dynamics (MQCD) algorithms, wherein the motion of nuclei progresses classically but electron dynamics are treated on a quantum level, are the method of choice in this respect because they offer a good balance between accuracy and efficiency. There are two primary implementations that have shown some success in modelling nonadiabatic effects at surfaces: the MQCD algorithms of molecular dynamics with electronic friction (MDEF) [85] and independent electron surface hopping (IESH) [18] combined with a Newns-Anderson Hamiltonian (Section 2.4).

What follows is a summary of some key computational results in simulating the nonadiabatic dynamics of the NO vibrational (de)excitation molecular beam scattering results, described in Section 3.1.1, using IESH and MDEF.

The first applications of both IESH and MDEF to the NO scattering from Au(111) surface used very high initial vibrational states $\nu_i = 15$ and low incidence kinetic energy $E_i = 0.05$ eV [86, 87]. Both MDEF and IESH are able to capture the significant vibrational deexcitation seen in experiment, which is missing in the purely adiabatic dynamics. Both models seem to overestimate the deexcitation to lower-lying states, however the experiments do not capture data for molecules in ν_f

lower than 5. It is also not entirely clear how much the disagreement with experiment stems from the MQCD method compared to potential flaws in the underlying PES used in either case. Both studies used PES generated using the PW91 functional and a Au(111) slab with a single NO molecule per unit cell. However, the IESH results used neutral and anionic diabatic PESs generated by applying an electric field across the unit cell, which is less ideal than a proper charged constrained scheme [19]. The MDEF PES was restricted to two DOF: the vertical molecule-surface separation and the NO internal bond stretch.

When trajectories were initiated in the lowest vibrational state, $\nu_i = 0$, IESH was still able to qualitatively reproduce experimental trends of vibrational excitation, although the discrepancy between simulation and experiment increased with higher final vibrational state $\nu_f \in \{1, 2, 3\}$ [88]. MDEF predicted no excitation at all, leading to the conclusion that IESH is the method best suited to modelling nonadiabatic surface scattering under these conditions.

The IESH simulations also indicated that there was a strong steric effect that produces a dynamical steering force that increases the likelihood that the molecules would impact the surface with N facing towards the surface [86]. This prompted further beam scattering experiments that proved this was a real effect and not an artifact of theory [69, 71]. The confirmation of the steering force shows that even with the limited models available, theoretical simulations can offer valuable insights for experimentalists that can inform a deeper understanding of dynamics at surfaces. Despite the initial observation of the steric effect coming from simulation, the IESH results underestimated the orientation dependence compared to experiment. A potential cause for this is forces are derived from the underlying PESs, which are approximate.

With the success of those initial nonadiabatic computational studies, and with improved experimental techniques, a much larger set of experimental results were gathered over a much wider range of incidence energies and initial vibrational states [88]. Subsequent comparison between simulation and experiment revealed much more deviation in observed trends. Scattering experiments were performed with $\nu_i \in \{3, 11, 16\}$ with $E_i \in \{0.5, 1.0\}$ eV. When the final state distributions were compared to IESH and MDEF, both methods showed an underestimation of multiquantum deexcitation in all cases [88]. For the $\nu_i = 3$ results, the differences were relatively small, however for $\nu_i = 11$ and especially for $\nu_i = 16$ the discrepancy was very large. It was found that many of the trajectories included multiple bounces from the surface. Based on angular distribution analysis in experiment, the multi-bounce phenomenon was deemed to be an artifact of the simulations and

not something seen in experiment. This was attributed to the PES being too 'soft', enabling more sticking than expected. By excluding multi-bounce trajectories from the analysis both MDEF and IESH result were improved, but still significantly underestimated multiquantum deexcitation. The potential explanations for the deviation from experiment are primarily associated with the PES. The neutral and anionic PESs used in IESH were calculated by applying a electric field across the unit-cell, rather than an explicit excited state method [19]. Additionally, the interpolation of the explicitly calculated energies may result is surfaces that are too corrugated. It is also suggested that geometries approaching the dissociation barrier of NO, which is not included in the PES, may also be relevant in facilitating vibrational deexcitation [10]. This is especially the case in the $\nu_i = 16$ case where the outer turning point of the vibration is close to the dissociation barrier. Further evidence that inaccurate PESs may be a significant factor comes from analysis of the final molecular translational energy distribution. IESH and adiabatic molecular dynamics both underestimate the final translational energy by a similar amount, even though, by definition, adiabatic molecular dynamics do not include any nonadiabatic energy transfer. Although it seems clear that at least some of the issues with the simulations can be attributed to the PESs, there may also be a contribution from the underlying IESH method, especially at high ν_i where disagreement is strongest. As currently implemented only one excited state of NO is included (the anion) and spin effects were ignored. It is possible that where there is such large vibrational energy, other excited state(s) are involved that make the vibrational relaxation process much more efficient. Nothing in the theoretical framework of IESH would prohibit including more states, but doing so would be much more complex, especially transitioning from the simple 2×2 model Hamiltonian representation of the diabatic energies and coupling (see Section 2.4) to a 3×3 or potentially even larger model Hamiltonian and deriving new diabatic coupling terms. The most sensible approach would be to first focus efforts on generating the most accurate PESs that are reasonably possible and investigate how much discrepancy between simulation and experiment remains, before making the model more complex. The construction of accurate PESs, particularly anionic and neutral diabatic PES, using the le-ΔSCF method is a central goal of the work in this thesis.

Chapter 4

Assessing the le-ΔSCF Method

The primary goal of the work presented in this thesis is to construct meaningful excited PESs that can be used in NAD simulations to model the physics of molecular beam scattering experiments. Before this work, the only existing excited state PES for these type of systems was that of NO on an Au(111) surface where the diabatic potentials were constructed using an applied electric field [89]. In this work, we examine the constrained DFT excited state method le-ΔSCF which is used to build accurate diabatic PESs. This chapter discusses the method and how it can be applied to these systems. There are two implementations of le-ΔSCF: density-based (ρle-ΔSCF) implemented in the real space projector augmented wave electronic structure software package GPAW and wavefunction-based (Ψle-ΔSCF) which is implemented in the planewave pseudopotential electronic software package CASTEP [16, 17, 82, 90]. Although they both fall under the umbrella of le-ΔSCF, they are different and will produce quite different PESs for the same charge state of a given system. What they share in common is that they both construct resonance orbitals based on FSMO orbitals and the constraints are defined with respect to the resonance orbitals.

4.1 ρle-ΔSCF

The first practical implementation of le-ΔSCF used the projector augmented wave based electronic structure software package GPAW [16]. It enforces constraints by modifying the electron density, as opposed to the wavefunctions, and will therefore be referred to as the ρle-ΔSCF method. The first step is to create a resonance

orbital via a linear expansion of the set of Kohn-Sham states.

$$|\Psi^c\rangle = \sum_{\text{subspace}} C_i \left|\Psi^i\right\rangle, \tag{4.1}$$

Where c is the index referring to the given constraint. The expansion coefficients differ from Eqn (2.65) by the inclusion of a normalisation term.

$$C_i = \frac{\langle \Psi_i | \phi_j \rangle}{(\sum_{\text{subspace}} |\langle \Psi_i | \phi_j \rangle|^2)^{\frac{1}{2}}} \tag{4.2}$$

The aim is that $|\Psi^c\rangle$ should be a good representation of a molecular orbital of the FSMO ($|\phi_j\rangle$), such that constraining charge to $|\Psi^c\rangle$ will effectively constrain charge to the molecule. Within ρle-ΔSCF constraints are enforced by creating a constrained electron density ($\tilde{\rho}(\boldsymbol{r})$). Each constraint specifies the amount of negative charge (Δq^c) that should be added to the full-system density, based on the shape and location of $|\Psi^c\rangle$. To construct $\tilde{\rho}(\boldsymbol{r})$, first, a Fermi distribution is calculated for the system but containing only $N_e - \sum_c \Delta q^c$ electrons and used to construct a pre-density ($\rho^{\text{pd}}(\boldsymbol{r})$). Secondly, densities corresponding to each constraint ($\rho^c(\boldsymbol{r})$) are constructed by taking the outer product of the resonance orbital with itself and multiplying by total electrons being constrained (N_c), as in Eqn (4.3), and added to $\rho^{\text{pd}}(\boldsymbol{r})$.

$$\rho^c(\boldsymbol{r}) = |\Psi^c\rangle \langle \Psi^c| N_c \tag{4.3}$$

$$\tilde{\rho}(\boldsymbol{r}) = \rho^{\text{pd}}(\boldsymbol{r}) + \sum_c \rho^c(\boldsymbol{r}) \tag{4.4}$$

It is important to note that $\tilde{\rho}(\boldsymbol{r})$ is not used directly as the input density ($\rho^{\text{in}}(\boldsymbol{r})$) or the output density ($\rho^{\text{out}}(\boldsymbol{r})$) during an SCF cycle. Whether an le-ΔSCF (or ground-state DFT) calculation has converged is determined by whether the difference between $\rho^{\text{in}}(\boldsymbol{r})$ and $\rho^{\text{out}}(\boldsymbol{r})$ is smaller than the chosen tolerance (E_{tol}) as shown in Figure 4.1. $\tilde{\rho}(\boldsymbol{r})$ indirectly affects the $\rho^{\text{out}}(\boldsymbol{r})$ that the SCF cycle will arrive at because the effective Kohn-Sham potential (V_{ks}) is calculated using $\tilde{\rho}(\boldsymbol{r})$. V_{ks}, in turn, enters the Kohn-Sham equations, which are solved to give a new estimate of the KS wave functions that are used to construct $\rho^{\text{out}}(\boldsymbol{r})$.

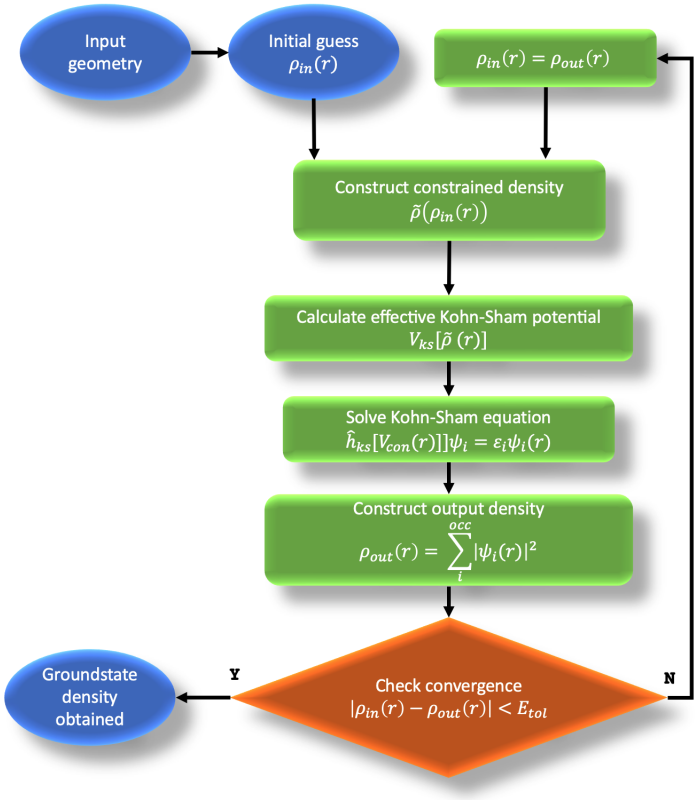

Figure 4.1: Flowchart showing the modified SCF procedure used during a ρle-ΔSCF calculation.

Eqn (2.64) implies that the sum for the expansion should run over all $|\Psi_i\rangle$, but in Eqn (4.1) the sum only runs over a subset of $|\Psi_i\rangle$. While in principle any state could be included in the linear expansion, in practice ρle-ΔSCF requires that only a sub-set of all states are included, either all the unoccupied states or all occupied states, to enforce orthogonality [16]. If states outside the correct subspace are included the SCF procedure will (usually) converge, but will return incorrect energies due to a violation of constant N_e and therefore a breakdown of the variational principle.

The most common charge transfer excitations for molecules at metal surfaces are molecular anions, where the molecule accepts charge from the metal states [91]. To model this, the charge constraints must involve moving charge from a state at the Fermi level to a resonance orbital resembling the molecular LUMO. In cases where the charge density of the resonance orbital is increased, the sum in Eqn (4.1) should run over the unoccupied states only, because these are already orthogonal to the occupied states and therefore the resulting resonance orbital will also be

orthogonal to all other occupied states. In cases where electron density should be removed from the resonance orbital e.g. to approximate a cationic molecule on the surface, the sum should instead run over the occupied states, since these are the states that contribute to the density on the molecule. The use of resonance orbitals and constraints makes the le-ΔSCF methodology ideal for modelling excited states at molecule/metal interfaces and in particular charge transfer states. However it also imposes some limitations compared to ground state DFT. The Hellman-Feynman theorem can not be applied to le-ΔSCF because it is only valid for eigenstates of the KS-Hamiltonian, not for linear combinations of eigenstates [92]. Gavnholt showed that le-ΔSCF forces based on the Hellman-Feynman theorem are incorrect [16]. This results in one of the key limitations of the le-ΔSCF method: it cannot provide analytical forces. The introduction of non-KS states also means the formal justification for simple ΔSCF does not apply to le-ΔSCF and it reverts to being an *ad-hoc* method. Despite these drawbacks, it can still produce very useful results, provided the system and constraints are chosen carefully [17, 44, 45].

In a previous study, ρle-ΔSCF was tested on several systems that showed that higher lying excited states are less accurately modelled than low lying ones, therefore this method is likely only suitable for low lying excitations [16]. In that study, and all other previously published ρle-ΔSCF studies, charge transfer states were modelled by adding/removing one full electron [16, 44]. This choice assumes the molecule adsorbed on the surface will retain its gas phase occupations, *i.e.*, in a neutral charge state, and ignores the fact that in the ground-state the molecule will exchange charge with the surface Δq_{gs}. Neglecting Δq_{gs} leads to too much charge being added for anions and too little charge being removed for cations. The work presented in this thesis uses a modified approach where the constraints are based on the difference between Δq_{gs} and the charge state of interest. As an example, if a resonance orbital representing the FSMO LUMO ($|\Psi^c_{\mathrm{L}}\rangle$) has an occupation of 0.0 far from the surface and picks up 0.25 electrons upon adsorption on the surface, to approximate a molecular anion 0.75 electrons should be added to $|\Psi^c_{\mathrm{L}}\rangle$. Δq_{gs} is calculated using molecular orbital projected density of states (MODOS) analysis for each FSMO state $|\phi_j\rangle$.

MODOS analysis is a method for gaining insight into how molecular states are hybridised upon interaction with a surface and can be integrated to obtain MODOS charges, which are a measure of the amount of charge transferred to the molecule [93]. Similarly to le-ΔSCF, the molecular states are modelled by FSMO

states ($|\phi_j\rangle$). The MODOS ($P_j(E)$) of FSMO state $|\phi_j\rangle$ is given by:

$$P_j(E) = \sum_i |\langle\phi_j|\Psi_i\rangle|^2 \delta(E - \epsilon_i), \tag{4.5}$$

where E is energy and ϵ_i is the eigenvalue of $|\Psi_i\rangle$. Figure 4.1 shows two examples of MODOS analysis performed for the system of CO in an upright orientation, with C atom facing down, above the top site of an Au(111) surface, modelled using a $p(3\times3)$ four layer slab, an $8 \times 8 \times 1$ Monkhorst-Pack **k**-point grid and the RPBE functional in GPAW 20.1.0 [90, 94]. In panel A of Figure 4.1 the distance between the C atom and the Au(111) surface ($Z_{\mathrm{Au-C}}$) is 7.0 Å. ($P_j(E)$) of the FSMO HOMO (green) and LUMO (blue) is plotted on top of the DOS of the full system (black). At this distance, there is almost no hybridisation between molecular and metal states and so both HOMO and LUMO peaks are narrow. The HOMO peak sits entirely below E_{F}, indicating that the state is fully occupied and the LUMO is entirely above E_{F}, meaning it is completely unoccupied, as would be expected of the neutral molecule in the limit of no interaction with the metal. In panel B of Figure 4.1, $Z_{\mathrm{Au-C}}$=2.5 Å and there is significant hybridisation between molecule and metal states, which is seen as a broadening of the HOMO and LUMO peaks across a wider range of energies. Parts of the LUMO peak are now also below E_{F}, meaning the molecule has picked up some charge from the surface, *i.e.*, $\Delta q_{\mathrm{gs}} > 0$.

Integrating ($P_j(E)$) to the Fermi level gives MODOS charge (q_j) associated with state $|\phi_j\rangle$ as in Eqn (4.6), which can used to infer how much charge a molecular state has gained or lost upon interaction with the surface relative to the charge in the neutral FSMO.

$$q_j = \int_{-\infty}^{E_F} P_j(E), \tag{4.6}$$

The full molecular charge (q_{mol}) can be obtained by summing all q_j:

$$q_{\mathrm{mol}} = \sum_j q_j. \tag{4.7}$$

The difference between q_{mol} at a given full system geometry and q_{mol} in the limit of infinite $Z_{\mathrm{Au-C}}$, *i.e.*, the number of electrons in the neutral molecule) gives q_{gs}.

As an example of how to apply MODOS analysis to define constraints in a ρle-ΔSCF calculation consider the anion case: in order to model a molecular anion on the surface, there must be one electron in the LUMO. Therefore, the resonance orbital must be constructed from unoccupied full-system states only. Δq_c

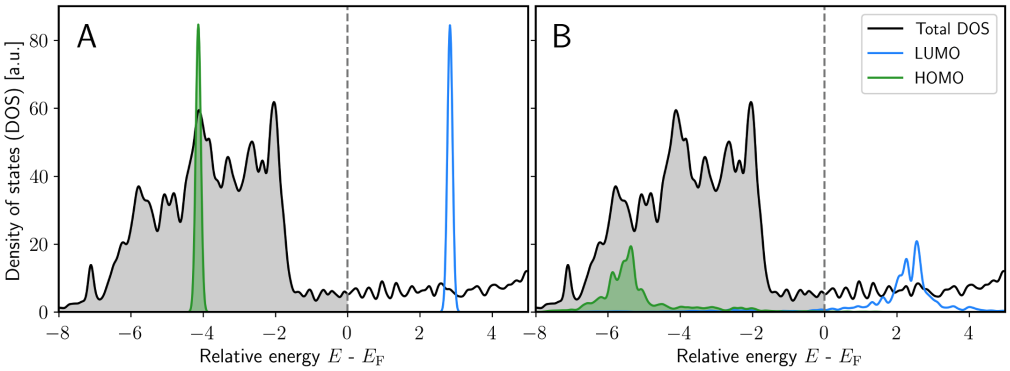

Figure 4.2: Molecular orbital projected density of states (MODOS) of the HOMO (green) and LUMO (blue) of a CO molecule in a upright orientation with C atom facing the surface above a top site of Au(111). The DOS of the full system is shown in black. Shaded areas represent occupied states, *i.e.*, states that are below the Fermi energy (dashed line). In panel A, the molecule is 7 Å above the surface and the molecular peaks are narrow because there is little hybridisation with the metal states. Panel B shows the same peaks when the molecule is 2.5 Å above the surface, where the molecular peaks have broadened due to hybridisation. Some of the contribution to the LUMO is below the Fermi energy, meaning the molecule has picked up charge from the metal. It should be noted the molecular peaks have been scaled by a factor of 20 to aid visualisation.

should be a positive number and the difference between the ground-state MODOS occupation and the desired occupation. If occupied states were included in the linear expansion, adding Δq_c would overfill the states and result in a breakdown of the variational principle because N_e is not conserved. Conversely, if the excited state of interest is the neutral molecule then the LUMO should be emptied of any charge it picked up from the surface. Therefore, the expansion should only include occupied full-system states and Δq_c should be negative. The example of LUMO occupations and the choice of anionic and neutral charge states are arbitrary. The consistent principle applied to any system when performing a ρle-ΔSCF calculation is that increases in occupation of resonance orbitals should use only unoccupied states and decreases should use only occupied states to construct $|\Psi^c\rangle$. Subspace selection provides versatility for modeling a wide range of systems and charge states. However, it also places limits on system size. There must be sufficiently many states in the relevant subspace that the resonance orbital is a good representation of the FSMO orbital. For the occupied subspace, this is not an issue because any calculation will always include the required states. The unoccupied subspace is more often an issue because increasing the number of unoccupied states increases

the cost of the calculation, but does not provide any additional accuracy to the ground-state energies. Any results based on a poor representation of the FSMO orbital are physically meaningless. Therefore, the cost of increasing the number of bands included in the calculation is simply part of the cost of using this method. The quality of the representation is assessed using Eqn (4.8), where values range from 0 to 1 with 1 meaning a perfect representation.

$$\|\Psi^c(\boldsymbol{r})\| = \sum_i |\langle \Psi_i | \phi_j \rangle|^2 \tag{4.8}$$

The main benefit of this approach, as opposed to Ψle-ΔSCF, is that the problem the SCF procedure is attempting to solve is very similar in complexity to that of finding the ground state, but with a partially rearranged density regardless of the number of constraints. One drawback is that one must include a lot of unoccupied states to ensure there are enough terms in the expansion to properly approximate the molecular resonance. If the incorrect subspace, or even the full space is used the code will still return an energy but it will be unphysical. Often, particularly in the case of anions, the energies will be several eV below the ground-state energy, which is a very obvious sign that the energies should not be trusted. However, sometimes the energies are wrong but are not below the groundstate energy and therefore it can be difficult to tell that the results are wrong and instead one relies on having some physical/chemical intuition for how the system should behave if the constraints are correctly applied. Often this will be the case, but it can somewhat limit the applicability.

4.2 Ψle-ΔSCF

The more recent implementation of le-ΔSCF by Maurer and Reuter (Ψle-ΔSCF) defines the expansion coefficients and enforces constraints differently [17]. It uses both occupied and unoccupied full system KS states for construction of resonance orbitals:

$$|\Psi^c\rangle = \sum_i |\Psi_i\rangle \langle \Psi_i | \phi \rangle \tag{4.9}$$

This process of constructing the resonance state can be conceptualised as projecting the FSMO states onto each full system KS state and scaling the latter based on the magnitude of overlap.

Constraints are enforced by directly modifying the wavefunctions during each SCF cycle and modifying the occupations. First, the full-system KS-state that

has the largest overlap with the resonance orbital is removed and replaced by the resonance orbital. The problem of enforcing orthogonality between the KS orbitals and the resonance orbitals is solved by explicitly performing a reorthogonalization procedure during each SCF step:

$$\left|\tilde{\Psi}_i\right\rangle = |\Psi_i\rangle - \sum_j |\phi_j\rangle \langle\phi_j|\Psi_i\rangle. \tag{4.10}$$

This renders all modified KS states $\{\left|\tilde{\Psi}_i\right\rangle\}$ orthogonal to the resonance orbitals $\{\left|\Psi^R\right\rangle\}$, but breaks the orthonormality of the complete set of orbitals used in the calculation: $\{\left|\tilde{\Psi}_i\right\rangle, \left|\Psi^R\right\rangle\}$. Therefore, a separate re-orthonormalization procedure is performed at each SCF step. The constraints are enforced by restricting the occupation of the resonance orbital and applying a modified Fermi distribution to the non-constrained states, such that N_e is conserved. During each SCF cycle, all non-resonance wavefunctions are optimised, while the resonance orbital must remain unchanged. This is in contrast to simple ΔSCF where all wavefunctions, including constrained ones, can be optimised. The modification was seen to produce more accurate results compared to simple ΔSCF, when tested on the system of azobenzene on Ag(111) [17].

The main benefit of the Ψle-ΔSCF implementation compared to ρle-ΔSCF is that including the resonance orbitals in the set of wavefunctions and explicitly enforcing the excited state occupations means the kinetic energy is treated correctly. However, each additional constraint applied to the system replaces a KS state with a resonance orbital (non-KS state) and further modifies the remaining KS states, and therefore moves the calculation further from the KS-DFT formalism. Additionally, each constraint significantly increases the difficulty of the constrained optimisation problem that must be solved. This is not the case in ρle-ΔSCF where no wavefunctions are modified and constraints act through a single rearrangement of the density. The explicit orthogonalization step negates the need to select a subspace when constructing the resonance orbital. Therefore, all full-system states are included in the expansion. This reduces the number of full-system bands that must be included in order to obtain a good representation of the FSMO orbital, and therefore the computational cost of the calculation compared to ρle-ΔSCF. However, in practice Ψle-ΔSCF calculations tend to suffer from more SCF convergence issues and so any reduction in cost is minimal.

4.3 Results

4.3.1 Ψle-ΔSCF results

A key goal of the work presented in this thesis is to construct high-quality PESs of charge transfer states of molecules interacting with metal surfaces that can then be used to perform nonadiabatic dynamics simulations of molecular scattering. As the nonadiabatic dynamics method chosen for this project is IESH, the PESs required are neutral and anionic diabatic PESs. The neutral diabatic state (neutral diabat) is modeled be enforcing that the molecule remains neutral and does not exchange any charge with the metal. Similarly the anionic diabat is modelled by enforcing the molecule has a charge of -1 and does not exchange charge with the metal. The initial work for this thesis, towards this goal, used the Ψle-ΔSCF implementation in CASTEP 18.1 to model diabatic anionic and neutral states for NO on Au(111) [17, 82]. The GGA functional PBE, norm-conserving pseudopotentials and a plane wave cutoff of 600 eV were used [95]. The Au surface was made from a 6-layer $p(2 \times 2)$ unit cell with 20 Å of vacuum above the slab. Vertical binding energy curves above a bridge site on the surface were constructed. The NO molecule was fixed parallel to the surface normal, with the N atom closest to the surface, at the gas phase equilibrium bond length of 1.195 Å. The molecule was then displaced vertically, and the energy sampled at each geometry.

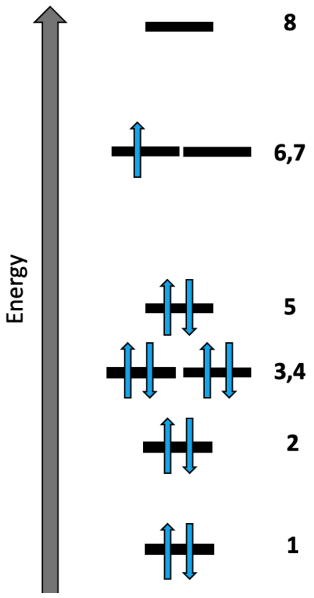

Figure 4.3: A graphical representation of the molecular orbitals of an NO molecule (equivalently a FSMO of NO molecules). States 6 and 7 are degenerate and together they represent the highest single occupied molecular orbital. All lower states are fully occupied and state 8 is fully unoccupied.

To model the neutral and anionic diabatic state, resonance orbitals for all FSMO states from 1-8 (see Figure 4.3) were constrained, with states 6 and 7 forming the degenerate highest singly occupied molecular orbital (HSOMO). The resulting vertical binding energy curves are shown in Figure 4.4.

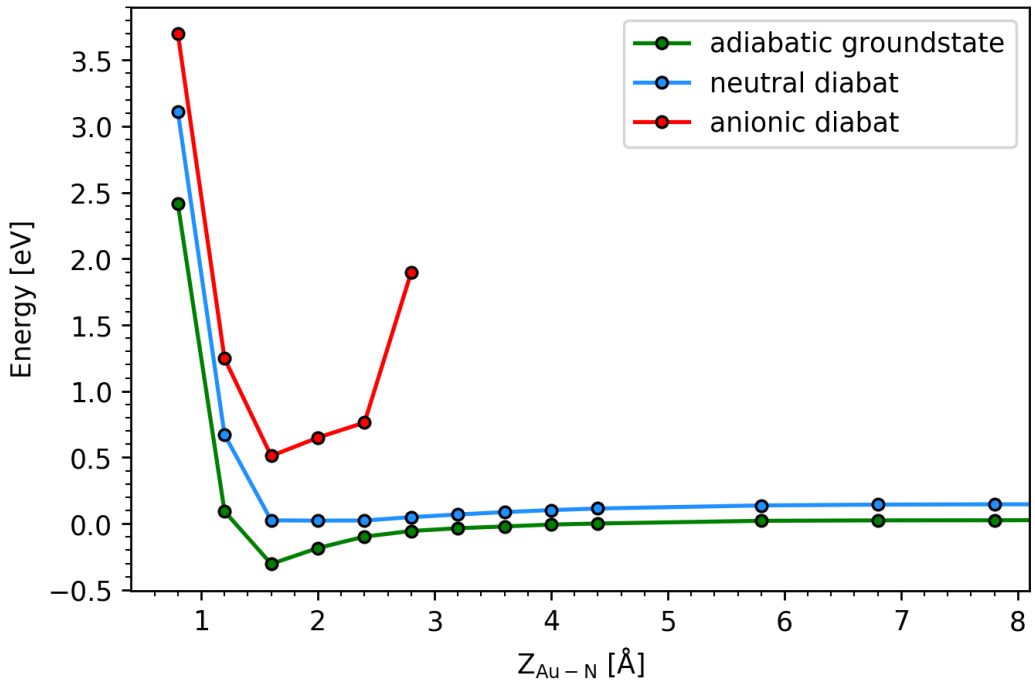

Figure 4.4: Vertical binding energy curves of NO above the bridge site of a $p(2 \times 2)$ 6-layer Au(111) surface. DFT ground state (green), Ψle-ΔSCF neutral (blue) and anionic (red) diabats.

For geometries with a larger molecule-surface separation ($Z_{\mathrm{Au-N}}$) than 3.0 Å, converging the anionic diabat calculations was not possible. In each failed calculation the SCF procedure continued over several hundred cycles without approaching the convergence criteria. The basic principle of an SCF optimisation is that, starting from some initial guess of the density, in each step the model improves upon the previous guess of the ground-state density (in this case a charge constrained density), until certain criteria of convergence parameters are met. The most important convergence parameter in CASTEP SCF optimisations is the energy gain per atom; the log of which must be less that -6 for three consecutive SCF cycles for the calculation to be converged. In Figure 4.5 the log of energy gain per atom is tracked for a successful SCF optimisation which converges within 77 steps (blue line) and a non-converging SCF optimisation (red line). In the well-behaved example, although not every sequential SCF cycle reduced the log of energy gain per atom, there is a clear downwards trend. This is not the case for the non-converging calculation where the value moves up and down throughout the calculation but does not generally result in lower log of energy gain per atom, *i.e.*, does not tend towards SCF

convergence.

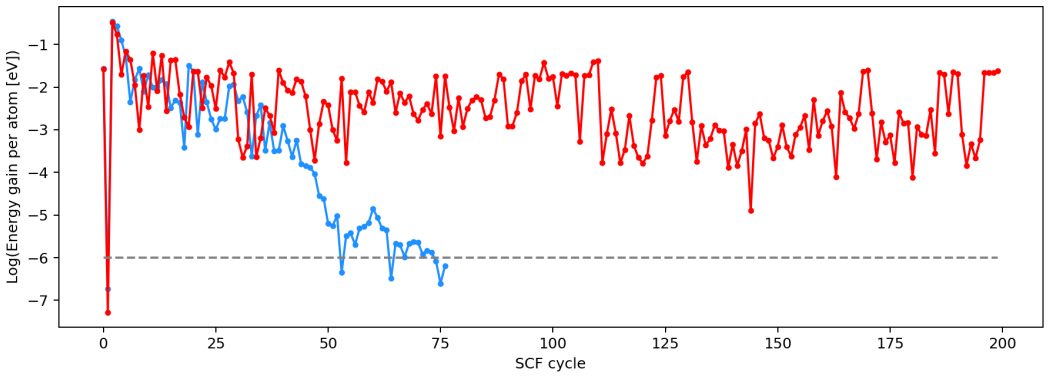

Figure 4.5: Representative examples of SCF convergence behaviour. The blue curve shows a well behaved SCF procedure where convergence occurs after 77 SCF steps. The red curve shows typical behaviour of a non-converging calculation. The dashed grey line indicates the threshold for convergence, where the log of energy gain per atom must be less than -6 for three consecutive SCF steps.

The typical recourse when facing SCF convergence issues in DFT is to modify the density mixing settings. During the SCF optimisation process each new density is constructed, in part, using densities from previous steps. Density mixing settings refer to choices for how the previous densities are included in the construction of the newest density. The density mixing setting parameters are: the density mixing amplitude (β), the history length ($h_{\max}$), the maximum reciprocal lattice vector to be included in the density mixing ($G_{\max}$) and the density mixing algorithm itself, which in CASTEP is either the Broyden or the Pulay algorithm [96, 97]. β determines the proportion of the new density that will be made up of contributions from previous densities and $h_{\max}$ is the number of previous densities that will contribute to the new density. Using both Broyden and Pulay algorithms, all possible combinations of $\beta \in \{0.05, 0.1, 0.2, 0.3, 0.4, 0.5, 0.6, 0.7, 0.8\}$, $h_{\max} \in \{1, 2, 3, ...12\}$ and $h_{\max} \in \{0.5, 1.0, 1.5\}$ Å^{-1} were trialled to converge the anionic calculations using a test system which had the same numerical settings and physical parameters as those described above and shown in Figure 4.4, with $Z_{\mathrm{Au-N}} = 4.0$ Å. None of the calculations had converged after 400 SCF cycles, at which point the calculation was terminated. No change in the general trends of convergence parameters was observed under any of the modified density mixing settings, *i.e.*, allowing more SCF cycles would not have resulted in convergence. Since such a large set of combinations of density mixing parameters had not resulted in improved convergence behaviour

it was important to investigate whether something about the physical model being used may be somehow causing the issues, my modifying the model. The physical parameters that were modified to improve convergence were the vacuum spacing in the z direction (10, 15, 20, 25 and 30 Å), the MP **k**-point grid density ($k \in \{2, 4, 6, 8, 12\}$ in a $k \times k \times 1$ grid), surface coverage ($p(2 \times 2)$, $p(3 \times 3)$ and $p(4 \times 4)$ unit cells), Fermi-surface smearing (0.1 and 0.15 eV), initial spin state and overall spin constraints (unrestricted, single, doublet). However, none of these resulted in improved convergence behaviour.

As described above, an SCF optimisation starts with an initial guess of the density. In CASTEP, this initial guess is based in a random seed. However, a user can choose the initial guess to be a different density. It was hoped that by choosing an initial density that is closer to the desired solution than a random guess, convergence trends might be improved. Two options were trialled for the initial density. Firstly, using the converged groundstate density. Secondly, using the density of an anionic calculation with similar geometry that had converged, which in practice meant an anionic calculation in which the molecule is closer to the surface. Neither approach resulted in convergence and after the first few steps the relevance of the initial density is lost, and typical non-converging behaviour is observed.

Having encountered such serious difficulties in obtaining convergence with NO, it was decided that the molecular species should be changed. Another system that is highly relevant to nonadiabatic molecule-surface scattering is CO on Au(111). This system was also modelled using the Ψle-ΔSCF method with the same model as in Figure 4.4, but exchanging the molecule for CO, with some limited success (see Figure 4.6). While issues converging some geometries remain, the system is overall more conducive to convergence than NO. However, this system suffers from other issues. The anionic vertical binding energy curve was not smooth in the region of the adsorption minimum. Varying the MP **k**-point grid density ($k \in \{6, 8, 12\}$ in a $k \times k \times 1$ grid), surface coverage ($p(3 \times 3)$ and $p(4 \times 4)$ unit cells), Fermi-surface smearing (0.1 and 0.15 eV) did not result in a less jagged adsorption minimum.

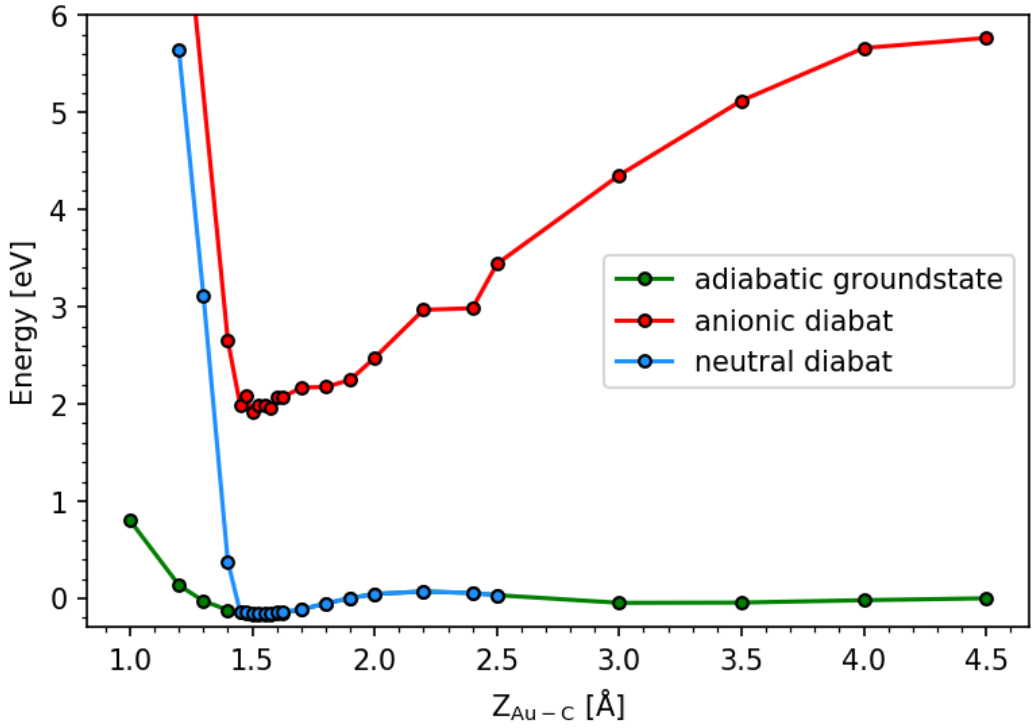

Figure 4.6: Vertical binding energy curves of CO on a Au(111) surface. DFT ground state (green), Ψle-ΔSCF neutral (blue) and anionic (red) diabats.

The neutral diabat also shows unphysical behaviour. As the molecule approaches the surface, the neutral diabat exactly follows the ground-state energy until ∼1.7 Å where the neutral energy is ∼0.015 eV above the ground-state energy and hits a strong repulsive wall at 1.45 Å. At large $Z_{\mathrm{Au-C}}$, it is correct that the neutral and ground-state energies should be identical, since in the absence of the influence of the surface the ground state of the molecule is the neutral state. However, charge analysis using MODOS, Eqn (4.7), shows that at $Z_{\mathrm{Au-C}} < 4.5$ Å the molecule has picked up charge from the surface, meaning that enforcing that the molecule should remain neutral must incur an energy penalty and the neutral and ground-state energies must be different. In the range that the neutral curve does start to deviate from the ground-state energy 1.45–1.70 Å, the ground-state molecule has gained 1.98–2.00 electrons from the surface according to MODOS analysis. To remove this much charge from the molecule should cause much more than 0.015 eV energy difference. This is an indication that the molecule may not be in a truly neutral charge state.

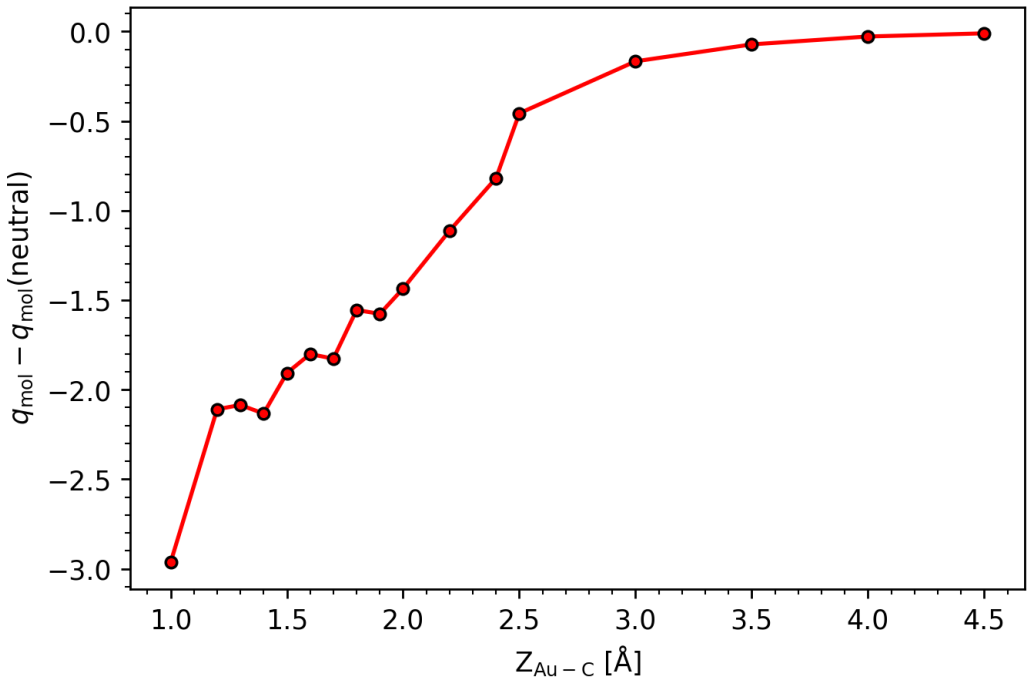

Figure 4.7: Net charge of the CO molecule, relative to neutral CO as a function of distance between molecule (C atom) and the top layer of the Au(111) slab, using MODOS charge analysis.

It was clear at this point that there are severe limitations in how the ΨIe-ΔSCF method can be applied to these systems. With the SCF convergence issues being an important limitation, a series of test calculations were applied to a set of molecular species with different bonding and chemical character to investigate which systems might be prone to SCF convergence issues. Anionic calculations were applied to the following species: H_2, CO, NO, CO_2, ethane, benzene, pyrole, pyridine, cyclohexane and azobenzene at heights of 2.5, 5.0 and 8.0 Å above a Au(111) surface. The CASTEP default density mixing settings were used throughout: $\beta = 0.8$, $h_{\max} = 7$ and $G_{\max} = 1.5\text{Å}^{-1}$. The results are shown in Table 4.3.1 where the green cells indicate calculations that converged within 200 SCF steps and red for calculations that did not converge. In all cases of failed convergence, the trend of convergence parameters do not indicate that more SCF steps would increase the probability of convergence, as can be seen in Figure 4.5. The qualitative trends are that the convergence of diatomic species is highly geometry dependent; for non-conjugated molecules convergence is very difficult; and that conjugated molecules readily converge without issue. This is consistent with behaviour reported by Mau-

rer and Reuter [17, 98].

Table 4.1: Table indicating success (green) or failure (red) of anionic Ψle-ΔSCF calculations.

Height	H_2	CO	NO	CO_2	ethane	benzene	pyrole	pyridine	cyclohexane	azobenzene
2.5										
5.0										
8.0										

The polarizability of LUMO orbitals in conjugated species may mean that there is more variational freedom in charge transfer state calculations compared to fully sigma bonded species. However, this would need to be investigated more systematically to draw strong conclusions beyond the qualitative trend.

Having found such extensive convergence issues with Ψle-ΔSCF as well as unphysical behaviour for the CO/Au(111) diabats, attention turned to ρle-ΔSCF. The same test set of molecular species were tested for convergence using the ρle-ΔSCF method, as implemented in GPAW 20.1.0, and all systems converged in under 60 SCF steps. This led to a shifting of focus with respect to modelling the CO/NO systems using ρle-ΔSCF.

4.3.2 ρle-ΔSCF results

As with the Ψle-ΔSCF work, the first task was to construct vertical binding energy curves. Equivalent $p(3 \times 3)$ NO on Au(111) geometries as those used in Ψle-ΔSCF calculations were used in conjunction with the projector augmented wave electronic structure package GPAW 20.1 [83, 90], using a real-space finite difference basis set with grid-spacing of 0.2 Å, RPBE functional, $8 \times 8 \times 1$ Monkhurst-Pack **k**-point grid [94, 99].

Before any excited state calculations can be carried out, good quality ground-state solutions must be obtained in order to allow the MODOS analysis that defines constraints in ρle-ΔSCF. Far from the surface the NO molecule in the ground state should have doublet character, *i.e.*, one unpaired spin as shown in Figure 4.3. How the energies of the spin states might change if the molecule were to approach the surface is not so clear. For this reason, three ground state vertical binding energy curves were constructed, one with unrestricted spin, another with a net magnetic moment of 0.0 (singlet) and one with magnetic moment of 1.0 (doublet). These three curves are shown in Figure 4.8. Far from the surface the doublet energy is indeed lower than the other two solutions, by around 0.2 eV, and remains lower in energy for most geometries as the molecule approaches the surface until $Z_{Au-N} <$

2.2Å. However, the doublet energies at $Z_{Au-N} = 4.0$, 4.5 and 5.0 Å are significantly higher than even the singlet and unrestricted energies. The source of this behaviour stems from the way in which the spin constraints are fulfilled. Ground-state DFT calculations only allow restriction of the net spin of the full system, rather than to specific atoms or molecules. This means the SCF procedure will tend towards one of two solutions. The first matches the physics we seek to capture, where the excess unpaired spin density is primarily associated with the molecule; the other solution puts the excess spin density onto the surface. This can be seen in Figure 4.8, where the projected atomic magnetic moments of the sub systems (molecule and slab) are plotted. The geometries where the doublet energy jumps up above the singlet in the top panel of Figure 4.8 are the same ones in which the sign of the net magnetic moments associated with the molecule and surface change sign in the bottom panel of Figure 4.8. Attempts were made to force the SCF optimisation towards the desired solution in three different ways. Firstly, the calculations were initialised with the local atomic magnetic moments set so the molecule had the correct spin state. Secondly, by sampling different density mixing amplitude coefficients (β) and finally by using the converged density of a calculation in a similar geometry which had converged to the desired spin solution as the initial input density. All these attempts were unsuccessful and there appears to be no way to enforce the correct molecular spin character. Defining meaningful constraints for ρle-ΔSCF is impossible for those points where the excess spin density is associated with the surface because the constraints are based on MODOS analysis and MODOS charges would carry over the incorrect spin character.

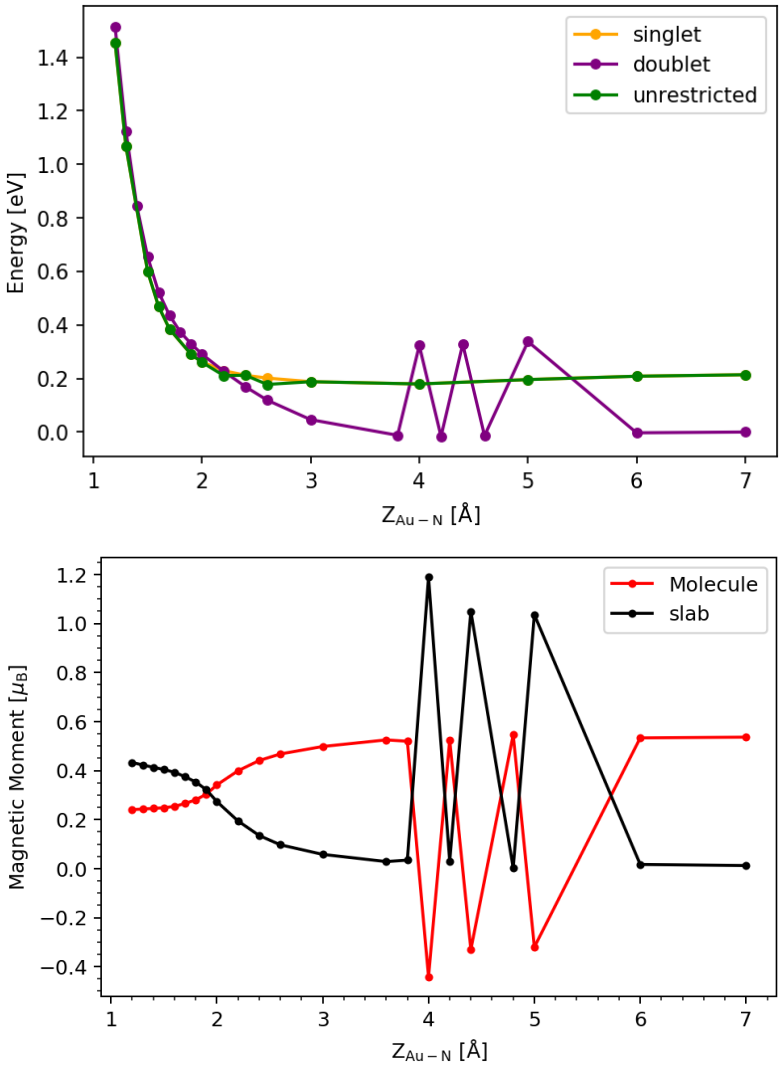

Figure 4.8: Top panel: Vertical binding energy curves of NO above the bridge site of an Au(111) surface for three spin constraints: singlet (orange), doublet (purple) and unrestricted spin (green). Bottom panel: Sum of projected atomic magnetic moments for NO molecule (red) and Au(111) slab (black) for the doublet restricted calculations. The spike in the doublet energy corresponds to instances where the doublet constraint of the full system is enforced by placing the excess spin density primarily on the surface and not the molecule (an inversion of the intended solution)

The ground-state calculations for the CO on Au(111) system are much simpler, since the CO molecule has a singlet ground state and any issues with spin restrictions only apply in the anionic state. Figure 4.9 shows vertical binding energy curves for CO in an upright orientation above the HCP site of a $p(2 \times 2)$

Au(111) slab, with C facing towards the surface, calculated using GPAW 20.1 [83], with a real-space finite difference basis set with grid-spacing of 0.2 Å, PBE functional and $4 \times 4 \times 1$ Monkhorst-Pack **k**-point grid [95, 99]. The diabatic states are modelled using ρle-ΔSCF and the constraints are defined according to the difference between ground-state MODOS charges and desired charge state, as described above in Section 4.1. All three curves are smooth and display qualitatively correct physics. However, similarly to the Ψle-ΔSCF calculations, the anionic state could not be converged beyond 3.0 Å from the surface.

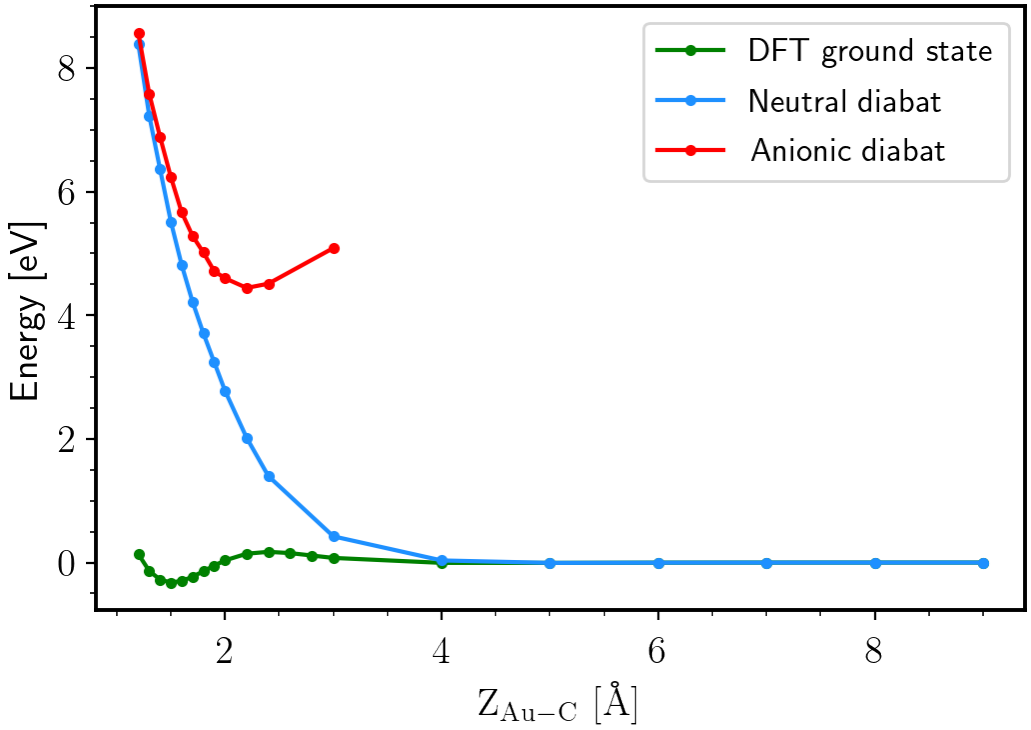

Figure 4.9: Vertical binding energy curves of CO in an upright orientation above a top site of a $p(2 \times 2)$ Au(111) slab. Anionic (red) and neutral (blue) diabatic states are modeled using ρle-ΔSCF.

With spin being such a significant obstacle to constructing meaningful potentials, it was decided that simplifying the model by removing spin polarisation entirely may be the best route towards progress. Figure 4.10 shows energies of the DFT ground state, neutral diabat and anionic diabat as a CO molecule is vertically displaced above a top site of a $p(2 \times 2)$ Au(111) slab using the same settings as in Figure 4.9 but with spin polarisation switched off.

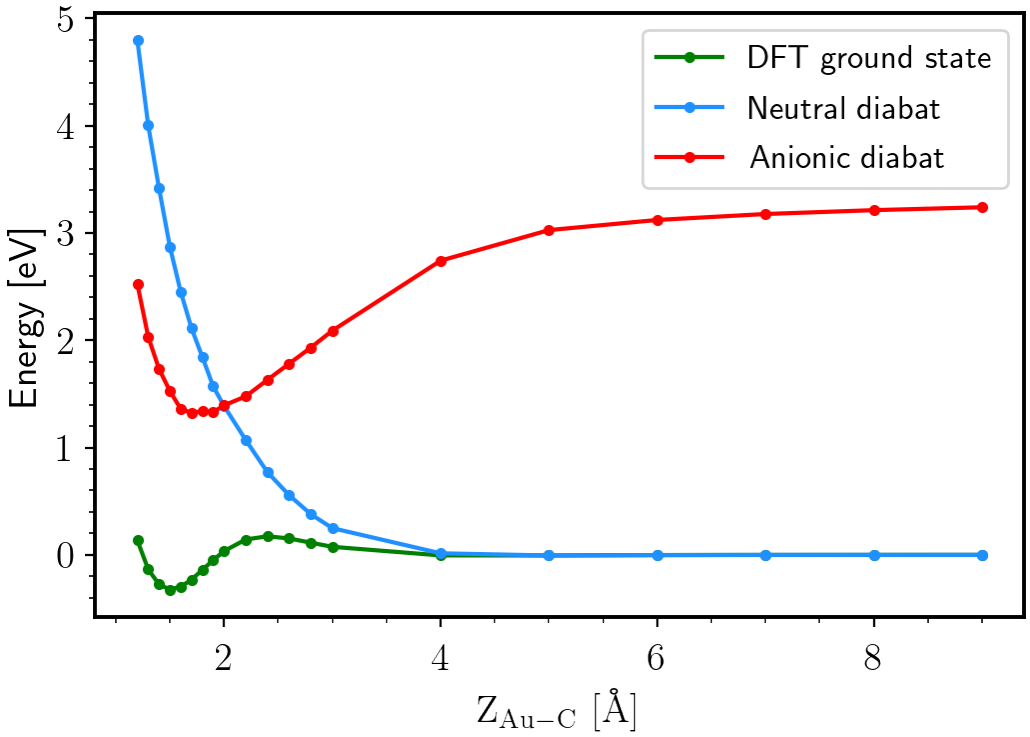

Figure 4.10: Non-spin polarised vertical binding energy curves of CO in an upright orientation above a top site of a $p(2 \times 2)$ Au(111) slab. Diabatic states are modeled using ρle-ΔSCF.

All non-spin polarised ρle-ΔSCF calculations converged without issue and the resulting curves are smooth and display qualitatively correct physics, *i.e.*, upon approaching the surface the neutral curve exactly matches the ground state until the molecule picks up charge in the ground state, where the neutral curves becomes repulsive. This is expected as transferring charge to the molecule lowers the energy of the system and the neutral diabat does not allow this stabilisation. Additionally the anionic curve is around 2.5 eV above the ground state far from the surface, where a neutral CO molecule should be far more stable. As the anionic molecule approaches the surface the energy is lowered, due to the image charge stabilisation (ICS) effect, until very close to the surface where steric repulsion overcomes ICS, resulting in an adsorption minimum. However, the excitation energy, $E_{\text{anion}} - E_{\text{neutral}}$, far from the surface is too low (discussed in more detail in Chapter 5).

Ultimately, these calculations were aimed at finding parameters and constraint sets that will facilitate the construction of PESs that can then be used to perform NAD simulations. As only the non-spin polarised system could produce

reliable convergence and qualitatively correct physics, this is the model that was used to construct PESs that are described in detail in the next chapter.

4.4 Conclusion

The goals of this chapter have been to describe the two implementations of le-ΔSCF: ρle-ΔSCF and Ψle-ΔSCF and assess their suitability for constructing diabatic PESs for systems relevant to nonadiabatic molecular scattering at metal surfaces: CO and NO on Au(111). While both implementations can produce energies of the anionic and neutral diabats, the SCF convergence issues severely limit their applicability to the construction of large PESs because convergence behaviour is highly geometry dependent. Ψle-ΔSCF calculations in particular are very difficult to reliably converge. Simple 1D vertical binding energy curves using Ψle-ΔSCF could not be completed for either NO-Au(111) or CO-Au(111) because of difficulty converging anionic calculations for the former and neutral calculations for the latter.

An investigation into SCF convergence behaviours across a set of different molecular species on Au(111) surfaces using Ψle-ΔSCF produced a qualitative trend that conjugated species converge far more readily than sigma bonded species, such as ethane or cyclohexane. In smaller (2-3 atom) species, convergence behaviour is highly geometry dependent, as noted above in the CO and NO cases.

ρle-ΔSCF was shown to have far less SCF convergence issues than Ψle-ΔSCF. However, difficulty in enforcing the correct spin state meant it was not possible to construct meaningful spin polarised PESs using the method. A simpler model using ρle-ΔSCF, excluding spin polarisation, was able to reliably produce smooth and qualitatively correct PESs for CO-Au(111) without any significant convergence issues.

As a result of the limitations described above, the construction of PES throughout the remainder of this thesis will use a non-spin polarised ρle-ΔSCF model and the molecular species will be limited to CO.

Chapter 5

Potential Energy Surfaces

There is a deep desire to understand the non-adiabatic effects that are known to occur during some molecular scattering events at metal surfaces. An important avenue towards that goal is to perform nonadiabatic molecular dynamics (NAMD) simulations and observe trends and compare to experiment. In order to obtain the most accurate results possible from NAMD simulations and evaluate how well various methods, such as IESH, are able to capture experimentally observed physics, high quality PESs must first be generated upon which the dynamics will unfold.

This chapter will describe and discuss PESs of two chemical systems that have been used in molecular beam scattering experiments to study nonadiabatic dynamics, namely CO on Au(111) and CO on Ag(111). These two systems have been chosen on the basis of two factors: first, there is high quality experimental data that shows nonadiabatic energy transfer occurs during molecular beam scattering experiments. Secondly, the le-ΔSCF methodology allows for the reliable construction of PESs over a wide range of geometries, as discussed in the previous chapter.

5.1 Methodology

All results shown in this chapter used the ρle-ΔSCF formalism implemented in the projector-augmented-wave electronic structure package GPAW [90], using a real-space grid basis set with a grid spacing of 0.2 Å, an 8×8×1 Monkhorst-Pack **k**-point grid and the RPBE XC functional [94]. Au(111) and Ag(111) optimised lattice constants were calculated to be 4.154 and 4.116 Å, respectively. Each metal surface was modelled using a $p(3 \times 3)$ 4-layer slab and 36 Å of vacuum. The top two layers were relaxed using the BFGS algorithm implemented in ASE, while the bottom two layers were fixed in their bulk positions. The unit cells were periodic in x and y

but non-periodic in z. A dipole correction was applied along the z coordinate. 500 non-spin polarised bands were included in each full system single point calculation.

For each geometry, two single point ground-state DFT calculations were carried out in order to define the constraints of the ρle-ΔSCF calculation. The first is a standard DFT ground-state calculation of the full system (*i.e.*, molecule and metal surface). The second is a 'gas phase' calculation of the molecule in the same position in the unit cell as it is in the full system, but with metal atoms removed. This 'gas phase' system is more accurately described as a free standing molecular over-layer (FSMO). This is because to accurately model a gas phase molecule, one would typically use non-periodic boundary conditions and only a single **k**-point . However, in order to perform MODOS analysis and also to construct a resonance orbital, the unit cell, PBC and **k**-point sampling of the full system must be retained. Therefore, what is being modeled in a FSMO calculation is an infinite 2D periodic array of free standing molecules, rather than a single molecule in isolation. The full-system wavefunction, denoted $|\Psi_i\rangle$, and the FSMO wavefunction, denoted $|\phi_j\rangle$, are used to perform MODOS analysis according to Eqn (4.5) to obtain $P_j(E)$ for each $|\phi_j\rangle$. Integrating $P_j(E)$ up to E_F returns the MODOS occupation, which is a value between 0 and 1, with 0 indicating the state is fully unoccupied and 1 indicating a fully occupied state. In the previous chapter, the quantity returned upon integration was referred to as a MODOS charge (q_j). This is valid if $|\phi_j\rangle$ is spin polarised because a fully occupied state contains exactly one electron and so the terms occupation and charge can be used interchangeably, provided it is understood that any charges that are being counted are referring to negative charges. However, if $|\phi_j\rangle$ is a spatial orbital, a MODOS occupation of 1.0 corresponds to two electrons. All the calculations discussed in this chapter are non-spin polarised and so any MODOS occupation can be converted to a MODOS charge by dividing by two.

Figure 5.1 shows a simple graphical representation of the MOs of a neutral CO molecule. It shows that the HOMO is fully occupied and that the LUMO is degenerate. This degeneracy is important because it means any constraints applied to the LUMO are shared equally between the two orbitals. For example, adding one electron to the LUMO would correspond to adding half an electron to each orbital.

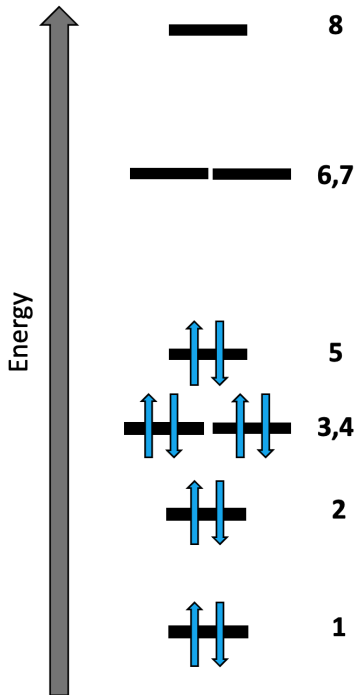

Figure 5.1: A graphical representation of the molecular orbitals of a neutral CO molecule. The HOMO (state 5) is fully occupied. The LUMO consists of two degenerate states (6 and 7). (Note: MOs made from the 1s orbitals of C and O have been excluded, meaning state 1 corresponds to the third lowest eigenstate of a real CO molecule).

Neutral and anionic diabats were modeled by performing ρle-ΔSCF calculations in which the net charge on the molecule is constrained to be 0.0 (neutral) or -1.0 (anion) relative to a neutral CO molecule. This was performed by first integrating the MODOS of each $|\phi_j\rangle$ separately, to obtain the charge q_j of $|\phi_j\rangle$, and then comparing the set of occupations to the idealised occupations in the charge state of interest. The resonance orbitals ($\left|\Psi_j^c\right\rangle$) used in the ρle-ΔSCF calculations correspond to all $|\phi_j\rangle$ that have occupations different to the idealised occupations (excluding unbound states) and the constraints are the difference between the ideal and the observed ground-state MODOS occupations for each $|\phi_j\rangle$, in order to correct from the ground state to the charge state of interest. An illustrative example of this is shown in Figure 5.2 below, where 4 resonance orbitals are required to model both anion and neutral diabats. In both cases, $|\Psi_5^c\rangle$ needs a constraint to add a small charge to take the occupation to 1.0 and $|\Psi_8^c\rangle$ needs a constraint to remove charge and return the occupation to 0.0. Two more constraints are required to increase the occupations of $|\Psi_6^c\rangle$ and $|\Psi_7^c\rangle$ to 0.25 (anion) or decrease to 0.00 (neutral). All lower

states match the desired charge occupation and all higher lying states are unbound.

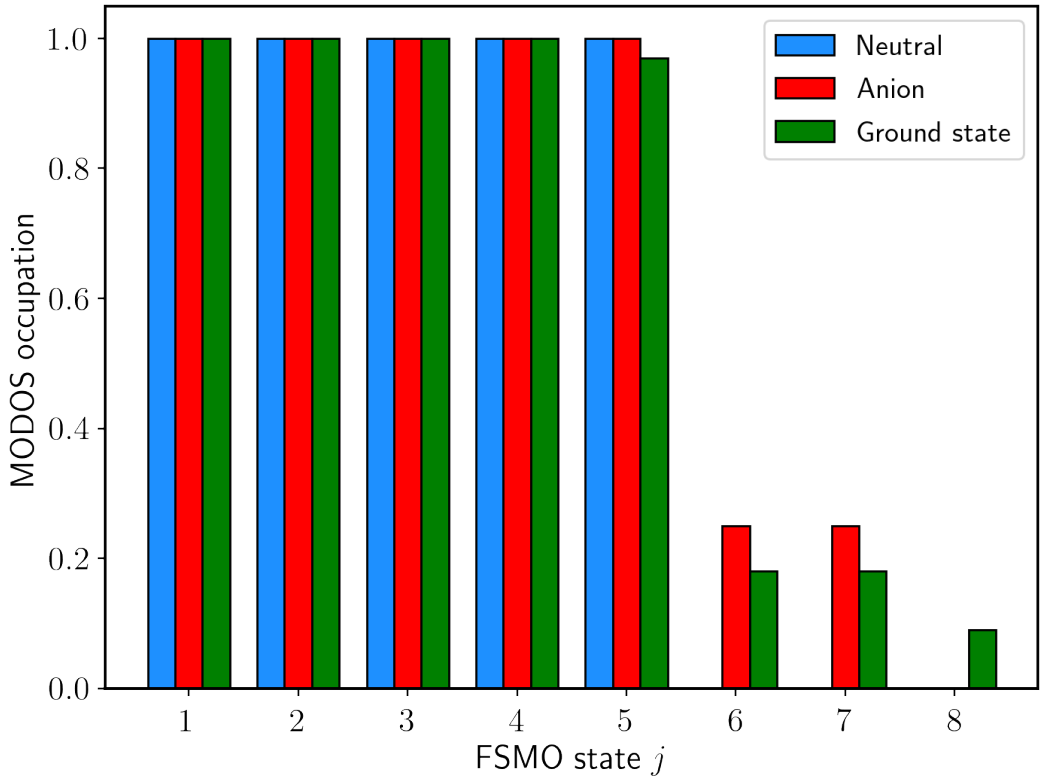

Figure 5.2: An illustrative example of MODOS occupations of an idealised neutral (blue) and anionic (red) CO molecule interacting with a metal surface. The green bars represent the occupations derived by performing MODOS analysis on DFT ground-state wavefunctions, where state 5 is the HOMO and states 6 and 7 are the degenerate LUMO (see Figure 5.1).

All calculations were performed using ARCHER2, UK National Supercomputing Service, using 4 nodes with 128 cores per node. Four calculations were run for each system geometry and the average computational costs were: full-system gound-state = 271.8 CPUh, FSMO ground-state = 5.7 CPUh, full-system anion 354.4 CPUh and full-system neutral 312.0 CPUh. A step-by-step guide to performing the ρle-ΔSCF calculations that produced the results shown in the remainder of this chapter, including example scripts is included in Appendix A.

5.2 1D Potential energy curves

In the following section, 1D slices of the PES for diabatic and adiabatic states for CO on Au(111) and CO on Ag(111) are described as a function of various degrees of freedom. However, the during the development of a reliably convergeable methodology for producing diabatic curves, established in Chapter 4, both $p(2 \times 2)$ and $p(3 \times 3)$ were used. For the construction of meaningful PESs, that are presented in this chapter, it is essential to first establish whether either of these system sizes if sufficiently large in x and y to exclude lateral interactions between molecules in neighbouring unit cells. Figure 5.3 shows band structure diagrams for CO FSMOs using both $p(2 \times 2)$ and $p(3 \times 3)$ unit cells. An isolated molecule should produce flat bands and curvature of bands indicates there are significant lateral interactions between neighbouring unit cells. The two LUMO states should be degenerate. This is the case for $p(3 \times 3)$ (lines in Figure 5.3 overlap), but not for $p(2 \times 2)$ where the bands are neither flat or degenerate. Therefore, a $p(2 \times 2)$ unit cell is too small. The LUMO+1 band is significantly curved in both cases. However, even in a $p(6 \times 6)$ unit cell where the The LUMO+1 band is much closer to flat (90 meV bandwidth), the state is so weakly bound that the orbital will be highly diffuse and applying constraints to the state will not constrain charge locally on the molecule. Therefore the best option is to only apply constraints to the LUMO and lower states; meaning a $p(3 \times 3)$ unit cell is sufficiently large to produce sensible binding curves and for this reason was used for all ρle-ΔSCF data presented in the remainder of this thesis.

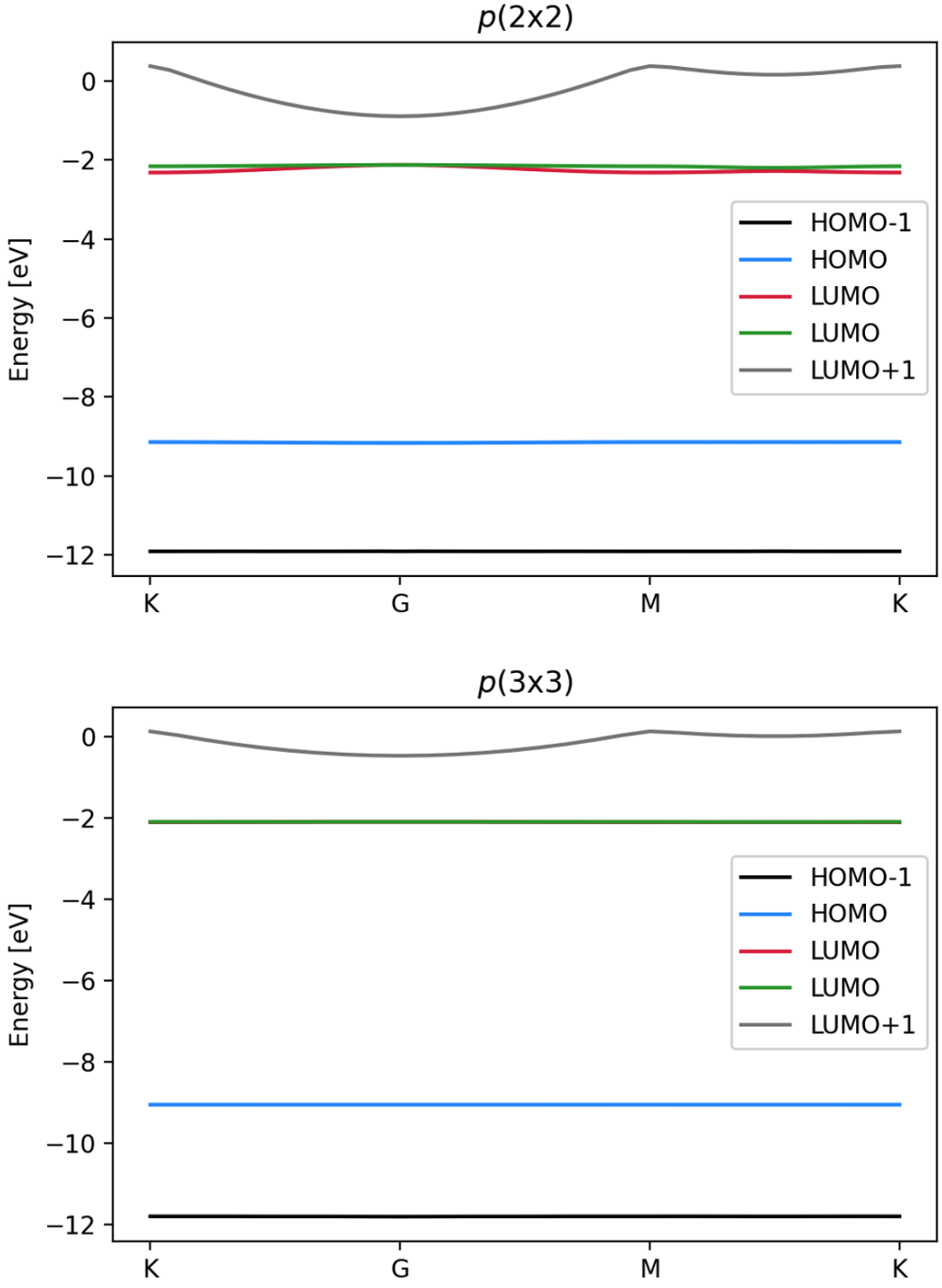

Figure 5.3: Band structure diagrams for a single CO molecule in a $p(2 \times 2)$ (top) and $p(3 \times 3)$ (bottom) unit cell.

The remainder of this section presents and discusses 1D PES slices for diabatic and adiabatic states for CO on Au(111) and CO on Ag(111). Firstly, vertical displacement curves of the molecule fixed at the gas phase equilibrium bond length of 1.14 Å, above either a top site or HCP hollow site, are discussed. In each plot the molecule is held in one of three different orientations relative to the surface: parallel to the surface normal with C closest to the surface (upright); orthogonal to the surface normal (flat); and parallel to the surface normal with the O atom closest to the surface (upside down). The ground-state energies were calculated using KS-DFT and the anionic and neutral diabats were calculated using ρle-ΔSCF. The diabatic coupling (V_c) was calculated according to Eqn (5.1). The adiabatic excited state was not explicitly calculated using DFT but rather by diagonalising a 2×2 Hamiltonian as shown in Eqn (5.2).

$$V_\mathrm{c} = \sqrt{(E_\mathrm{neu} - E_\mathrm{gs}) + (E_\mathrm{an} - E_\mathrm{gs})}. \tag{5.1}$$

$$H_\mathrm{a} = \begin{pmatrix} E_\mathrm{neu} & V_\mathrm{c} \\ V_\mathrm{c} & E_\mathrm{an} \end{pmatrix}. \tag{5.2}$$

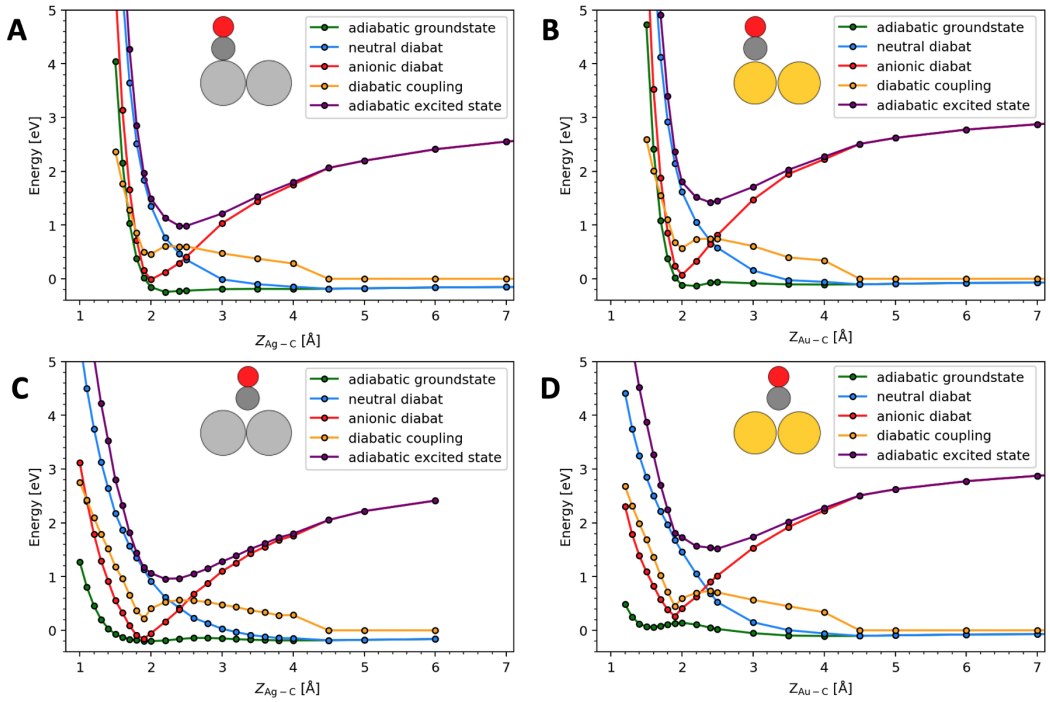

Figure 5.4: Vertical binding energy curves of a CO with r_{C-O} fixed at the gas phase equilibrium value of 1.14 Å over a frozen, bulk truncated, metal surface. The molecular axis is orthogonal to the surface plane with C atom closest to the surface, *i.e.*, the 'upright' orientation. Panel A shows the molecule above a top site of Ag(111), panel B above a top site of Au(111), panel C above a HCP site of Ag(111) and panel D above a HCP site of Au(111).

The top site is the more energetically favourable of the two adsorption sites in the ground state for both surfaces, with binding energies of −0.13 and −0.24 eV for Ag(111) and Au(111), respectively, compared to −0.10 and −0.19 eV for the HCP sites. In the case of adsorption at the HCP site on Au(111), the chemisorption well is clearly defined but is higher in energy than the fully desorbed molecule. There is a physisorption well further from the surface, which is the most favourable geometry sampled for the HCP-Au(111) system. For the HCP site on Ag(111), there are also both chemisorption and physisorption wells, but the chemisorption well is the lower in energy of the two. This is consistent with evidence from literature, where Ag(111) is known to interact more strongly with most adsorbates [100, 101]. The adiabatic excited state, which corresponds to the molecule having one more electron than in the ground state, including any charge the molecule picks up from the surface upon adsorption in the ground state, possesses a deep minimum in all four systems in

Figure 5.4. This is expected for a charged species approaching a metal surface, due to the image charge stabilisation effect, wherein the electron density of the surface rearranges to form a partial positive charge that compensates the negative charge of the approaching molecule. The location of the adiabatic excited state minima is fairly consistent across all four systems, occurring at 2.2–2.5 Å from the surface. This is also consistent with the stabilisation being mainly due to the image charge effect.

Similarly, the anionic diabat also sees a deep minimum in all four systems, which can be largely attributed to the image charge effect, since the well cannot be due to an exchange of charge with the surface as in the ground state. The anionic diabats are the only states in Figure 5.4 that are not entirely smooth, as they have a sharp turning point at the minima. The reason for this behaviour, and the locations of the minima, are that the MODOS analysis of the ground-state wavefunctions, which defines the le-ΔSCF constraints, sees the molecule pick up more than one full electron close to the surface. As the anionic diabat is defined as the molecule having a charge of exactly −1.0 at all times, when approaching the surface, there comes a point where the constraints switch from adding charge to removing charge from the molecule. This inevitably means there is a height at which the anionic diabat touches the ground-state curve because the constraints are zero and this ultimately determines the position and shape of the minima. The neutral diabats, in contrast, are always repulsive. This is expected as the molecule exchanges charge with the surface, in the ground state, to stabilise the interaction, but the neutral diabat enforces that no charge may be exchanged and so there is no stabilisation. The general behaviour is very similar between all four systems. The onset of the repulsion in the neutral diabats is always around 4 Å from the surface, but the rate at which it increases is slightly different for the two adsorption sites, with the top site curves rising more rapidly. The reason for this is that the molecule approaches directly over a metal atom in the top site and the energetic cost of moving the density away from the molecule and therefore also away from the metal atom is greater than in the case of the HCP site, were density is primarily removed from the space in between metal atoms. The neutral diabats are very similar between the two metal surfaces and the adsorption site plays a bigger role in determining the energetic profile of the curve than the type of the metal. The distance from the surface at which the diabats cross is very similar for both surfaces and at both adsorption sites, at 2.4–2.5 Å. This represents an area of high coupling and the coupling reduces as the molecule moves closer to the surface, before rising again steeply upon close approach to the surface. As will be seen below, the upright

orientation is consistently the most energetically favourable, which matches previous models of CO adsorption on Ag(111) and Au(111) surfaces [102, 103]. A feature which does not match physical considerations and is present in all four systems is that the differences between the ground and excited adiabatic states (E_{ex}) at distances far from the surface are too small; the nature and cause of this error is discussed in detail in Section 5.3 below.

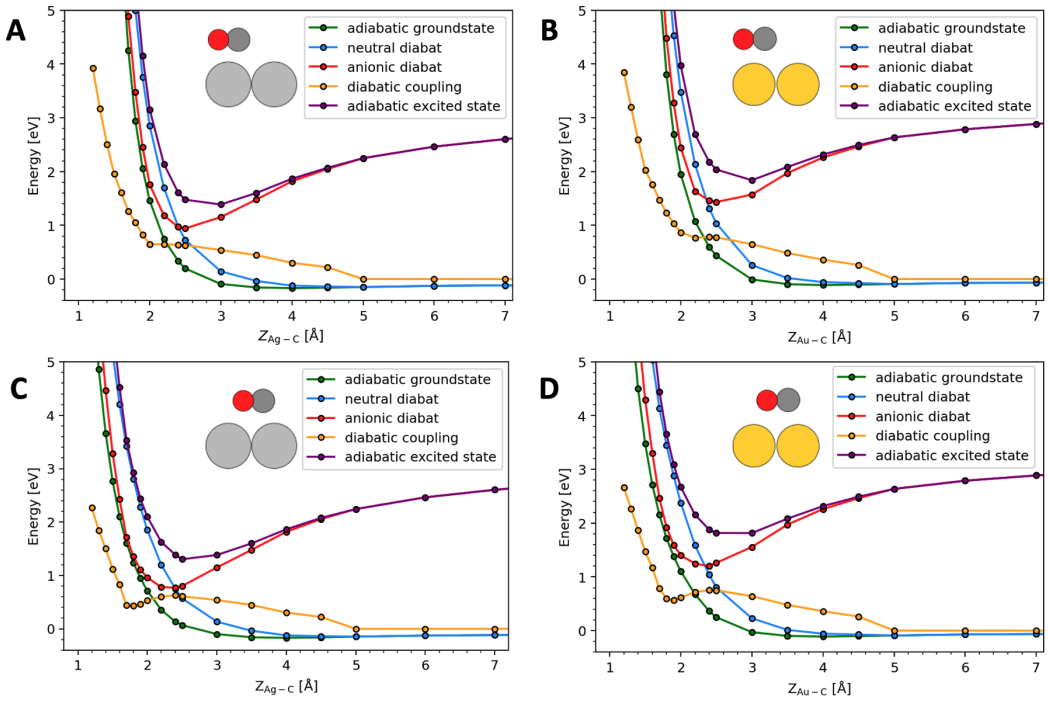

Figure 5.5: Vertical binding energy curves of a CO with $r_{\mathrm{C-O}}$ fixed at the gas phase equilibrium value of 1.14 Å over a frozen, bulk truncated, metal surface. The molecular axis is parallel to the surface plane in the 'flat' orientation. Panel A shows the molecule above a top site of Ag(111), panel B above a top site of Au(111), panel C above a HCP site of Ag(111) and panel D above a HCP site of Au(111).

Figure 5.5 shows equivalent data as Figure 5.4 but with the molecule in the flat orientation. The adiabatic ground-state curves show the most dramatic change in behaviour as all chemisorption wells have been removed and the curves are repulsive further from the surface compared to the upright orientation. The diabatic anion wells are shallower and further form the surface in the flat orientation. This is partly because the MODOS charges on the molecule associated with the ground-state curves do not exceed 1.0 at the same geometries as for the upright orientation and so there is no touching of the ground-state curve, as described above, until

around 1.4–1.7 Å where the the ground-state and all other curves have already hit the Pauli repulsion wall. Another reason for the shallower wells in the diabatic anion and adiabatic excited state curves is that, with the molecule parallel to the surface plane, any repulsion due to overlap of molecule and metal densities occurs over a larger surface area along the surface plane. This larger overlap also explains why the neutral curve rises more steeply in the flat orientation compared to upright. The $Z_{\mathrm{Au-C}}$ at which the crossing of the two diabats occurs is retained from the upright curves; however, they sit at around 0.4 eV higher in energy. The higher energy curves of the flat orientation qualitatively match the experimental observation that there are dynamical steering forces that reorient molecules to display a higher likelihood of impacting the surface in the most energetically favorable orientation (C atom first in this case) when gas phase molecules are scattered from the surface [71].

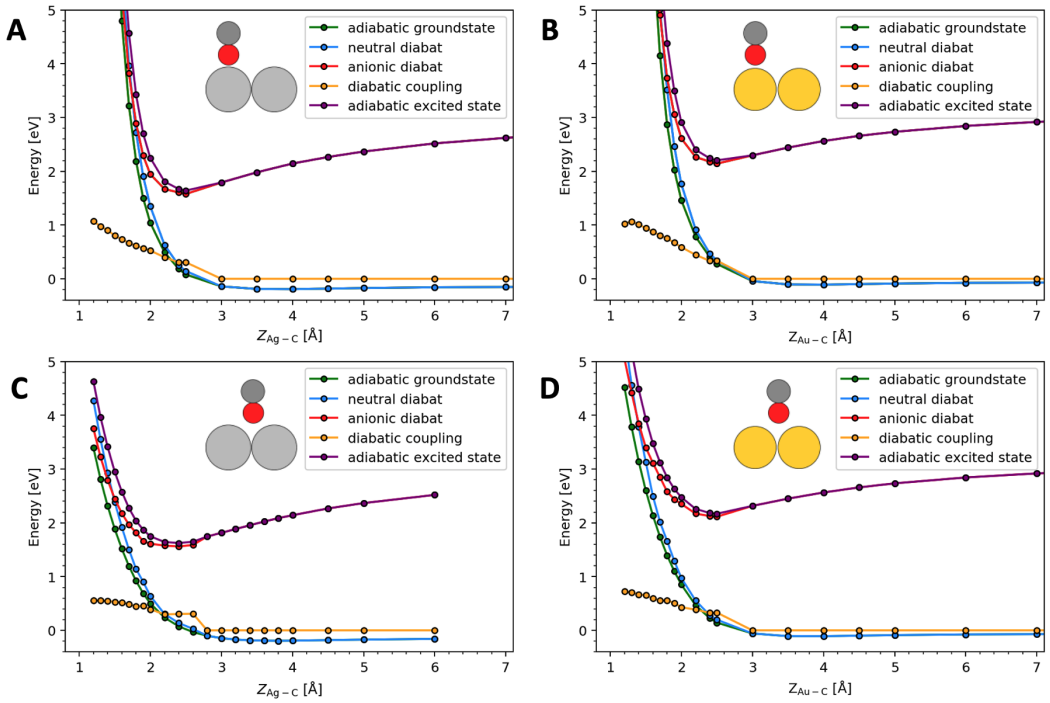

Figure 5.6: Vertical binding energy curves of a CO with $r_{\mathrm{C-O}}$ fixed at the gas phase equilibrium value of 1.14 Å over a frozen, bulk truncated, metal surface. The molecular axis is orthogonal to the surface plane with O atom closest to the surface, *i.e.*, the 'upside down' orientation. Panel A shows the molecule above a top site of Ag(111), panel B above a top site of Au(111), panel C above a HCP site of Ag(111) and panel D above a HCP site of Au(111).

The final set of vertical binding energy curves, in Figure 5.6, show the

molecule in the upside-down orientation, *i.e.*, with the O atom closest to the surface. This is clearly significantly less favourable than the previous two orientations. The ground-state and neutral curves are very closely aligned and the same is true for the anionic diabat with the adiabatic excited state. The reason for this is that the molecule in the ground state exchanges very little charge with the surface. The lack of charge transfer qualitatively matches experimental evidence that significantly less vibrational (de)excitation is seen in state-to-state molecular beam scattering experiments when CO (or NO) molecules are forced to impact the surface O first, since the auto-detachment mechanism relies on efficient charge transfer [71]. It also further supports the claim that this model captures the dynamical steering force experienced by molecules approaching the surface.

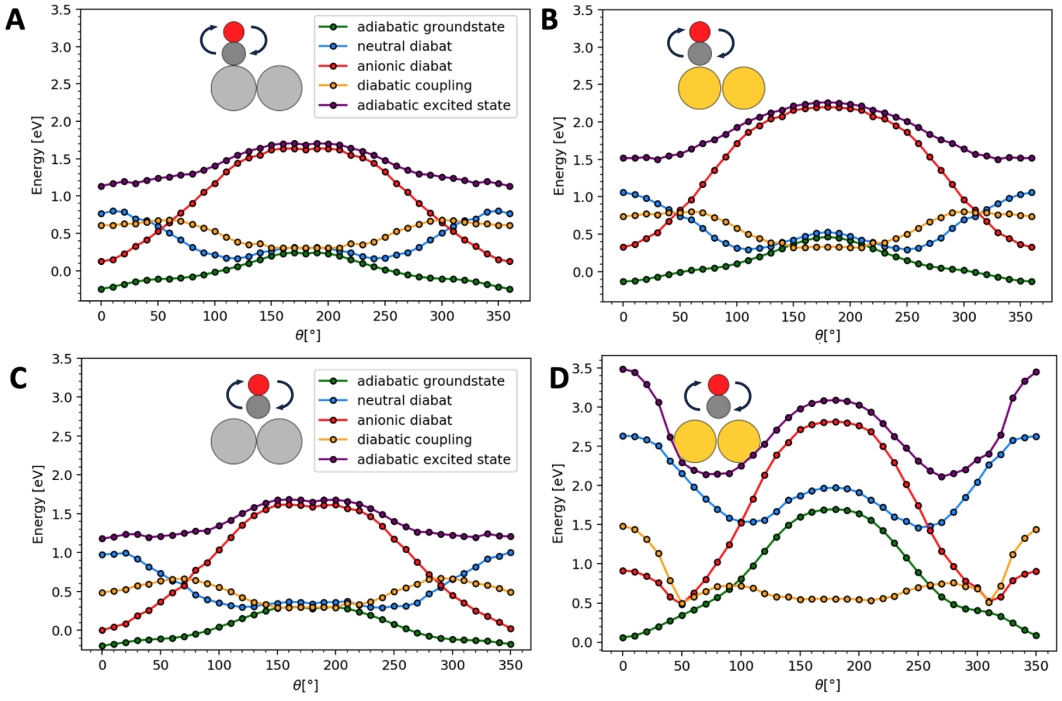

Figure 5.7: Binding energy as a function of molecule surface angle θ of CO relative to the surface normal, with the upright orientation corresponding to 0°. r_{C-O} is fixed at the gas phase equilibrium value of 1.14 Å over a frozen, bulk truncated, metal surface. Panel A shows the molecule above a topsite of Ag(111), panel B above a top site of Au(111), panel C above a HCP site of Ag(111) and panel D above a HCP site of Au(111).

The DOF in Figure 5.7 is the molecular angle relative to the surface normal (θ), with 0° corresponding to the upright geometry. The molecule is positioned

at its equilibrium adsorption height in the ground state, 2.20 Å for top sites and 1.55 and 2.0 Å for HCP sites on Au(111) and Ag(111), respectively. The molecule is then rotated around its centre of position and the energy is sampled in 10° intervals, where the plane of rotation is such that, for HCP curve, 90° has O atom over top-site and C over bridge site and 270° has the opposite. For the top site curve, 90° has the O atom over a FCC hollow-site and C over a HCP hollow-site. The systems appear largely similar except the HCP-Au(111) case, where the shorter distance between molecule and surface causes increased repulsion. As expected from the vertical binding energy analysis above, the adiabatic ground state is at a minimum at $\theta = 0°$ and smoothly transitions to a maximum at 180°. The anionic diabats and the adiabatic excited states follow a similar trend to the ground state albeit at higher energies. However there is a slight deviation for the Ag(111) surfaces where there is a slight reduction in energy at 180°. The other very obvious difference is the HCP-Au(111) case where the upright geometry shows maxima for the diabatic anion and adiabatic excited state and the minima are instead shifted to a tilted geometry. This is likely due to a balance being struck between factors: firstly, the upright orientation is the most favourable geometry at larger separations and secondly there is increased steric repulsion experienced by a molecule so close to a surface.

The neutral diabats show maxima at the upright orientations, as expected from examination of the vertical binding energy curves. However, $\theta = 180°$ does not show a minimum, but a second maximum. The neutral rotational minima are at 100° and 260°, which is close to the flat geometry. This is because it minimises the overlap of the molecule and metal density and therefore repulsion. The reason the minima are not exactly at the flat geometry is that this would cause a repulsive interaction between molecule and metal over two metal sites, a top site and a bridge site. By tilting the molecule slightly the overall repulsive interaction is reduced. It is consistently the C end of the molecule that is rotated away from the surface to obtain the neutral minima, whether C is over the top site or the bridge site. This is somewhat unexpected as there is greater total electron density at the O end of the molecule in the gas phase. A likely explanation is that the lobes of molecular LUMO are larger on the C end of the molecule and therefore LUMO overlap with the surface is higher, and charge transfer greater, when C is closer to the surface. Since the neutral diabat does not allow charge transfer, having the C end closer to the surface would be more energetically costly in a neutral state.

The anionic curves are all similar except the HCP site on Au(111). This is due to the equilibrium adsorption height about which the molecule is rotated

being closer to the surface. The close proximity to the surface means that a balance is struck between reducing steric repulsion and facilitating good overlap between the molecular LUMO and the orbitals of the metal, resulting in the minima at 50^o (equivalently at 310^o). In the other three systems, the minima are at 0^o and the energy smoothly increases as the molecule is tilted.

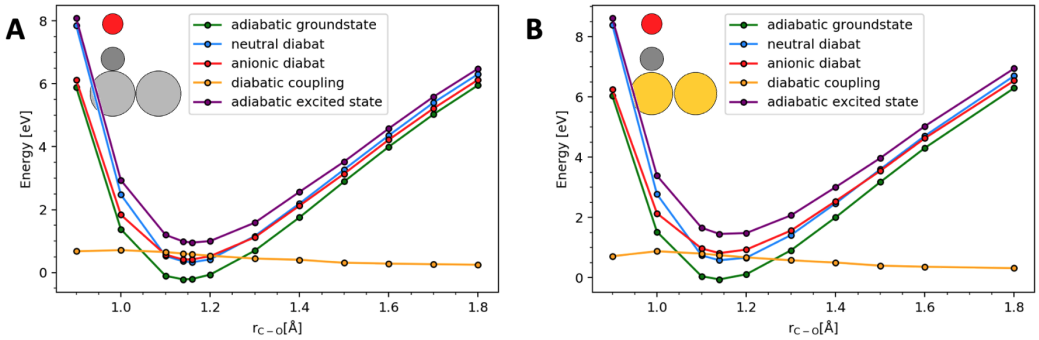

Figure 5.8: Binding energy as a function of r_{C-O} with the C atom fixed in the same position, in the equilibrium adsorption geometry for $r_{C-O} = 1.14$ Å, over a frozen metal surface. Panel A shows the molecule above a top site of Ag(111), panel B shows the molecule above a top site of Au(111).

In the final set of 1D curves, Figure 5.8 the DOF sampled in the C-O bond length. The C atom is held fixed at 2.0 Å above top site of the Ag(111) and Au(111) surfaces, while the O atom is displaced along the bond axis, stretching and compressing the C-O bond. The bond stretch curves, in contrast to the previous degrees of freedom sampled, produce qualitatively incorrect results. The explanations of the auto-detachment mechanism given in literature invoke the crossing of neutral and anionic diabats when the C-O bond is stretched and compressed, with the anion being more stable at large bond-lengths and the neutral more stable under compression [67]. The results in Figure 5.8 do show a crossing, and the anionic state is slightly lower in energy at extended bond lengths; however, the anion also appears to be significantly lower in energy when the bond is compressed, which is the opposite of the expected behaviour. In addition, when r_{C-O} is sampled at any other fixed distance from the surface, the neutral and anionic diabats do not cross at all. Close to the surface the anion is more stable at all values of r_{C-O} and far from the surface the neutral is more stable. The ordering of the diabatic states is primarily controlled by Z_{Au-C}. The lack of dependence on r_{C-O} is likely due to the resonance orbitals to which the charge constraints are applied. Resonance orbitals are based on the FSMO orbitals and so their shape and size is independent of the proximity of

the molecule to the surface. The FSMO orbitals are quite diffuse, especially at short bond lengths where the LUMO becomes weakly bound. To model the neutral state, when the molecule is close to the surface, density must be removed from where it would otherwise reside in the adiabatic ground state, *i.e.*, around the metal atoms. The energy penalty for carving out this density is greater than for adding additional density to this region and so the anionic state appears more stable. Using a more spatially confined reference orbital to construct the resonance orbitals would likely move this model towards more physically accurate predictions of $r_{\mathrm{C-O}}$ dependence close to the surface. Alternatively, using reference orbitals that respond to the presence of the metal surface, without causing the hybridisation of states seen in the full system, perhaps by applying an artificial potential to the FSMO model, may also aid in solving the problem. As a more short term fix, it may be beneficial to experiment with alternative XC functionals to select one which does not cause the LUMO to become more weakly bound, and therefore more diffuse when the bond is compressed. The outlook section of this thesis discusses these potential modifications in more detail.

Overall, the quality of the ρle-ΔSCF PES based on the 1D cuts is good and most trends are correct, and all states vary smoothly, which is important for the prospect of applying dynamics and machine learning to these models. However, there are two major issues. 1. The energy difference between ground and excited state PESs is too small, meaning that any dynamics based on these surfaces would likely see too much surface hopping. 2. The neutral and anionic diabats do not cross when bond length is varied near the surface, which does not match expectations based on considerations of the auto-detachment mechanism. The diabats do however cross when the distance from the surface is varied, meaning surface hopping will likely be observed during scattering dynamics.

The nature and origins of these flaws are described in the following section via the analysis of a 2D PES and a function for molecule-surface separation and C-O bond length.

5.3 2D PES

2D PESs were constructed for both the CO-Au(111) and CO-Ag(111) systems, with CO in the upright orientation above a top site, by scanning through a 2D grid of geometries as a function of $r_{\mathrm{C-O}}$ and $Z_{\mathrm{Au-C}}$. Figure 5.9 shows contour plots for the CO-Au(111) (right) and CO-Ag(111) (left) systems in adiabatic ground and excited states.

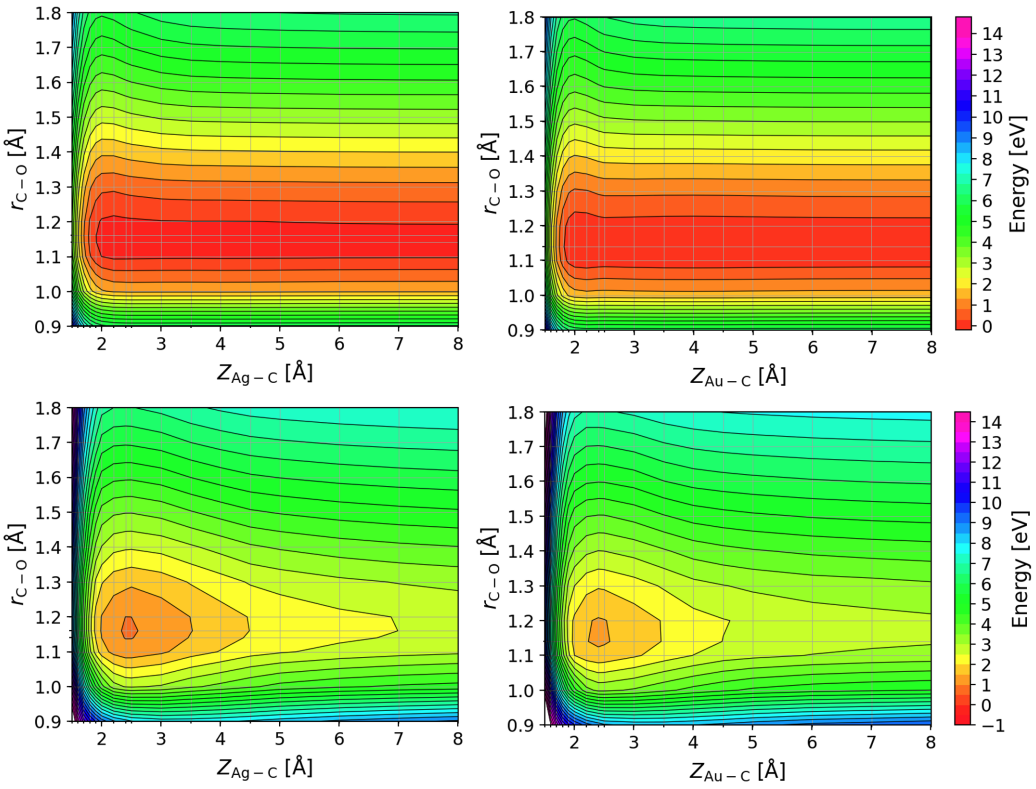

Figure 5.9: 2D Binding energy PES as a function of r_{C-O} and Z_{Au-C} for CO-Ag(111) (left) and CO-Au(111) (right) in the adiabatic ground state (top) and adiabatic excited state (bottom). Gridlines indicate the parts of each PES that were explicitly calculated, where an intersection of two grid lines corresponds to a sampled data point.

The adiabatic surfaces for the Ag(111) and Au(111) systems are very similar. The Ag(111) surfaces produce slightly steeper minima in both states and extends further from the surface in the excited state compared to Au(111). The locations of the minima are also very similar between the two systems, with both ground-state surfaces having a minimum at $Z_{M-C} = 2.2$ Å and $r_{C-O} = 1.14$ Å. In the excited state, the minima are shifted away from the surface and both lie at $Z_{M-C} = 2.4$ Å. The length of r_{C-O} for the excited state minima is slightly less clear. Within the data points sampled during construction of the 2D PES, for the Au(111) system the minimum is at $r_{C-O} = 1.14$ Å, which is the same as the groundstate; however, for Ag(111), where an additional 1D binding curve of data at $r_{C-O} = 1.16$ Å has been sampled, the minimum lies at 1.16 Å, approximately 30 meV lower than $r_{C-O} = 1.14$ Å. In both cases, the next largest r_{C-O} sampled is at 1.20 Å. In order to determine

the precise value of r_{C-O} of the excited state minima, much finer sampling of data would be required. The additional sampling would be costly, while offering very little in terms of improvement of the overall model and has therefore not been included in this work. For clarity, it should be noted that the additional 1D binding curve worth of data points at $r_{C-O} = 1.16$ Å was only generated due to a typo in the script used to create the full 2D PES and was not an intentional choice. All four PESs in Figure 5.9 vary smoothly, which will be important if future works are to apply this methodology with machine learning to construct larger and higher dimensional models. The surfaces largely match physical expectations: in the ground states the lowest energy r_{C-O} are in the region of the gas phase equilibrium bond length for CO of 1.14 Å. The energy rises steeply upon deviation from this bond length, with compression causing a steeper rise in energy than extension. A steep repulsive wall is seen in both states upon close approach to the surface. The excited state shows stronger repulsion, which is expected for a negatively charged molecule approaching a surface. The location and shape of the repulsive walls are very similar between the two systems and do not depend strongly on the metal species.

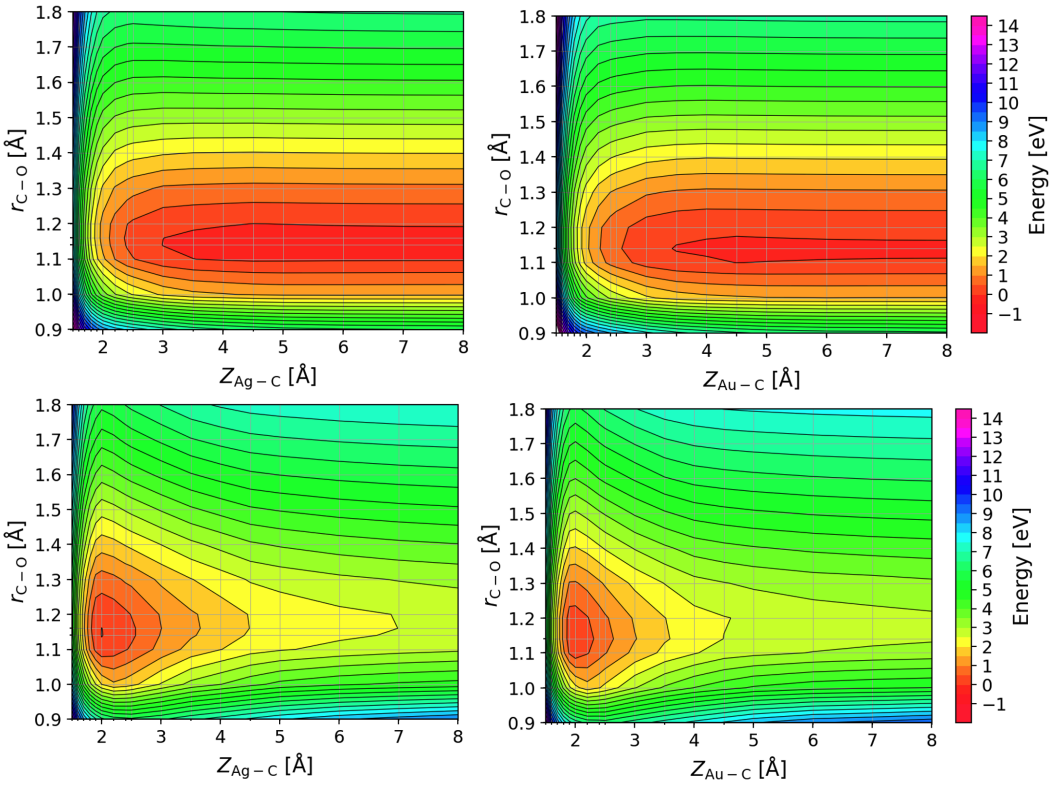

Figure 5.10: 2D Binding energy PES as a function of r_{C-O} and Z_{Au-C} for CO-Ag(111) (left) and CO-Au(111) (right) systems in the neutral diabatic state (top) and anionic diabatic state (bottom). Gridlines indicate the parts of each PES that were explicitly calculated, where an intersection of two grid lines corresponds to a sampled data point.

The neutral diabatic PESs also show similar typologies between the Ag(111) and Au(111) systems. In the Au(111) system, as the molecule approaches the metal, the neutral surface starts to become repulsive at a greater distance from the surface; however, below ∼2 Å from the surface the two systems are almost identical. A similar trend is seen for the anionic PESs, where the Ag(111) adsorption well is slightly deeper and extends further from the surface, but close to the surface there is very little difference.

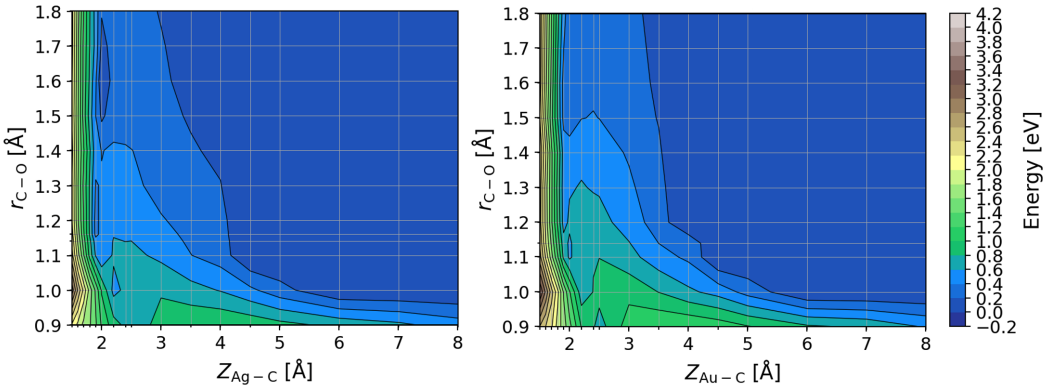

Figure 5.11: 2D diabatic coupling surface as a function of $r_{\mathrm{C-O}}$ and $Z_{\mathrm{Au-C}}$ for CO-Ag(111) (left) and CO-Au(111) (right). Gridlines indicate the parts of each PES that were explicitly calculated, where an intersection of two grid lines corresponds to a sampled data point.

The diabatic coupling (Figure 5.11) covers a range from 0.0 eV to a maximum of 2.69 and 2.49 eV for the Ag and Au systems, respectively. The areas of zero coupling are far from the surface and at extended bond lengths. This is because in these regions there is no exchange of charge between molecule and surface and therefore the ground-state and neutral energies are identical. The same is true for the anion and adiabatic excited state. Compressing the bond below 1.0 Å always results in increased coupling. The regions of maximum diabatic coupling are at small $Z_{\mathrm{M-C}}$ with maxima at $r_{\mathrm{C-O}}$ of 1.0 Å in both systems.

Both systems show a feature that is unphysical and may lead to inaccuracies when using le-ΔSCF based PESs for nonadiabatic dynamics: the difference between the ground and excited adiabatic states (ΔE_{ex}) is too small. Consider the case in which the molecule is far enough from the surface that there is no exchange of charge with the surface. The energetic cost of moving from the ground state to the excited state would be the sum of the cost of removing an electron from the surface to the vacuum (*i.e.*, the work function) Φ_{surf} and the change in energy when attaching an electron from vacuum to the neutral molecule, *i.e.*, the electron affinity (E_{aff}). The work functions were calculated by using the same slab model from the full system calculations and are equal to the difference in energy between the Fermi level (E_{F}) and the averaged electrostatic potential far from the surface, and were found to be 5.04 eV for Au(111) and 4.26 eV for Ag(111). E_{aff} of CO could not be calculated using GPAW, which had been used for all other calculations, because when the charged molecule is placed in a unit cell, even a very large one, the ground-state

LUMO becomes an unbound state. This means any anion energy would be highly unphysical. For this reason an experimentally determined E_{aff} of 1.34 eV [104, 105] was used in the determination of expected ΔE_{ex}. In the absence of any charge exchange between molecule and metal, the expected ΔE_{ex} for Au(111) and Ag(111) are 6.34 and 5.60 eV, respectively, however, in the ρle-ΔSCF model at $Z_{\text{M}-\text{C}} = 8.0$ Å and $r_{\text{C}-\text{O}}$ =1.14 Å ΔE_{ex} is 3.01 and 2.09 eV for the Au(111) and Ag(111) systems respectively. This is a very large underestimation and would have a dramatic effect on any dynamics simulations that rely on these PESs. As an immediate, if only partial, solution to this problem of underestimated ΔE_{ex}, a rigid vertical shift was applied to the anionic surfaces, such that ΔE_{ex} at $Z_{\text{M}-\text{C}} = 8.0$ Å and $r_{\text{C}-\text{O}}$ =1.14 Å matches the estimation based on the sum of Φ_{surf} and E_{aff}. This, of course, does not address any potential errors in the way the energy changes as $Z_{\text{M}-\text{C}}$ and $r_{\text{C}-\text{O}}$ are varied from this single geometry, but using the shifted surfaces will still likely result in more physically accurate surface hopping dynamics compared to the non-shifted surfaces. The adiabatic ground state and the neutral diabatic state remain unchanged; however, the diabatic coupling and the adiabatic excited state are both calculated using the anionic energy and so will change significantly. Figure 5.12 shows the shifted anionic, adiabatic excited state and diabatic coupling PESs for the Au(111) and Ag(111) models. All dynamics simulations in the next chapter are performed on both shifted and non-shifted PESs and the results are compared.

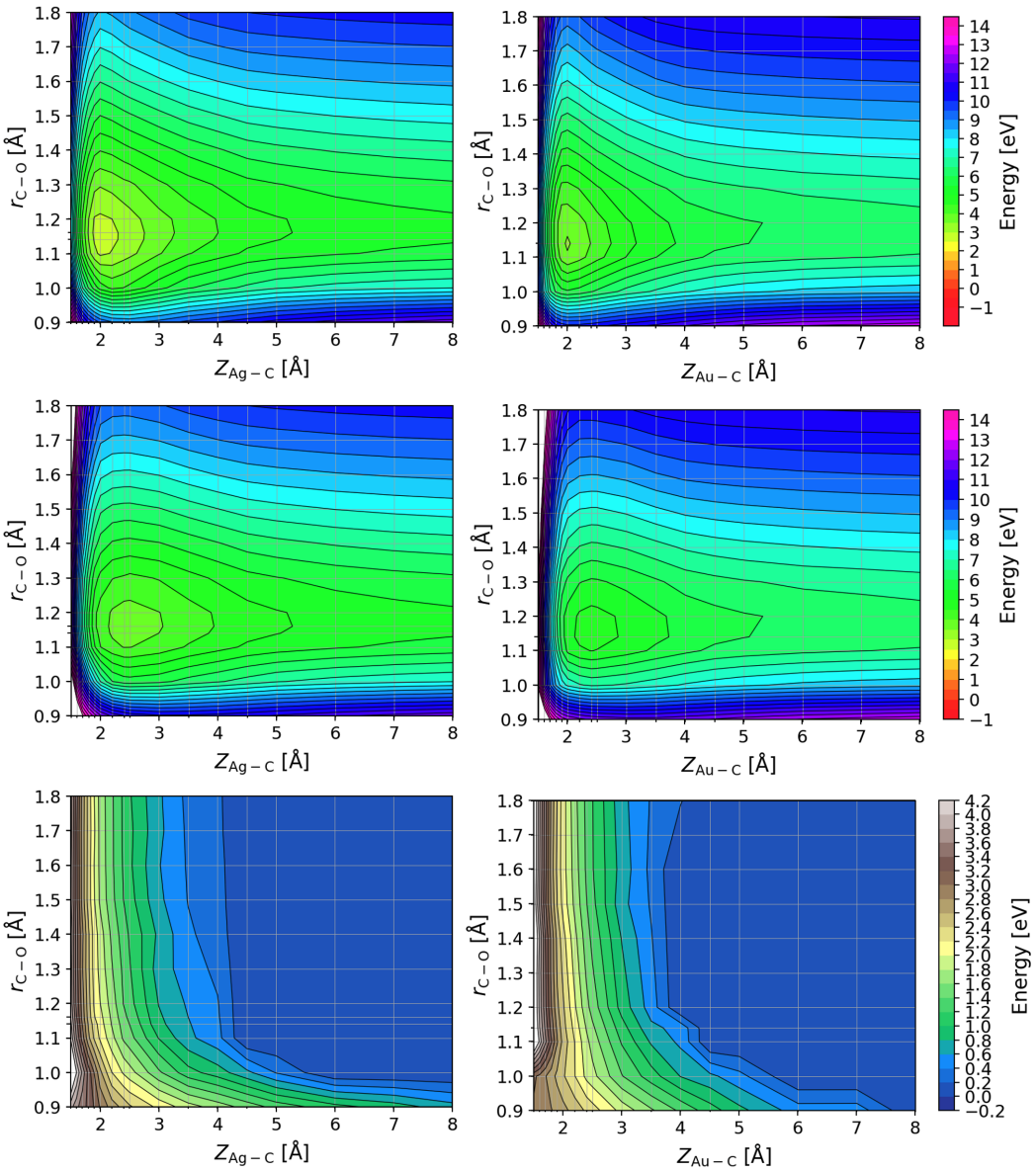

Figure 5.12: 2D shifted PESs with Ag(111) PESs on the left and Au(111) on the right. Anionic (top row), adiabatic excited state (middle row), diabatic coupling (bottom row). Gridlines indicate the parts of each PES that were explicitly calculated, where an intersection of two grid lines corresponds to a sampled data point.

ΔE_{ex} as a function of geometry in the different PES sets will have a direct impact on the results of any nonadiabtic dynamics. This is because the magnitude of ΔE_{ex} directly affects the probability that an electron hopping event, in which an electron from a bath state transfers to the molecule, will occur during a time-

step of an IESH dynamics trajectory. 2D PES of ΔE_{ex} are shown in Figure 5.13 for the shifted and non-shifted models. Both Ag(111) and Au(111) show a very similar distribution of ΔE_{ex}, indicating that they will likely produce very similar dynamics results. It can also be seen that fewer hopping events will occur during dynamical trajectories using the shifted surfaces, as opposed to the non-shifted surfaces, because of the greater excitation energies.

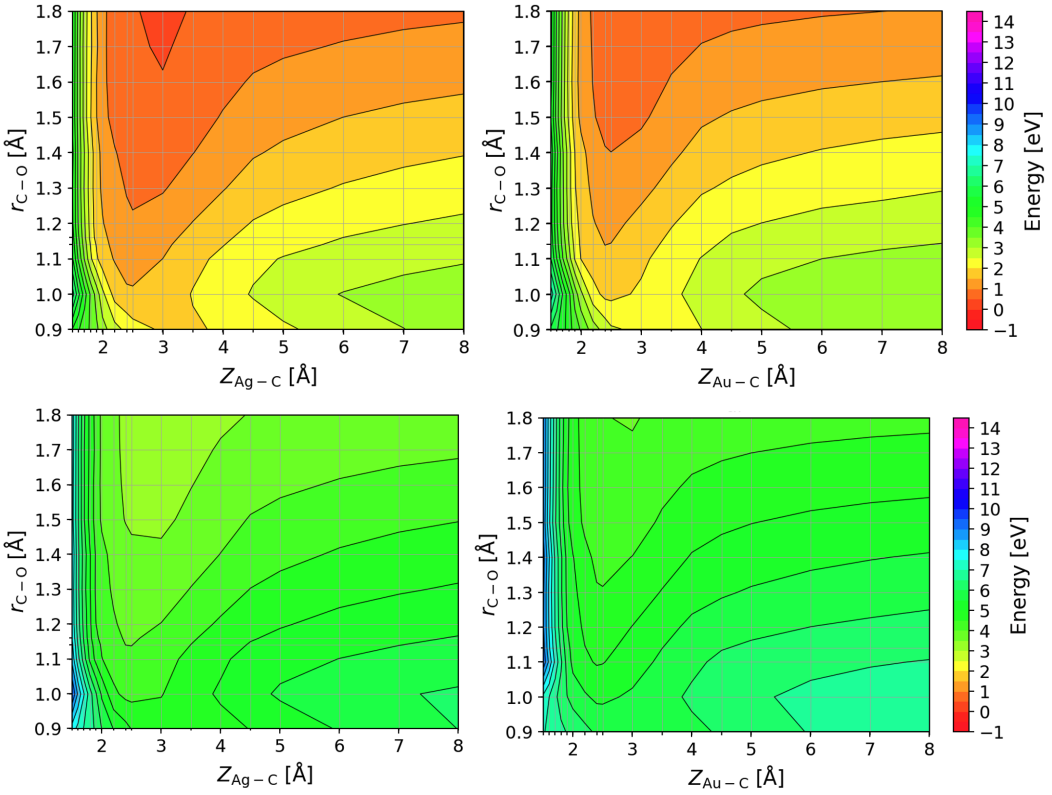

Figure 5.13: ΔE_{ex} (E_{es} - E_{gs}) of non-shifted surfaces (top) and after shift is applied (bottom). Ag(111) on the left and Au(111) on the right. Gridlines indicate the parts of each PES that were explicitly calculated, where an intersection of two grid lines corresponds to a sampled data point.

5.3.1 Constrained DFT

Disclaimer: The results presented in this subsection are based on outputs of a machine learned model provided by collaborators Gang Meng and Bin Jiang working at the University of Science and Technology of China. I had no involvement in the creation of this model; however, I have used the outputs of the model to construct potential energy surfaces.

At the time of writing, in order to move beyond the simple electric field method previously used by Tully and coworkers, there are only two viable methods for accurately modelling the types of diabatic charge transfer PESs that are required to simulate the type of charge transfer states at metal surfaces that are of central interest in this work; and that are important for gaining a deep understanding of the non-adiabatic processes that occur during molecular beam scattering experiments [19]. Those two methods are le-ΔSCF and constrained DFT (CDFT) [106]. Equivalent PESs to those from le-ΔSCF discussed in this chapter have been created using a machine learned model based on CDFT data, so that a comprehensive comparison of the two methods can be performed.

All CDFT derived energies and coupling presented here are the outputs of a machine learning model produced by collaborators Gang Meng and Bin Jiang at the University of Science and Technology of China [107]. Any reference to the training data used to train the model will be referred to as CDFT data and any outputs of the model will be referred to as ML-CDFT data. The CDFT training data was produced using the CP2K electronic structure package [108] with a Gaussian plane wave triple-zeta TZ2VP-MOLOPT-GHT basis set and Geodecker-Teter-Hutter pseudopotentials using the vdW-DF xc functional [109]. All calculations were non-spin polarised. The Au(111) surface was modelled using a 6×6 super cell with 4 metal layers, 25 Å of vacuum spacing and a single **k**-point centered at Γ. The volumes to which the charge constraints were applied were based on Hirshfeld volumes [110] and the charge was assessed using the Bader charge partitioning scheme [111].

Parameter	le-ΔSCF	CDFT
unit cell	$p(3 \times 3)$	$p(6 \times 6)$
K-grid	8 8 1	1 1 1
XC functional	RPBE+vdW$^{\text{surf}}$	vdW-DF
basis set	tripple-zeta	finite difference
ionic cores	pseudopotential	PAW
vacuum height	36 Å	25 Å
metal layers	4	4

Table 5.1: A comparison of parameters used in DFT ground-state and excited state calculations associated with le-ΔSCF and CDFT based models.

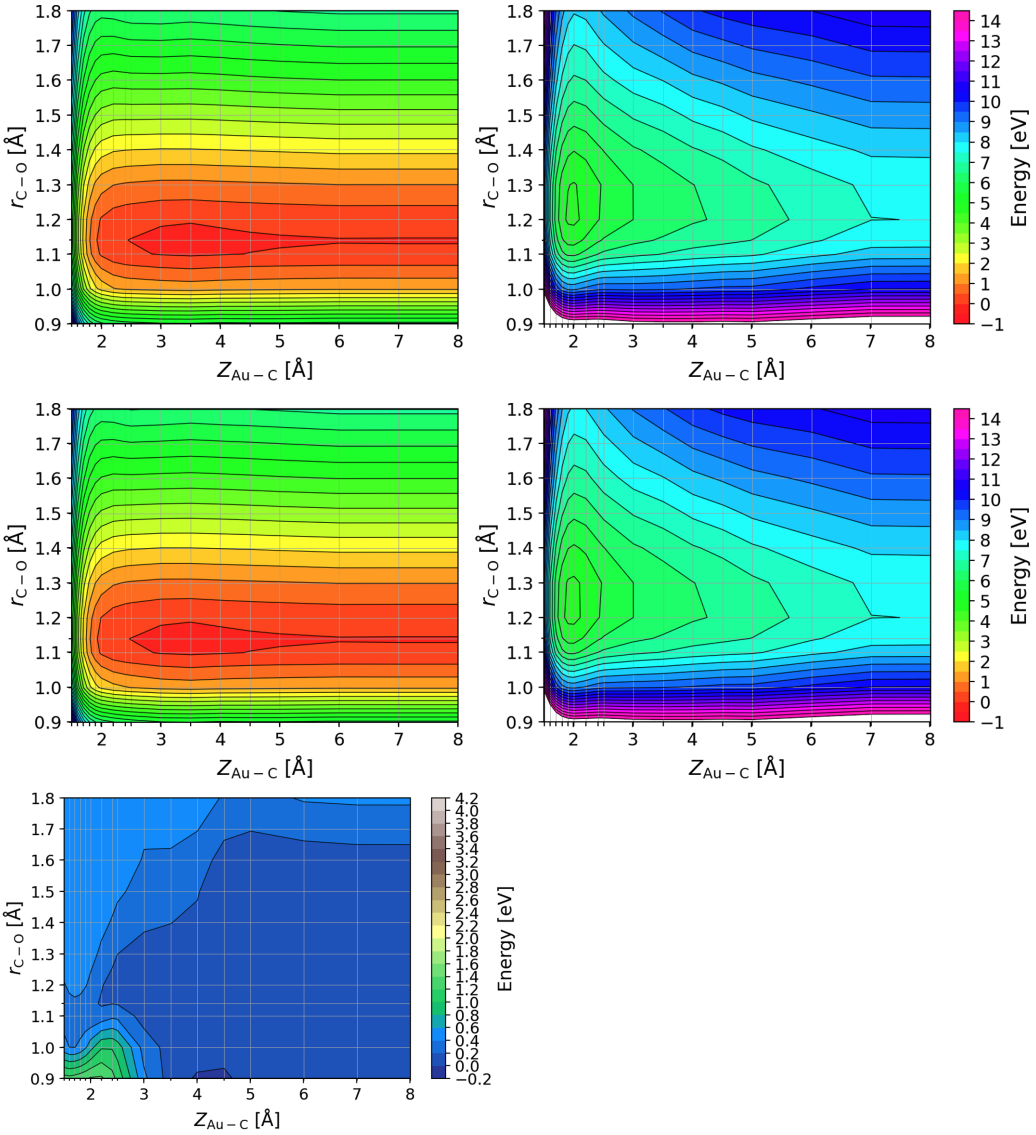

Figure 5.14: 2D PESs of CO on Au(111) based on ML-CDFT energies: adiabatic ground state (top left) adiabatic excited state (top right), diabatic neutral (middle left), diabatic anion (middle right) and diabatic coupling (bottom). Gridlines indicate the parts of each PES that were extracted from the ML model, where an intersection of two grid lines corresponds to a sampled data point.

The ground-state PES looks very similar to the one produced using GPAW. This is expected because no excited state method has been applied, and any differences are due to differences in the computational and numerical parameters, as shown in Table 5.1. Several of the different parameters are due to the different soft-

ware used. The CDFT implementation in CP2K is not parallelised over **k**-points, and so only a single **k**-point can be sampled. To account for this a much larger unit cell ($p(6 \times 6)$) was used. This is not the case in GPAW where a smaller unit cell ($p(3 \times 3)$) and many **k**-points were used. The differences in basis sets and treatment of ionic cores are also due to the different software because CP2K is a plane-wave pseudopotential based software and GPAW is a real-space projector augmented wave code.

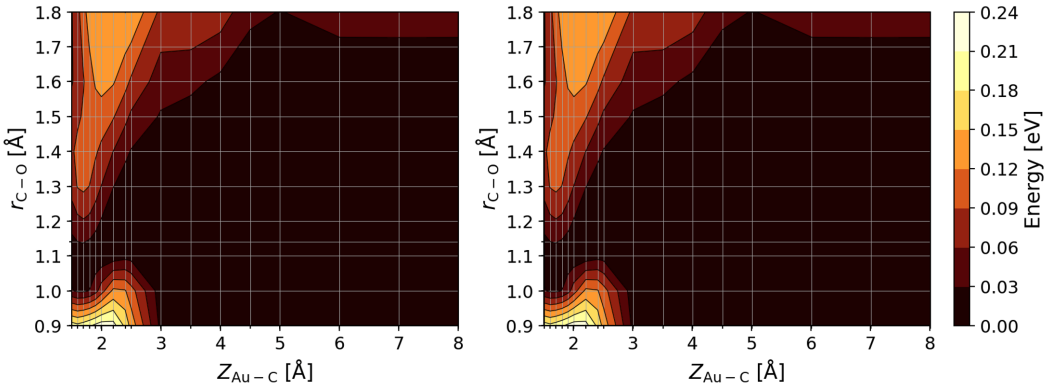

Figure 5.15: 2D PESs of the difference between adiabatic excited state and anionic diabat, referred to as the upper states (left) and neutral diabat and adiabatic ground-state referred to as the lower states (right), for the CO on Au(111) ML-CDFT set of PESs. Despite one being an adiabatic representation and the other being a diabatic representation the upper states are highly similar to one another and the the same is true for the pair of lower states

The diabatic anion and adiabatic excited state surfaces (upper surfaces) are extremely similar to one another and the same is true for the diabatic neutral and adiabatic ground-state (lower surfaces). For clarity, Figure 5.15 shows only the differences between the upper surfaces (left) and the lower surfaces (right). The key point to take from Figure 5.15 is that the similarities in the set of ML-CDFT PESs are much greater than is the case for the le-ΔSCF surfaces. This is because the area of zero/low coupling in the ML-CDFT model covers much more of the PES and the maximum coupling observed is only 1.43 eV, compared to 4.69 eV for the shifted le-ΔSCF model. By the definition of the diabatic coupling (V_c), where the coupling is zero, the differences must also be zero, which is why the difference plots in Figure 5.15 map almost perfectly onto the diabatic coupling in Figure 5.14. The overall distribution of the diabatic coupling is also quite different between the ML-CDFT and le-ΔSCF models. In the ML-CDFT model the coupling

is only high where both $Z_{\mathrm{Au-C}}$ and $r_{\mathrm{C-O}}$ are small. In contrast, the le-ΔSCF model predicts high coupling close to the surface, at $Z_{\mathrm{Au-C}}$ below ∼3.0 Å regardless of $r_{\mathrm{C-O}}$. the differences in coupling are likely to affect the hopping dynamics in any IESH simulations. The small area of negative coupling around $Z_{\mathrm{Au-C}}$ = 4–4.5 Å and $Z_{\mathrm{Au-C}}$ = 0.9 Å in the ML-CDFT coupling should not be possible based on Eqn (5.1) and is an indication that the machine learned model that produced this coupling might require additional training; however, it should not have a significant impact on any dynamics simulations.

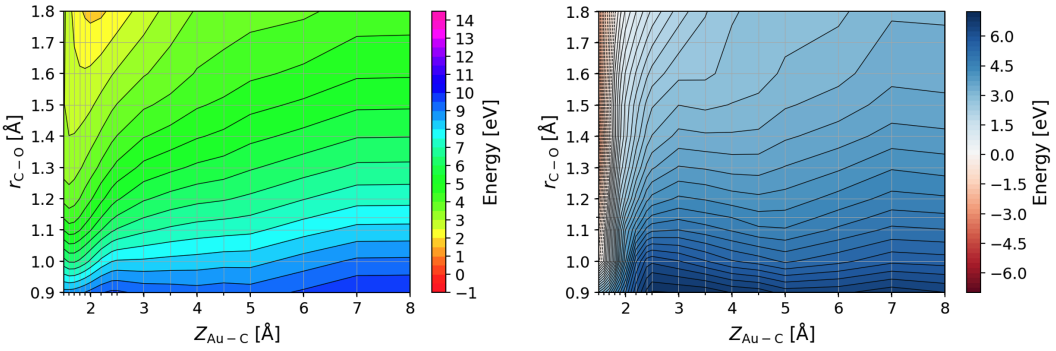

Figure 5.16: 2D PESs of adiabatic excitation energies for CO on Au(111) ML-CDFT model (left). Difference in excitation energy between models: ML-CDFT - (non-shifted) le-ΔSCF (right).

Figure 5.16 compares ΔE_{ex} between the ML-CDFT and le-ΔSCF models. The shifted le-ΔSCF ΔE_{ex} values are much more similar to those of ML-CDFT than the non-shifted surface. The overall distribution of high and low areas of ΔE_{ex} are broadly similar between the two methods. However, ML-CDFT shows more dependence on $r_{\mathrm{C-O}}$, with the largest values of ΔE_{ex} in either method seen at compressed $r_{\mathrm{C-O}}$ far from the surface. While le-ΔSCF also sees relatively high ΔE_{ex} in this region, the greater dependence on $Z_{\mathrm{Au-C}}$ means the maximum of ΔE_{ex} is seen close to the surface and largely invariant to extension of $r_{\mathrm{C-O}}$. Since both $Z_{\mathrm{Au-C}}$ and $r_{\mathrm{C-O}}$ should significantly affect the magnitude of excitation energy, it is not immediately clear which of these models best captures the physics of the real system. The only way to determine the superior model is to run nonadiabatic dynamics simulations and compare the results to experimental results. This will be the basis of the next chapter.

Chapter 6

Dynamics

6.1 Introduction

This chapter will present and discuss results of nonadiabatic molecular dynamics (NAMD) simulations. The 2D PESs presented in the previous chapter were used in conjunction with the independent electron surface hopping (IESH) algorithm to simulate molecular scattering events of CO molecules impacting Au(111) and Ag(111) surfaces. The initial vibrational state (ν_i) and the incident translational kinetic energy (E_i) of the molecule were systematically varied to assess nonadiabatic vibrational (de)excitation. The goal of these simulations was to assess the suitability of the ρle-ΔSCF and ML-CDFT methodologies of constructing PESs that, in combination with the IESH algorithm, can accurately capture the nonadiabatic physics that occurs within these systems. The trajectories were initialised with the molecule traveling toward the surface with a translational kinetic energy (E_i) between 0.2-1.2 eV. For each set of initial conditions, 1000 trajectories were simulated. A given initial condition comprises of a value for ν_i and E_i.

6.2 Convergence tests

To enable meaningful conclusion to be drawn from any dynamics simulations, numerical convergence testing must be performed. The key numerical settings that must be chosen in order to produce meaningful results from IESH dynamics are the time-step ($\mathrm{d}t$) and the number of bath states. In principle an infinitesimally short time step should be used to maximise accuracy, but real-world computations require that $\mathrm{d}t$ is finite. Provided the $\mathrm{d}t$ used is only a fraction of the fastest dynamical process unfolding during the dynamics, almost no information is lost and the results

are reliable. Within IESH the fastest occurring process is the hopping of electrons between states and so dt must be sufficiently small that all hopping events are captured; if two or more hops would be likely to occur during a single time-step then dt is too large. The property that was converged as a function of decreasing dt was the nonadiabatic contribution to the IESH energy (E_{NA}):

$$E_{\mathrm{NA}} = E_{\mathrm{IESH}}(\boldsymbol{R}, t, s) - E_{\mathrm{IESH}}(\boldsymbol{R}, t, s^0). \tag{6.1}$$

E_{NA} is the difference between the full IESH energy ($E_{\mathrm{IESH}}(\boldsymbol{R}, t, s)$) and the IESH energy when s corresponds to the ground state (s^0), *i.e.*, when the N_e electrons occupy the lowest N_e bath states. Eqn (6.2) shows the functional form of $E_{\mathrm{IESH}}(\boldsymbol{R}, t, s)$:

$$E_{\mathrm{IESH}}(\boldsymbol{R}, t, s) = T_{\mathrm{nuc}}(\boldsymbol{R}) + E_{\mathrm{neu}}(\boldsymbol{R}) + \sum_{k \in \mathbf{s}(t)} \lambda_k(\boldsymbol{R}). \tag{6.2}$$

where $\lambda_k(\boldsymbol{R})$ is the energy of the k^{th} bath state and the sum runs over occupied bath states.

For each d$t \in \{0.5, 0.2, 0.1\}$ fs, 1000 IESH trajectories were calculated. Each trajectory was initiated with $Z_{\mathrm{M-C}} = 5.0$ Å and 1.0 eV translational kinetic energy (E_{i}) in the direction of the surface. At each time step, E_{NA} was averaged over the 1000 trajectories and the results are shown in Figure 6.1.

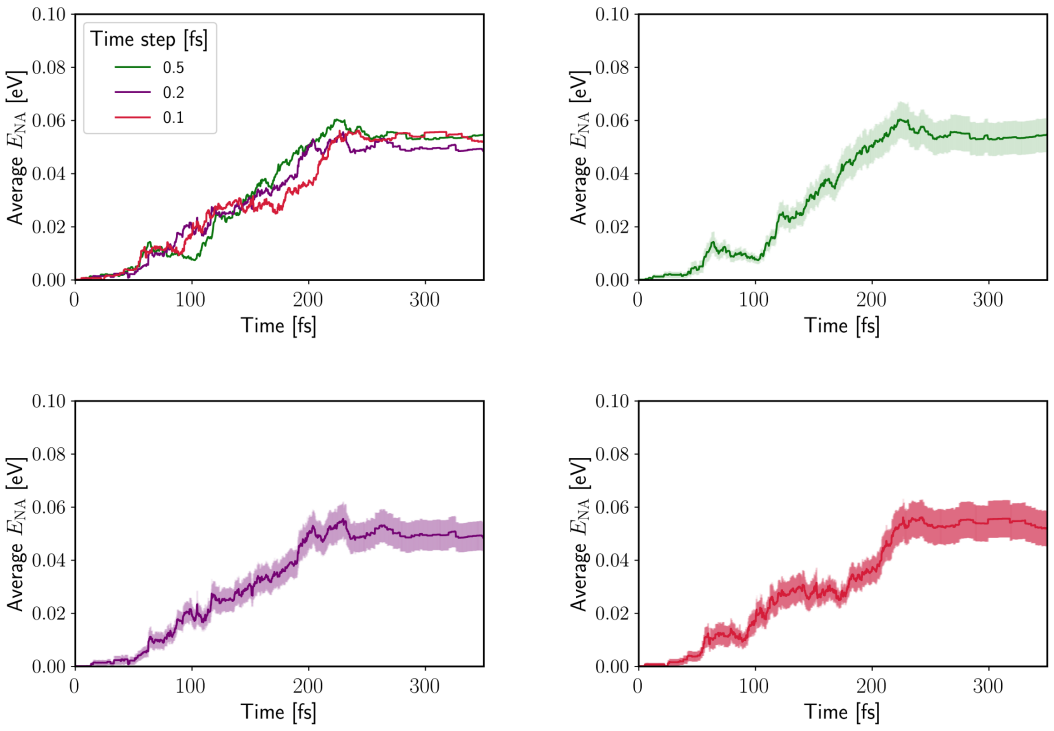

Figure 6.1: E_{NA} averaged over 1000 trajectories for $\mathrm{d}t \in \{0.5, 0.2, 0.1\}$ fs. The top left panel show results for all three values of $\mathrm{d}t$ without error bars because the overlapping error bars would make the plot difficult to interpret. The other three panels show a line for a single $\mathrm{d}t$ value with error bars showing standard deviation. Each trajectory was initialised with E_{i}=1.0 eV, $\nu_{\mathrm{i}} = 8$ and the molecule 5.0 Å above the surface. The PES set used was the shifted ρle-ΔSCF CO-Au(111) model. There is little difference between the $\mathrm{d}t$ values, indicating that $\mathrm{d}t$=0.5 is already well converged.

The time step is well converged at even the largest $\mathrm{d}t$ sampled, 0.5 fs. However, all results presented in the remainder of this thesis use a time step of 0.1 fs. While this is not the most economic way of running calculations it a very well converged parameter and results are reliable. The reason simulations were carried out using $\mathrm{d}t = 0.1$ fs is that a previous set of convergence tests, using an incorrectly implemented version of the IESH code, had suggested $\mathrm{d}t$ was not well converged at values larger than 0.1 fs; and $\mathrm{d}t$ was not changed when the code was corrected. All dynamics results presented in this thesis use the correct implementation of IESH in the updated NQCD.jl package.

The second parameter which requires convergence testing is the number of bath states. In IESH simulations, nonadiabatic energy transfer is accounted for via

electronic transitions (hops) between an impurity (molecular) state and a set of bath states representing metal states. As described in Section 2.4, to make a practical implementation of IESH theory, a continuum of metal states must be discretised into a finite set of (bath) states. Increasing the number of bath states more closely mimics the continuum and increases the accuracy of any dynamics simulations, but also increases the computational cost. Similarly to the dt convergence tests, a series of simulations were carried out using different numbers of bath states to find the point at which adding more states no longer increases the average E_{NA}. The set of bath states in this work were discretised using the Gaussian quadrature scheme, wherein there is a greater density of states around the Fermi level, as previous work has shown that fewer bath states are required to reach numerical convergence than if a set of evenly spaced states are used [49]. The convergence tests for dt were repeated for the total number of bath states (N_{b}), but with dt fixed at 0.1 fs, ν_{i}=6 and E_{i} = 1.0 eV. The results are shown in Figure 6.2. The results are converged at N_{b} = 150 bath states, therefore 150 bath states will be used in all subsequent results presented in this chapter.

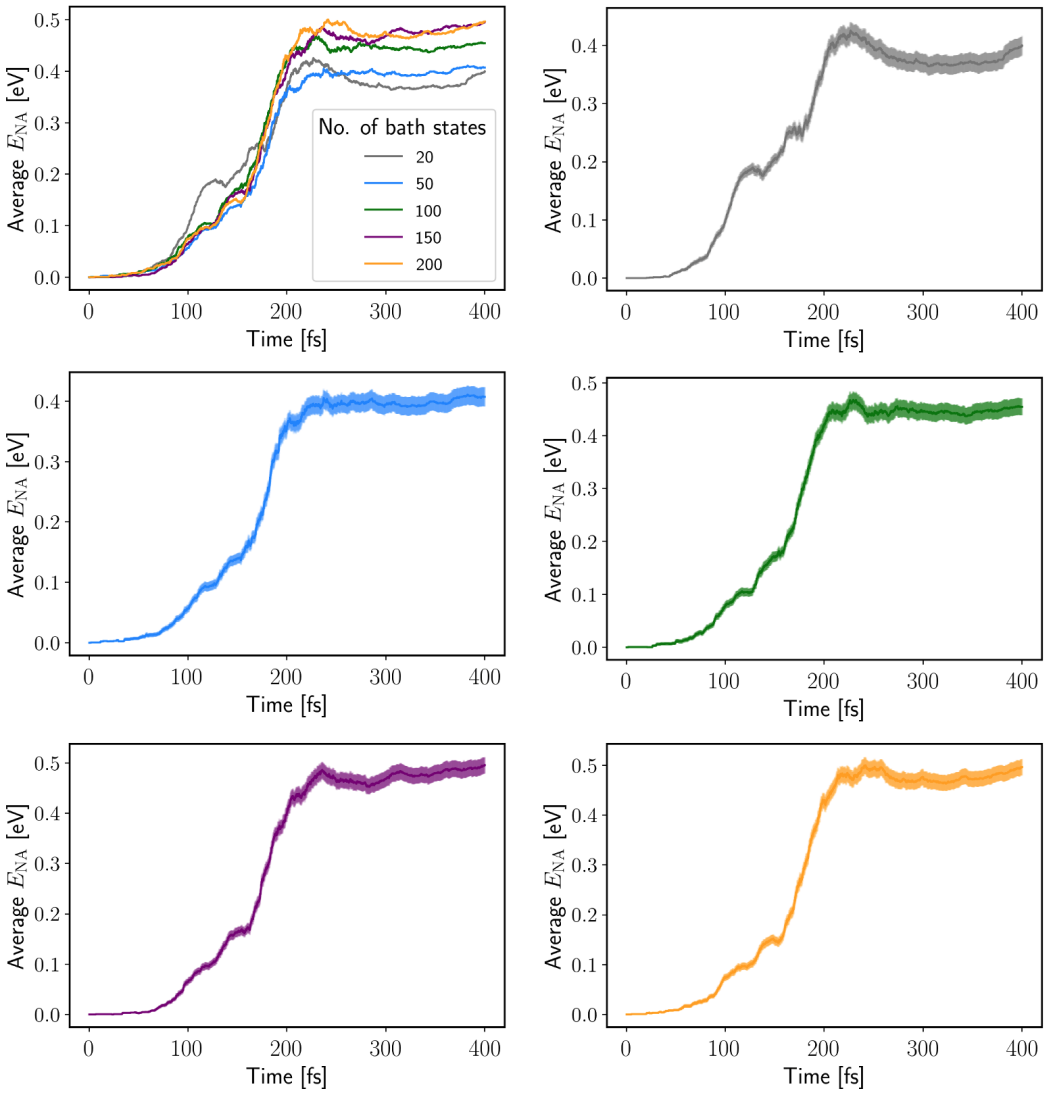

Figure 6.2: E_{NA} averaged over 1000 trajectories for $N_b \in \{20, 50, 100, 150, 200\}$. The top left panel show results for all values of N_b without error bars because the overlapping error bars would make the results difficult to interpret. The remaining panels each show a single N_b value with error bars representing standard deviation. The bath width was 7.0 eV in all cases. Each trajectory was initialised with $E_i = 1.0$ eV, $\nu_i = 6$ and the molecule 5.0 Å above the surface. The PES set used was the shifted ρle-ΔSCF CO-Au(111) model. E_{NA} is converged at $N_b = 150$.

6.3 Methodology

All simulations were performed using the IESH implementation in the NQCDynamics.jl package in the Julia programming language [57, 112]. All 2D PESs described in the previous chapter were fitted using the spline2D function in the Dierckx.jl package prior to being used for any dynamics simulations. Based on convergence tests, the bath of metallic states was discretized using the Gaussian quadrature scheme [113] and 150 states. The width of the bath was 7.0 eV in order to mimic the s band of Au/Ag and is in line with previous work by Tully et al [18, 19]. Each trajectory used a time step of 0.1 fs and simulated a maximum of 400 fs; however, the simulation was truncated if $Z_{\mathrm{Au-C}}$ of 8 Å was reached after scattering from the surface. The initial bond length ($r_{\mathrm{C-O}}$) and bond velocity of the CO molecule, for each trajectory, was sampled from a distribution created using the Einstein-Brillouin-Keller quantization scheme (EBK) [114] and corresponding to the initial vibrational state (ν_{i}) of choice. The results section that follows corresponds to analysis of a large set of dynamical trajectories that model CO scattering from Au(111) or Ag(111). The trajectories vary in the initial conditions: $\nu_i \in \{0, 2, 8, 12, 17\}$ and $E_i \in \{0.2, 0.4, 0.6, 0.8, 1.0, 1.2\}$ eV. For each set of initial conditions, 1000 trajectories were simulated. The dynamic simulations were performed using all sets of PESs described in the previous chapter: shifted and non-shifted ρle-ΔSCF Au(111) and Ag(111), and ML-CDFT Au(111). A set of 4 PESs (adiabatic ground and excited state plus neutral and anionic diabatic states) will be referred to as a PES set. All simulations were preformed using both IESH and classical AIMD. All trajectories used $\mathrm{d}t = 0.1$ fs and 150 bath states based on the results of the convergence tests. The initial $Z_{\mathrm{M-C}}$ was 5.0 Å. The initial $r_{\mathrm{C-O}}$ and bond velocity were randomly sampled from a distribution based on the appropriate ν_i generated using the EBK method [114].

6.3.1 Error bars

For each set of initial conditions using a given dynamics method and PES set an inelastic probability (Υ) is calculated as the proportion of the 1000 trajectories for which $\nu_{\mathrm{i}} \neq \nu_{\mathrm{f}}$. An error bar associated with each Υ had to be calculated. The method for determining the standard deviation is as follows:

1. Divide the set of 1000 trajectories into the following smaller groups:
    - 20 groups of 50 trajectories
    - 10 groups of 100 trajectories

- 5 groups of 200 trajectories
- 4 groups of 250 trajectories

2. calculate Υ for each group.
3. Calculate the variance over the groups of a given size
4. Shuffle the order of the initial 1000 trajectories and repeat steps 1–3 50 times, recording the variances each time
5. Average the variance over the 50 shuffles
6. Plot inverse variance against group size
7. Use a linear regression to fit the inverse variance
8. Extrapolate the fit of inverse variance to a group size of 1000
9. Calculate the standard error from the extrapolated inverse variance

6.4 Trapping probabilities

The trapping probability (P_{trp}) is the probability that a molecule will not escape the surface during the course of a trajectory, after it has impacted the surface. In the context of this work, a molecule is deemed to have scattered from the surface if the trajectory reaches $Z_{\mathrm{M-C}} > 5.0$ Å, after contact with the surface. P_{trp} was calculated for each set of initial conditions and using each PES set. For all AIMD calculations, P_{trp} was always 0.0. This is expected as the dynamics unfold on the ground-state PES only, and therefore no transitions between electronic states can occur which could offer a significant energy dissipation pathway, and the molecule always escapes the ground-state well.

The P_{trp} of the IESH dynamics is very different between the different PES sets. Figure 6.3 shows P_{trp} for all four ρle-ΔSCF derived PES sets, as a function of the initial conditions. P_{trp} tends towards zero with increasing E_{i}. Generally, higher ν_i leads to higher P_{trp}, however the influence of ν_i is reduced with increasing E_{i}. Both of these trends match simple physical considerations. Greater initial translational kinetic energy means that even if the scattering event is translationally inelastic, the final translational kinetic energy is more likely to be great enough to escape the potential well near the surface. A larger initial vibrational energy increases the likelihood of a hopping event close to the surface. If an electron hops from the surface to the molecule then the dynamics proceed on the excited state PES, until

the electron hops back to a metal state. The excited state surfaces have deep minima of around 1.6 eV, meaning that escape from the surface requires greater translational kinetic energy than if the dynamics were proceeding on the ground-state PES. Based on these considerations it should be expected that, when comparing results using the shifted PES set, the trends should remain, but the magnitude of P_{trp} should be smaller. Indeed, this is exactly what is seen in Figure 6.3; the Au(111) trapping probability is consistently slightly higher than for Ag(111). The maximum depth of the excited state wells are very similar, within 0.1 eV of each other. However, the Au(111) well is steeper, so for a given translational kinetic energy, trapping is more likely.

Interestingly, the ML-CDFT P_{trp} is always exactly zero for the IESH dynamics. This is likely due to a lower hopping probability when using the ML-CDFT PESs compared to the shifted ρle-ΔSCF PESs. As was shown in the previous chapter, for most of the geometries covered by the PESs, E_{ex} was significantly larger in the ML-CDFT case. Therefore, it is reasonable to consider the lack of trapping in the ML-CDFT IESH dynamics as an 'extension' of the suppression of trapping probabilities that was seen when moving from non-shifted to shifted ρle-ΔSCF PESs.

Experimentally observed trapping probabilities for CO scattered from an Au(111) surface are only available for the $\nu_{\mathrm{i}} = 0$ case [115]. There is good agreement between simulations presented here and experiment, especially in the respect that trapping is practically non-existent for E_{i} above 0.4 eV. This is in contrast to molecular dynamics with electronic friction (MDEF), where the method has been shown to overpredict trapping probabilities, when tested for NO scattering from an Au(111) surface [116].

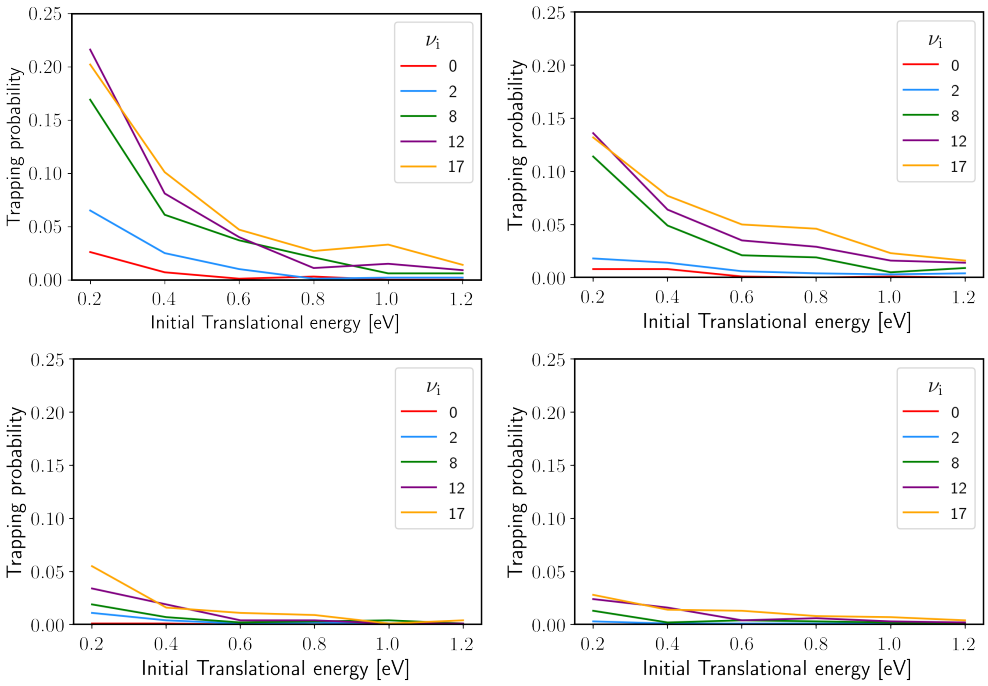

Figure 6.3: IESH trapping probabilities (P_{trp}) for CO scattering from Au(111) (left) and Ag(111) (right) using shifted (top) and non-shifted (bottom) ρle-ΔSCF PESs

6.5 Final state distributions

The key experiments that have shown nonadiabatic energy transfer during molecular scattering events from metal surfaces, and which this work seeks to model, rely on the observation of (multi-quantum) vibrational (de)excitation. With this in mind, an essential measure of how well the methodology of PES construction and IESH dynamics are able to capture the essential physics of such systems are the distributions of ν_f as a function of the PESs set and initial conditions. This section will discuss such results in detail.

Figure 6.4 shows examples of the final vibrational state distributions corresponding to CO scattering from Au(111), for three different ν_i: 2, 8 and 17; and at E_i=0.6 eV. Similar plots for all other initial conditions are included in Appendix B.

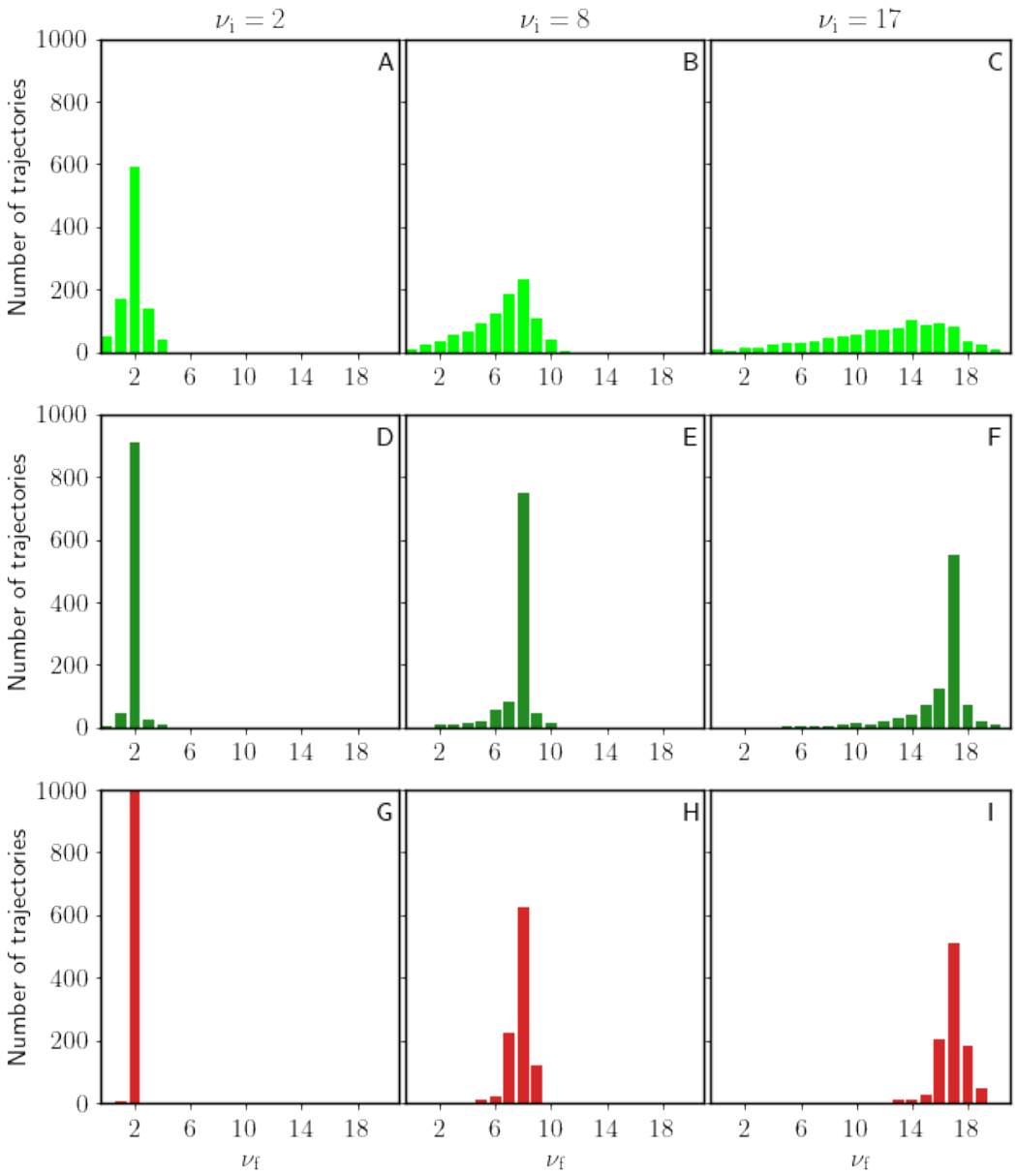

Figure 6.4: Final state distributions of IESH scattering trajectories for CO and Au(111) with $E_i = 0.6$ eV and $\nu_i = 2$, 8 or 17 using non-shifted ρle-ΔSCF Au(111) PES set in light green (A, B and C), shifted ρle-ΔSCF Au(111) PES set in dark green (D, E and F) and ML-CDFT Au(111) PES set in red (G, H, I).

The final state distributions of the non-shifted ρle-ΔSCF PESs (top row, light green in Figure 6.4) show far more vibrational inelasticity than the shifted ρle-ΔSCF or ML-CDFT PESs, both in the proportion of trajectories that were inelastic and in

the magnitude of $\Delta\nu$. As discussed above in regard to P_{trp}, the underestimation of E_{ex} that is present in the non-shifted PES set leads to an increase in the prevalence of electron hopping events during a trajectory. As it is the electron hopping events that facilitate the transfer of vibrational energy, it is expected that dynamics using the non-shifted PESs would result in greater inelasticity.

The distributions based on the shifted PESs (middle row, dark green in Figure 6.4) show very different behaviour. For all three sets of initial conditions, by far the largest peak is at $\nu_f = \nu_i$, *i.e.*, most scattering events are elastic. The proportion of trajectories that are inelastic and the maximum magnitude of $\Delta\nu$ increases with increasing ν_i. This trend matches expectations as greater vibrational energy increases the probability of electron hopping events and therefore the likelihood of vibrational (de)excitation.

The trends in the final state distributions based of the ML-CDFT PES set are broadly similar to the shifted ρle-ΔSCF results, especially in regard to the proportion of trajectories that are inelastic. Where the ML-CDFT distributions differ is in the spread of final state peaks around the elastic ($\nu_i = \nu_f$) peak. For all three values of ν_i the significant majority of inelastic trajectories showed $\Delta\nu = \pm 1$, whereas the shifted ρle-ΔSCF distributions are much broader. This is because the excitation energies in the ML-CDFT PES set are larger than the ρle-ΔSCF PES sets.

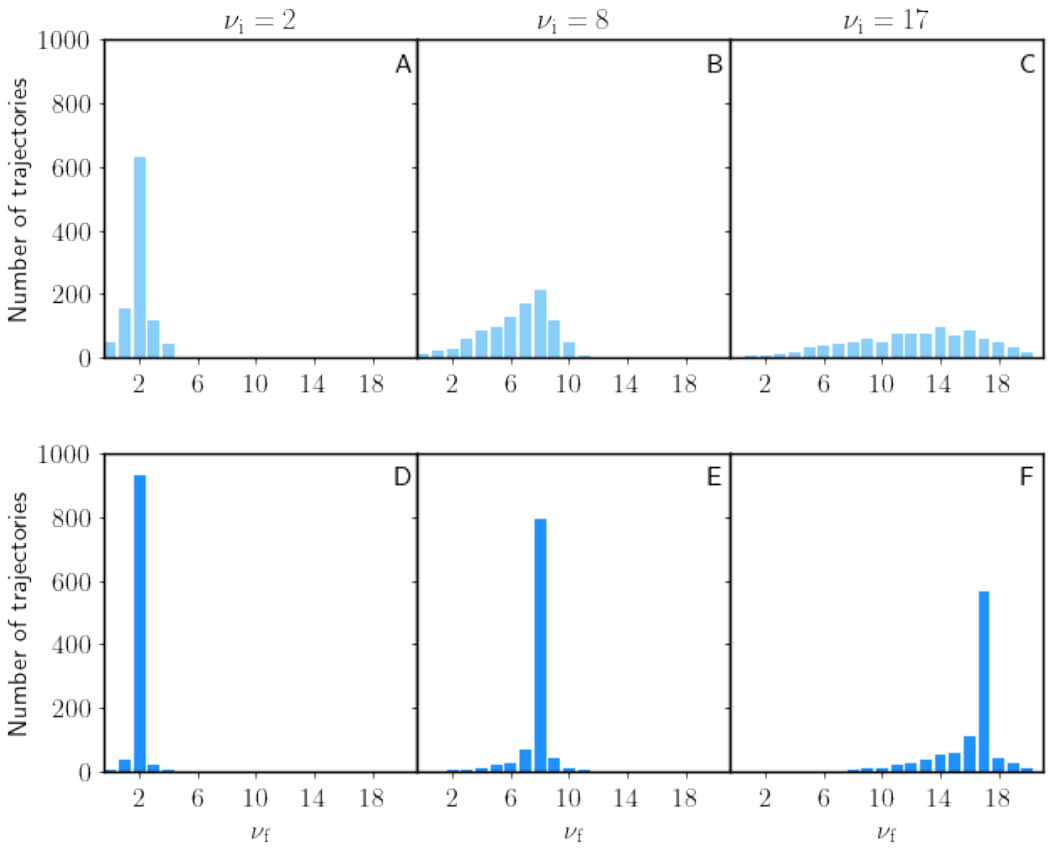

Figure 6.5: Final state distributions of scattering trajectories for CO and Ag(111) with $E_i = 0.6$ eV and $\nu_i = 2$, 8 or 17 using non-shifted ρle-ΔSCF Au(111) PES set in light blue (A, B and C), shifted ρle-ΔSCF Ag(111) PES set dark blue (D, E and F).

Final state distributions using the shifted and non-shifted ρle-ΔSCF PES sets for Ag(111) are shown in Figure 6.5. The trends are very similar to what was seen in the Au(111) case, with the non-shifted surfaces resulting in greater inelasticity and a wider range of final states. It is striking that the Au(111) and Ag(111) PES sets produce such similar results that any influence of the surface is barely visible; whereas different methods using the same surface (*i.e.*, shifted-le-ΔSCF vs ML-CDFT) do show distinctly different behaviour. This does not match experimental observations, where the influence of the surface (via the work function) is seen to be an important predictor of vibrational inelastic probabilities and leads to greater inelastic scattering from Ag(111) than Au(111) surfaces [74]. This can be understood by noting that the auto-detachment mechanism, that facilitates nonadiabatic vibrational energy transfer, involves the transfer of an electron from the

surface to the molecule, therefore a lower work function increases the likelihood an electron transfer will occur.

A key goal of this work is to assess the suitability of the excited state methods (le-ΔSCF and ML-CDFT) and IESH dynamics to replicate experimentally observed behaviour. It is therefore essential to compare the results in this work to published experimental data. However, such comparisons are limited in several ways. Firstly, the PESs used only include two degrees of freedom and as such exclude any effects that arise from rotational motion of the molecule. It also means every trajectory results in the molecule impacting the surface in a perfectly upright orientation with the carbon atom closest to the surface, above a top site and leaving the surface again along the same coordinate. Secondly, substrate motion is also excluded and the frozen surface approximation is used. Finally, there are only a limited number of experimental results available of the CO-Ag(111) and CO-Au(111) systems and these do not cover the full range of initial conditions sampled here. The results that do exist are incomplete because the technique used to determine ν_{f}, REMPI, is only sensitive to ν_{f} between 14-17 and cannot detect CO molecules with ν_{f} outside this range [69]. Nevertheless, it is informative to investigate how well this simple model is able to capture experimental trends and how differences in PES landscapes affect the final state distributions.

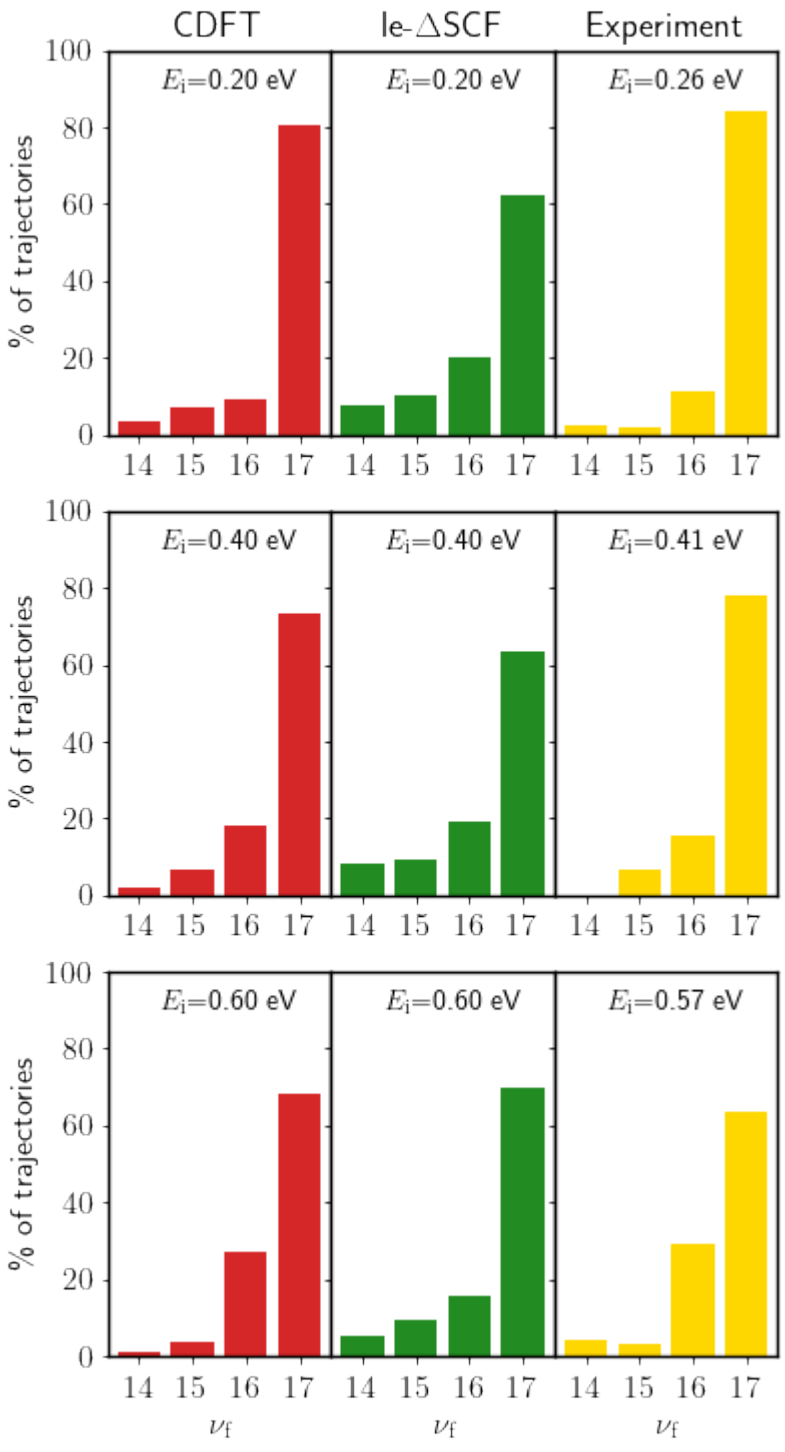

Figure 6.6: Comparison of IESH dynamics results to experiment for CO scattering from Au(111) with ν_i=17. ν_f distributions using ML-CDFT PES set (red), shifted ρle-ΔSCF PES set (green) and experimental data (yellow) from refs [74, 117].

Figure 6.6 shows final state distributions for CO molecules scattered from a Au(111) surface, in the format published in [117]. Experimental E_i do not precisely match those of the dynamics simulations and in each case the closest value has been included. The experimental $\nu_\mathrm{f} = 14 - 17$ peaks for a given E_i sum to 100%; *i.e.*, an assumption is made that no scattered molecules had ν_f outside of this range. IESH results in Figure 6.6 are plotted in the same way to enable meaningful comparison. However, IESH dynamics does result in molecules with ν_f outside of this range using both the ML-CDFT and shifted ρle-ΔSCF PES sets and the results shown in Figure 6.6 only account for approximately 80% of trajectories. It is also likely experimental scattering resulted in molecules with ν_f outside of the detectable range.

Despite the model limitations described above, the IESH results match experiment quite well, but IESH tends to overestimate the extent of multiquantum deexcitation within the experimentally observable range. The elastic channel in the ρle-ΔSCF data does not vary much with increasing E_i and, in fact, elasticity appears to increase with increasing E_i. This is the opposite to the experimentally observed trend of increasing E_i leading to increasing inelastic scattering. Overall, there is no systematic variation of elasticity with E_i for either ML-CDFT or ρle-ΔSCF when a wider range of E_i are taken into account. The experimental results display a strong dependence on E_i, with higher E_i leading to increased inelastic scattering. The E_i dependence is a consistent feature of nonadiabatic molecular beam scattering experiments [74]. The IESH results, in contrast, show a much weaker dependence on E_i, especially the ρle-ΔSCF where the final state distributions are essentially independent of E_i.

Figure 6.7 compares IESH and experimentally observed final state distributions for CO scattering from an Ag(111) surface [74]. In this case the experimental peaks do not sum to 100% and the results account for the fact many molecules will have ν_f outside the experimentally detectable range (ν_f = 14–17). The IESH results are plotted to match this format in order to enable meaningful comparison. Only IESH results based on ρle-ΔSCF PESs could be used as currently available ML-CDFT PES data is limited to Au(111). The IESH results are very similar to the Au(111) model, which is expected given how similar the PES sets are for the two metal surfaces. However, this is not the case for the experimental results, where Ag(111) surfaces show far more inelastic scattering, which means that the IESH results offer a very poor representation experimentally observed behaviour. As with Au, the ρle-ΔSCF results show almost no dependence on E_i. The E_i dependence in experiment is still present, but is less pronounced than for Au due to the large error bars across the distribution (no error bars were included in the published results

for the Au scattering experiments). Also a significant proportion of the scattered molecules ($\sim$ 60%) had ν_{f} outside the detectable range (14-17), making the detectable signal weaker. Despite limitations in the experimental data, it is clear that the IESH results significantly underestimate inelastic scattering.

Overall, IESH does a reasonable job of modeling the Au scattering experiments using both the ρle-ΔSCF and ML-CDFT derived PES sets, even with the limited models used in this work, but the Ag results are poor. It is not straightforward to determine how much of the shortcomings are due to 1. reduced dimensionality of the model, 2. excited state methods used to generate PESs and 3. the IESH method itself. However, the fact that the Au and Ag ρle-ΔSCF PESs are so similar make it inevitable that any dynamics results will also be similar, which is in contrast to experiment, even if IESH were able to perfectly capture the nonadiabatic behaviour. Expanding the methodology used in this work to larger, higher dimensional models, including a CDFT based model of the Ag system and expanding to include NO as the molecule would help make clearer where shortcoming originate. This is discussed in more detail in chapter 7.

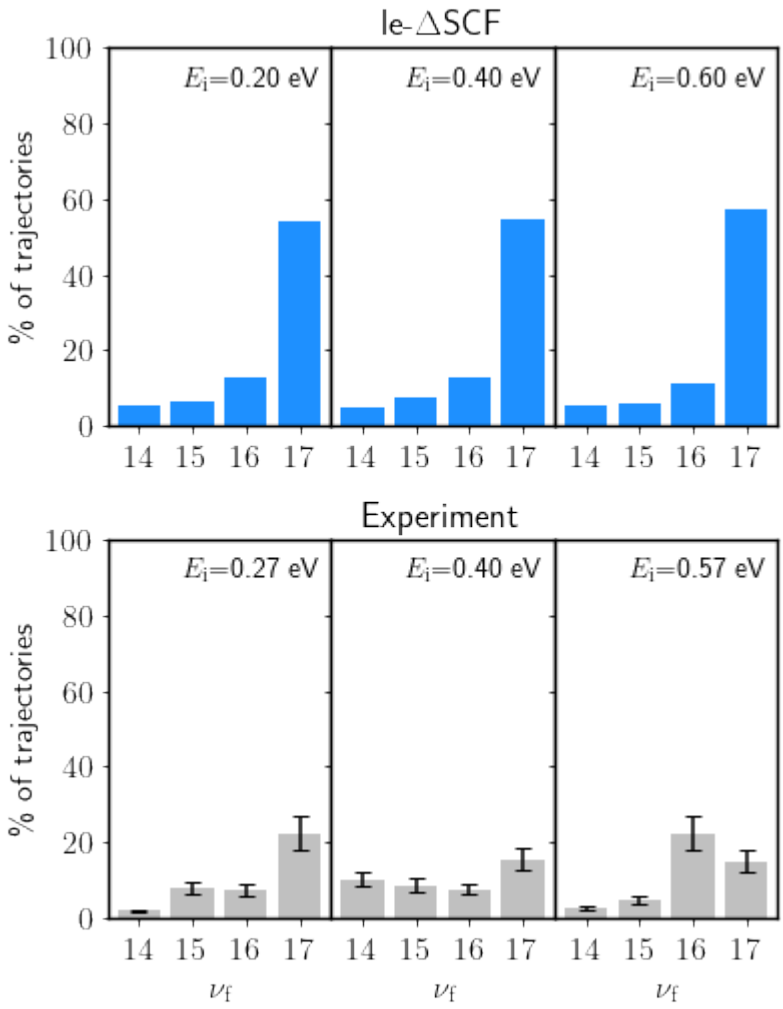

Figure 6.7: Comparison of IESH dynamics results to experiment for CO scattering from Ag(111). ν_f distributions using shifted ρle-ΔSCF PES set (blue) and experimental data (grey) from ref [74].

6.6 Vibrational inelasticity

6.6.1 Classical dynamics

The key factor during molecular beam scattering experiments that indicate nonadiabatic energy transfer has occurred is that the scattering events are vibrationally inelastic, *i.e.*, $\nu_i \neq \nu_f$. However, not all vibrationally inelastic scattering events are solely due to nonadiabatic effects. To better understand how well IESH can capture the behaviour of nonadiabatic molecular scattering, it is essential to investigate the

inelasticity seen during classical molecular dynamics, to establish a baseline that can later be used to disentangle nonadiabatic energy transfer from effects that are due to the groundstate PES. Figure 6.8 shows vibrational inelastic probability (Υ) calculated from AIMD trajectories. Υ is calculated as the ratio of trajectories where $\nu_\mathrm{i} \neq \nu_\mathrm{f}$ to the total number of trajectories (1000). For each combination of ν_i and E_i, 1000 AIMD trajectories were simulated for each of the groundstate PES from each PES set.

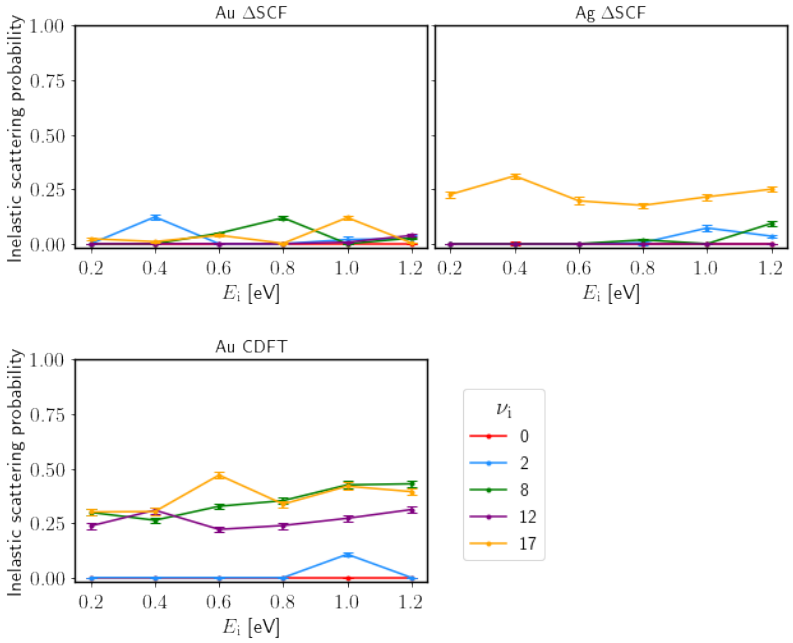

Figure 6.8: Inelastic scattering probabilities of adiabatic molecular dynamics simulations using the DFT ground state of the ρle-ΔSCF CO-Au(111) PES set (top left), ρle-ΔSCF CO-Ag(111) PES set (top right) and ML-CDFT CO-Au PES set (bottom). The ML-CDFT results show significantly more vibrational inelasticity for ν_i of 8 and above.

Figure 6.8 does not distinguish between the shifted and non-shifted ρle-ΔSCF models because only the groundstate PES is used, which remains unshifted at all times. There are some low levels of inelasticity seen in the ρle-ΔSCF results for Au but it does not vary systematically with either ν_i or E_i. The Ag scattering is mostly elastic apart from ν_i=17, which is significantly higher and Υ sits around 20-30% across the full range of E_i sampled. ML-CDFT trajectories show low Υ at ν_i = 0, 2 similar to the ρle-ΔSCF Au equivalent. However, where ν_i = 8, 12, 17 there is significantly higher Υ. Although it is the three highest ν_i that show higher Υ,

there is no systematic ordering to indicate a general rule that higher ν_i should mean higher v.

The models used to obtain the groundstate PESs associated with the ML-CDFT and ρle-ΔSCF PES sets, and their differences, are described in Table 5.1. Despite attempting to model the same physical system the groundstate PESs are distinct and it is those differences that are responsible for the differences in Υ. Figure 6.9 shows a contour plot of the difference between the ML-CDFT and ρle-ΔSCF groundstate PESs.

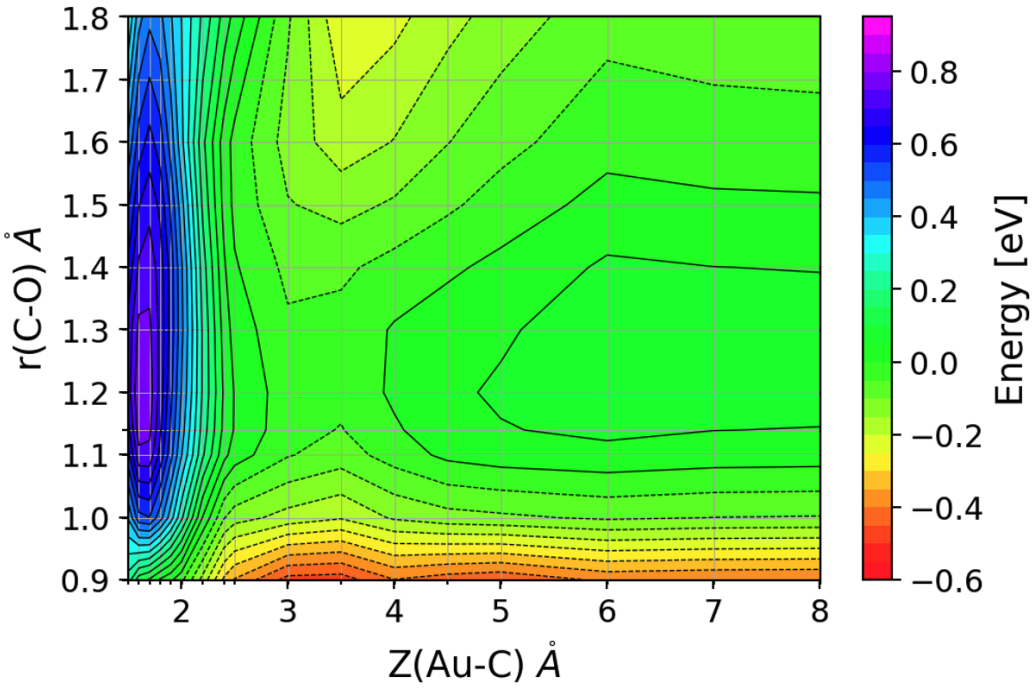

Figure 6.9: Contour plot of the difference between the groundstate PESs associated with the ML-CDFT and ρle-ΔSCF PES sets ($E_{\mathrm{CDFT}} - E_{\mathrm{le-\Delta SCF}}$) for Au.

Figure 6.9 shows that the ML-CDFT groundstate has a much steeper repulsive wall as the molecule approaches the surface. This is likely the cause of greater inelasticity a softer potential wall, as seen in the ρle-ΔSCF, is more likely to allow elastic scattering. The key point in the AIMD data is that a small amount of vibrational inelasticity seen in IESH trajectories will be due to purely adiabatic effects and that, assuming all other factors are equal, ML-CDFT IESH trajectories will contain a higher inelasticity that is independent of nonadiabatic electron hopping.

6.6.2 IESH dynamics

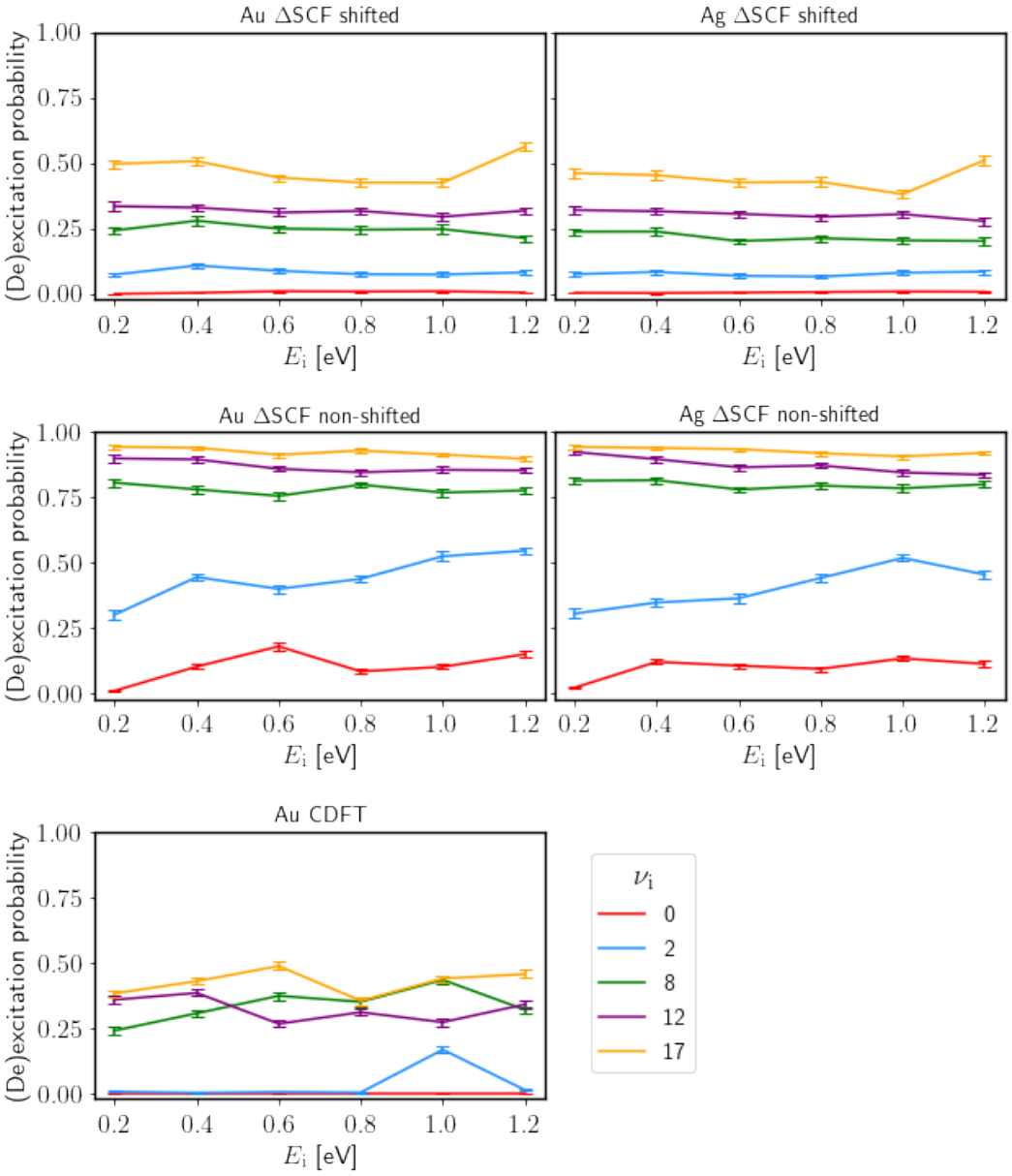

Figure 6.10: Inelastic scattering probabilities of IESH molecular dynamics simulations using shifted ρle-ΔSCF PES sets (top row), non-shifted ρle-ΔSCF PES sets (middle row) and ML-CDFT CO-Au PES set (bottom). Inelasticity for all ρle-ΔSCF PES sets is highly ordered according to ν_i. The shifted PES set see significantly more inelasticity. ML-CDFT inelasticities are similar to results seen for adiabatic dynamics.

The Υ of the ρle-ΔSCF IESH data is well ordered with respect to ν_i, but is largely independent of E_i. Where there is variation along the E_i axis, it is not a systematic increase that is expected based on experimental results [74]. There is a dramatic reduction in inelasticity when the ρle-ΔSCF surfaces are shifted, with the maximum observed inelasticity increasing by around 50%. This behaviour is expected because the shift increases the energetic cost of an electron hopping event, which is the primary factor in determining nonadiabatic energy transfer. The Υ observed in the IESH results using the ML-CDFT PES set are much less well-ordered in relation to ν_i than for the ρle-ΔSCF case. While there is still a general trend of higher ν_i producing higher inelasticity, at several points the ordering is swapped so that, for example, $\nu_\mathrm{i} = 12$ shows less inelasticity than $\nu_\mathrm{i} = 8$ at $E_\mathrm{i} = 0.6$ eV. This is due to the combination of two factors. Firstly, trajectories unfolding on the ML-CDFT groundstate PES show significant vibrationally inelastic behaviour, which is disordered with respect to ν_i, before any nonadiabatic effect are taken into account. Secondly, as discussed below in sub-section 6.7, IESH trajectories using the ML-CDFT PES set contain fewer hops than the ρle-ΔSCF equivalent, resulting in less nonadiabatic vibrational (de)excitation. This means the adiabatic inelasticity is a significant contribution to the final ML-CDFT Υ shown in Figure 6.10. In contrast, the ρle-ΔSCF Υ is low in the adiabatic trajectories and higher hopping rates in IESH mean nonadiabatic energy transfer dominates the IESH Υ; and nonadiabatic contributions to Υ are very sensitive to ν_i.

Using the same data shown in Figure 6.10, Figure6.11 compares IESH values for Υ to experimental data from [74].

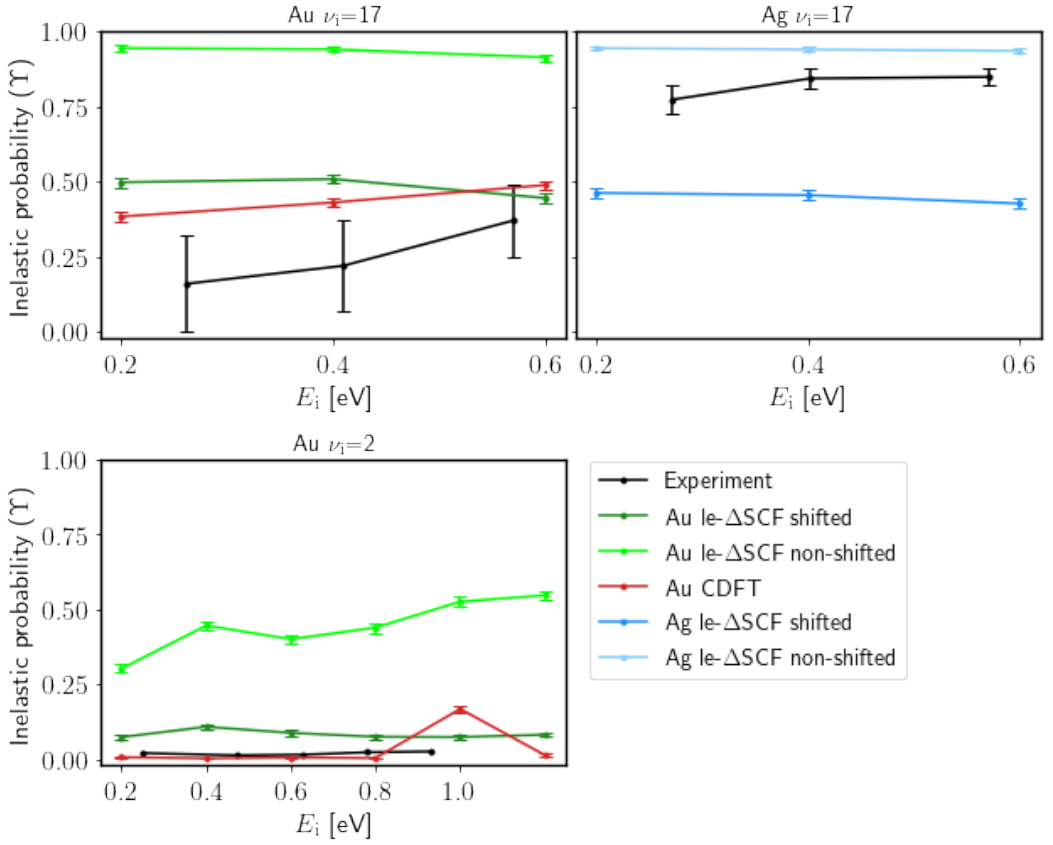

Figure 6.11: Comparison of Υ to experimentally determined data from refs [74, 117]. Results are shown for ν_i=17 using a Au(111) surface (top left) and a Ag(111) surface (top right) and ν_i=2 on a Au(111) surface (bottom left).

Where $\nu_i = 2$ and using an Au(111) surface, experiment predicts almost no inelasticity. Using both the shifted and non-shifted ρle-ΔSCF PES sets causes an overestimation of inelasticity. ML-CDFT performs better, except at $E_i = 1.0$ eV. However, fully adiabatic models are able to describe this behaviour and IESH is not required. Where $\nu_i = 17$, all PES sets significantly overestimate inelasticity. The opposite is true with respect to the Ag surface, where the shifted PES set underestimates inelasticity and the non-shifted PES set performs best, despite overestimating Υ. All error bars (not including those from experimental data) using both methods are very small, indicating that the features in the inelasticity plots are all genuine predictions of the model and are not due to statistical variation. As described above, the 2D PESs used in this work mean that meaningful comparison to experiment is limited. In order to rigorously test the methods used in this work, higher dimensional PES would need to be constructed.

6.7 Hopping probabilities

IESH attempts to account for nonadiabatic contributions to energy transfer between molecule and metal surfaces by allowing so-called electron hops to occur during the course of a dynamics trajectory. This is when an electron 'hops' from one state to another, whether that is a bath-state or an 'impurity' (molecular) state. Therefore, an important factor to consider in this work is the rate of electron hops during trajectories and how that changes based on initial conditions.

Figure 6.12 shows the number of hops per trajectory (N_H) averaged over 1000 trajectories, for a given initial condition. The difference in average N_H between the three methods (ML-CDFT, shifted and non-shifted ρle-ΔSCF) is very large. This is reflected in the y axis scales in Figure 6.12, which are shared within a row (method) but are very different between rows to make all the data visible. The difference between Ag and Au results, within a given method, is small. However, Ag does show slightly increased hopping compared to the Au at $\nu_\mathrm{i} > 8$. The non-shifted trajectories show far higher hopping rates than either the shifted ρle-ΔSCF or ML-CDFT results. Amongst the 72,000 trajectories sampled using the non-shifted method, only 12 had no hopping events. The shifted trajectories show much lower rates of hopping, but even at $\nu_\mathrm{i} = 0$ the average N_H is above 1.0 meaning a trajectory is more likely than not to contain a hopping event. Only within the ML-CDFT trajectories are hopping events rare, with the average N_H always below one.

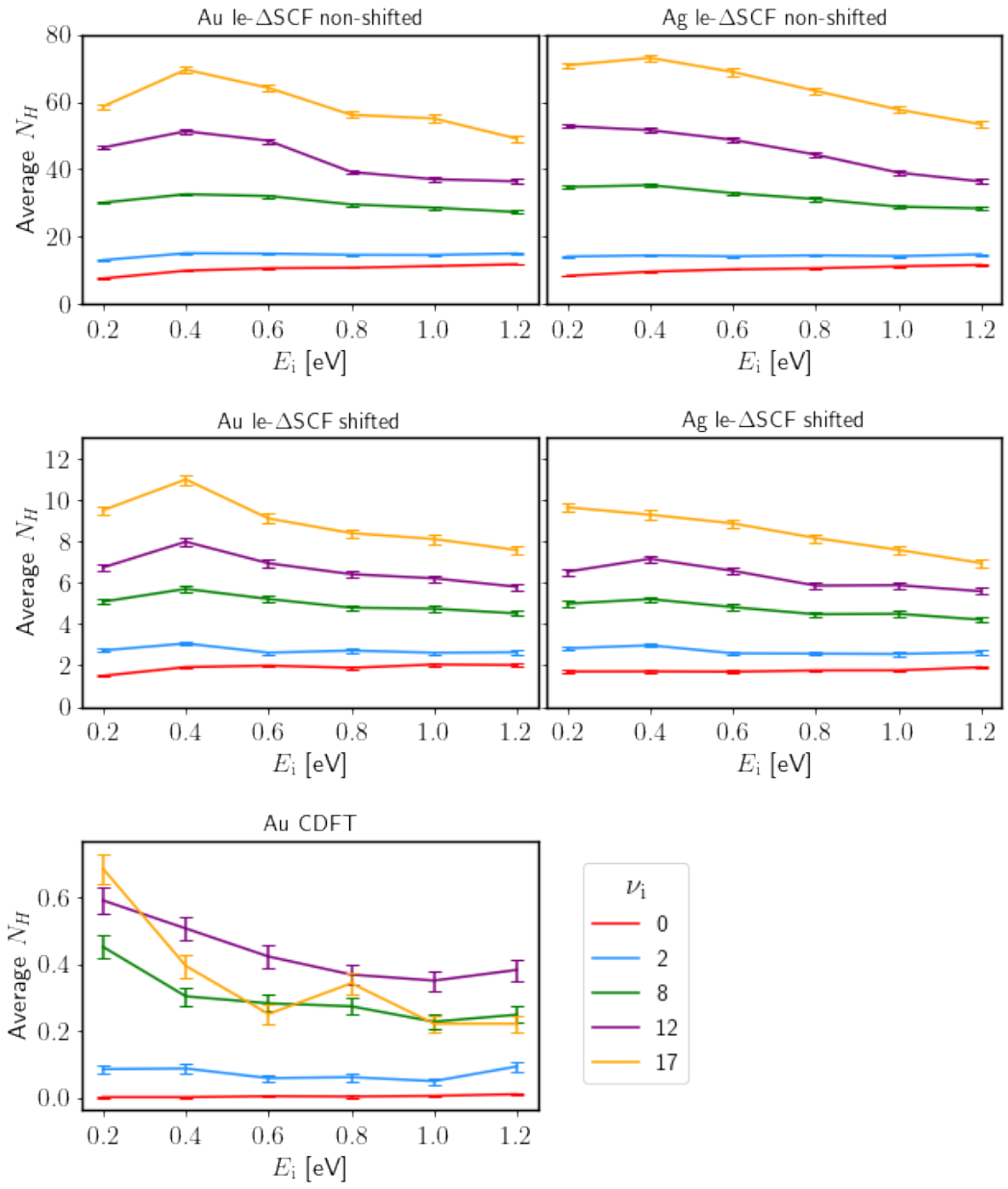

Figure 6.12: Average N_H as a function of E_i with each line representing a different ν_i. Each subplot shows data for a different PES set: non-shifted ρle-ΔSCF Au (top left) and Ag (top right), shifted ρle-ΔSCF Au (middle left) and Ag (middle right) and ML-CDFT Au (bottom). The error bars show the standard error of N_H

The pattern of inelastic probabilities being strictly ordered by ν_i in the ρle-ΔSCF data is reflected in the average N_H per trajectory. Similarly, the ML-CDFT data shows a general trend that higher ν_i causes increased hopping; however, $\nu_\mathrm{i} = 17$

violates this rule. Nevertheless, the ML-CDFT average hopping data is more well ordered than the Υ data. The presence of the same disorder in the AIMD data for ML-CDFT indicates that the disorder in Υ with respect to ν_{i} is primarily from the topology of the groundstate PES and not the IESH method. The greater hopping rates seen in the ρle-ΔSCF trajectories mean that any disorder in Υ that is present in the AIMD results is washed out in IESH trajectories and a clear ordering with respect to ν_{i} emerges. The relationship between average N_H and E_{i} is not what might be expected based on experimental observations. Although the influence of E_{i} is weak, there is an observable trend that the average N_H tends to decrease with increasing E_{i}. This may be due to the fact that the key factor determining whether a hop occurs during a given time step is the excitation energy (E_{ex}), and greater E_{i} means the molecule spends less time in the regions of the PES where E_{ex} is small.

6.8 Conclusion

Overall, the methods used in this work show some promise in replicating nonadiabatic behaviour at surfaces. The ML-CDFT PES set performed best in terms of matching experiment, despite the limitations of the 2D model used in this work [74, 117]. The ρle-ΔSCF PES set performed similarly to ML-CDFT when the surfaces are shifted. However, having to apply a rigid shift of several eV points to significant problems with this method when producing diabatic PESs. The origins of, and potential solutions to, these issues are discussed in detail in the following chapter. The similarity between the ρle-ΔSCF Au(111) and Ag(111) PES sets, and consequently the IESH dynamics results, are another indication that the method cannot capture all the physics required to model the types of nonadiabatic dynamics in this work. Nevertheless, this methodology of combining a form of (occupation) constrained DFT with IESH represents a step forward from the overly simplistic models previously used in this field. The final chapter in this thesis will discuss the outlook for the type of methodology used in this work and how it might be improved and expanded on to enable accurate simulation of nonadiabatic dynamics and metal surfaces.

Chapter 7

Conclusions and outlook

7.1 Conclusions

Modelling charge transfer states of molecules interacting with metal surfaces, in particular with a view to capture nonadiabatic effects, is an ongoing challenge to the computational chemistry community. Understanding nonadiabatic dynamics of molecules at metal surfaces is an essential step to gaining a deeper understanding of the fundamental processes that occur during heterogeneous catalysis reactions. If modelling methods become sufficiently accurate, the insights they offer can inform the design of the next generation of catalysts. The path towards progress in developing more accurate first principles models for performing nonadiabatic dynamics simulations can be broken into two complementary routes. The first is the development of methods that produce high quality and accurate PESs. The second is the development of dynamics algorithms that incorporate nonadiabatic effects, such as electronic friction or IESH dynamics [18, 85]. Improvements in both directions are needed to arrive at models that can accurately reproduce physics seen in experiment. Deficiencies in both PESs and dynamical algorithms can contribute to inaccuracies found in results.

The central goal of the work presented in this thesis has been to build on previous works by constructing high quality diabatic (anionic and neutral) PESs for systems known to display nonadiabatic physics, using the le-ΔSCF method. When the project started, the only diabatic PESs that had been used in combination with the IESH algorithm for this purpose were those developed by Roy, Shenvi and Tully using an applied electric field to enforce charge constraints for the system of NO interacting with an Au(111) surface [19]. The le-ΔSCF method was developed with the express goal of being an excited state method capable of accurately modelling

charge transfer states of molecules at metal surfaces and as such is a natural choice for constructing more accurate PESs that could improve on the previously published works [16]. The works of Roy *et al*, focused on the NO-Au(111) system because in the preceding few years several experimental works of the group of Wodtke were able to gain detailed state-to-state information of energy transferred from NO molecules scattered from an Au(111) surface which provided an ideal benchmark against which to test the method [64, 66, 118].

The NO-Au(111) system was one of the targets of the work in this thesis, but as described in Chapter 4, SCF convergence issues meant that ultimately no PESs were constructed for NO-Au(111) and the PESs used were limited to the CO-Au(111) and CO-Ag(111) systems. Fortunately, since the original works using NO, the state-to-state scattering experiments of Wodtke and coworkers have been expanded to include CO scattering from both Au(111) and Ag(111) surfaces, which offers high quality experimental data with which to compare results in this thesis [74, 117]. During the course of this project, other CO on Au(111) diabatic PESs were reported in literature by Meng and Jiang using CDFT [107]. PESs created using an EANN machine learned model that was trained using CDFT data have been included in this thesis and compared to le-ΔSCF PESs.

A secondary goal of this thesis was to use the PESs created using le-ΔSCF and ML-CDFT, in combination with IESH, to perform nonadiabatic dynamics simulations to compare and assess the differences between methods and compare to state of the art in this field, such as the various electronic friction based methods.

In Chapter 4, I assessed the ability of the le-ΔSCF method to model diabatic states CO/NO on Au(111)/Ag(111) surfaces. Both the density and wavefunction based methodologies suffer from serious convergence issues that significantly limit their ability to be used for constructing large PESs. Even a simple 1D vertical binding energy curve of anionic NO above a Au(111) surface proved unfeasible because several important geometries could not reach SCF convergence, despite sampling a wide range of density mixing parameters and modifications to model parameters. Applying the Ψle-ΔSCF method to the CO on Au(111) system saw improved convergence behaviour in the anionic state, but the neutral state could not be converged in geometries where the molecule is far from the surface. Additionally, the areas of the diabatic curves that did converge displayed incorrect physics; the anionic curve for this system had a jagged adsorption minimum, which indicated the system may be attempting to converge to two or more near degenerate SCF solutions.

An investigation into SCF convergence behaviours across a set of different molecular species on Au(111) surfaces produced a qualitative trend that conjugated

species converge far more readily than sigma bonded species, such as ethane or cyclohexane. In smaller (2–3 atom) species, convergence behaviour is highly geometry dependent, as noted above in the CO and NO cases. This explains why Maurer *et al.* did not encounter SCF convergence issues when applying Ψle-ΔSCF to Azobenzene [17, 98].

ρle-ΔSCF was shown to experience far fewer SCF convergence issues than Ψle-ΔSCF; however, difficulty in enforcing the correct spin state meant it was not possible to construct meaningful spin polarised PESs using the method. A simpler model, using ρle-ΔSCF but excluding spin polarisation, was able to reliably produce smooth and qualitative correct PESs without any significant convergence issues.

The ρle-ΔSCF results in Chapters 4 and 5 use an improved method for defining charge constraints compared to previous work in literature. Older works used integer charge constraints and assumed the molecule absorbed at the metal surface was in the same charge state as the gas phase molecule [16, 17, 44, 45]. This ignores the exchange of charge that occurs when the molecule approaches a metal surface. The methodology used in this thesis instead quantifies the charge transfer that occurs during the molecule absorption using MODOS analysis and defines constraints by adding or removing charge based on the difference between the ground-state MODOS charge and the charge state of interest.

In Chapter 5, the non-spin polarised ρle-ΔSCF method was used to construct a series of 1D potential energy curves as a function of different molecular degrees of freedom and orientations. The curves are well-behaved and physically reasonable. The neutral vertical binding energy curves are always repulsive as the molecule cannot exchange charge with the surface, as it would in the ground state. The anionic vertical binding energy curves all have deep minima due to the image charge stabilisation effect of a charged molecule approaching a metal surface. The orientational dependence of nonadiabatic vibrational inelasticity is captured by the method, which can be seen in the 1D curves as an increased excitation energy when CO is rotated away from the 'upright' C-down orientation, with the O-down orientation having the largest excitation energy. However, not all properties of the curves match expectations based on experimental observations. Explanations of the auto-detachment mechanism in literature require that the energetic ordering of neutral and anionic states change as r_{C-O} is varied when the molecule is near its equilibrium absorption height, with compressed r_{C-O} favouring the neutral state and extended r_{C-O} favouring the anion [117, 119]. This is not seen in the ρle-ΔSCF curves, where the difference in energy between the anionic and neutral states does not vary strongly with r_{C-O} and the anionic state is slightly more stable at com-

pressed r_{C-O}. A major flaw of the non-spin polarised ρle-ΔSCF model is that it underestimates the excitation energy. When the molecule is in its equilibrium bond length and far from the surface, the excitation energy should be equal to the sum of the electron affinity (E_{aff}) and the work function of the metal surface (ϕ_{surf}). The model underpredicts the excitation energy at this geometry by around 3.2–3.3 eV.

In order to perform nonadiabatic dynamics simulations, 2D PES sets of CO interacting with Ag(111) and Au(111) surfaces were constructed by varying r_{C-O} and Z_{M-C}, using the ρle-ΔSCF method. The 2D PESs are well-behaved and vary smoothly. They contain the qualitatively correct physics described for the 1D curves, but also the flaws, chiefly the underestimation of excitation energy. To address this, two additional PES sets were created in which the anionic surface has been shifted upwards in energy to match expectations of excitation energy based on the sum of E_{aff} and ϕ_{surf} at large Z_{M-C} and equilibrium r_{C-O}. A final PESs set was constructed using an EANN model trained on CDFT data of CO on Au(111) using the protocol described in [107]. This allowed a comparison of le-ΔSCF and CDFT which, at the time of writing, are the only two viable methods for creating accurate diabatic PESs of charge transfer states of a molecule interacting with a metal surface that go beyond the simple electric field method used by Roy *et al.* without resorting to prohibitively computationally intensive methods.

The primary differences between the ML-CDFT and ρle-ΔSCF PES sets are energy gaps between the lower states (ground state and diabatic neutral) and upper states (adiabatic excited and diabatic anion). The lower states in the ρle-ΔSCF model are very different from one another. The ground-state PES shows both physisorption and chemisorption wells, whereas the neutral state is only repulsive. The two become equal in energy only far from the surface. In the ML-CDFT model, the lower states are very similar to one another; the neutral state has a chemisorption minimum that should not be seen when a strictly neutral molecule approaches the surface, since it is exchange of charge that creates the well. The upper states follow a similar but subdued trend. The ρle-ΔSCF model predicts a deeper well in the anionic state than the adiabatic excited state, for both metals. The ML-CDFT model produces upper states that are almost identical to one another. As a consequence of this trend, ρle-ΔSCF predicts significantly higher diabatic coupling. The ML-CDFT model does not contain the issue of underestimation of the excitation energy and in fact ML-CDFT predicts E_{ex} that is 1.48 eV above the expected value, based on the sum of Au(111) work function and the electron affinity of CO.

In Chapter 6 the results of molecular scattering dynamics trajectories were discussed, using both the nonadiabatic dynamics algorithm IESH and standard adi-

abatic MD algorithms. Each of the 2D PES sets described in Chapter 5 were used as the underlying PESs upon which the dynamics unfolded. A large range of initial conditions were sampled, with a given initial condition consisting of a value for ν_{i} ranging from 0 to 17 and a value for E_{i} from 0.2-1.2 eV.

Adiabatic results were compared to IESH results to distinguish between adiabatic and nonadiabatic effects. Some vibrational inelasticity was seen in ν_{i} distributions of the adiabatic dynamics with ML-CDFT showing significantly higher adiabatic inelasticity compared to ρle-ΔSCF. This is attributed to the steeper repulsive wall encountered as the molecule approaches the surface in the ground-state PES associated with the ML-CDFT PES set, compared to the ρle-ΔSCF equivalent. This shows the precise nature of the DFT ground-state PES is important in determining vibrational inelasticity and that not all vibrational inelasticity seen in IESH dynamics can be attributed to nonadiabatic effects. Any study of nonadiabatic energy transfer using IESH requires simulations to be repeated using adiabatic MD to distinguish between adiabatic and nonadiabatic energy transfer.

While all AIMD trajectories saw P_{trp} of zero, IESH trajectories using both shifted and non-shifted le-ΔSCF PES sets displayed significant trapping, with the non-shifted PES set showing the highest P_{trp}. For all PES sets, higher ν_{i} is associated with higher P_{trp}. Increasing E_{i} causes a strong reduction in P_{trp}, which matches experimental data [115]. Switching from the non-shifted PES sets to the shifted PES sets maintains the general trends described above, but reduces the magnitude of P_{trp}. ML-CDFT IESH trajectories showed no trapping due to the significantly lower rates of hopping, which stems from the greater excitation energy over large regions of the PESs compared to ρle-ΔSCF PESs.

The PES set associated with the three methods: non-shifted ρle-ΔSCF, shifted ρle-ΔSCF and ML-CDFT produced different ν_{f} distributions. The low excitation energies of the non-shifted ρle-ΔSCF PES sets caused a large overestimation of inelasticity, in both the proportion of trajectories that were inelastic and also the magnitude of $\Delta\nu$. The distributions based on the Au(111) and Ag(111) PES sets produced very similar results. The shifted ρle-ΔSCF PES sets led to less vibrational inelasticity and ν_{f} distributions that are closer to experiment in the case of Au(111). Again, the Au(111) and Ag(111) shifted ρle-ΔSCF PES sets produced very similar ν_{f} distributions to one another, which does not match experiment where Ag(111) is observed to cause significantly higher inelasticity [120]. The least vibrational inelasticity was seen when using the ML-CDFT PES set, due to much lower hopping rate. The proportion of trajectories that were inelastic is similar to shifted ρle-ΔSCF; however, the magnitude of $\Delta\nu$ is smaller and most trajectories that are

vibrationally inelastic only see $\Delta\nu = \pm 1$. The ML-CDFT distributions are also the best match to experimental data, although only Au(111) data is available for ML-CDFT so it is not clear whether the trend of a good match to experiment for Au(111) and a poor match for Ag(111), seen in shifted ρle-ΔSCF, would be repeated for ML-CDFT.

The dominant factor in determining nonadiabatic vibrational inelasticity is ν_i, with higher ν_i leading to a greater probability of a trajectory being vibrationally inelastic, which matches experimentally observed trends [74]. All vibrational inelastic probability (Υ) results, using either shifted or non-shifted le-ΔSCF PES sets, were highly ordered with respect to ν_i. While Υ using the ML-CDFT PES set are mostly ordered according to ν_i, the ordering is not strictly adhered to. This is due to the combination of greater adiabatic vibrational inelasticity and lower rate of hopping when using the ML-CDFT PES set. The value of E_i, in contrast, has almost no effect upon vibrational inelasticity and any variation is not systematic. This is in stark contrast to experimental evidence, where E_i is known to be an important predictor of vibrational inelasticity. The invariance of Υ with respect to E_i was seen for all PES sets used in this work and so is likely a flaw in the IESH method; however, the dynamics trajectories in this thesis have been limited to a 2D model so including more molecular and substrate DOF may impact this trend.

In summary, the work presented in this thesis has assessed the le-ΔSCF method's ability to model charge transfer states of NO and CO interacting with Au(111) and Ag(111) surfaces. A new protocol for defining constraints that takes into account ground-state charge transfer between molecule and metal has been developed and implemented. The Ψle-ΔSCF and ρle-ΔSCF methodologies have been compared and the latter was used to construct 2D diabatic PES for CO interacting with Au(111) and Ag(111) surfaces. The PESs were used in nonadiabatic dynamics simulations, using the IESH method, to model nonadiabatic vibrational inelasticity observed in state-to-state molecular beam scattering experiments. In the case of CO-Au(111), an equivalent set of PESs were constructed based on ML-CDFT energies, and nonadiabatic dynamics simulations were performed. A comparison between the ρle-ΔSCF and ML-CDFT dynamics results show both were able to qualitatively reproduce experimental results for the CO-Au(111) system although a vertical shift in energy had to be applied to the ρle-ΔSCF anionic PES in order to achieve this outcome.

7.2 Outlook and future work

The work presented in this thesis shows that the ρle-ΔSCF method can be used to model diabatic states and construct PESs that can be used, in combination with IESH, to model nonadiabatic energy transfer of CO interacting with Au(111) and Ag(111) surfaces. However, there is significant room for an expansion of the work and improvements to the method more generally.

The model PESs constructed in this work only had two DOF: molecule surface distance ($Z_{\mathrm{M-C}}$) and CO bond length ($r_{\mathrm{C-O}}$). Adding additional DOF would improve the model and allow for a more meaningful comparison to experiment. Firstly, molecular translations in x and y directions would allow the molecule to interact with different absorption sites on the metal surface. The 1D vertical binding energy curves in Chapter 4 show that the absorption well depth and position of the minima (in the z direction) differ between the top site included in the 2D model and the HCP site, and as such would affect the dynamics. Secondly, molecular rotations would allow both the orientational dependence of vibrational elasticity and the dynamical steering effects that have been observed in nonadiabatic molecular scattering experiments and simulations to be accounted for [86]. Finally, substrate motion was shown in the works of Roy *et al.* to significantly affect the trapping probabilities and vibrational inelasticity and so substrate DOF should also ideally be included in future models [18]. The expansion of the number of DOF any model includes can be achieved without any changes to the current ρle-ΔSCF method used in this work. Of course, including more DOF will greatly increase the number of single point calculations required to generate a PES and a balance must be struck between sampling as many points as possible and computational cost. This balance would best be achieved by training a machine learning model to predict the 2×2 diabatic Hamiltonian, using ρle-ΔSCF diabatic state calculations of AIMD molecular scattering trajectories.

The biggest flaw in the ρle-ΔSCF model used to construct PESs in this thesis is the significant underestimation of the excitation energy. As a simple but incomplete solution, the anionic PES was shifted upwards in energy to match expected excitation energies far from the surface. The non-shifted PES sets performed far worse than the shifted versions, by overestimating vibrational inelasticity. This shows the shifting of the surface was a sensible choice; however, it does not address the underlying cause of the underestimation of excitation energy. Figure 7.1 compares vertical binding energy curves for the neutral and anionic diabatic state with and without spin polarisation for CO above a top site of 2×2 4-layer Au(111)

slab. The diabatic states of spin polarised and non-spin polarised systems are quite different. When spin is included, the neutral curve has a steeper repulsive wall and the position of the anionic minimum is significantly higher in energy and further from the surface. While shifting the anionic curve up in energy brings the non-spin polarised system more in line with the spin polarised system, it clearly is not enough to make the systems match. Although spin-polarised anionic calculations with CO beyond 3 Å from the surface could not be converged, based on the partial curve in Figure 7.1, it is reasonable to assume the curve would plateau around 6–7 eV. This would match the expected excitation energy, based on the assumption that far from the surface the energetic cost of removing an electron from the Fermi level and attaching it to the molecule is the sum of the ϕ_{surf} and E_{aff}: 6.34 eV. The tendency of the non-spin polarised calculations to underestimate the excitation energy can be explained by consideration of Janak's theorem and the work of Perdew and Levy [121, 122]. The energy of an orbital in DFT varies smoothly as its occupation is increased, which is unlike a true orbital, which should be piecewise linear with respect to integer occupation. In the spin-polarised model, a constraint that enforces that a molecular charge of -1.0 corresponds to the full occupation of a resonance orbital, and therefore a greater energy than if it were partially occupied. However, when spatial orbitals are used, moving one electron into such an orbital would only half occupy that orbital and it would not be as high in energy.

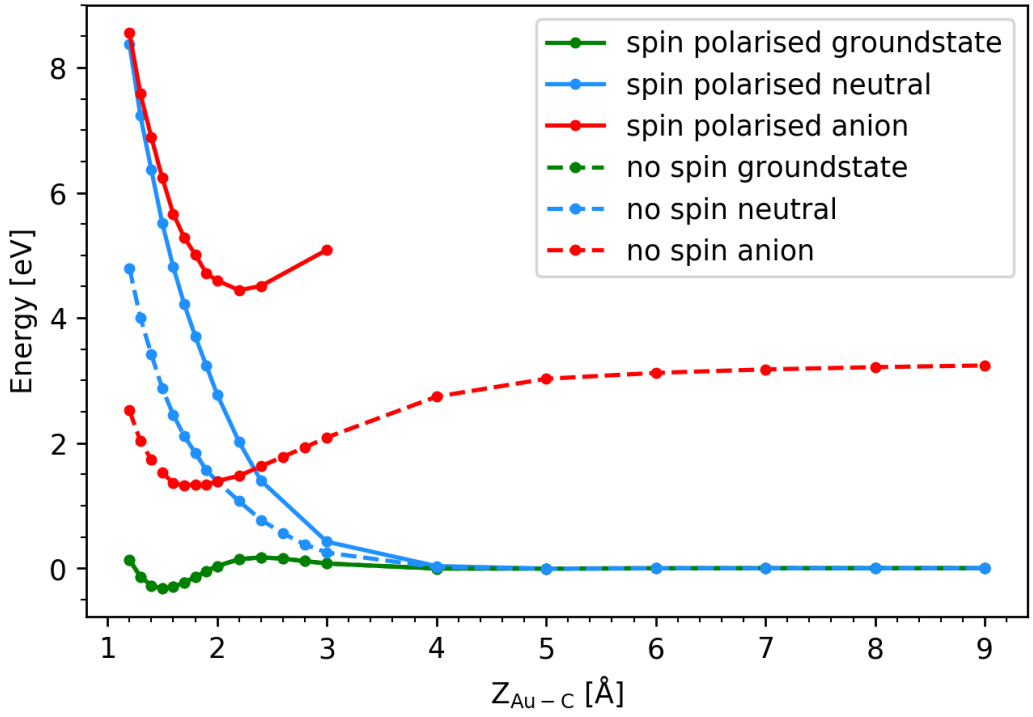

Figure 7.1: Comparison of spin polarised and non-spin polarised binding energy curves of CO above a 2×2 4 layer Au(111) slab, using ρle-ΔSCF.

The reason that a non-spin polarised model had to be used in the construction of PESs for this thesis was the difficulty in converging the SCF process of spin polarised ρle-ΔSCF calculations. It is also the reason the use of NO as the molecular species was abandoned. SCF convergence issues have been by far the single biggest hindrance to the progress of the work in this thesis. Despite trialing a large range of density mixing parameters and many modifications to the model and constraints, it was not feasible to converge diabatic state calculations at enough different geometries to construct PESs that could be used for dynamics. Both the ρle-ΔSCF and Ψle-ΔSCF formalisms suffer from difficulty in reaching convergence, although the issue is more prevalent in Ψle-ΔSCF. Chapter 4 showed the results of anionic test calculations on a range of molecular species on an Au(111) surface, which indicates that calculations involving conjugated molecules converge much more readily than smaller, sigma bonded, species. This observation fits with previous work by Maurer [17, 45]. While modelling charge transfer states of conjugated molecules on metal surfaces is useful in many cases, being restricted to such systems is a huge limitation on the applicability of le-ΔSCF. Clearly, overcoming the chronic SCF

convergence issues of le-ΔSCF is something that would greatly increase the ability of the method to be applied to not just the diatomic nonadiabtic energy transfer systems that are the focus of this thesis but many other important charge transfer systems in chemistry and physics.

Moving away from the density mixing method of energy minimisation and instead implementing an ensemble DFT (EDFT) based approach is a viable route to reducing the convergence issues [123]. Within the density mixing formalism, the KS wavefunctions are constructed from the density of the current SCF cycle. The density of the next SCF cycle is constructed by combing the newest density with densities from previous steps, according to the density mixing parameters, to arrive at a new estimate of the ground-state density. There is no guarantee that the total energy from one SCF cycle to the next will be reduced. Typically variation of the density mixing parameters is sufficient to achieve convergence; however, this is not always the case. EDFT, in contrast, does not mix densities at all. Instead, the density is always constructed directly from the current estimate of the KS wavefunctions. Each update to the KS wavefunctions can only proceed if it lowers the total energy, and thus is a much more robust method of minimising energy compared to density mixing. CASTEP (the code in which Ψle-ΔSCF is implemented) already has an EDFT minimisation implementation for DFT groundstate calculations, which makes it a sensible choice for any future work which seeks to combine the EDFT minimisation algorithm with le-ΔSCF [124].

Another area in which improvements to the le-ΔSCF method can be made relates to the molecular reference state used to construct the resonance orbital, to which constraints are applied. In order to construct resonance orbitals, a molecular reference system calculation is required. Conceptually, this simply means the gas phase molecular orbitals; for example, consider the case of modelling a charge transfer state in which a molecular anion is absorbed on a metal surface: a resonance orbital based on the gas phase molecular LUMO should be constrained to have one electron in it. Additionally, a resonance orbital based on the gas phase molecular LUMO+1 may be included and constrained to be empty, to avoid any additional charge from the surface being transferred to the molecule. However, in practice those gas phase molecular orbitals are free-standing molecular over-layer (FSMO) orbitals, made by deleting the metal atoms from the full system unit cell and running a ground-state calculation, *i.e.*, using the same **k**-point sampling and unit cell as the full molecule-metal system. The use of FSMO orbitals, apart from not being true gas phase orbitals, create issues with unbound states. An unbound state is one that has a positive eigenvalue, meaning it is not energetically favorable

for an electron to occupy the state. Unbound orbitals are also highly delocalised, meaning that applying a constraint to a resonance orbital based on an unbound orbital does not correspond to constraining charge to the molecule. Even without a unit cell, virtual orbitals are often poorly represented in molecular calculations because semi-local functionals predict fewer bound states than are present in the real system. Using a unit cell further increases the tendency of virtual orbitals to be unbound. Which orbitals are bound and unbound is a function of the molecular geometry. For example, a state that is strongly bound when bond lengths are set at their equilibrium lengths may become unbound upon elongation (or compression) of the bond, which means enforcing a set of constraints in a consistent set of states over a large range of geometries is not always possible. There are two steps that can be taken towards solving this issue. Firstly, implementing the le-ΔSCF method in a code that does not use basis sets that require a unit-cell, for example the numerical atomic orbitals used in the FHI-Aims electronic structure package would reduce the tendency for states to be unbound [125]. Secondly, moving beyond the GGA level of XC functional, for example by using hybrid functionals, will further reduce the prevalence of unbound states. The use of hybrid functionals would increase the cost of calculations considerably, but with the increase in availability of machine learning techniques to construct accurate models, far fewer data points are needed compared to explicitly calculated PESs

Even in cases where the target orbitals are fully bound, the orbitals tend to be very diffuse, which means the molecular orbital protrudes into a region that has high metal electron density in the full system when the molecule is close to the surface and a greater repulsion is seen that would be in the real system if charge is constrained to this orbital. This effect might be reduced by introducing some form of influence in the molecular (FSMO) system that represents the influence of the metal slab and would modify the shape of the molecular orbital, without the hybridisation of those orbitals that would result from the explicit inclusion of the metal states.

Le-ΔSCF is one way to model charge transfer at metal surfaces, but it is not the only potentially viable method. There is currently no consensus regarding the best method to produce accurate PESs of excited states at metal surfaces that can be used for nonadiabatic dynamics simulations. One example of another potentially very useful method is constrained DFT, as described in this thesis [107]. However, considerable work has gone into developing modifications to the traditional CDFT method, such as orthogonality constrained DFT and transition-based Constrained DFT [126, 127]. Another promising area that has seen recent developments is em-

bedded wavefunction methods [128], in which a high level correlated wavefunction method is used to model a cluster that is embedded into a DFT model of a metal surface. Much more work is required to determine the best methods for modelling nonadiabatic charge transfer at metal surfaces, and the work presented in this thesis is step in the long journey towards being able to reliably reproduce the nonadiabatic effects seen in nature.

Appendix A

Running ρle-ΔSCF calculations

The following section will describe a protocol for running a ρle-ΔSCF calculation, with example scripts used during the construction of PESs described in Chapter 5.

The first step is to run ordinary DFT ground state calculations in GPAW of the full molecule metal system and the FSMO and then write the wavefunctions to .gpw files. Listing A.1 below shows an example script that does this:

```
from gpaw import GPAW, restart
from gpaw.mixer import MixerSum
import gpaw.dscf as dscf
from gpaw.analyse.hirshfeld import HirshfeldPartitioning
from gpaw.analyse.vdwradii import vdWradii
from ase.calculators.vdwcorrection import vdWTkatchenko09prl
from ase.io import read, write
from ase.units import Bohr
import sys

def make_gas_ref(atoms_obj):
    """Make a FSMO Atoms object from the full system Atoms object"""
    gas_ref = atoms_obj.copy()
    mask = [atom.index for atom in gas_ref if atom.symbol not in ['Au'
    , 'Ag', 'Pt', 'Cu']]
    return gas_ref[mask]

def get_mol_indicies(atoms_obj):
    """make a list of the molecular indicies of the full system"""
    mol_indicies =  [atom.index for atom in atoms_obj if atom.symbol
    not in ['Au', 'Ag', 'Pt', 'Cu']]
    return mol_indicies

#Make sure path to system geometry file is given as command line
    argument
```

```
23 if len(sys.argv) != 2:
24     raise ValueError('path to input geometry should be given as a
       command line argument')
25
26 ####### Get the full system geometry ############
27 geom_file = sys.argv[1]
28
29 # Settings for 'gasphase' FSMO DFT groundstate calculation
30 gascalc = GPAW(nbands=7,
31                h=0.2,
32                mode='fd',
33                xc='RPBE',
34                kpts=(8, 8, 1),
35                spinpol=False,
36                convergence={'bands': 7},
37                poissonsolver={'dipolelayer': 'xy'},
38                txt='gasphase.txt')
39
40 # Settings for full-system DFT groundstate calculation
41 gscalc = GPAW(h=0.2,
42               nbands=500,
43               xc='RPBE',
44               kpts=(8, 8, 1),
45               eigensolver='cg',
46               spinpol=False,
47 #              mixer=MixerSum(nmaxold=5, beta=0.05, weight=50),
48               poissonsolver={'dipolelayer': 'xy'},
49               txt='gs.txt')
50
51 # Make Atoms object from geometry file
52 slab = read(geom_file)
53 slab.pbc = [True, True, False]
54
55 # run molecule calculation
56 molecule = make_gas_ref(slab)
57 molecule.calc = gascalc
58 molecule.get_potential_energy()
59
60 ## vdw correction##
61 cc = vdWTkatchenko09prl(HirshfeldPartitioning(gascalc),vdWradii(
       molecule.get_chemical_symbols(),
62      'RPBE'), vdWDB_alphaC6={'Au': [134, 15.6], 'Ag': [122,15.4], 'N':
       [7.4, 24.2], 'O': [5.4, 15.6], 'C': [12, 46.6], 'H': [4.5, 6.5]})
63 molecule.calc = cc
64 molecule.get_potential_energy()
65
```

```
# write density and wavefunctions
mol_den = gascalc.get_all_electron_density()
write('molden.cube', molecule, data=mol_den)
gascalc.write('molecule.gpw', mode='all')

##################  full system  calculation ##############
slab.calc = gscalc
slab.get_potential_energy()

## vdW correction ##
vdwrads = []
for atom in slab:
    if atom.symbol == 'Au':
        vdwrads.append(2.91)
    else:
        vdwrads.append(vdWradii([atom.symbol], 'RPBE')[0])

cc = vdWTkatchenko09prl(HirshfeldPartitioning(gscalc),
                        vdWradii(slab.get_chemical_symbols(),'PBE'),
                        vdWDB_alphaC6={'Au': [134, 15.6],
                                       'Ag': [122, 15.4],
                                       'N' : [7.4, 24.2],
                                       'O' : [5.4, 15.6],
                                       'C' : [12., 46.6],
                                       'H' : [4.5, 6.5]}
                       )
slab.calc = cc
slab.get_potential_energy()

### write density and wavefunctions  ####
den = gscalc.get_all_electron_density()
write('gs.cube', slab, data=den * Bohr**3)
gscalc.write('gs.gpw', mode='all')
```

Listing A.1: A python script to run DFT ground-state calculations, using GPAW, for a full CO on Au(111) system and the corrisponding CO FSMO. The script writes the final wavefunctions to files, which are required to perform ρle-ΔSCF calculations.

The second step is to use the wavefunction files to perform MODOS analysis. An an example script is shown in Listing A.2.

```
from gpaw import GPAW, restart
import gpaw.dscf as dscf
from ase.io import read, write
import sys

def get_mol_indicies(atoms_obj):
```

```
    """ make a list of the molecular indicies of the full system"""
    mol_indicies =  [atom.index for atom in atoms_obj if atom.symbol
    not in ['Au', 'Ag', 'Pt', 'Cu']]
    return mol_indicies

#read in wavefunctions from completed calculations
slab, gscalc = restart('gs.gpw', txt=None)
molecule, gascalc = restart('molecule.gpw', txt=None)

#####  perform MODOS analysis ######

# full system density of States
fullsys_e, fullsys_dos = gscalc.get_dos(spin=0, npts=3001, width=0.1)
# Shift energies so that Fermi energy sits a zero
e_f = gscalc.get_fermi_level()
fullsys_e = fullsys_e - e_f

#Write the total DOS
with open('TotalDOS_gs.dat', 'w') as f:
    for i,j in zip(fullsys_e,fullsys_dos):
        f.write('{},{} \n'.format(i,j))

## MO projected dos
mol = get_mol_indicies(slab)
# Calculate MODOS for selected states and write to files
for n in range(3, 8):
    # PDOS on the band n and spin s
    wf_k = [kpt.psit_nG[n] for kpt in gascalc.wfs.kpt_u]
    P_aui = [[kpt.P_ani[a][n] for kpt in gascalc.wfs.kpt_u]
             for a in range(len(molecule))]
    e, dos = gscalc.get_all_electron_ldos(mol=mol, spin=0, npts=3001,
                                          width=0.1, wf_k=wf_k, P_aui=
    P_aui)
    corr_e = e - e_f
    with open('MODOS_CO_gs_{}_{}.dat'.format(n,0), 'w') as f:
        for i,j in zip(corr_e, dos):
            f.write('{},{} \n'.format(i,j))
```

Listing A.2: Example script to perform MODOS analysis for FSMO states 3–8, using wavefunctions output by Listing A.1

The MODOS data should be integrated up to the Fermi level to obtain the MODOS occupations for each FSMO state, and the difference between the MODOS occupations and the ideal occupations of the neutral and anionic systems then used to define constraints. The script shown in Listing A.3 does this and writes input

files for the ρle-ΔSCF calculations.

```
import numpy as np

def intergrate_MODOS(modos_file):
    # Read in MODOS file for a given state and integrate up to the Fermi level
    occ = 0.0
    modos = np.genfromtxt(modos_file, delimiter=',')
    de = modos[0][0] - modos[1][0]
    for i in modos:
        if i[0] < 0:
            occ += de * i[1]
        else:
            pass

    return(occ * -1)

def prep_excited_states(directory, states=[4,5,6]):
    """This function takes a path to a diectory, which should contain MODOS files, and creates inputs for neutral and anionic charge states"""

    #Idialised state charges for neutral and anion.
    charge_states = ['neutral', 'anion']
    if len(states) == 3:
        ideal_neu_occs = (1.0, 0.0, 0.0)
        ideal_an_occs = (1.0, 0.25, 0.25)
    elif len(states) == 2:
        ideal_neu_occs = (0.0, 0.0)
        ideal_an_occs = (0.25, 0.25)

    #Container for MODOS ocupations, fill by inntegrating MODOS
    modos_occs = {}

    for state in states:
        modos_occs = [intergrate_MODOS('{}/MODOS_CO_gs_{}_0.dat'.format(directory, state)) for state in states]

    # use occupations to define neutral charge constraints
    neu_cons = []
    for ideal_occ, real_occ in zip(ideal_neu_occs, modos_occs):
        neu_cons.append(ideal_occ - real_occ)
    rounded_neu_cons = ['{:.2f}'.format(con) for con in neu_cons]
    neu_subspace = []
    for con in neu_cons:
```

```
        if con < 0.0:
            neu_subspace.append('occ_res')
        elif con >= 0.0:
            neu_subspace.append('unocc_res')

    if len(states) == 3:
        neu_con_string = 'dscf.dscf_calculation(neucalc, [[{}, {}4,
    0],[{}, {}5, 0],[{}, {}6,0]], slab)\n'.format(
        rounded_neu_cons[0], neu_subspace[0], rounded_neu_cons[1],
    neu_subspace[1], rounded_neu_cons[2], neu_subspace[2])

    elif len(states) == 2:
        neu_con_string = 'dscf.dscf_calculation(neucalc, [[{}, {}5,
    0],[{}, {}6,0]], slab)\n'.format(
        rounded_neu_cons[0], neu_subspace[0], rounded_neu_cons[1],
    neu_subspace[1])

    # read in a default excited state python script with blank
    constraints
    with open('/storage/chem/msrtzm/main_project/PBE+vdW_surf/GPAW/CO/
    Ag/defaults/COneutral.py', 'r') as f:
        neu_lines = f.readlines()
    # Write new xcited state python script including constraints
    with open('{}/COneutral.py'.format(directory), 'w') as g:
        for line in neu_lines:
            if 'dscf.dscf_calculation' in line:
                g.write(neu_con_string)
            else:
                g.write(line)

    # use occupations to define anion charge constraints
    an_cons = []
    for ideal_occ, real_occ in zip(ideal_an_occs, modos_occs):
        an_cons.append(ideal_occ - real_occ)
    rounded_an_cons = ['{:.2f}'.format(con) for con in an_cons]

    # select appropriate subspace for construction of resonance orbial
     (occ vs unocc)
    an_subspace = []
    for con in an_cons:
        if con < 0.0:
            an_subspace.append('occ_res')
        elif con >= 0.0:
            an_subspace.append('unocc_res')

    # defonce constraints for anion calcuation
```

```
    if len(states) == 3:
        an_con_string = 'dscf.dscf_calculation(ancalc, [[{}, {}4,
    0],[{}, {}5, 0],[{}, {}6,0]], slab)\n'.format(
        rounded_an_cons[0], an_subspace[0], rounded_an_cons[1],
    an_subspace[1], rounded_an_cons[2], an_subspace[2])

    elif len(states) == 2:
        an_con_string = 'dscf.dscf_calculation(ancalc, [[{}, {}5,
    0],[{}, {}6,0]], slab)\n'.format(
        rounded_an_cons[0], an_subspace[0], rounded_an_cons[1],
    an_subspace[1])

    # read in a default annion excited state python script with blank
    constraints
    with open('/storage/chem/msrtzm/main_project/PBE+vdW_surf/GPAW/CO/
    Ag/defaults/COanion.py', 'r') as f:
        an_lines = f.readlines()

    # Write new xcited state python script including constraints
    with open('{}/COanion.py'.format(directory), 'w') as g:
        for line in an_lines:
            if 'dscf.dscf_calculation' in line:
                g.write(an_con_string)
            else:
                g.write(line)

prep_excited_states('./', states=[4,5,6])
```

Listing A.3: A script that integrates MODOS data and uses it to define constraints for neutral and anionic ρle-ΔSCF calculations. The script then writes two python files: COanion.py and COneutral.py, which run will run the exciited state calculatioins when executed.

An example of an script that will perform a anionic ρle-ΔSCF calculation and that was prepared using the script in Listing A.3 is shown in Listing A.4.

```
from numpy import reshape, dot
from gpaw import GPAW, restart, Davidson
from gpaw.mixer import MixerSum
import gpaw.dscf as dscf
from gpaw.analyse.hirshfeld import HirshfeldPartitioning
from gpaw.analyse.vdwradii import vdWradii
from ase.calculators.vdwcorrection import vdWTkatchenko09prl
from ase.io import read, write
from ase.units import Bohr
import sys
```

```
11
12 def make_gas_ref(atoms_obj):
13     """Make a FSMO Atoms object from the full system Atoms object"""
14     gas_ref = atoms_obj.copy()
15     mask = [atom.index for atom in gas_ref if atom.symbol not in ['Au'
       , 'Ag', 'Pt', 'Cu']]
16     return gas_ref[mask]
17
18 def get_mol_indicies(atoms_obj):
19     """make a list of the molecular indicies of the full system"""
20     mol_indicies =  [atom.index for atom in atoms_obj if atom.symbol
       not in ['Au', 'Ag', 'Pt', 'Cu']]
21     return mol_indicies
22
23 #Make sure path to system geometry file is given as command line
       argument
24 if len(sys.argv) != 2:
25     raise ValueError('path to input geometry should be given as a
       command line argument')
26
27 # Get the full system geometry
28 geom_file = sys.argv[1]
29
30 # settings and parameters for GPAW calculations
31 ancalc = GPAW(h=0.2,
32               nbands=500,
33               xc='RPBE',
34               kpts=(8, 8, 1),
35               eigensolver=Davidson(5),
36               spinpol=False,
37               poissonsolver={'dipolelayer': 'xy'},
38               txt='anion.txt')
39
40 slab = read(geom_file)
41 slab.pbc = [True, True, False]
42 slab.calc = ancalc
43
44 # read molecule data
45 molecule, gascalc = restart('molecule.gpw', txt=None)
46
47 ############## Setting up the for le-deltascf ################
48
49 # collect pseudowavefunctions and projector overlaps.
50 # required for all electron wavefunctions
51
52 mol = get_mol_indicies(slab)
```

```
53
54 wf_u_4 = [kpt.psit_nG[4] for kpt in gascalc.wfs.kpt_u]
55 p_uai_4 = [dict([(mol[a], P_ni[4]) for a, P_ni in kpt.P_ani.items()])
56          for kpt in gascalc.wfs.kpt_u]
57
58 wf_u_5 = [kpt.psit_nG[5] for kpt in gascalc.wfs.kpt_u]
59 p_uai_5 = [dict([(mol[a], P_ni[5]) for a, P_ni in kpt.P_ani.items()])
60          for kpt in gascalc.wfs.kpt_u]
61
62 wf_u_6 = [kpt.psit_nG[6] for kpt in gascalc.wfs.kpt_u]
63 p_uai_6 = [dict([(mol[a], P_ni[6]) for a, P_ni in kpt.P_ani.items()])
64          for kpt in gascalc.wfs.kpt_u]
65
66 wf_u_7 = [kpt.psit_nG[7] for kpt in gascalc.wfs.kpt_u]
67 p_uai_7 = [dict([(mol[a], P_ni[7]) for a, P_ni in kpt.P_ani.items()])
68          for kpt in gascalc.wfs.kpt_u]
69
70 # Making the resonance orbitals using occupied states
71 occ_res4 = dscf.AEOrbital(ancalc, wf_u_4, p_uai_4, Estart=-100.0, Eend
       =0.0)
72 occ_res5 = dscf.AEOrbital(ancalc, wf_u_5, p_uai_5, Estart=-100.0, Eend
       =0.0)
73 occ_res6 = dscf.AEOrbital(ancalc, wf_u_6, p_uai_6, Estart=-100.0, Eend
       =0.0)
74 occ_res7 = dscf.AEOrbital(ancalc, wf_u_7, p_uai_7, Estart=-100.0, Eend
       =0.0)
75
76 # Making the resonance orbitals using unnoccupied states
77 unocc_res4 = dscf.AEOrbital(ancalc, wf_u_4, p_uai_4, Estart=0.0, Eend
       =100)
78 unocc_res5 = dscf.AEOrbital(ancalc, wf_u_5, p_uai_5, Estart=0.0, Eend
       =100)
79 unocc_res6 = dscf.AEOrbital(ancalc, wf_u_6, p_uai_6, Estart=0.0, Eend
       =100)
80 unocc_res7 = dscf.AEOrbital(ancalc, wf_u_7, p_uai_7, Estart=0.0, Eend
       =100)
81
82 #Run le-DSCF excited state calculation
83 dscf.dscf_calculation(ancalc, [[0.05, unocc_res4, 0],[-0.10, occ_res5,
       0],[-0.10, occ_res6,0]], slab)
84 slab.calc = ancalc
85 slab.get_potential_energy()
86
87 ### write density and wavefunctions  ####
88 den = ancalc.get_all_electron_density()
89 write('anion.cube', slab, data=den * Bohr**3)
```

```
#ancalc.write('anion.gpw', mode='all')

## vdW correction ##
vdwrads = []
for atom in slab:
    if atom.symbol == 'Ag':
        vdwrads.append(2.57)
    elif atom.symbol == 'Au':
        vdwrads.append(2.91)
    else:
        vdwrads.append(vdWradii([atom.symbol], 'RPBE')[0])

cc = vdWTkatchenko09prl(HirshfeldPartitioning(ancalc),
                        #vdWradii(slab.get_chemical_symbols(),'RPBE'),
                        vdwrads,
                        vdWDB_alphaC6={'Au': [15.6, 134],
                                       'Ag': [15.4, 122],
                                       'N' : [7.4, 24.2],
                                       'O' : [5.4, 15.6],
                                       'C' : [12., 46.6],
                                       'H' : [4.5, 6.5]}
                       )
slab.calc = cc
slab.get_potential_energy()
```

Listing A.4: A python script, output by Listing A.3, that will perform an anionic ρle-ΔSCF calculation

Appendix B

Final vibrational state distributions

In Chapter 6, an illustrative selection of final vibrational state (ν_f) distributions were shown. However, ν_f distributions were calculated for all PES sets using both adiabatic (AIMD) and IESH dynamics. All ν_f distributions are shown below.

B.1 ρle-ΔSCF CO-Au(111)

B.1.1 IESH dynamics using Non-shifted PES

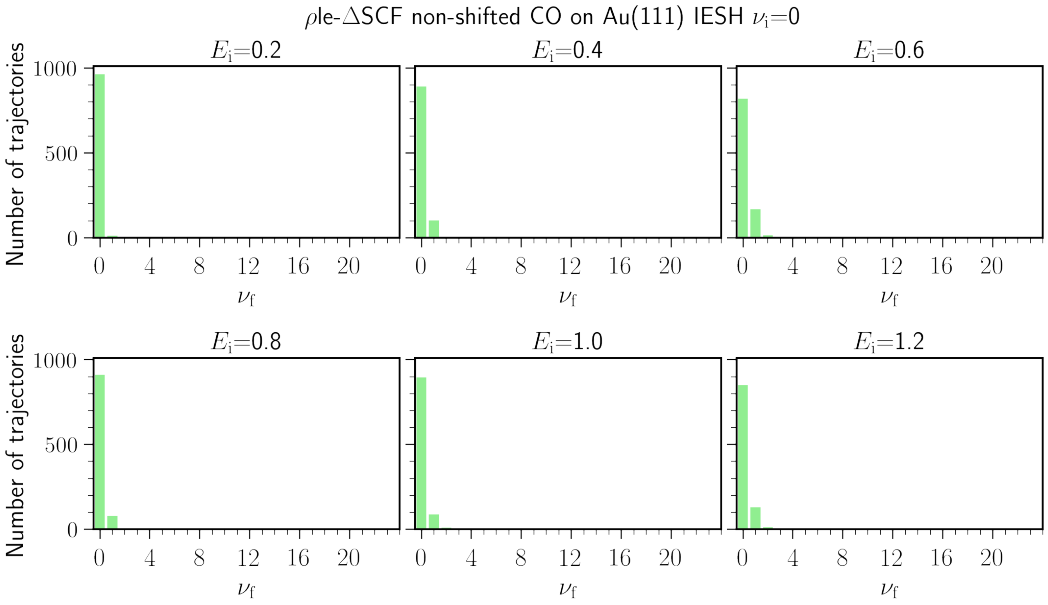

Figure B.1: IESH final state distributions for the non-shifted ρle-ΔSCF CO-Au PES set where $\nu_i = 0$. The value of E_i is indicated at the top of each subplot

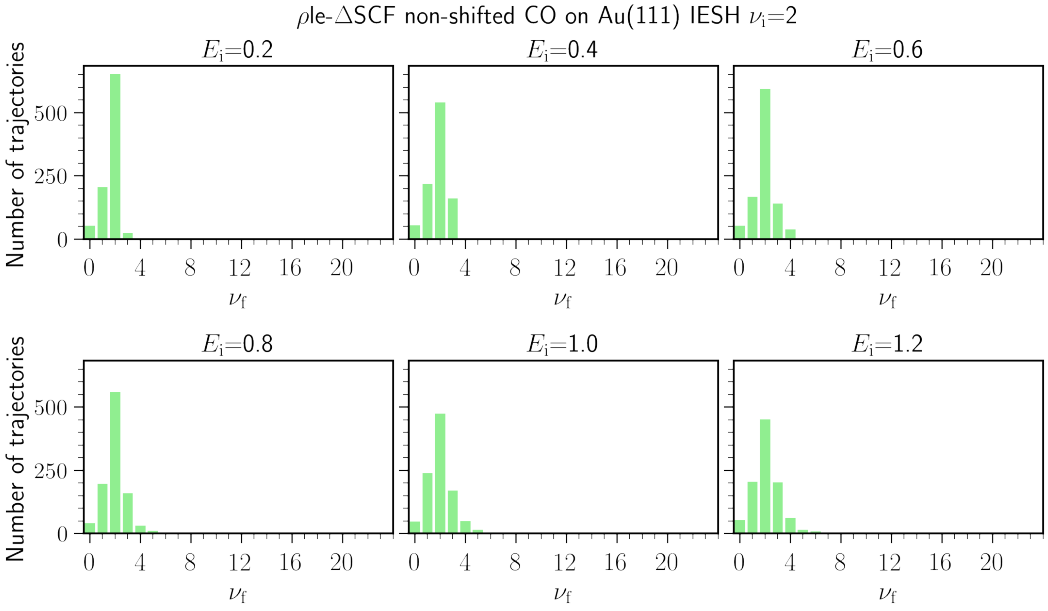

Figure B.2: IESH final state distributions for the non-shifted ρle-ΔSCF CO-Au PES set where $\nu_i = 2$. The value of E_i is indicated at the top of each subplot

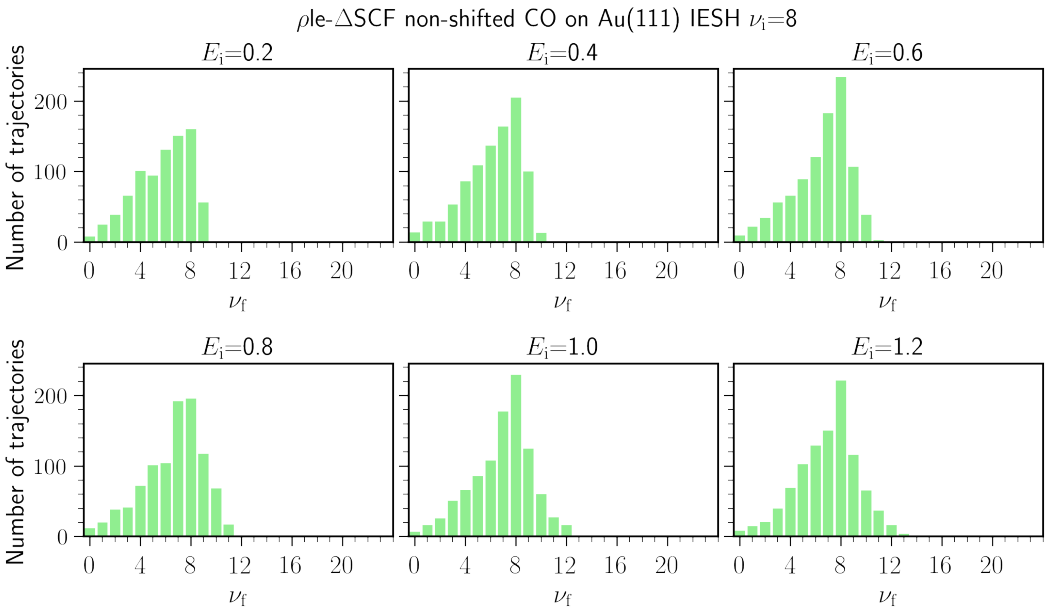

Figure B.3: IESH final state distributions for the non-shifted ρle-ΔSCF CO-Au PES set where $\nu_i = 8$. The value of E_i is indicated at the top of each subplot

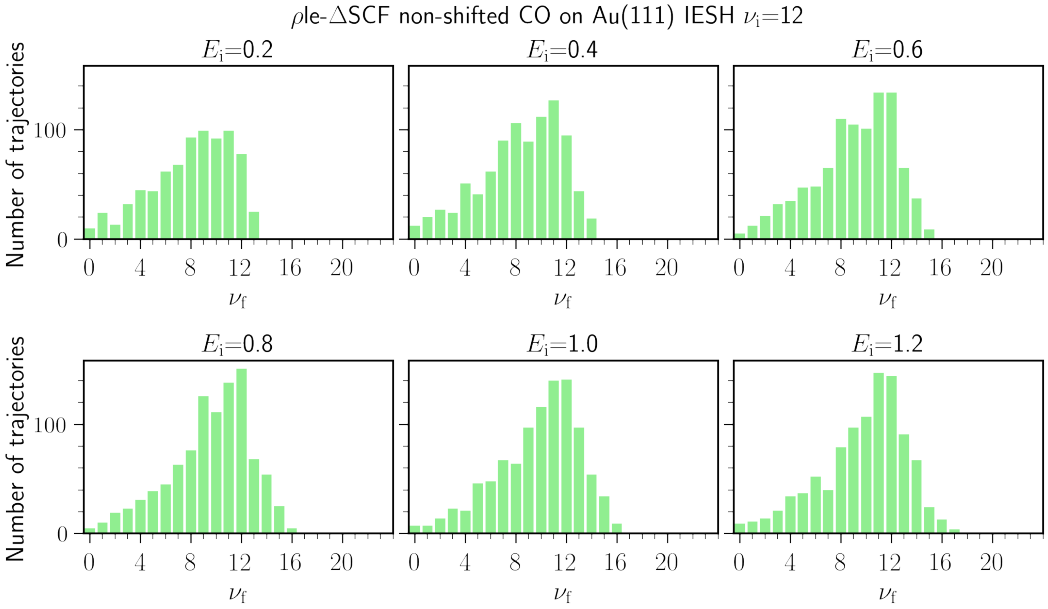

Figure B.4: IESH final state distributions for the non-shifted ρle-ΔSCF CO-Au PES set where $\nu_i = 12$. The value of E_i is indicated at the top of each subplot

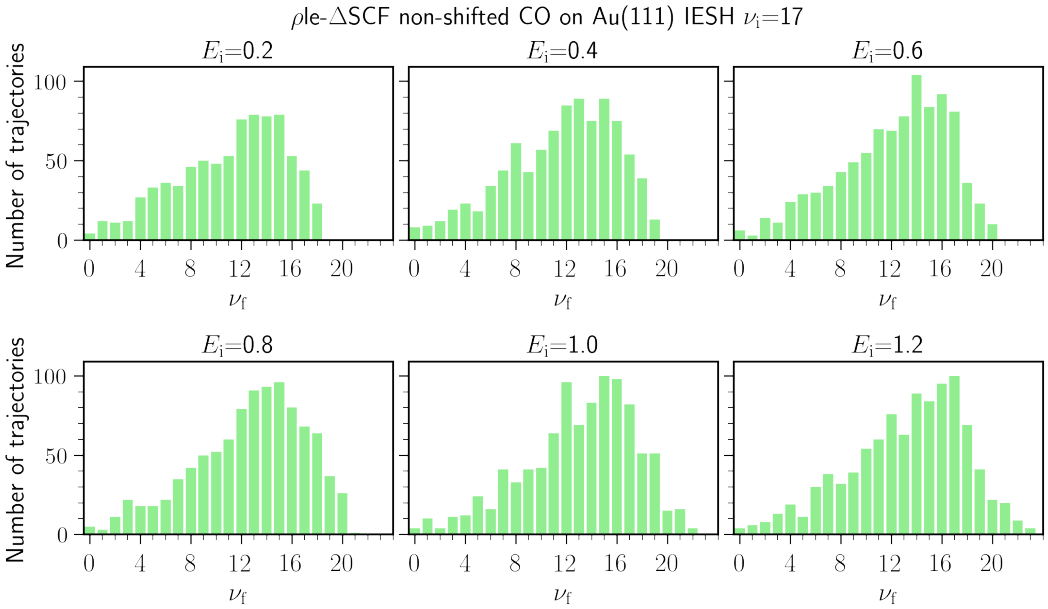

Figure B.5: IESH final state distributions for the non-shifted ρle-ΔSCF CO-Au PES set where $\nu_i = 17$. The value of E_i is indicated at the top of each subplot

B.1.2 Shifted PES IESH dynamics

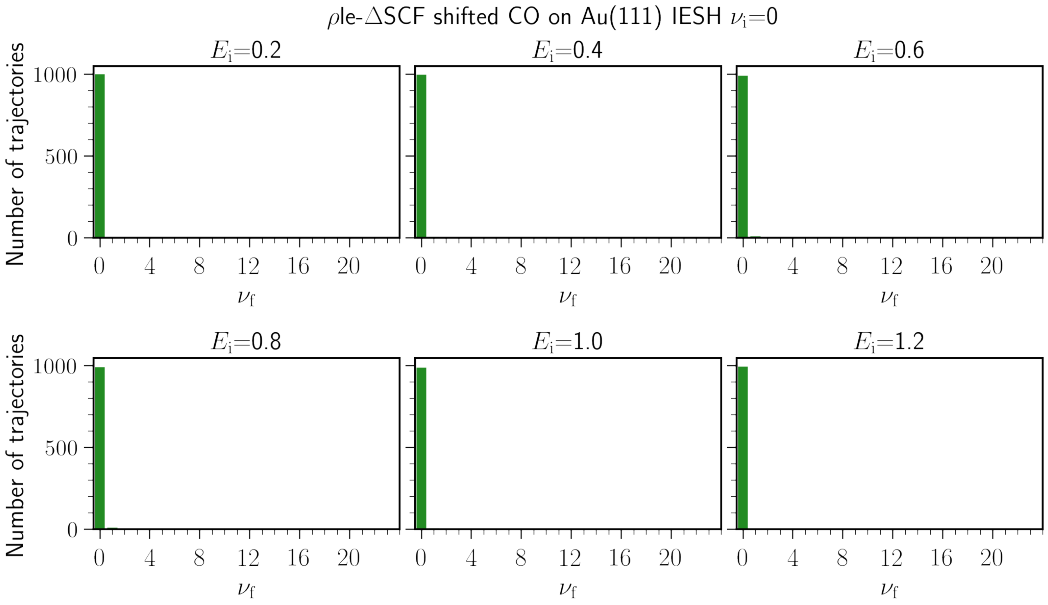

Figure B.6: IESH final state distributions for the shifted ρle-ΔSCF CO-Au PES set where $\nu_i = 0$. The value of E_i is indicated at the top of each subplot

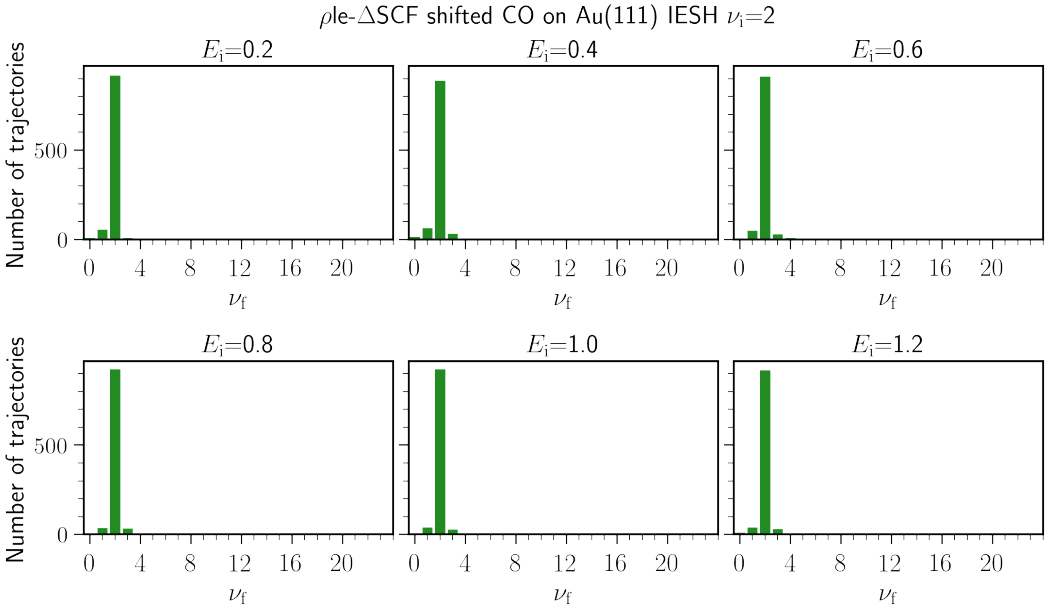

Figure B.7: IESH final state distributions for the shifted ρle-ΔSCF CO-Au PES set where $\nu_i = 2$. The value of E_i is indicated at the top of each subplot

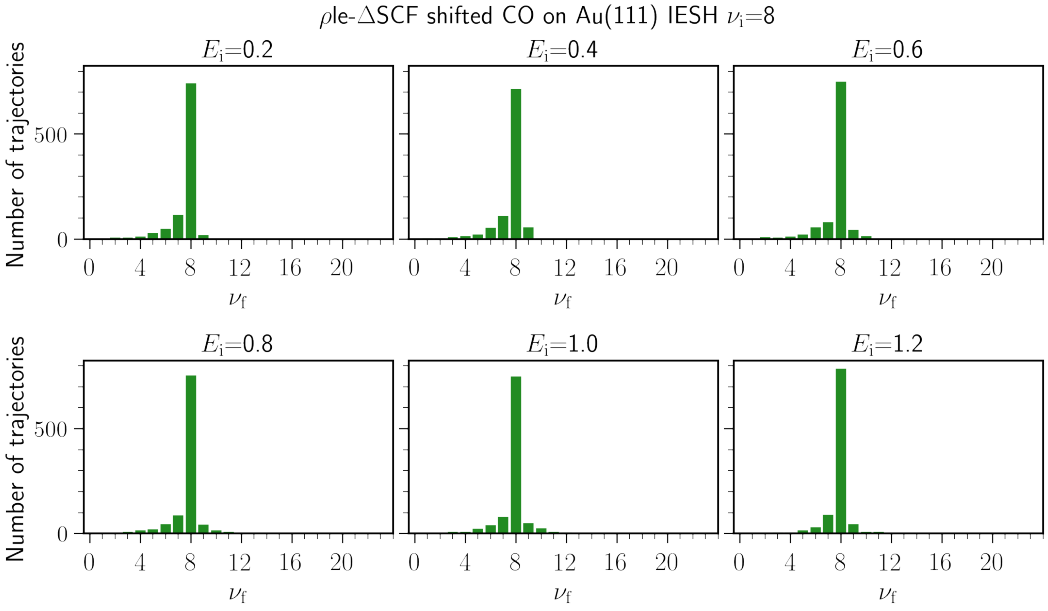

Figure B.8: IESH final state distributions for the shifted ρle-ΔSCF CO-Au PES set where $\nu_i = 8$. The value of E_i is indicated at the top of each subplot

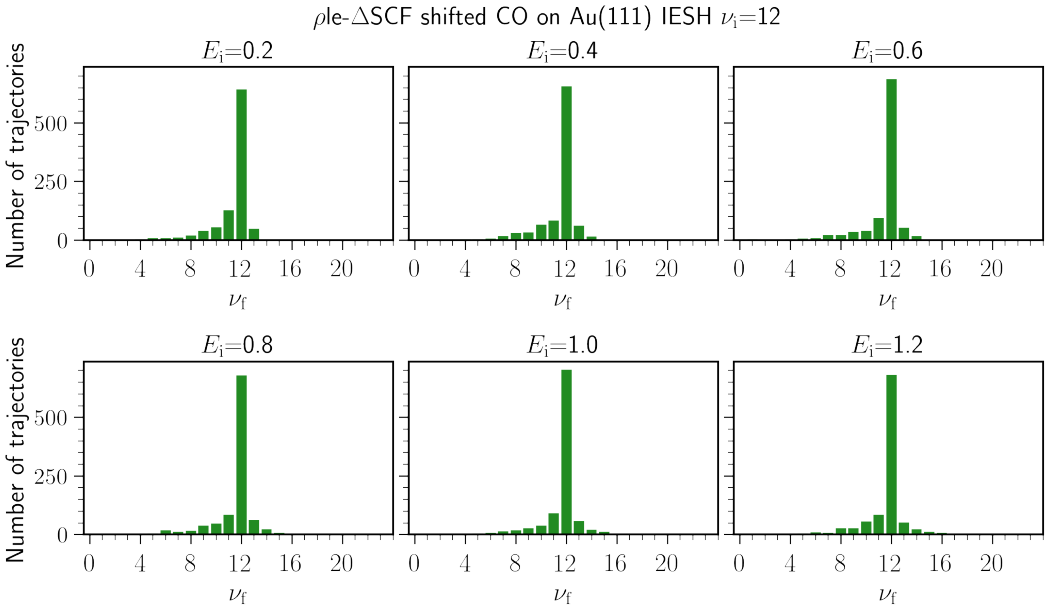

Figure B.9: IESH final state distributions for the shifted ρle-ΔSCF CO-Au PES set where $\nu_i = 12$. The value of E_i is indicated at the top of each subplot

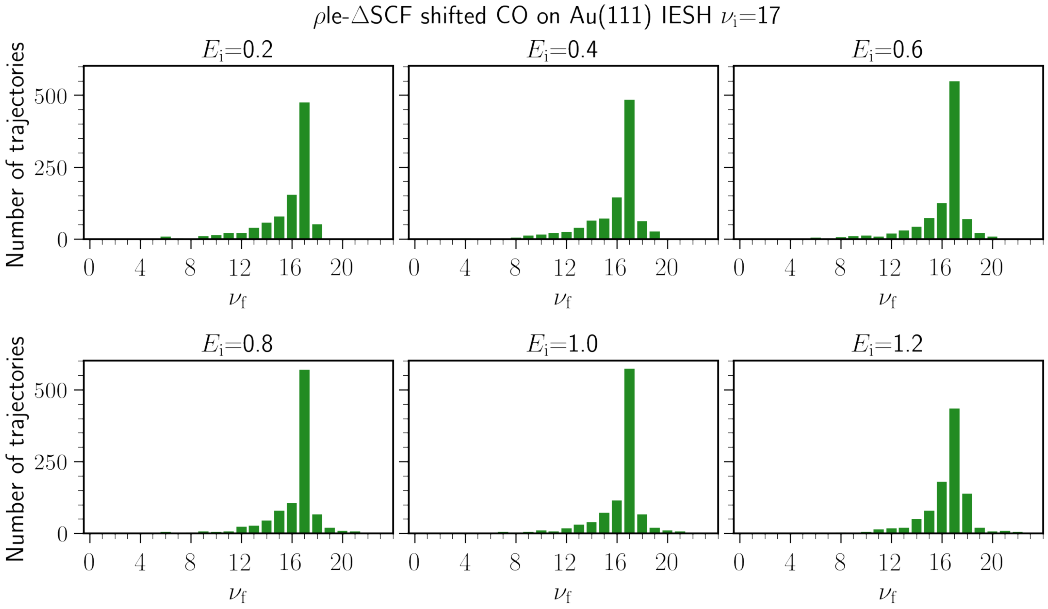

Figure B.10: IESH final state distributions for the shifted ρle-ΔSCF CO-Au PES set where $\nu_i = 17$. The value of E_i is indicated at the top of each subplot

B.1.3 Adiabatic dynamics

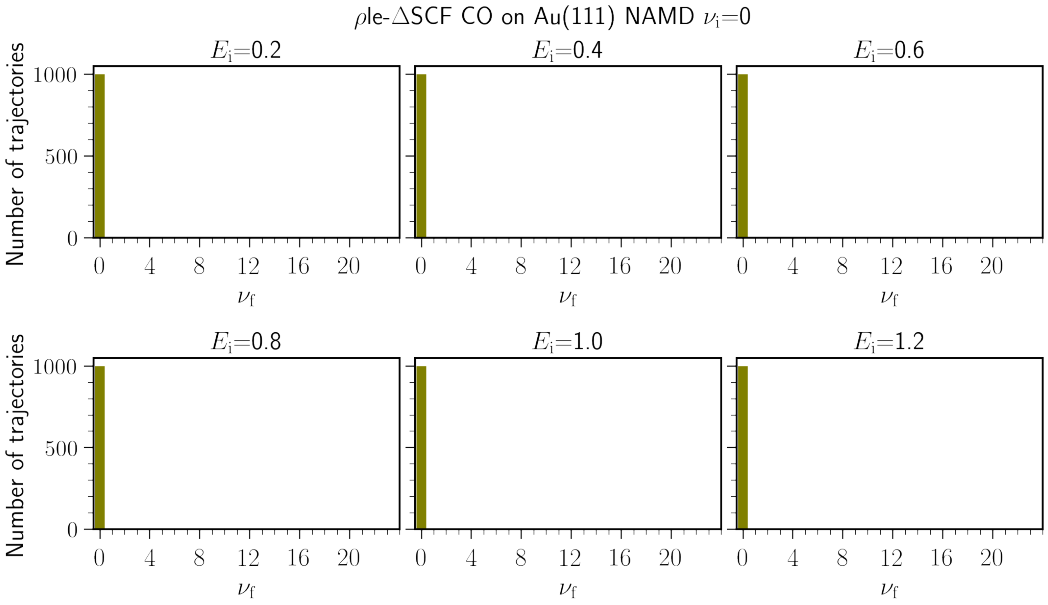

Figure B.11: Adiabatic dynamics final state distributions for the ground-state CO-Au PES associated with the ρle-ΔSCF PES set where $\nu_i = 0$. The value of E_i is indicated at the top of each subplot.

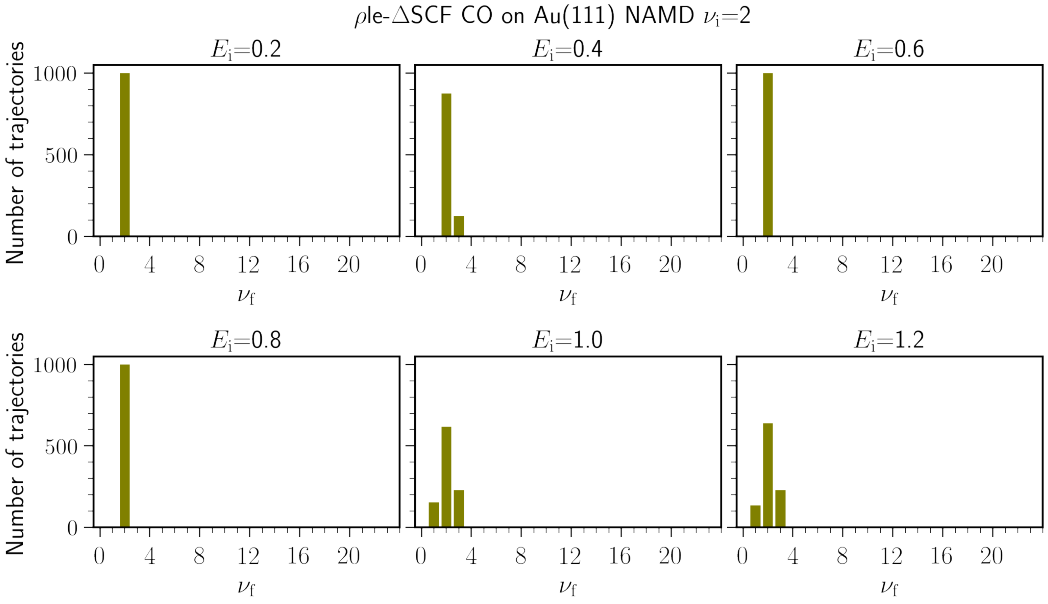

Figure B.12: Adiabatic dynamics final state distributions for the ground-state CO-Au PES associated with the ρle-ΔSCF PES set where $\nu_i = 2$. The value of E_i is indicated at the top of each subplot.

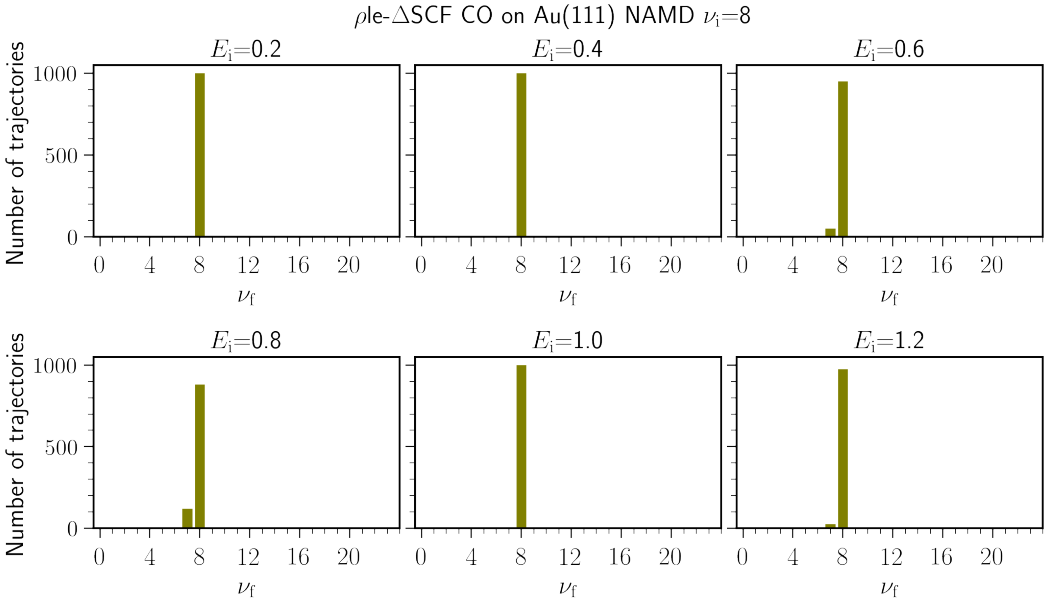

Figure B.13: Adiabatic dynamics final state distributions for the ground-state CO-Au PES associated with the ρle-ΔSCF PES set where $\nu_i = 8$. The value of E_i is indicated at the top of each subplot.

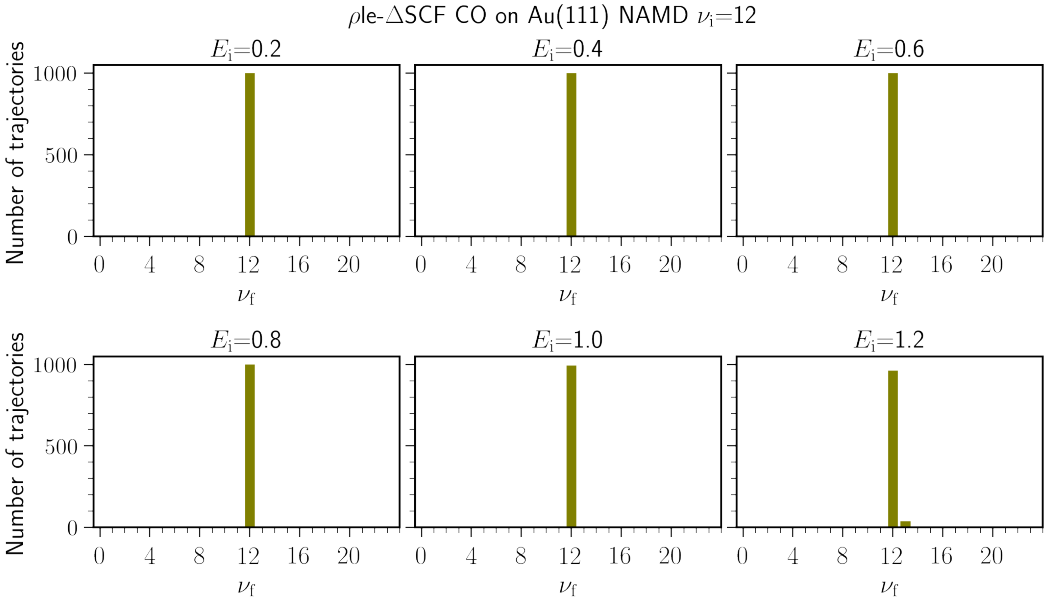

Figure B.14: Adiabatic dynamics final state distributions for the ground-state CO-Au PES associated with the ρle-ΔSCF PES set where $\nu_i = 12$. The value of E_i is indicated at the top of each subplot.

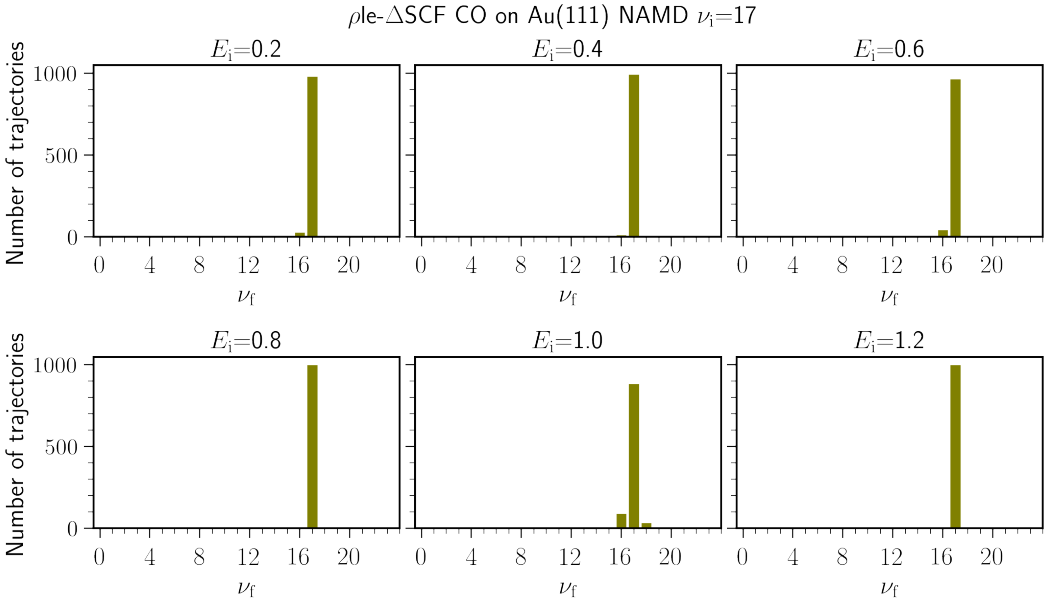

Figure B.15: Adiabatic dynamics final state distributions for the ground-state CO-Au PES associated with the ρle-ΔSCF PES set where $\nu_i = 17$. The value of E_i is indicated at the top of each subplot.

B.2 ρle-ΔSCF CO-Ag(111)

B.2.1 Non-shifted PES IESH dynamics

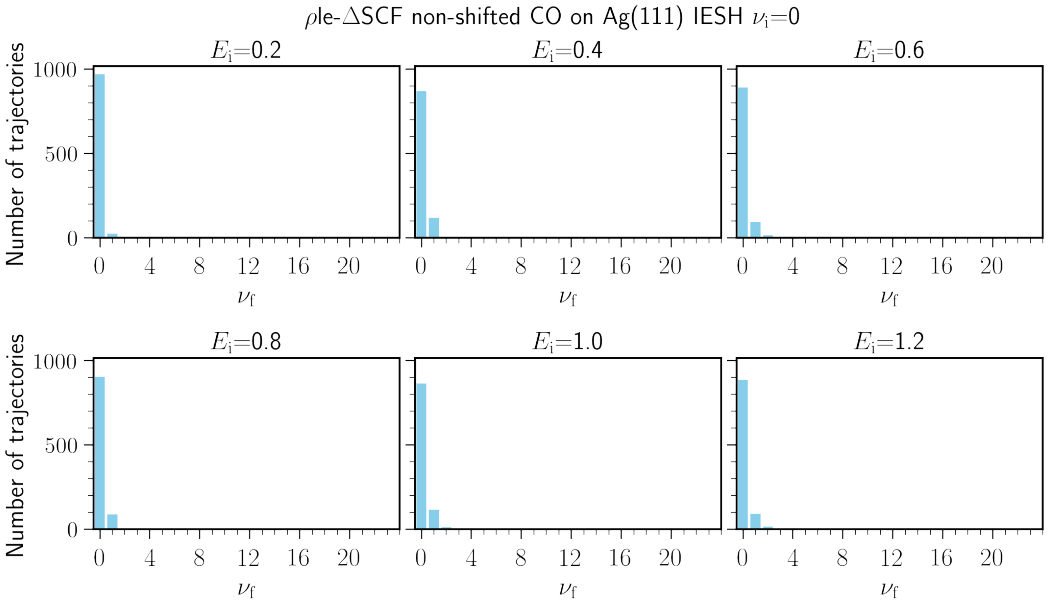

Figure B.16: IESH final state distributions for the non-shifted ρle-ΔSCF CO-Ag PES set where $\nu_i = 0$. The value of E_i is indicated at the top of each subplot

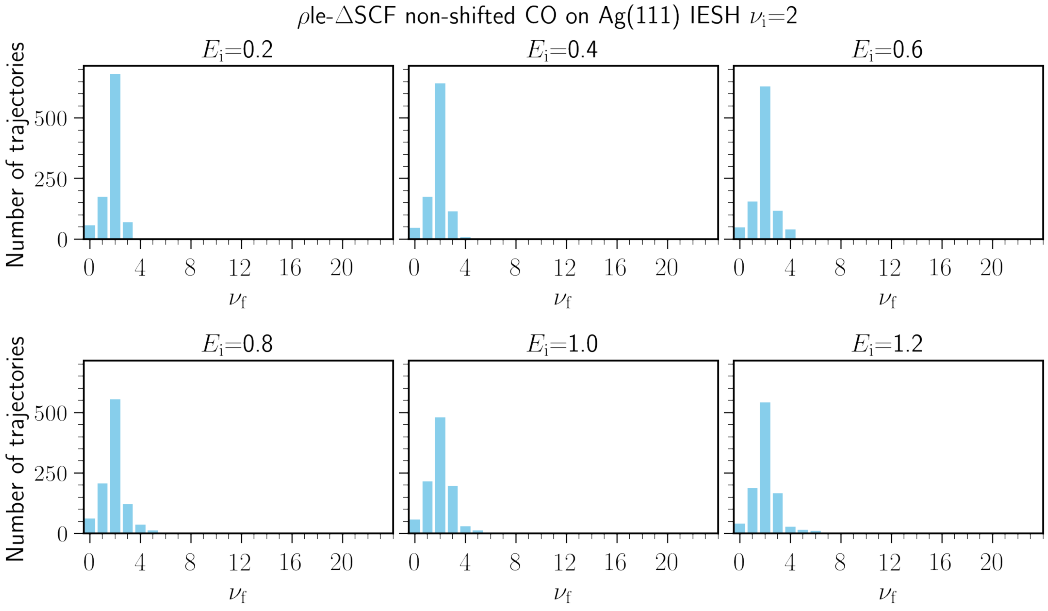

Figure B.17: IESH final state distributions for the non-shifted ρle-ΔSCF CO-Ag PES set where $\nu_i = 2$. The value of E_i is indicated at the top of each subplot

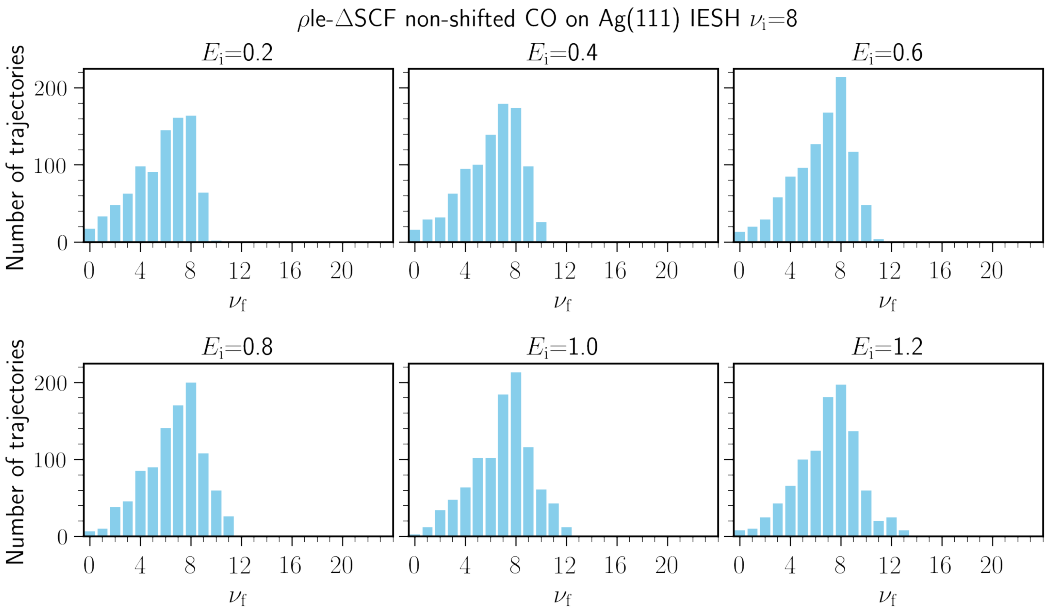

Figure B.18: IESH final state distributions for the non-shifted ρle-ΔSCF CO-Ag PES set where $\nu_i = 8$. The value of E_i is indicated at the top of each subplot

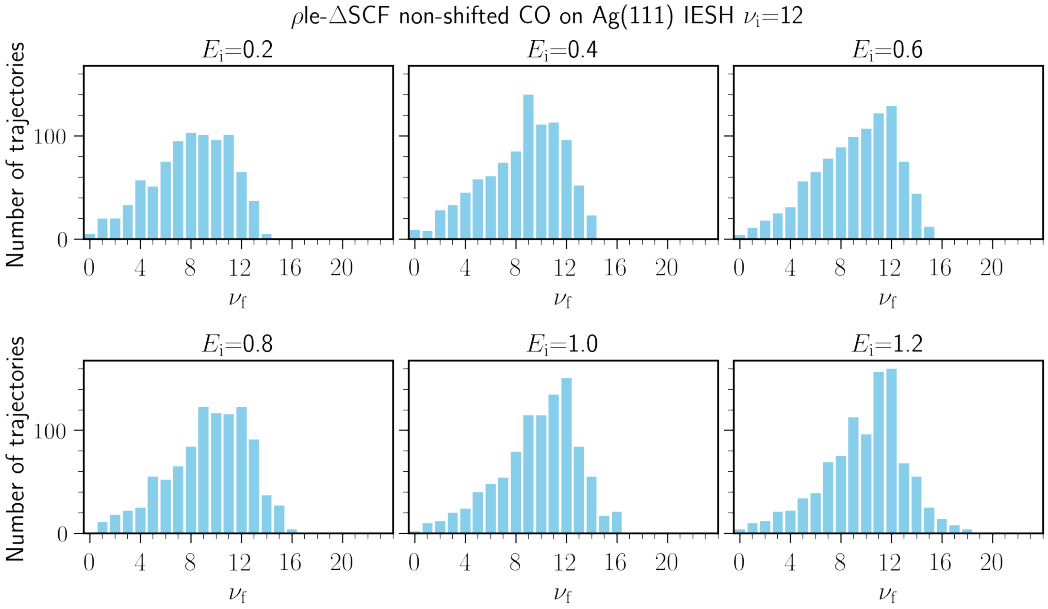

Figure B.19: IESH final state distributions for the non-shifted ρle-ΔSCF CO-Ag PES set where $\nu_i = 12$. The value of E_i is indicated at the top of each subplot

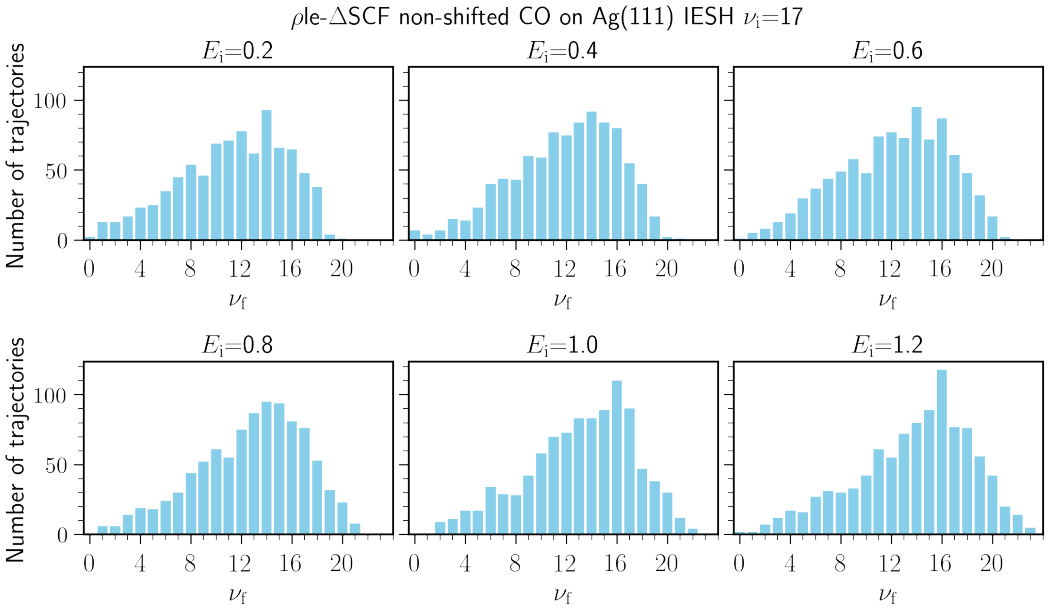

Figure B.20: IESH final state distributions for the non-shifted ρle-ΔSCF CO-Ag PES set where $\nu_i = 17$. The value of E_i is indicated at the top of each subplot

B.2.2 Shifted PES IESH dynamics

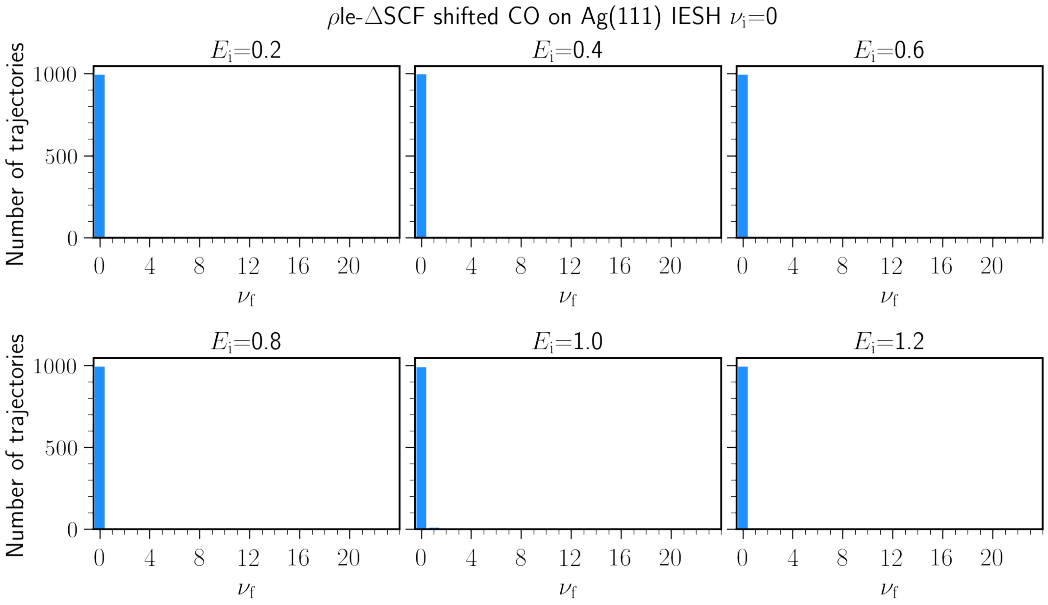

Figure B.21: IESH final state distributions for the shifted ρle-ΔSCF CO-Ag PES set where $\nu_i = 0$. The value of E_i is indicated at the top of each subplot

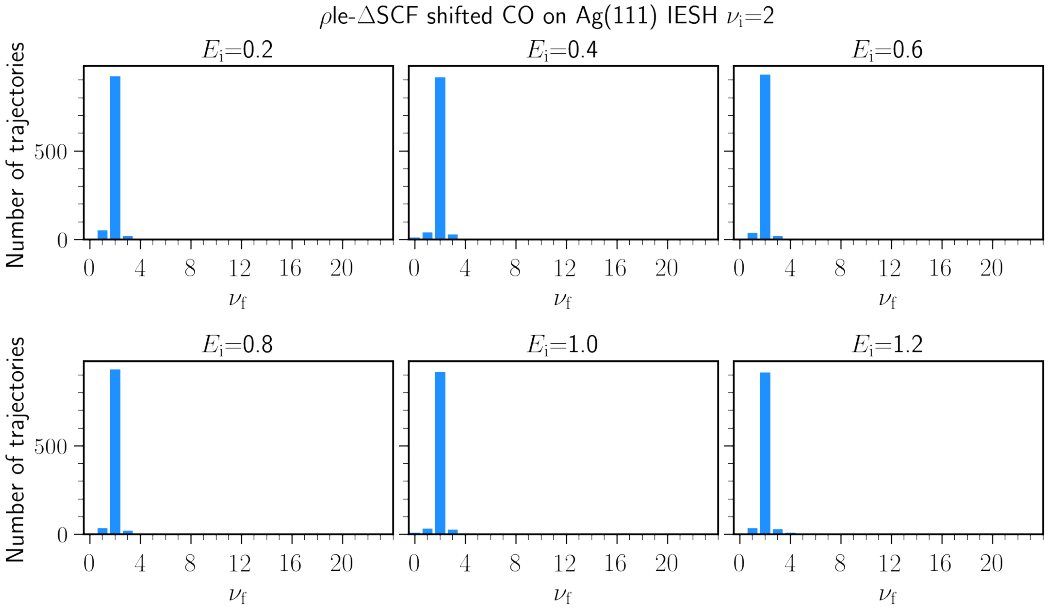

Figure B.22: IESH final state distributions for the shifted ρle-ΔSCF CO-Ag PES set where $\nu_i = 2$. The value of E_i is indicated at the top of each subplot

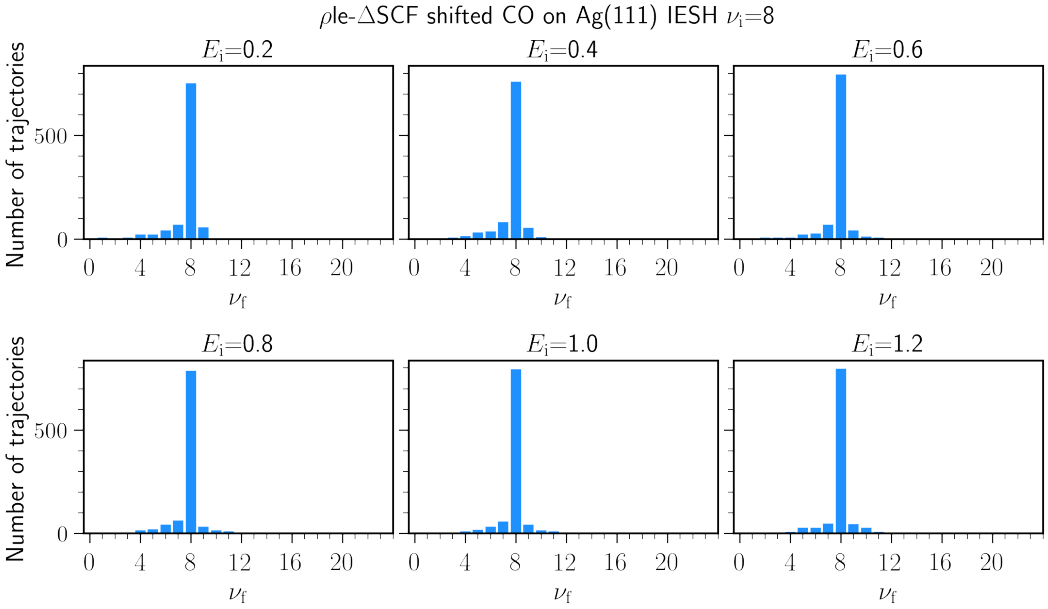

Figure B.23: IESH final state distributions for the shifted ρle-ΔSCF CO-Ag PES set where $\nu_i = 8$. The value of E_i is indicated at the top of each subplot

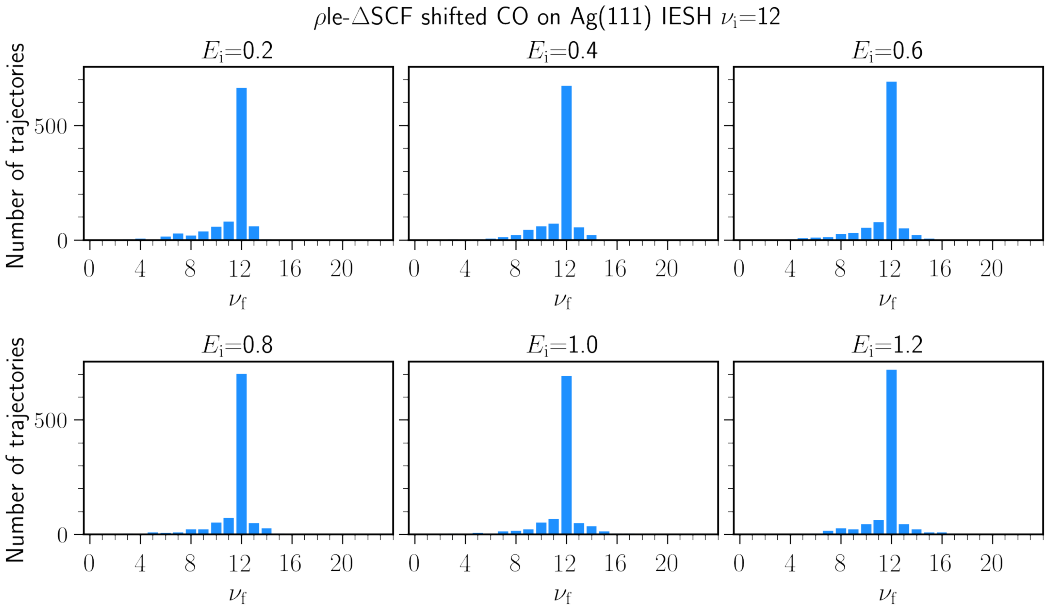

Figure B.24: IESH final state distributions for the shifted ρle-ΔSCF CO-Ag PES set where $\nu_i = 12$. The value of E_i is indicated at the top of each subplot

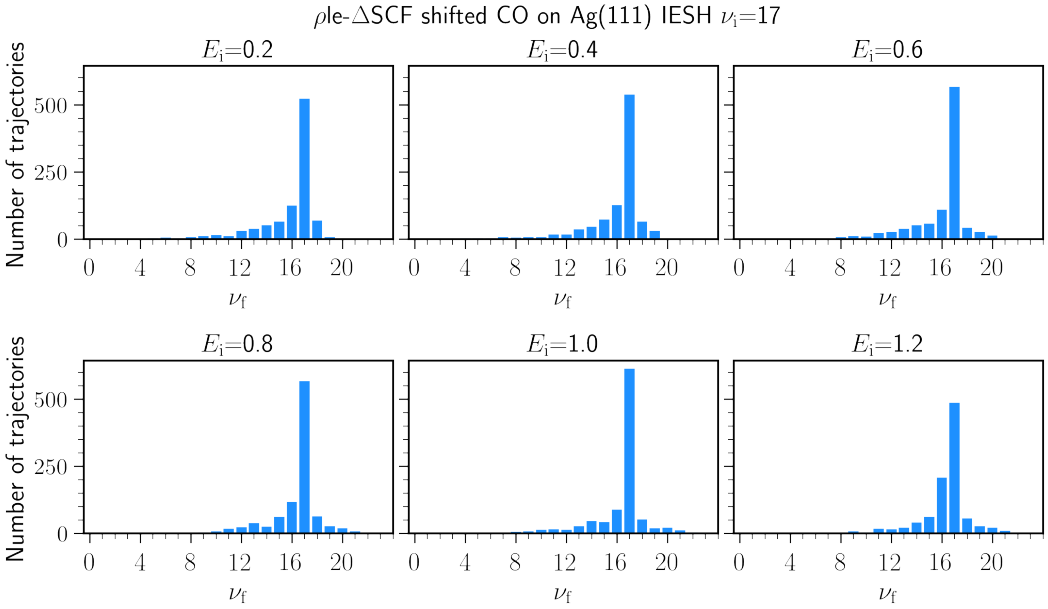

Figure B.25: IESH final state distributions for the shifted ρle-ΔSCF CO-Ag PES set where $\nu_i = 17$. The value of E_i is indicated at the top of each subplot

B.2.3 Adiabatic dynamics

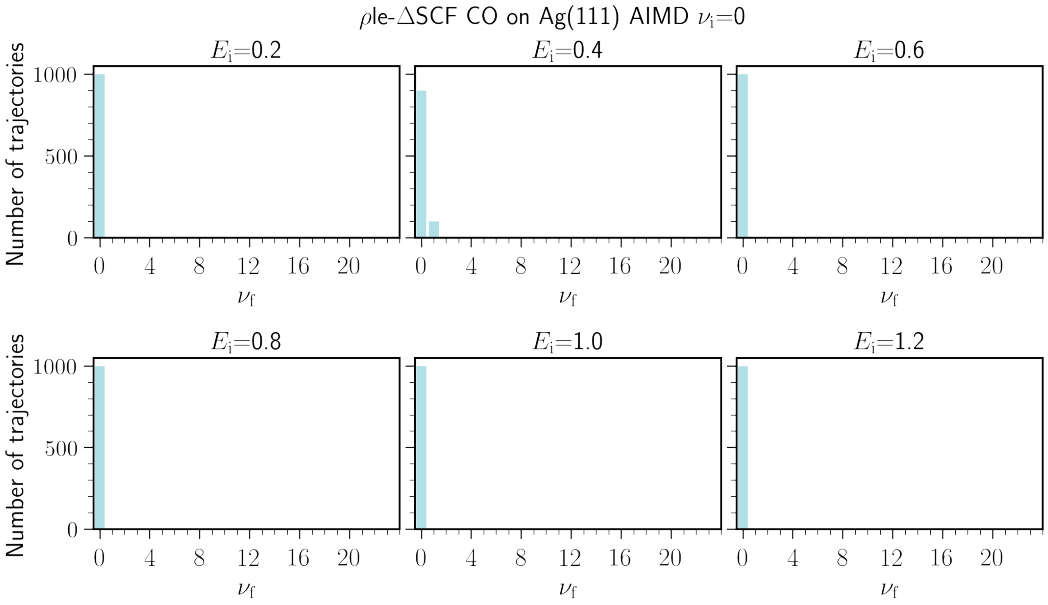

Figure B.26: Adiabatic dynamics final state distributions for the ground-state CO-Ag PES associated with the ρle-ΔSCF PES set where $\nu_i = 0$. The value of E_i is indicated at the top of each subplot.

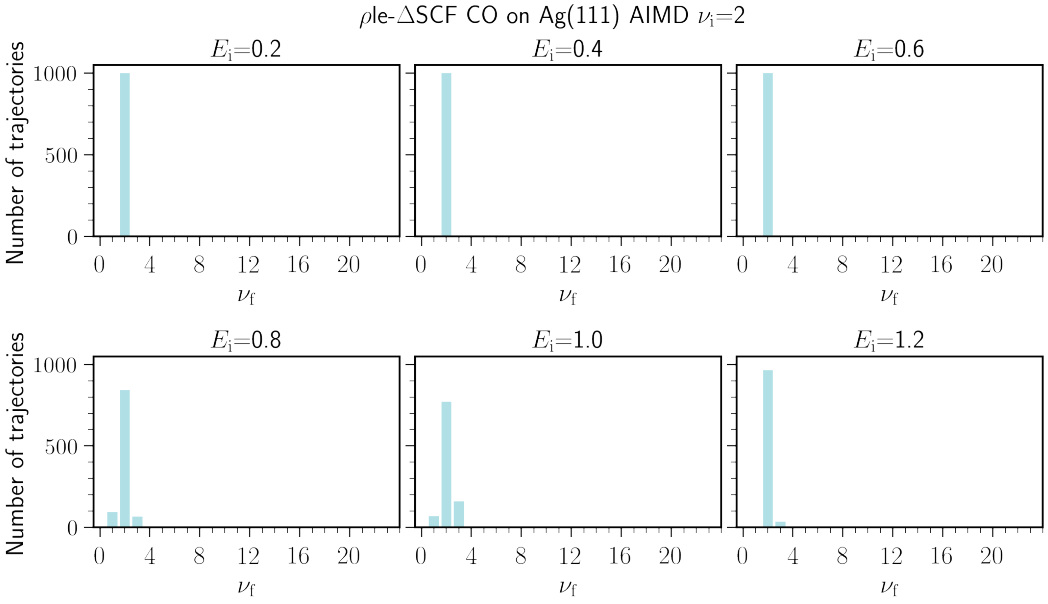

Figure B.27: Adiabatic dynamics final state distributions for the ground-state CO-Ag PES associated with the ρle-ΔSCF PES set where $\nu_i = 2$. The value of E_i is indicated at the top of each subplot.

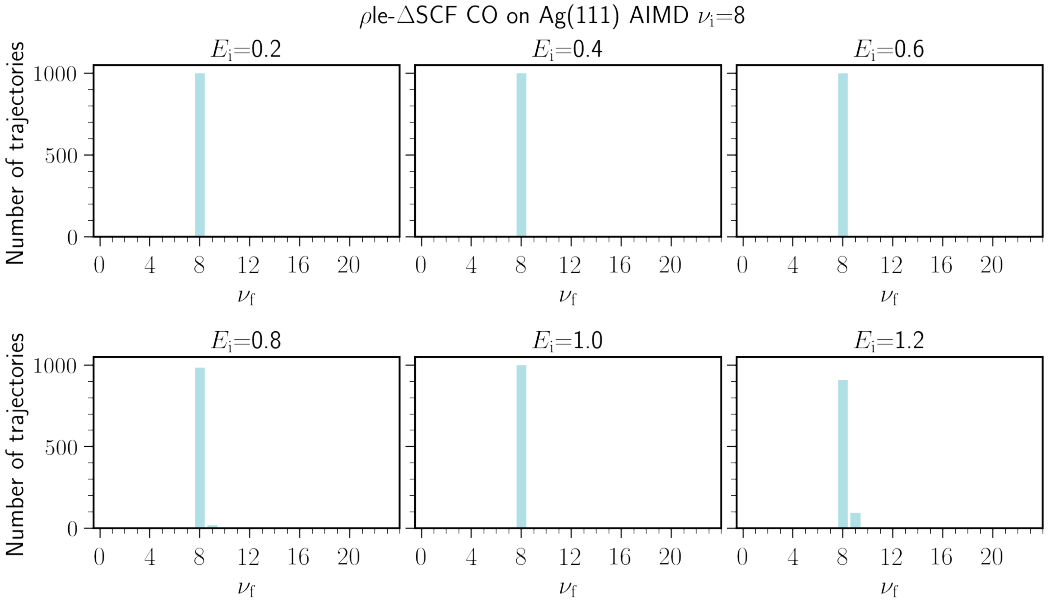

Figure B.28: Adiabatic dynamics final state distributions for the ground-state CO-Ag PES associated with the ρle-ΔSCF PES set where $\nu_i = 8$. The value of E_i is indicated at the top of each subplot.

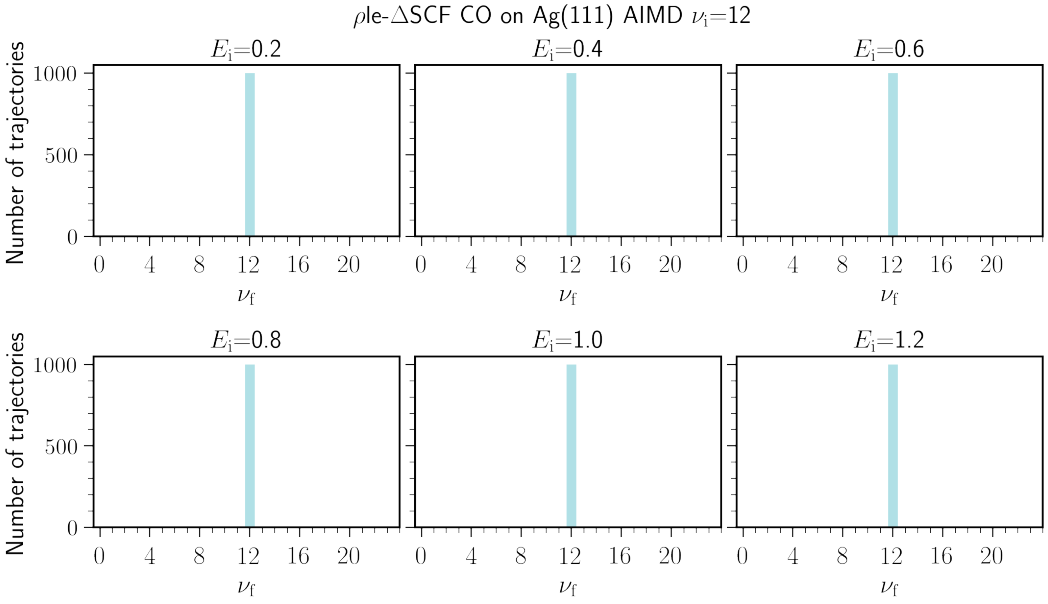

Figure B.29: Adiabatic dynamics final state distributions for the ground-state CO-Ag PES associated with the ρle-ΔSCF PES set where $\nu_i = 12$. The value of E_i is indicated at the top of each subplot.

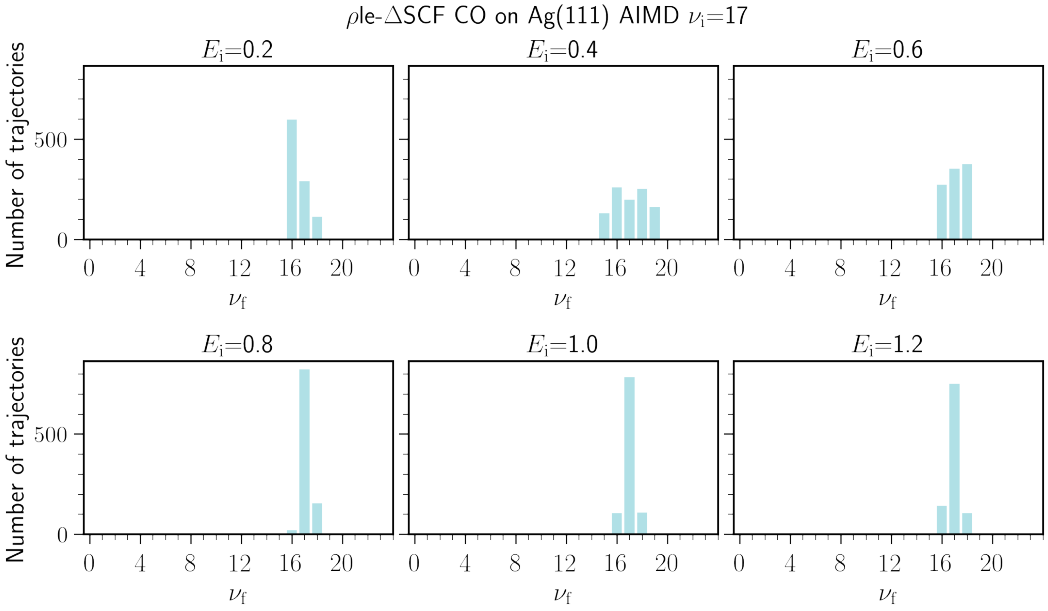

Figure B.30: Adiabatic dynamics final state distributions for the ground-state CO-Ag PES associated with the ρle-ΔSCF PES set where $\nu_i = 17$. The value of E_i is indicated at the top of each subplot.

B.3 ML-CDFT CO-Au(111)

B.3.1 IESH dynamics

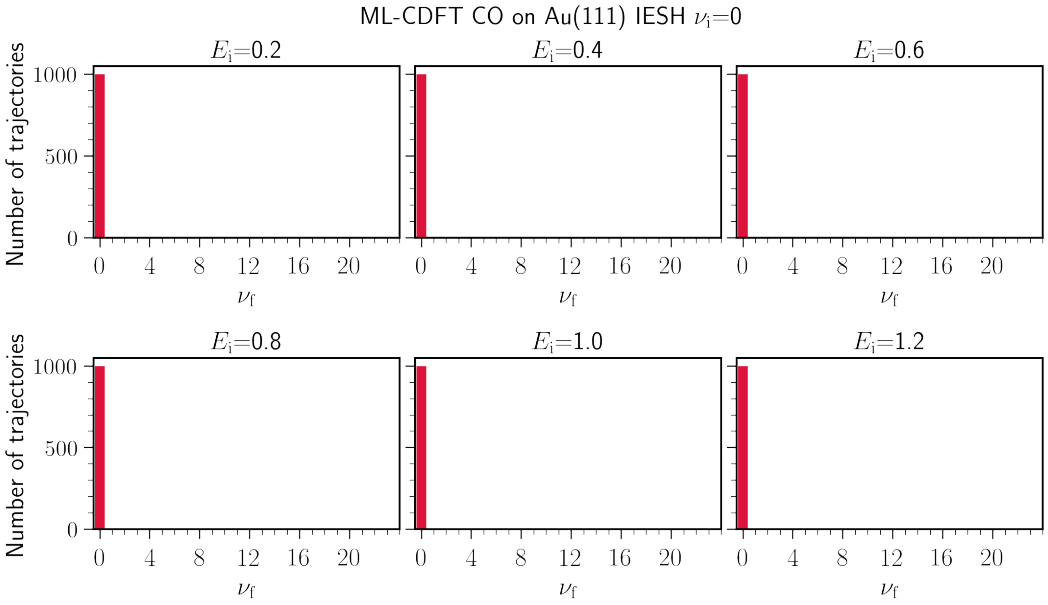

Figure B.31: IESH final state distributions for the ML-CDFT CO-Au PES set where $\nu_i = 0$. The value of E_i is indicated at the top of each subplot

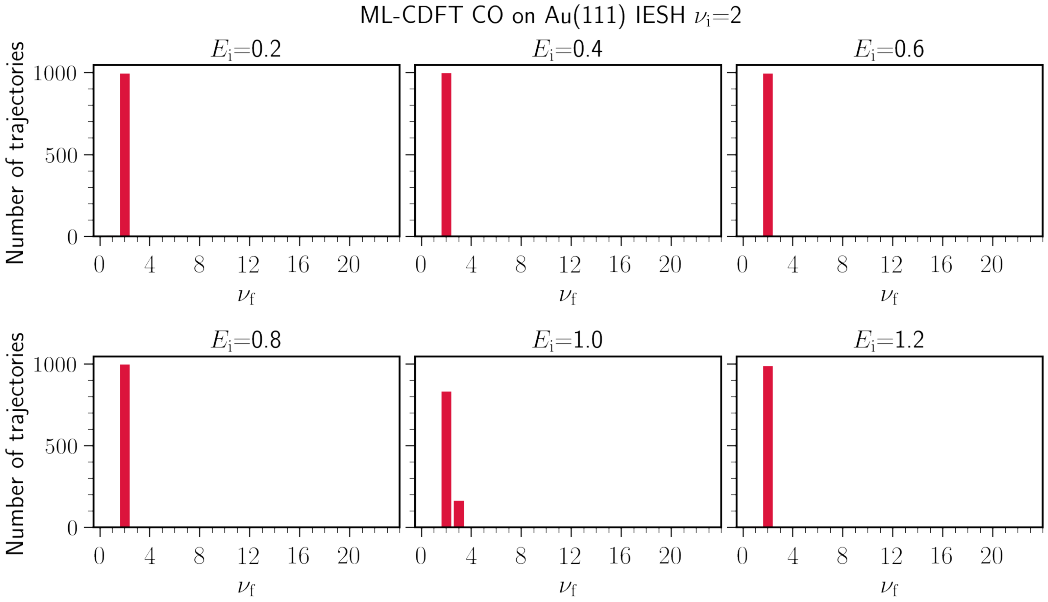

Figure B.32: IESH final state distributions for the ML-CDFT CO-Au PES set where $\nu_i = 2$. The value of E_i is indicated at the top of each subplot

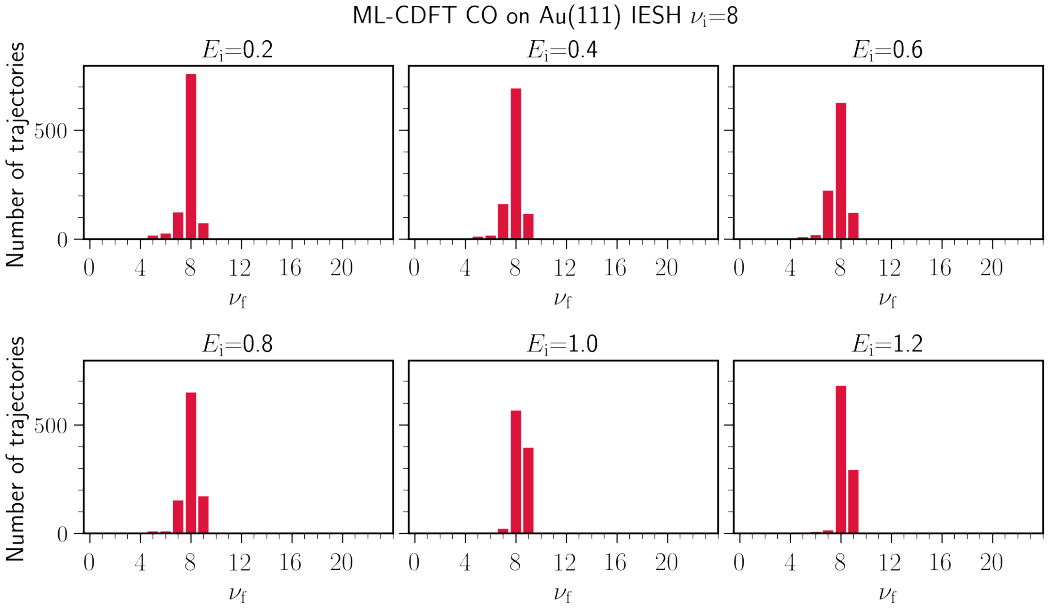

Figure B.33: IESH final state distributions for the ML-CDFT CO-Au PES set where $\nu_i = 8$. The value of E_i is indicated at the top of each subplot

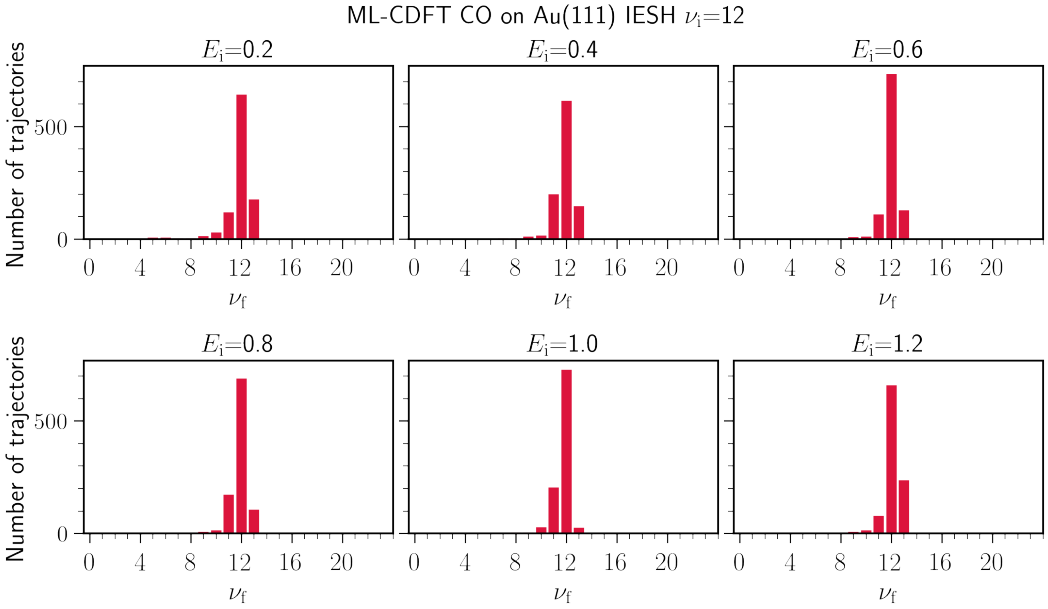

Figure B.34: IESH final state distributions for the ML-CDFT CO-Au PES set where $\nu_i = 12$. The value of E_i is indicated at the top of each subplot

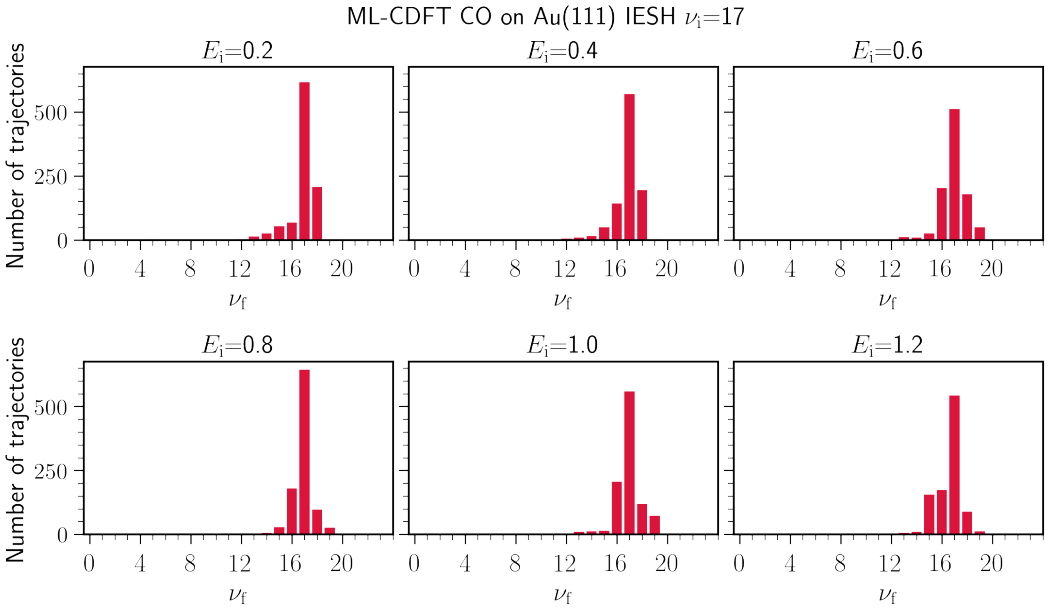

Figure B.35: IESH final state distributions for the ML-CDFT CO-Au PES set where $\nu_i = 17$. The value of E_i is indicated at the top of each subplot

B.3.2 Adiabatic dynamics

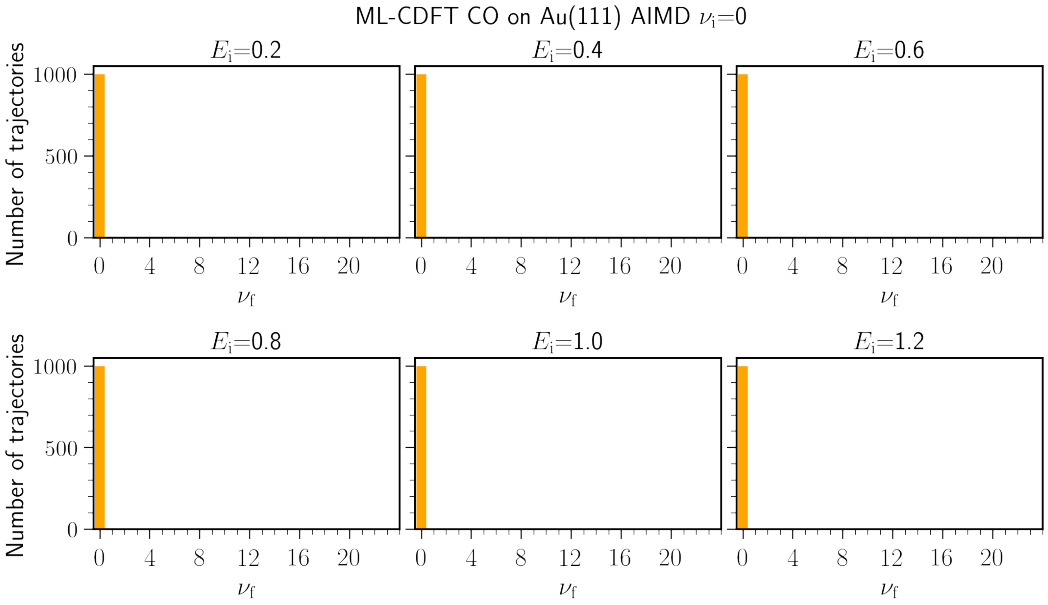

Figure B.36: Adiabatic dynamics final state distributions for the ground-state CO-Ag PES associated with the ML-CDFT PES set where $\nu_i = 0$. The value of E_i is indicated at the top of each subplot.

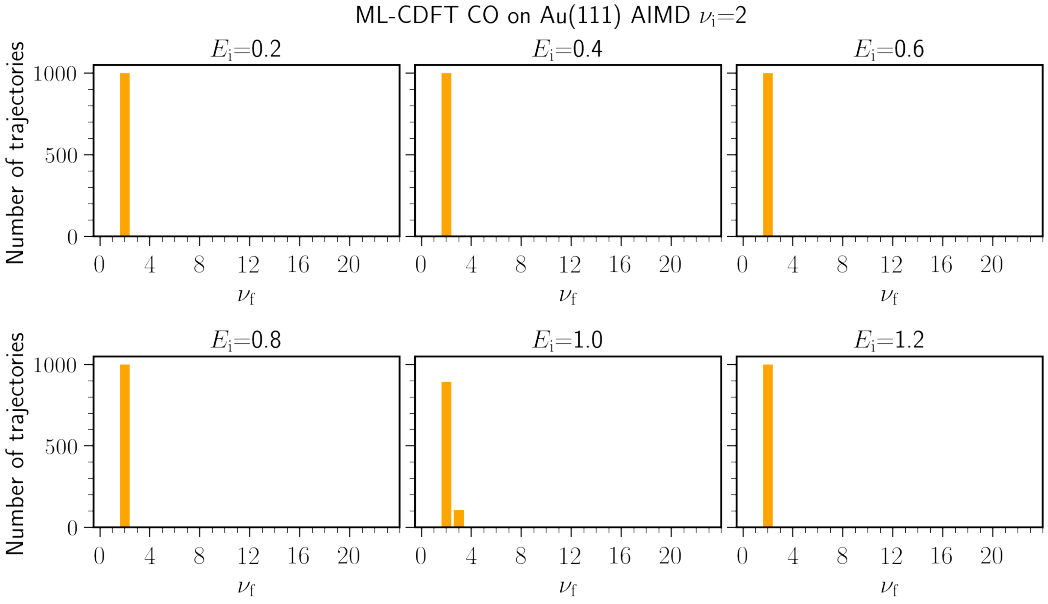

Figure B.37: Adiabatic dynamics final state distributions for the ground-state CO-Ag PES associated with the ML-CDFT PES set where $\nu_i = 2$. The value of E_i is indicated at the top of each subplot.

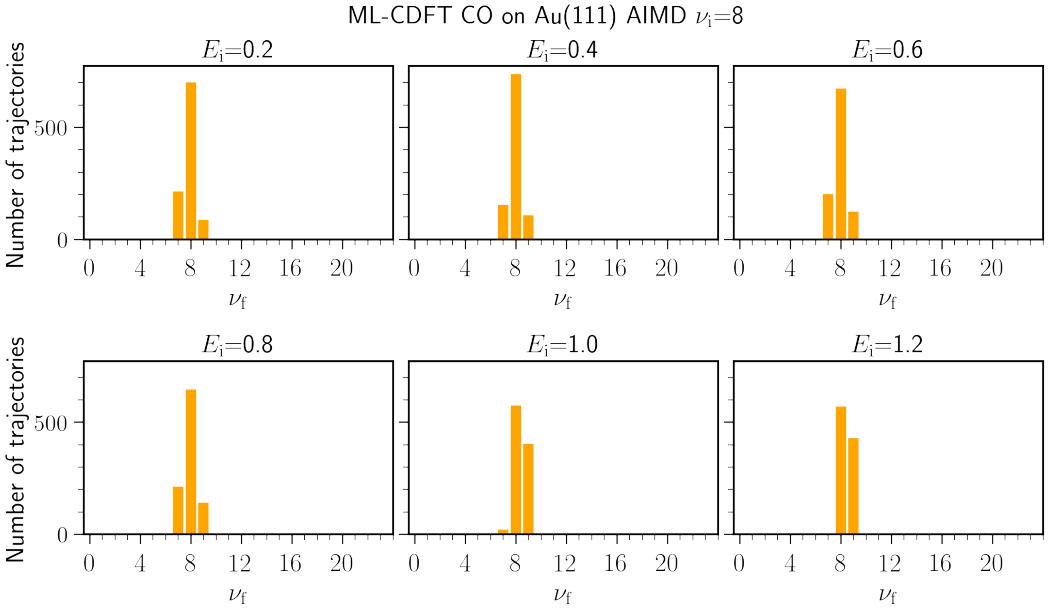

Figure B.38: Adiabatic dynamics final state distributions for the ground-state CO-Ag PES associated with the ML-CDFT PES set where $\nu_i = 8$. The value of E_i is indicated at the top of each subplot.

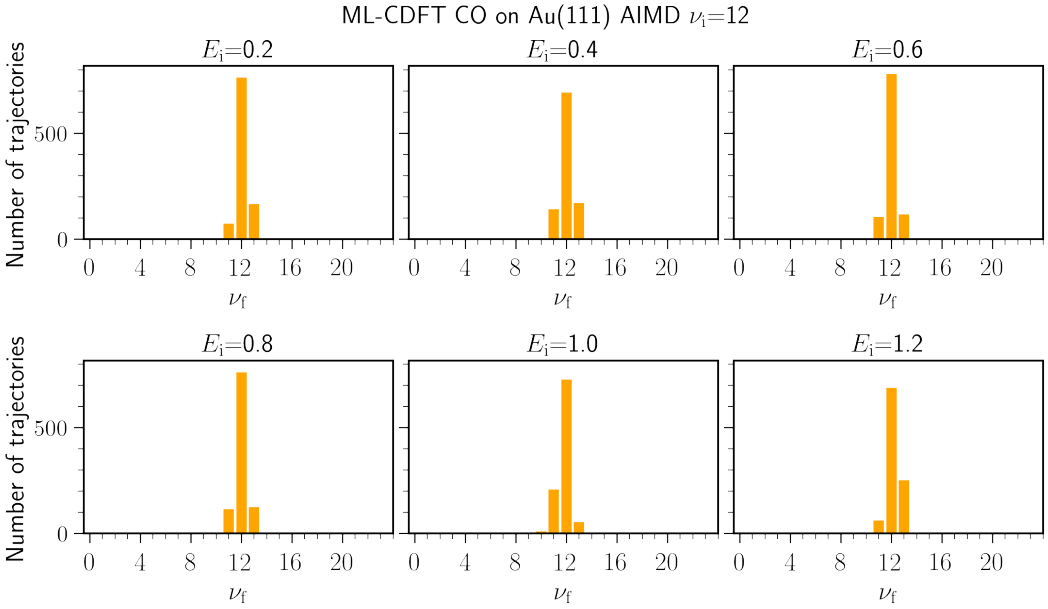

Figure B.39: Adiabatic dynamics final state distributions for the ground-state CO-Ag PES associated with the ML-CDFT PES set where $\nu_i = 12$. The value of E_i is indicated at the top of each subplot.

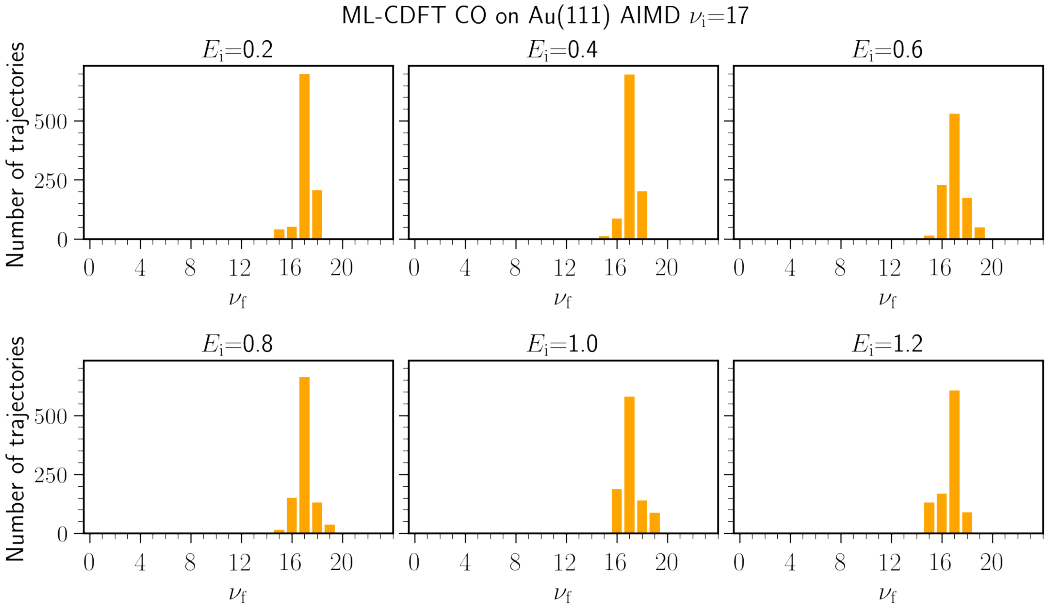

Figure B.40: Adiabatic dynamics final state distributions for the ground-state CO-Ag PES associated with the ML-CDFT PES set where $\nu_i = 17$. The value of E_i is indicated at the top of each subplot.

Bibliography

(1) D. P. Woodruff, *Modern techniques of surface science*, Cambridge University Press, Cambridge, United Kingdom, Third edition, 2016.

(2) G. A. Somorjai, *Chem. Rev.*, 1996, **96**, 1223–1236.

(3) F. Haber, *Z. Elektrochem. Angew. Phys. Chem.*, 1910, **16**, 244–246.

(4) D. Sheppard, *Roy Soc Hist. Sci.*, 2017, **71**, 263–296.

(5) J Murray, *Report of the British Association for the Advancement of Science*, Pages: 1-1382, London, 1899, vol. 68.

(6) J. Humphreys, R. Lan and S. Tao, *Adv. Energy. Sust. Res.*, 2021, **2**, 2000043.

(7) K. C. Taylor, in *Catalysis: Science and Technology Volume 5*, ed. J. R. Anderson and M. Boudart, Springer, Berlin, Heidelberg, 1984, pp. 119–170.

(8) A. Mittasch and W. Frankenburg, in ed. W. G. Frankenburg, V. I. Komarewsky and E. K. Rideal, Academic Press, 1950, vol. 2, pp. 81–104.

(9) K. Golibrzuch, N. Bartels, D. J. Auerbach and A. M. Wodtke, *Annu. Rev. Phys. Chem.*, 2015, **66**, 399–425.

(10) A. M. Wodtke, *Chem. Soc. Rev.*, 2016, **45**, 3641–3657.

(11) P. A. M. Dirac and R. H. Fowler, *Proc. R. Soc. Lond. A*, 1929, **123**, 714–733.

(12) M. Born and R. Oppenheimer, *Ann. Phys*, 1927, **389**, 457–484.

(13) A. M. Wodtke, X. Yang and D. McGuire, *J. Mol. Spectrosc.*, 1992, **154**, 361–371.

(14) A. M. Wodtke, H. Yuhui and D. J. Auerbach, *Chem. Phys. Lett.*, 2005, **414**, 138–142.

(15) A Wodtke, D Matsiev and D Auerbach, *Prog. Surf. Sci.*, 2008, **83**, 167–214.

(16) J. Gavnholt, T. Olsen, M. Engelund and J. Schiøtz, *Phys. Rev. B*, 2008, **78**, 075441.

(17) R. J. Maurer and K. Reuter, *J. Chem. Phys.*, 2013, **139**, 014708.

(18) N. Shenvi, S. Roy and J. C. Tully, *J. Chem. Phys.*, 2009, **130**, 174107.

(19) S. Roy, N. A. Shenvi and J. C. Tully, *J. Chem. Phys.*, 2009, **130**, 174716.

(20) E. Schrödinger, *Ann. Phys*, 1926, **384**, 361–376.

(21) A. Szabo and N. Ostlund, *Modern Quantum Chemistry:Introduction to advanced electronic structure theory*, General Publishing Company Ltd., 1st edn., 1996.

(22) J. C. Slater, *Phys. Rev.*, 1928, **32**, 339–348.

(23) D. R. Hartree, *Math. Proc. Camb. Phil. Soc.*, 1928, **24**, 111–132.

(24) V. Fock, *Z. Physik*, 1930, **61**, 126–148.

(25) V. Magnasco, in *Elementary Molecular Quantum Mechanics (Second Edition)*, ed. V. Magnasco, Elsevier, Oxford, Second Edition, 2013, pp. 681–722.

(26) L. H. Thomas, *Math. Proc. Camb. Phil. Soc.*, 1927, **23**, 542–548.

(27) E. Fermi, *Z. Physik*, 1928, **48**, 73–79.

(28) P. Hohenberg and W. Kohn, *Phys. Rev.*, 1964, **136**, B864–B871.

(29) J. T. Chayes, L. Chayes and M. B. Ruskai, *J Stat Phys*, 1985, **38**, 497–518.

(30) W. Kohn and L. J. Sham, *Phys. Rev.*, 1965, **140**, A1133–A1138.

(31) E. Runge and E. K. U. Gross, *Phys. Rev. Lett.*, 1984, **52**, Publisher: American Physical Society, 997–1000.

(32) M. R. Silva-Junior, M. Schreiber, S. P. A. Sauer and W. Thiel, *J. Chem. Phys.*, 2008, **129**, 104103.

(33) E. Brémond, M. Savarese, C. Adamo and D. Jacquemin, *J. Chem. Theory Comput.*, 2018, **14**, 3715–3727.

(34) A. Dreuw, G. R. Fleming and M. Head-Gordon, *J. Phys. Chem. B*, 2003, **107**, 6500–6503.

(35) D. J. Tozer, R. D. Amos, N. C. Handy, B. O. Roos and L. Serrano-Andres, *Mol. Phys.*, 1999, **97**, 859–868.

(36) A. L. Sobolewski and W. Domcke, *Chem. Phys.*, 2003, **294**, 73–83.

(37) T. Kowalczyk, S. R. Yost and T. V. Voorhis, *J. Chem. Phys.*, 2011, **134**, 054128.

(38) E. Clementi, C. C. J. Roothaan and M. Yoshimine, *Phys. Rev.*, 1962, **127**, 1618–1620.

(39) O. Gunnarsson and B. I. Lundqvist, *Phys. Rev. B*, 1976, **13**, 4274–4298.

(40) T. Ziegler, A. Rauk and E. J. Baerends, *Theoret. Chim. Acta*, 1977, **43**, 261–271.

(41) U. von Barth, *Phys. Rev. A*, 1979, **20**, 1693–1703.

(42) A. Görling, *Phys. Rev. A*, 1999, **59**, 3359–3374.

(43) A. Dittmer, R. Izsák, F. Neese and D. Maganas, *Inorg. Chem.*, 2019, **58**, 9303–9315.

(44) T. Olsen, J. Gavnholt and J. Schiøtz, *Phys. Rev. B*, 2009, **79**, 035403.

(45) R. J. Maurer and K. Reuter, *J. Phys.: Condens. Matter*, 2019, **31**, 044003.

(46) B. Leimkuhler and S. Reich, *Simulating Hamiltonian Dynamics*, Cambridge University Press, Cambridge, 2005.

(47) D. M. Newns, *Phys. Rev.*, 1969, **178**, 1123–1135.

(48) W. Dou and J. E. Subotnik, *J. Phys. Chem. A*, 2020, **124**, 757–771.

(49) I. de Vega, U. Schollwöck and F. A. Wolf, *Phys. Rev. B*, 2015, **92**, 155126.

(50) D. A. Micha, *J. Chem. Phys.*, 1983, **78**, 7138–7145.

(51) Z. Kirson, R. B. Gerber, A. Nitzan and M. A. Ratner, *Surf. Sci.*, 1984, **137**, 527–550.

(52) S.-I. Sawada, A. Nitzan and H. Metiu, *Phys. Rev. B*, 1985, **32**, 851–867.

(53) M. Head-Gordon and J. C. Tully, *J. Chem. Phys.*, 1995, **103**, 10137–10145.

(54) N. Shenvi, S. Roy and J. C. Tully, *J. Chem. Phys.*, 2009, **130**, 174107.

(55) C. L. Box, Y. Zhang, R. Yin, B. Jiang and R. J. Maurer, *JACS Au*, 2021, **1**, 164–173.

(56) J. C. Tully, *J. Chem. Phys.*, 1990, **93**, 1061–1071.

(57) J. Gardner, D. Corken, S. M. Janke, S. Habershon and R. J. Maurer, *J. Chem. Phys.*, 2023, **158**, 064101.

(58) Y. T. Lee, J. D. McDonald, P. R. LeBreton and D. R. Herschbach, *Rev. Sci. Instrum.*, 1969, **40**, 1402–1408.

(59) R. Ryberg, *Surf. Sci.*, 1982, **114**, 627–641.

(60) M Morin, N. J. Levinos and A. L. Harris, *J. Chem. Phys.*, 1992, **96**, 8.

(61) H.-C. Chang and G. E. Ewing, *Phys. Rev. Lett.*, 1990, **65**, 2125–2128.

(62) A. Gross and W. Brenig, *Surf. Sci.*, 1993, **289**, 335–339.

(63) A. Gross and W. Brenig, *Chem. Phys.*, 1993, **177**, 497–508.

(64) Y Huang, A. M. Wodtke, H Hou, C. T. Rettner and D. J. Auerbach, *Phys. Rev. Lett.*, 2000, **84**, 4.

(65) N. H. Nahler, J. D. White, J. LaRue, D. J. Auerbach and A. M. Wodtke, *Science*, 2008, **321**, 1191–1194.

(66) J. D. White, J. Chen, D. Matsiev, D. J. Auerbach and A. M. Wodtke, *Nature*, 2005, **433**, 3.

(67) J. D. White, J. Chen, D. Matsiev, D. J. Auerbach and A. M. Wodtke, *J. Chem. Phys.*, 2006, **124**, 064702.

(68) N. Bartels, B. C. Krüger, S. Meyer, A. M. Wodtke and T. Schäfer, *J. Phys. Chem. Lett.*, 2013, **4**, 2367–2370.

(69) N. Bartels, B. C. Krüger, D. J. Auerbach, A. M. Wodtke and T. Schäfer, *Angew. Chem. Int. Edit.*, 2014, **53**, 13690–13694.

(70) T. Schäfer, N. Bartels, N. Hocke, X. Yang and A. M. Wodtke, *Chem. Phys. Lett.*, 2012, **535**, 1–11.

(71) N. Bartels, K. Golibrzuch, C. Bartels, L. Chen, D. J. Auerbach, A. M. Wodtke and T. Schäfer, *J. Chem. Phys.*, 2014, **140**, 054710.

(72) B. C. Krüger, S. Meyer, A. Kandratsenka, A. M. Wodtke and T. Schäfer, *J. Phys. Chem. Lett.*, 2016, **7**, 441–446.

(73) C. T. Rettner, D. J. Auerbach and H. A. Michelsen, *Phys. Rev. Lett.*, 1992, **68**, 2547–2550.

(74) R. J. V. Wagner, B. C. Krüger, G. B. Park, M. Wallrabe, A. M. Wodtke and T. Schäfer, *Phys. Chem. Chem. Phys.*, 2019, **21**, 1650–1655.

(75) D. Diesing and E. Hasselbrink, *Chem. Soc. Rev.*, 2016, **45**, 3747–3755.

(76) H. Nienhaus, *Surf. Sci. Rep.*, 2002, **45**, 1–78.

(77) H. Nienhaus, H. Bergh, B. Gergen, A. Majumdar, W. Weinberg and E. McFarland, *Surf. Sci.*, 2000, **445**, 335–342.

(78) J. E. Hurst, C. A. Becker, J. P. Cowin, K. C. Janda, L. Wharton and D. J. Auerbach, *Phys. Rev. Lett.*, 1979, **43**, 1175–1177.

(79) B. Gergen, H. Nienhaus, W. H. Weinberg and E. W. McFarland, *Science*, 2001, **294**, 2521–2523.

(80) N. Gerrits, E. W. Smeets, S. Vuckovic, A. D. Powell, K. Doblhoff-Dier and G.-J. Kroes, *J. Phys. Chem. Lett.*, 2020, **11**, 10552–10560.

(81) V. N. Staroverov, G. E. Scuseria, J. Tao and J. P. Perdew, *Phys. Rev. B*, 2004, **69**, 075102.

(82) S. J. Clark, M. D. Segall, C. J. Pickard, P. J. Hasnip, M. I. J. Probert, K. Refson and M. C. Payne, *J. Crystallorg. Cryst. Mat.*, 2005, **220**, 567–570.

(83) J. J. Mortensen, L. B. Hansen and K. W. Jacobsen, *Phys. Rev. B*, 2005, **71**, 035109.

(84) P. E. Blöchl, C. J. Först and J. Schimpl, *Bull Mater Sci*, 2003, **26**, 33–41.

(85) M. Head-Gordon and J. C. Tully, *J. Chem. Phys.*, 1995, **103**, 10137–10145.

(86) N. Shenvi, S. Roy and J. C. Tully, *Science*, 2009, **326**, 829–832.

(87) S. Monturet and P. Saalfrank, *Phys. Rev. B*, 2010, **82**, 075404.

(88) K. Golibrzuch, A. Kandratsenka, I. Rahinov, R. Cooper, D. J. Auerbach, A. M. Wodtke and C. Bartels, *J. Phys. Chem. A*, 2013, **117**, 7091–7101.

(89) S. Roy, N. A. Shenvi and J. C. Tully, *J. Chem. Phys.*, 2009, **130**, 174716.

(90) J. Enkovaara, C. Rostgaard, J. J. Mortensen, J. Chen, M. Dułak, L. Ferrighi, J. Gavnholt, C. Glinsvad, V. Haikola, H. A. Hansen, H. H. Kristoffersen, M. Kuisma, A. H. Larsen, L. Lehtovaara, M. Ljungberg, O. Lopez-Acevedo, P. G. Moses, J. Ojanen, T. Olsen, V. Petzold, N. A. Romero, J. Stausholm-Møller, M. Strange, G. A. Tritsaris, M. Vanin, M. Walter, B. Hammer, H. Häkkinen, G. K. H. Madsen, R. M. Nieminen, J. K. Nørskov, M. Puska, T. T. Rantala, J. Schiøtz, K. S. Thygesen and K. W. Jacobsen, *J. Phys.: Condens. Matter*, 2010, **22**, 253202.

(91) R. Otero, A. L. Vázquez de Parga and J. M. Gallego, *Surf. Sci. Rep.*, 2017, **72**, 105–145.

(92) R. P. Feynman, *Phys. Rev.*, 1939, **56**, 340–343.

(93) G. M. Rangger, L. Romaner, G. Heimel and E. Zojer, *Surf. Interface. Ana.*, 2008, **40**, 371–378.

(94) B. Hammer, L. B. Hansen and J. K. Nørskov, *Phys. Rev. B*, 1999, **59**, 7413–7421.

(95) J. P. Perdew, K. Burke and M. Ernzerhof, *Phys. Rev. Lett.*, 1996, **77**, 3865–3868.

(96) C. G. Broyden, *Math. Comp.*, 1965, **19**, 577–593.

(97) P. Pulay, *Chem. Phys. Lett.*, 1980, **73**.

(98) R. J. Maurer, C. Freysoldt, A. M. Reilly, J. G. Brandenburg, O. T. Hofmann, T. Björkman, S. Lebègue and A. Tkatchenko, *Annu. Rev. Mater. Res.*, 2019, **49**, 1–30.

(99) H. J. Monkhorst and J. D. Pack, *Phys. Rev. B*, 1976, **13**, 5188–5192.

(100) B. Hammer and J. K. Norskov, *Nature*, 1995, **376**, 238–240.

(101) L. Pettersson and A. Nilsson, *Top. Catal.*, 2014, **57**.

(102) Y. Santiago-Rodríguez, J. A. Herron, M. C. Curet-Arana and M. Mavrikakis, *Surf. Sci.*, 2014, **627**, 57–69.

(103) B. W. J. Chen, D. Kirvassilis, Y. Bai and M. Mavrikakis, *J. Phys. Chem. C*, 2019, **123**, 7551–7566.

(104) K. Huber, *Molecular Spectra and Molecular Structure: IV. Constants of Diatomic Molecules*, Springer Science & Business Media, 2013.

(105) I. Magoulas, A. Papakondylis and A. Mavridis, *Int. J. Quantum. Chem.*, 2015, **115**, 771–778.

(106) Q. Wu and T. Van Voorhis, *Phys. Rev. A*, 2005, **72**, 024502.

(107) G. Meng and B. Jiang, *J. Chem. Phys.*, 2022, **157**, 214103.

(108) T. D. Kühne, M. Iannuzzi, M. Del Ben, V. V. Rybkin, P. Seewald, F. Stein, T. Laino, R. Z. Khaliullin, O. Schütt, F. Schiffmann, D. Golze, J. Wilhelm, S. Chulkov, M. H. Bani-Hashemian, V. Weber, U. Borštnik, M. Taillefumier, A. S. Jakobovits, A. Lazzaro, H. Pabst, T. Müller, R. Schade, M. Guidon, S. Andermatt, N. Holmberg, G. K. Schenter, A. Hehn, A. Bussy, F. Belleflamme, G. Tabacchi, A. Glöß, M. Lass, I. Bethune, C. J. Mundy, C. Plessl, M. Watkins, J. VandeVondele, M. Krack and J. Hutter, *J. Chem. Phys.*, 2020, **152**, 194103.

(109) M. Dion, H. Rydberg, E. Schröder, D. C. Langreth and B. I. Lundqvist, *Phys. Rev. Lett.*, 2004, **92**, 246401.

(110) F. L. Hirshfeld, *Theoret. Chim. Acta*, 1977, **44**, 129–138.

(111) G. Henkelman, A. Arnaldsson and H. Jónsson, *Comp. Mat. Sci.*, 2006, **36**, 354–360.

(112) J. Gardner, O. A. Douglas-Gallardo, W. G. Stark, J. Westermayr, S. M. Janke, S. Habershon and R. J. Maurer, *J. Chem. Phys.*, 2022, **156**, 174801.

(113) N. Shenvi, J. R. Schmidt, S. T. Edwards and J. C. Tully, *Phys. Rev. A*, 2008, **78**, 022502.

(114) A. J. Larkoski, D. G. Ellis and L. J. Curtis, *Am. J. Phys.*, 2006, **74**, 572–577.

(115) C. T. Rettner, *J. Chem. Phys.*, 1993, **99**, 5481–5489.

(116) C. L. Box, Y. Zhang, R. Yin, B. Jiang and R. J. Maurer, *JACS Au*, 2021, **1**, 164–173.

(117) R. J. V. Wagner, N. Henning, B. C. Krüger, G. B. Park, J. Altschäffel, A. Kandratsenka, A. M. Wodtke and T. Schäfer, *J. Phys. Chem. Lett.*, 2017, **8**, 4887–4892.

(118) Y. Huang, C. T. Rettner, D. J. Auerbach and A. M. Wodtke, *Science*, 2000, **290**, 111–114.

(119) J. W. Gadzuk, *J. Chem. Phys*, 1983, **79**, 6341–6348.

(120) C. Steinsiek, P. R. Shirhatti, J. Geweke, J. A. Lau, J. Altschäffel, A. Kandratsenka, C. Bartels and A. M. Wodtke, *J. Phys. Chem. C*, 2018, **122**, 18942–18948.

(121) J. F. Janak, *Phys. Rev. B*, 1978, **18**, 7165–7168.

(122) J. P. Perdew and M. Levy, *Phys. Rev. Lett.*, 1983, **51**, 1884–1887.

(123) E. K. U. Gross, L. N. Oliveira and W. Kohn, *Phys. Rev. A*, 1988, **37**, 2809–2820.

(124) N. Marzari, D. Vanderbilt and M. C. Payne, *Phys. Rev. Lett.*, 1997, **79**, 1337–1340.

(125) V. Blum, R. Gehrke, F. Hanke, P. Havu, V. Havu, X. Ren, K. Reuter and M. Scheffler, *Comp. Phys. Commun.*, 2009, **180**, 2175–2196.

(126) F. A. Evangelista, P. Shushkov and J. C. Tully, *J. Phys. Chem. A*, 2013, **117**, 7378–7392.

(127) M. Stella, K. Thapa, L. Genovese and L. E. Ratcliff, *J. Chem. Theory Comput.*, 2022, **18**, 3027–3038.

(128) F. Libisch, C. Huang and E. A. Carter, *Acc. Chem. Res.*, 2014, **47**, 2768–2775.